

The structure of three-dimensional sheet cavitation

PROEFSCHRIFT

ter verkrijging van de graad van doctor
aan de Technische Universiteit Delft
op gezag van de Rector Magnificus prof.dr.ir. J.T. Fokkema
voorzitter van het College voor Promoties,
in het openbaar te verdedigen op
dinsdag, 22 april 2008 om 15:00 uur

door

Evert-Jan FOETH
maritiem ingenieur
geboren te Ede

Dit proefschrift is goedgekeurd door de promotor(en)

Prof. dr. ir. T.J.C. van Terwisga

Prof. dr. ir. H.W.M. Hoeijmakers

Samenstelling promotiecommissie

Rector Magnificus, voorzitter

Prof. dr. ir. T.J.C. van Terwisga	Technische Universiteit Delft	promotor
Prof. dr. ir. H.W.M. Hoeijmakers	Universiteit Twente	promotor
Prof. dr. G. Bark	Chalmers University of Technology	
Prof. dr. J.P. Franc	Institut National Polytechnique De Grenoble	
Prof. dr. ir. A.A. van Steenhoven	Technische Universiteit Eindhoven	
Prof. dr. ir. J. Westerweel	Technische Universiteit Delft	
Dr. ir. G. Kuiper	www.cavitation.nl	

This research was financially supported by

The Dutch Technology Foundation STW (06170)

The Royal Netherlands Navy



Koninklijke Marine



Copyright ©2008 by E.J. Foeth

All rights reserved

ISBN 978-90-6464-236-4

Printed by Ponsen & Looijen bv, Wageningen

Dit werk is opgedragen aan mijn vader

Contents

Summary	9
Samenvatting	15
Nomenclature	21
Preface	25
1 Introduction	29
1.1 Introduction	29
1.1.1 Sheet cavitation	30
1.1.2 Vortex cavitation	33
1.2 An overview of previous work on cavitation	34
1.2.1 Three-dimensionality	36
1.2.2 Physical modeling	37
1.3 Objectives	38
2 Physical background	39
2.1 Introduction	39
2.2 Conservational relations	40
2.2.1 Reynolds Transport Theorem	40
2.2.2 Continuity equation	40
2.2.3 Conservation of momentum	41
2.2.4 Euler equations	42
2.2.5 Potential flow	43
2.3 Cavitation models	44
2.4 Transport of vorticity in two-phase flows	47
3 Measurement setup	57
3.1 Introduction	57
3.2 The cavitation tunnel	58
3.2.1 Water quality and leading edge roughness	61
3.3 Particle Image Velocimetry	65
3.3.1 Introduction	65

3.3.2	Application to cavitating flows	67
3.3.3	Performance of the PIV system	69
3.4	Hydrofoil geometry	70
3.4.1	Sectional profile	70
3.4.2	Geometric angle of attack of the Twist hydrofoils	72
3.5	Local pressure measurements	72
3.5.1	Placement	76
3.5.2	Sensor location	77
3.6	Force balance	78
3.7	Flow Oscillator	78
3.7.1	Introduction	78
3.7.2	Ensemble averaging	80
3.7.3	Frequency estimate	82
3.7.4	Observations	82
4	Applying Time resolved PIV to cavitating flows	85
4.1	Introduction	85
4.2	Image Analysis	87
4.2.1	Introduction	87
4.2.2	An overview of existing image analysis tools	87
4.2.3	Custom filtering	92
4.2.4	Preprocessing the PIV images	93
4.2.5	Finding the cavity interface	94
4.2.6	Time series	95
4.3	Performance of the Pre-Processing	95
4.4	Conclusions	96
5	The structure of attached cavitation	105
5.1	Introduction	105
5.2	Shedding behavior at steady inflow conditions	107
5.2.1	The Ellipse-11N hydrofoil	107
5.2.2	The Twist-8N hydrofoil	108
5.2.3	The Twist-11E hydrofoil	126
5.3	Shedding behavior at unsteady inflow conditions	129
5.3.1	The Twist-11N hydrofoil	129
5.3.2	The Twist-11E hydrofoil	132
5.4	Discussion	134
6	Conclusions and Recommendations	149
6.1	The application of PIV to cavitating flows	149
6.2	The structure of three-dimensional cavitation	150

A	Notation	157
A.1	Operators	157
A.2	Tensor operators	159
B	Uncertainty analysis and error propagation	161
C	The uncertainty in the velocity and cavitation number	170
C.1	Calibration uncertainty	170
C.2	Effects of temperature and contaminants	171
C.2.1	Velocity in the test section	173
C.2.2	Cavitation number in the test section	174
C.3	Example	175
D	PIV setup	178
D.1	Light sheet	178
D.2	Setup	179
E	Details of the hydrofoil geometry	181
E.1	NACA0009 section	181
E.2	Eppler YS-920 section	181
E.3	NACA63A010 section	181
E.4	Trailing edge thickness function	184
E.5	Geometry of the Ellipse hydrofoils	185
E.6	Miniature pressure transducer location	185
F	Force balance	187
G	Oscillator motion	191
H	Pre-processing sequence	193
I	Cavity outline sequence	196
J	Kelvin-Helmholtz instability	200
K	Additional experimental results	203
	Acknowledgements	219
	Curriculum Vitae	221

Summary

Attached cavitation is a form of cavitation that is prevalent on nearly all ship propellers. The technical and financial constraints of the hull form and propulsion plant rarely allow for a propeller with a low loading, a low rate of revolutions, and a favorable inflow. Although some science vessels and surface combatants have propellers designed to operate free of cavitation, above their so-called inception speed excessive sheet cavitation occurs. To design a propeller is to control its cavitation behavior. Although the extent of sheet cavitation can be predicted with reasonable accuracy, the collapse of that cavity (i.e., shedding) is ill-controlled and can lead to serious blade erosion and pressure fluctuations battering on the hull.

The accurate prediction of cavitation behavior is important to naval hydrodynamics and the tools to calculate that behavior require benchmark data, as well as an understanding of the mechanisms of the shedding behavior. Surprisingly, most cavitation experiments are aimed at either axisymmetric and two-dimensional objects, while the propeller is a highly three-dimensional object. In this thesis, the influence of three dimensionality is addressed by means of experiments using a series of foils with a spanwise-varying loading reminiscent to propeller loading. A gust-generator is used to simulate the inhomogeneous inflow to the propeller.

The application of PIV to cavitating flows

The application of Particle Image Velocimetry (PIV) to cavitating flows introduces several additional difficulties to the experimenter. Incident laser light reflected from the cavity can overexpose and locally saturate the camera, and even damage it. The use of fluorescent particles and optical filters is an easy and effective method to solve the problem of overexposure by removing all incident laser light and recording particles only. Nevertheless, two problems remain. The first remaining problem is the illumination of out-of-plane particles by the reflection and refraction of the light sheet, although this can be partially solved by purposely applying a very narrow focal depth so that out-of-plane particles quickly lose focus and give a low correlation (With the application of high speed PIV, the energy per pulse of the lasers is often low giving a modest light budget, so low f-stops are common). The second problem is the error introduced by the unintended correlation of vapor captured by the camera. The correlation of vapor is not necessarily a problem of PIV and

cavitating flows per se. From the two cameras that were used, no vapor was recorded when using the less sensitive (but faster) camera. One would prefer a more sensitive camera to capture more information from the light sheet. Whenever vapor is visible, the solution of the PIV interrogation will deteriorate due to correlation of illuminated vapor. This problem is inherent to the application of PIV to multiphase and multicomponent flows. Sheet cavitation is visible from length scales as large as the PIV image to the size of tracer particles, and the velocity scale of the vapor ranges to the maximum in the flow to a near standstill of vapor trapped in vaporous vortex cores. Various techniques have been proposed to distinguish between the phases, ranging from image pre-processing to processing of the so-called PIV correlation map.

The image-analysis presented in this thesis offers one solution to remove the cavity while leaving the solution of the fully-wetted flow unaffected, using an image processing kernel developed specifically for the retention of only tracer particles. Upon close inspection of the result of pre-processed and unprocessed images, it can be concluded that the solutions are virtually identical in the fully-wetted domain. With the use of synthetic PIV images it was shown that the error is reduced significantly when applying the pre-processing, so, removal of reflections by using fluorescent particles and optical filters alone is an insufficient condition for accurate PIV measurements. In order to apply PIV effectively and accurately to cavitating flows, the combined use of fluorescent particles and image pre-processing is strongly recommended.

Interface tracking

The cavitation was not visible without additional illumination with a less sensitive camera. With the use of image pre-processing, the cavity can be purposely lit and tracked. The cavity outline was deduced using a variation of image pre-processing used to track particles. So, both the velocity field and cavity outline could be determined from a single image without the need of a more complicated setup with several cameras and filters. By placing the camera perpendicular to the light sheet—placed at the plane of symmetry—with the optical axis striking the hydrofoil surface, combined with the knowledge from observations that the cavity surface is symmetric, it can be stated with confidence that the surface of the attached cavity is measured accurately even though it is a side view and not a slice of the cavity at the measurement plane. The visualizations offer an accessible view of the extent and frequency of the shedding, resolving waves on the interface of the stable cavity on the Twist-11E hydrofoil that were not visible in the observations.

Side-entrant flow

The re-entrant flow from the side of the cavity dictates the behavior of the shedding cycle and the flow from the sides depends on the cavity closure line. Its shape and motion govern

its behavior and the convex cavity shapes seem to be intrinsically unstable. The re-entrant flow direction is roughly mirrored at the cavity closure line, so the re-entrant flow can be both moving upstream but also in span wise direction denoted as the side-entrant component. For any convex cavity shapes, side-entrant components of the re-entrant flow focus in the closure region of the sheet, creating a disturbance causing a local break-off of the main sheet structure. Side-entrant components may collide before the re-entrant flow reaches the leading edge or the upstream directed re-entrant flow is too weak to cause shedding at the leading edge.

By using a hydrofoil with a flat pressure distribution—the Eppler YS-920—in a Twisted configuration, a cavity was created that was slender, covered 70% of the chord at the mid plane, and was relatively thin at moderate angles of attack. The slenderness of the cavity resulted in side-entrant jets continuously aimed at the closure causing an open closure. The thin cavity with its low pressure gradient had thin and weak re-entrant jets that did not disturb the sheet cavity upon contact. The re-entrant jet was recirculated over the cavity interface so that the cavity was stable in length for the entire observed period. From these observations follow that impingement of a re-entrant on the cavity detachment location is an insufficient condition for cloud shedding. This is distinctly different from the classical point of view that re-entrant flow always causes shedding, as is observed on two-dimensional hydrofoils.

The closure of the attached cavity

The shedding mechanism observed after side-entrant jet collision at the central plane is a pinch-off of a part of the attached cavity. The observed (cavitating) vortices after the shedding lead to the conclusion that a mixing layer is present with its characteristic span wise and stream wise vortices, clearly visible on the images presented for a large scale cavity. Thin cavities have a smooth pressure recovery at the cavity closure generating re-entrant flow with a minimum of momentum. In these experiments continuous mixing can be present with thick cavities with a significant length (over 50% chord) yet they have an open closure and do not show large structure shedding (Intermittent and irregular large structure shedding was sometimes observed). In the absence of shedding of large structures, the closure region is relatively steady with side-entrant flow continuously aimed at the same location of the sheet leading to continuous vortex shedding. A cavity does not need to be thin to have an open closure if its closure is continuously supplied with fluid from the sides. Therefore, a long and thin sheet cavity could be fully stable if its closure consists of a mixing layer and the weak adverse pressure gradient precludes the formation of a re-entrant jet as is the case on the Twist-11E hydrofoil. Again, the basic cause for break-off of these small structures is impingement of high-momentum flow on the cavity interface.

With three observed shedding mechanisms—from full-length cavity shedding, to local sheet break-off, and eventually the turbulent closure with its characteristic small vortex

shedding—the basic mechanism is sheet cavity interface impingement. With the experiments with the Twist hydrofoils primary and secondary sheddings were identified to be the same collapse mechanism on different scales. The scale of the eventual shedding is determined by the topology of the re-entrant flow. The importance of its (local) momentum was shown by the hydrofoils with a flat pressure distribution. So, the cavity topology largely dictates the re-entrant flow directions and focal points of this flow. It is therefore essential that the direction and momentum of the re-entrant flow are captured accurately in numerical simulations to simulate cloud shedding.

From photographs the shed structure indeed resembles an indefinite and opaque region, collapsing into bubbly remains, but from these experiments follows that the shed structure mainly consists of cavitating vortices. The low nuclei content in the water tunnel allows for the observation of the structure without bubbles clouding the view and at no time was a pure bubbly cluster observed. From the case study for the Twisted hydrofoil, it was shown that the wake of the sheet cavity consists of smaller stream wise vortices stretched around the main co-rotating span wise vortices. The entire wake quickly rolled up and convected into the central plane by the time it passed the trailing edge. As a result, the wake of the cavity is highly turbulent and it was difficult to perform PIV as many particles left the measurement plane due to a high out-of-plane velocity component.

When simulating cavitation shedding using volume-of-fluids methods, it is often difficult to capture the sharp interface of the sheet cavity, an interface, which is considered unsharp for the cloud structure. The cloud structure has been identified as a structure of vortices, not an agglomeration of bubbles. It is expected that for simulating the cloud one must try to conserve a sharp interface in order to prevent diffusion—either numerically or physically—of the vortex cores.

The two-dimensional cavity

The two-dimensional cavity has a highly three-dimensional structure making it a more difficult study object, either numerically or experimentally, with re-entrant flow constantly changing direction and forming new focal points. The alternating shedding seen for the presented hydrofoils results in a distinct cycle, but the two-dimensional hydrofoils used for most cavitation research lack the symmetry plane, resulting in the seemingly random local shedding along its cavity closure. Any disturbance at its closure will redirect the re-entrant flow into side-entrant flow resulting in focal points and subsequently into local shedding. The three-dimensional cavity is shown to have a repeatable collapse mechanism making it a more reliable candidate for numerical validation studies of cloud shedding. Also, the cavity does not interact with the boundary layer of a tunnel wall. These interactions are not captured when simulating cavitation using inviscid flow models.

Unsteady inflow

The shedding of the sheet cavity fully locks in with the frequency of perturbation generated by the oscillator when its frequency approaches the natural shedding frequency of the cavity. The naturally shedding cavity is shedding reasonably periodically, the frequency and phase show some modulation complicating ensemble averaging. This uncertainty is removed when using the flow oscillator. For validation purposes, the quality of the measurements is improved at the additional computational cost of simulating the flow oscillator. As the flow oscillator was designed to be able to be simulated by using a fixed mesh with a perturbation function, the additional computational cost is thought to be low. The Twist hydrofoil with the Eppler profile and its steady cavity with its open closure is exempt from this recommendation and can be considered stationary (or alternatively phrased: shedding from the open closure of a cavity occurs at a time scale unreachable by the flow oscillator). Rebounding structures, a sign of erosive cavitation, were observed during the experiments with unsteady inflow and not during natural shedding. The natural collapse is enhanced by the increase in pressure as the foil loading decreases. From hereon it is hypothesized that if the natural shedding frequency is lower than the frequency of the variations of the incoming flow field, the risk of erosion is reduced. This will have to be verified during erosion oriented experiments.

Samenvatting

Vliescavitatie is een vorm van cavitatie welke op nagenoeg alle schepsschroeven aanwezig is. De financiële en technische restricties van de rompvorm en voortstuwingsinstallatie laten zelden een schroef toe die opereert bij een lage belasting, laag toerental en bij een gunstige instroming. Alhoewel onderzoeksschepen en de schepen van de marine ontworpen worden cavitatievrij te varen zullen deze schroeven boven een cavitatie inceptionnelheid excessieve vliescavitatie vertonen. Het ontwerp van een schepsschroef is dan ook voornamelijk het beheersen van cavitatie. De extensie van vliescavitatie kan redelijk worden voorspeld, maar het opbreek- en afschudgedrag niet, at leidt tot erosie van de bladen en drukfluctuaties op de schepshuid.

Het nauwkeurig kunnen voorspellen van het afschudgedrag van vliescavitatie is dus belangrijk voor de schepshydraulica en de gereedschappen die dit gedrag voorspellen behoeven zowel experimenteel vergelijkingsmaterieel als een fysische interpretatie van het opbreekmechanisme. Verassend genoeg zijn nagenoeg alle experimentele studies naar cavitatie gericht op rotatiesymmetrische op tweedimensionale opstellingen terwijl de schepsschroef sterk driedimensionaal is. In dit proefschrift wordt aandacht geschonken aan het belang van driedimensionaliteit met een aantal experimenten met profielen met een in breedte variërende belasting, vergelijkbaar met de belasting op een schepsschroef. Een variërende instroom is opgewekt met een stromingsoscillator om het effect van een inhomogene instroming naar een schepsschroef te simuleren.

Het toepassing van PIV op cavitierende stromingen

Het toepassen van Particle Image Velocimetry (PIV) op cavitierende stroming confronteert de experimentator met een aantal nieuwe uitdagingen. Het laserlicht wordt op het oppervlak van de cavitatie weerkaatst wat kan leiden tot overbelichting van de camera of zelfs schade aan de optische chip. Fluorescente deeltjes en optische filters zijn een makkelijke manier op overbelichting te voorkomen door het laserlicht te blokkeren en slechts het fluorescente licht van de deeltjes door te laten. Echter zijn hiermee twee problemen nog niet opgelost. Ten eerste worden de deeltjes buiten het meetvlak ook verlicht door het laserlicht dat door de cavitatie weerkaatst wordt, alhoewel de toepassing van een zeer geringe scherptediepte er voor zorgt dat deze deeltjes slecht gefocust zijn en niet snel zullen bijdragen aan de correlatie van het PIV algoritme (Voor het toepassen van hoge snelheids-PIV is

de energie per laserpuls al zodanig laag dat er vaak met een maximale diafragmaopening gewerkt wordt). Ten tweede verlichten de fluorescente deeltjes de testsectie en de cavitatie welke dus ook door de camera worden opgenomen. Dit kan leiden tot een meetfout als de damp wordt meegenomen in de correlatie van het PIV algoritme. De correlatie van damp is niet noodzakelijkerwijs een typisch probleem van PIV in caverende stromingen. Bij sommige experimenten was de camera niet gevoelig genoeg om de damp waar te nemen, maar, een gevoeliger camera neemt wel meer informatie waar. Als dampaanwezig is op de opnames zal de oplossing van de PIV meting sterk achteruit gaan vanwege juist de correlatie van damp. Dit is een inherent probleem van het meten in meerfase of meercomponenten stromingen. Vliescavitatie kent sterk wisselende lengteschalen, variërende van de ordegrootte van de gehele opname tot enkele pixels, en sterk wisselende snelheden, variërende van de maximaal te verwachten snelheid in de meting tot nagenoeg stilstaande gebieden in bijvoorbeeld de caverende wervelkern. Voor het scheiden van de fasen zijn verscheidene technieken in het verleden gepresenteerd, voornamelijk beeldbewerkingstechnieken en het bewerken van de correlatiemap van het PIV algoritme.

Dit proefschrift presenteert een beeldbewerkingstechnieken welke de meting in de niet-caverende stroming niet aantast, door gebruik te maken van een techniek speciaal ontwikkeld voor het herkennen van deeltjes. Een studie naar het resultaat van PIV plaatjes met en zonder deze filtertechniek laat zien dat de stroming zonder cavitatie niet wordt aangetast. Met behulp van een synthetisch PIV plaatje is aangetoond dat de meetfout significant is gereduceerd bij gebieden met damp. Dus, het verwijderen van reflecties met fluorescente deeltjes is alleen niet genoeg voor een nauwkeurige meting in caverende stromingen. Voor het toepassen van PIV in caverende stromingen is het gecombineerd gebruik van optische filters met fluorescente deeltjes en beeldverwerking dat ook sterk aangeraden.

Het meting van de locatie van het cavitatieoppervlak.

De cavitatie was zonder extra verlichting niet zichtbaar met een relatief lichtongevoelige camera. Omdat de beeldverwerking in staat is deeltjes te volgen en niet gevoelig is voor achtergrond ruis, is de cavitatie bewust belicht. Met een variatie van het beeldbewerking algoritme om deeltjes te herkennen is de locatie van het cavitatieoppervlak afgeleid. Met de beeldverwerkingstechnieken is het dus mogelijk om zowel een PIV meting uit te voeren en tegelijkertijd de oppervlakte van de cavitatie vast te leggen met een enkele camera. Door de camera loodrecht op het lichtvlak te richten zodat het kijkgas van de camera net over het oppervlak van het profiel strijkt, en wetende dat het afschudden van de cavitatie symmetrisch is ten opzichte van het meetvlak, is het cavitatie oppervlak met redelijke zekerheid vast gesteld, ook al is dit oppervlak een zijaanzicht van alle cavitatie in de testsectie en niet alleen ter plaatse van het meetvlak. De resulterende visualisaties geven een toegankelijke representatie van de hoeveelheid cavitatie en het afschud gedrag. Kleine golfjes op het cavitatieoppervlak zijn zichtbaar gemaakt die uit de gewone observaties niet zijn opgemerkt.

Side-entrant flow

De zogenaamde re-entrant stroming van de zijkanten van de cavitatie bepalen het afschudgedrag van die cavitatie en de stroming van de zijkant van die cavitatie hangt af van de vorm van zijn achterrand. Vanwege de vorm en dynamica van die achterrand blijkt de convexe vliescavitatie inherent instabiel te zijn. De richting van de re-entrant jet wordt grofweg gespiegeld op de sluitingslijn zodat bij een driedimensionale stroming de re-entrant flow buiten een opwaartse snelheidscomponent ook een sterk zijwaartse snelheidscomponent bezit. Deze component wordt 'side-entrant jet' genoemd. Voor iedere convexe vliescavitatie zullen deze side-entrant jets zich focussen in het achter gebied van de vliescavitatie wat resulteert in een locale verstoring die een gedeelte van de achterrand van de vliescavitatie doet afschudden. Deze side-entrant jets kunnen elkaar raken voordat de re-entrant jet de voorrand van het profiel heeft bereikt en deze re-entrant het kan ook een dusdanig lage impuls hebben dat de vliescavitatie zich in het geheel niet afschud.

Er is een vliescavitatie gegenereerd op een profiel met een zeer vlakke drukverdeling—met een EPPLER YS-920 vleugelsectie—welke lang was (70% van de hoorde) en tegelijkertijd dun. Vanwege de hoge lengte-breedte verhouding was de stroming van de re-entrant jet bijna geheel in het achter gebied gericht waar een continuë afschudding van kleine caviterende werveltjes is geobserveerd. De re-entrant jet zelf is waargenomen tot aan de voorrand van het profiel maar in plaats van afschudding te veroorzaken werd het oppervlak van de cavitatie zichtbaar meer turbulent. Hieruit is afgeleid dat de re-entrant jet is afgevoerd via het oppervlak van de vliescavitatie. Blijkbaar is het bereiken van re-entrant jets van de voorrand van het profiel een onvoldoende voorwaarde voor het afschudden van vliescavitatie, een observatie die duidelijk anders is van de aanname dat het bereiken van die re-entrant jet aan de voorrand van het profiel altijd leidt tot instabiliteit.

De sluiting van vliescavitatie

Het afschudmechanisme volgende uit het botsen van side-entrant jets in het symmetrievlak van het profiel is het afschudden van het achter gebied van de vliescavitatie. Uit observatie van de structuur van dit gebied is geconcludeerd dat dit een 'mixing layer' is vanwege de typische wervelstructuren zowel in als haaks op de stromingsrichting. Zeer dunne vliescavitatie met een vlakke drukgradiënt stroomafwaarts van die vliescavitatie heeft een re-entrant jet met een relatief lage impuls en schudt kleine caviterende werveltjes af. Uit deze experimenten blijkt dat ook dikke vliescavitatie een afschudmechanisme kan hebben bestaande het kleine caviterende werveltjes, onder het afschudden van grote dampstructuren, als de side-entrant jets een continuë bron van verstoring vormen. Relatief grote vliescavitatie kan als gevolg stabiel zijn als de achterrand een 'mixing layer' vormt in een gebied van een lage drukgradiënt zoals op het Twist-11E profiel.

Van de drie geobserveerde afbreektypes—van het afschudden van de gehele vliescavi-

tatie, tot het afbreken van locale dampstructuren tot het continue afschudden van kleine cavitierende werveltjes—is het basismechanisme steeds het raken van re-entrant flow aan het vliescavitateoppervlak. Uit de experimenten met de Twist profielen is duidelijk dat primaire en secundaire afschuddingen hetzelfde mechanisme vormde maar op verschillende lenteschalen. Deze schalen worden beïnvloed door de stromingsrichting van de re-entrant flow. De vorm van de vliescavities bepaalt de richting van de re-entrant flow en het focuspunten van die re-entrant flow. Het is dus van essentieel belang dat zowel de richting als de impuls van de re-entrant flow nauwkeurig moet worden berekend om het afschudden van vliescavities nauwkeurig te kunnen voorspellen.

Uit opnamen lijkt het afgeschudde dampgebied vaak een diffuus en ondoorzichtig gebied dat verdwijnt naar een bellenwolk, maar uit de observaties in dit proefschrift volgt dat dit afgeschudde gebied een sterke wervelstructuur heeft. Juist omdat er weinig gaskernen in de watertunnel aanwezig waren kon de wervelstructuur goed worden geobserveerd en een bellenwolk is op geen enkel moment gezien. Deze wervelstructuur bestond uit een combinatie van wervels in zowel de stromingsrichting als haaks op deze richting en waren in een klein gebied geconcentreerd op het moment dat ze de achterrand van het profiel passeerden. De volgstroom van de vliescavities is als gevolg sterk turbulent. De damp-vloeistof scheiding is in numerieke methoden een overgangsgebied en de scherpe overgang van de vliescavities wordt hierdoor niet goed benaderd. Bij een bellenwolk wordt aangenomen dat deze vage overgang een goede beschrijving van de werkelijkheid is. Omdat het afgeschudde dampgebied een wervelstructuur is een geen diffuse bellenwolk is wordt verwacht dat voor het afgeschudde gebied de damp-vloeistof scheiding eveneens goed moet worden voorspeld.

Tweedimensionale cavitatie

Een tweedimensionale vliescavities heeft een zeer sterk driedimensionaal karakter met continue van richting veranderende re-entrant flow, waardoor een dergelijke cavitatie voor zowel numerieke als experimentele doeleinden minder geschikt is. Het afschudmechanisme van de hier gepresenteerde driedimensionale profielen is aantoonbaar gestructureerd en herhaalbaar, maar het tweedimensionale profiel zonder symmetrievlak vormt continue nieuwe focuspunten van re-entrant flow en heeft als gevolg een afschudmechanisme met een schijnbaar willekeurig karakter. Vanwege de structuur en herhaalbaarheid worden driedimensionale profiel geacht een betere kandidaat te zijn voor de validatie van numerieke modellen voor cavitatievoorspelling. Bijkomend voordeel is dat deze profielen geen cavitatie aan de tunnelwanden hebben, zodat men geen rekening hoeft te houden met de grenslaag aan die tunnelwand.

Instationaire instroming

De afschudfrequentie van de vliescavities is gelijk aan de frequentie van de verstoring van de stromingsoscillator, wanneer die frequentie in de buurt komt of groter is dan die van de natuurlijke afschudfrequentie van de vliescavities. Het natuurlijke afschudproces is redelijkerwijs periodiek, maar zowel de frequentie als fase laten een modulatie zien die het tijdsmiddelen bemoeilijkt. Deze onzekerheid wordt tenietgedaan bij het gebruik van de stromingsoscillator. Alhoewel het mee modelleren van deze stromingsoscillator voor numerieke complicaties kan zorgen wordt de kwaliteit van de validatiedata wel verhoogd voor het gebruik van die oscillator. De oscillator is wel zo ontworpen dat zijn bewegingsamplituden klein zijn zodat deze kan worden gemodelleerd als vast object met transpiratiesnelheden op de achterrand, zodat men met een tijdsinvariant rekenrooster kan werken. Zogenaamde 'rebounds', dat wil zeggen, het weer doen toenemen van dampvolume na het in elkaar klappen van dampstructuren, zijn slechts geobserveerd wanneer de stromingsoscillator is gebruikt en niet tijdens het natuurlijk afschudden. Hieruit wordt gepostuleerd dat het risico van cavitieserosie klein is als de natuurlijke afschudfrequentie van cavities lager is dan de frequentie van de variaties van de instroming.

Nomenclature

Small Roman

c	$[m/s]$	Speed of sound
c	$[mm]$	Chord length
c_R	$[mm]$	Chord length at the root (tunnel wall) of the Ellipse hydrofoil series
c_T	$[mm]$	Chord length at the tip of the Ellipse hydrofoil series
c_V	$[-]$	Correction constant for determining tunnel velocity
e	$[J]$	Internal energy
e_i	$[-]$	Unit vector
f	$[-]$	Probability distribution function, appendix B
	$[Hz]$	Frequency
f_{FO}	$[Hz]$	Foil oscillator frequency
f_r	$[-]$	Reduced frequency, see eq. 3.11
g	$[m/s^2]$	Gravitational acceleration
k	$[1/m]$	Wave number
p	$[N/m^2]$	Pressure
r	$[-]$	Pearson's correlation coefficient, appendix B
	$[-]$	Degrees of freedom, $r \equiv N - 1$, appendix B
r_T	$[^\circ]$	Maximum geometric rake
r_γ	$[-]$	Hydrofoil geometry definition parameter for rake
t	$[m]$	Profile thickness
	$[-]$	Student's variable, appendix B
u	$[%]$	Standard uncertainty
\mathbf{u}	$[m/s]$	Velocity vector
$\hat{x}, \hat{y}, \hat{z}$	$[-]$	Normalized coordinates

Large Roman

A	$[m^2]$	Cross sectional area of the water tunnel at some location
C_D	$[-]$	Drag coefficient, $C_D = \frac{D}{\frac{1}{2}\rho V^2 S_{ref}}$
C_L	$[-]$	Lift coefficient, similarly defined as C_L

D	$[N]$	Drag
\mathbf{D}	$[1/s]$	Deformation tensor, see eq. 2.38
E	$[\%]$	Total error
\mathbf{G}	$[var]$	Dyadic product tensor, see eq. A.14
$H(\xi)$	$[-]$	Heaviside step function
\mathbf{H}	$[var]$	Hessian tensor (operator), see eq. A.13
I	$[-]$	Image
\mathbf{J}	$[var]$	Jacobian, see eq. A.12
K_C	$[-]$	Kernel, circular, see eq. 4.4
K_G	$[-]$	Kernel, Gaussian, see eq. 4.5
K_L	$[-]$	Kernel, Laplacian, see eq. 4.7
K_M	$[-]$	Kernel, modified standard deviation, see eq. 4.13
K_ϕ	$[-]$	Kernel, with some function ϕ
K_σ	$[-]$	Kernel, standard deviation, see eq. 4.11
L	$[N]$	Lift
N	$[-]$	Number of independent parameters, measurement values, or trials
N_K	$[-]$	Unity Kernel
P	$[-]$	Cumulative probability distribution function
\mathbf{R}	$[1/s]$	Rotation tensor, see eq. 2.39
Re	$[-]$	Reynolds number
S	$[m]$	Span
S_{ref}	$[mm^2]$	Reference area for coefficients $C_{L,D}$
T	$[^\circ C]$	Temperature
V	$[m/s]$	Velocity

Small Greek

α_M	$[^\circ]$	Maximum geometric angle of attack
α_R	$[^\circ]$	Location of center of rotation
α_γ	$[-]$	Hydrofoil geometry definition parameter for α
δ_{ij}	$[-]$	Kronecker delta, see eq. A.3
ϵ_{ijk}	$[-]$	Levi-Civita permutation symbol, see eq. A.6
ϵ_B	$[\%]$	Bias error
ϵ_f	$[\%]$	Precision error
γ	$[-]$	Liquid fraction, s. 2.4
	$[J/m^2]$	Surface tension, appendix J
$\hat{\gamma}_i$	$[-]$	Skewness ($i = 1$) or kurtosis ($i = 2$)
ϕ	$[-]$	Statistical weighing function, s. 4.2
	$[rad]$	Phase angle
ϕ_Δ	$[-]$	Discretized phase angle
κ	$[kg/ms]$	Bulk viscosity
λ	$[m]$	Wave length

	$[kg/ms]$	Second viscosity term, equal to $\lambda = \kappa - \mu$
μ	$[kg/ms]$	Dynamic viscosity
$\hat{\mu}$	$[-]$	Sample mean
$\hat{\mu}_i$	$[-]$	i^{th} Order sample mean
$\hat{\mu}_M$	$[-]$	Population mode
ν	$[m^2/s]$	Kinematic viscosity
ρ	$[kg/m^3]$	Medium density
$\hat{\rho}_{ij}$	$[-]$	Correlation coefficient
σ	$[-]$	Cavitation number
$\hat{\sigma}$	$[-]$	Standard deviation
$\hat{\sigma}_M$	$[-]$	Modified standard deviation, see eq. 4.13
θ	$[\%]$	Sensitivity coefficient
ω	$[1/s]$	Vorticity

Large Greek

Γ	$[m]$ or $[m^2]$	1. Surface or volume integration boundary, chapter 2 2. Bound circulation, chapter 5 3. Gamma function, appendix B
Ω	$[m^2]$ or $[m^3]$	Surface or volume integration domain

Preface

Spithead, June the 26th, 1897. Each year, from the 14th century onward, the Royal Navy gathered her ships for her annual fleet review by the monarch, this year celebrating the 60th anniversary of the accension of Queen Victoria. One hundred and forty warships lay 4 rows wide, each 25 miles long, spearheaded by immense battleship hulls. Yachts and passenger ships carried European royalty to watch the event. The Royal yacht *Victoria*, carrying the Prince of Wales, was led by the Trinity House yacht *Irene*. The *Enchantress* carried the Lords of the Admiralty, *Danube* the House of Lords. The enormous Cunard Lines *Campania* hosted the members of the House of Commons and *Eldorado* carried the foreign dignitaries. Prince Henry of Prussia was aboard his ship König Wilhelm.

Just when Prince Edwards appeared and the band started playing the national anthem, a small craft darted through the lines at an astonishing speed of over 30 knots. Spectators shouted in excitement and amazement as a patrol craft sent to intercept her was easily outmaneuvered and nearly sunk in her wake as the unknown craft sped along the lines, barely avoiding ramming into the battleships. Although the futile pursuit lasted embarrassingly long for the navy, she finally escaped apprehension by the authorities as Prince Henry of Prussia requested an encore. The unknown craft was the *Turbinia*, the fastest ship the world had yet seen. *Turbinia* was unlike any of the ships present that day as she was powered by an engine that would revolutionize warship design; the steam turbine, the brainchild of Charles Parsons.

At the closure of the 19th century both merchant and warship were powered by the triple expansion steam engine. The steam engine as devised by James Watt used a cylinder where steam is alternatively entering either side of the cylinder (hence the name reciprocal) but Watt's engines were heavy and inefficient. For the warship, steam cylinders were not to be fitted vertically, as to not expose them to enemy fire, leading to horizontal reciprocating piston engines. The friction of the horizontal piston on its jacket reduced both its efficiency further and increased wear.

By expanding steam in two stages rather than one, the efficiency increased to twice the value of Watt's engines thought was theoretically possible but did require higher steam pressures. High pressure boilers were initially not used in ships due to the safety concerns. The more complex and unreliable machinery was initially not met with enthusiasm. It was

not until the introduction of Andrew Holt's relatively efficient compound steam engine that double stage expansion became a success and with it the long distance steamer. Although steamers required a wide range of refueling points and a skilled staff, the sailing ship was gradually replaced. The opening of the Suez Canal in 1869 finalized that success as it was prohibitively expensive to tow sailing ships through the canal, forcing them to make a quarter-year detour around the Cape.

Around 1880, boiler pressures increased further, largely due to the introduction of steel, a much stronger material than wrought iron. Adding a third cylinder to the compound engine was feasible, leading to the triple expansion engine. Furthermore, vertical engines could be used for warships due to improvements in engine technology, armor quality, and improved armor layout schemes. Steam was now used to generate on-board electricity to light the engine room and passenger spaces aboard ships. Large auxiliary plants powered fans to supply a forced draft to the water-tube boilers, producing steam faster and at a higher rate to multiple shafts and engine rooms. Warships attained speeds of 20 to 23 knots. Fuel consumption dropped significantly compared with the compound engine and many ships were refitted. Around 1890 the warship had grown sufficiently large to fit a vertical triple expansion engine with a good efficiency, though still heavy and requiring a large number of high-pressure boilers and stokers. Technology was directed to reduce both weight and size of the propulsion plant and to further increase fuel efficiency.

Despite being initially rather careful with adopting the steam turbine, the incident with the *Turbina* sparked the interest of the Royal Navy for this light-weight and powerful engine. The turbine was not necessarily more fuel efficient, therefore not of interest to the slower ships, comprising the bulk of the merchant fleet. But with the launch of the revolutionary 21-knot battleship *Dreadnought* in 1906—rendering all existing warships obsolete virtually overnight—the turbine was firmly established as the prime mover for both warships and fast passenger liners. Ten years later, on June the 31st 1916, while the largest naval battle between turbine driven battleships raged at Jutland, the keel of *HMS Hood* was laid. This 35,000 ton ship reached 32 knots with engines rated at 150,000 BHP, a more than six-fold increase in power, indicating the tremendous influence of Parsons' turbine on ship design. However, the turbine has the distinct disadvantage of operating at a very high rate of revolutions and reduction gears were difficult to construct with the power installed in the turbine-driven warship. Damage of naval propellers due to cavitation had become such a serious problem that the Admiralty initiated a special committee on cavitation erosion in 1915.

Parsons Marine Steam Engine Turbine Company started its trials with the *Turbinia* as early as 1894, experiencing the direct disadvantages of the high rotation rate first hand as the first trials resulted in a meager speed of only 20 knots. By building a torque-measuring coupling Parsons concluded that it was the propeller, not the turbine, that was at fault. In a letter, Parsons commented that "*there appears to be a vacuum behind the blades*". In 1885, a paper by Thornycroft supplied him with the proof Parsons needed. When the

thrust of a propeller exceeds a certain value, a vacuum occurs that was termed *cavitation* by William Froude. The thrust required to propel *Turbina* exceeded that critical value more than five times. The following two years, Parsons varied the number of propellers, pitch settings and number of blades before reaching a velocity of over 30 knots. During this period of testing, he built the first world's cavitation tunnel, heating water near its boiling point. To observe the rapidly rotating propeller, stroboscopic lighting triggered by the propeller's angular position was applied. Parsons observed that

"a cavity or blister first formed a little behind the leading edge and near the tip of the blade. [...] These cavities contained no air but only vapour of water, and the greater position of the power of the engine was consumed in the formation and maintenance of these cavities instead of the propulsion of the vessel".

Parsons finally settled with three turbines each driving a shaft. The high pressure turbine drove the starboard shaft, the remaining steam was fed to the intermediate pressure turbine at the port shaft and finally a low pressure turbine for the inner shaft. As steam turbines cannot be put into reverse, a separate astern turbine was fitted to the central shaft as well. *Turbinia* could manage 34.5 knots with 2000 *BHP* at 2000 *rpm*. Although the steam turbine would become a great success, Parsons later reminisced

"The advent of the marine steam turbine was greatly delayed, if not frustrated at its very inception, by difficulties due to cavitation in its most aggravated form".

While Parsons would be knighted in 1911 and would continue with a telescope workshop, the problem of cavitation erosion would linger on and is an active topic of research today. The *Turbinia* itself is presently on display at Newcastle-upon-Tyne's Discovery Museum.

Preface Bibliography

- [1] BURRILL, L.C. 1951 Sir Charles Parsons and cavitation. In *Transactions of the Institute of Marine Engineers*, **63(8)**.
- [2] GREENHILL, B. Editor 1992 *Steam, Steel and Shellfire: The Steam Warship, 1815-1905*. Conway Maritime Press.
- [3] GREENHILL, B. Editor 1993 *The Advent of Steam: the Merchant Ship before 1900*. Conway Maritime Press.
- [4] GRIFFITH, D. 1997 *Steam at Sea: Two Centuries of Steam-Powered Ships*. Conway Maritime Press.
- [5] PARSONS, C.A. 1911 *The Steam Turbine: The Rede Lecture*. Cambridge University Press.
- [6] PARSONS, R.H. *The Steam Turbine and other Inventions of Sir Charles Parsons*. e-book at <http://www.houseof david.ca/parsons.htm>.
- [7] SMITH, K. 1996 *Turbinia, the story of Charles Parsons and his Ocean Greyhound*. Newcastle Libraries & Information Service.

Chapter 1

Introduction

1.1 Introduction

The most common problem and challenge for a propeller designer is controlling cavitation; the explosive evaporation of liquid water in low pressure regions and the subsequent implosions when the pressure has increased again. The detrimental consequences range from noise and vibration and in worst cases to efficiency losses and severe erosion to the propeller. Nearly all ship propellers have cavitation to some degree and many can sail without any hindrance. Propeller efficiency is rarely affected, but cavitation restricts the number of design choices. Despite the advance of more sophisticated numerical simulation tools and model tests, unexpected cavitation erosion or excessive noise and vibration occasionally occur. The sources of cavitation noise are diverse, but cavitating tip vortices and collapsing sheet cavities are the main culprits. Not only is the propeller affected, the rudder can also be critically damaged by the cavitating vortices in the wake of the propeller or cavitation on the rudder itself. Cavitation is not a problem exclusive to the maritime industry. Hydraulic machinery such as pump impellers, water mains, dams, and spillways are all subjected to cavitation erosion as well. The damage may occur gradually but can be spectacularly catastrophic in case of failure of a fuel feed pump in a space rocket sending it plummeting back to earth. Although such incidents are more spectacular and prone to media coverage than the average eroding marine propeller or pump impeller, the total cost of repair and maintenance is a serious issue for ship yards and owners. Recently the brand new P&O cruise liner *Oriana* underwent a multi-million Euro conversion to counteract unexpected noise and vibration, despite initial model testing and calculations.

The difficulty with modern propeller design is not so much a matter of efficiency—as gaining a high efficiency is now well understood—but combining a high efficiency with low noise requirements within acceptable cavitation related constraints. Especially in the cruise and ferry market, noise requirements are becoming more stringent. Large container ships are now reaching the limits of a single propeller propulsion system with a very high loading leading to very high pressure fluctuations. Cruise ships, ferries, oceanographic re-

search vessels, and combatants have a well-designed twin propeller hull so that the propeller operates in a favorable wake field. Additionally, these ships are often extensively tested on model scale. However, ost ships are not subjected to thorough research and the wake field can be particularly bad as well. The operating conditions for a ship can vary greatly so that the propeller has to be designed for both high and low loading. The problem with low loading, especially in combination with a high rate of revolution, is that the propeller may begin to cavitate on the pressure side as well. Pressure side cavitation is currently a limiting design factor for highly loaded propellers with a poor wake field as its erosiveness is poorly understood. It is not surprising that a good prediction of cavitation behavior, sound production, and erosiveness is required by ship owners, yards, and propeller manufacturers.

Cavitation erosion is quite obviously a serious concern warranting continuous research, but is one of the last items in a chain of flow predictions. Before the eroding collapse of a cavity can be classified as harmful, one must first predict the cavity extent and collapse mechanism accurately. The influence of the wake field has a strong influence on the behavior of the propeller. The individual blades encounter a periodic inflow behavior that will on its turn influence the cavitation. It is known from experiments with hydrofoils that the erosiveness of a cavity can be greatly enhanced when the hydrofoil is oscillating. If one wants to understand cavitation on a propeller, it is necessary to not only study cavitation on a geometry other than two-dimensional, but to do so in a periodically changing flow.

Cavitation in all of its forms has been researched extensively. Depending on the inflow conditions and position of a test subject, many forms of cavitation can be found (Franc & Michel 1985). Cavitation is found in three basic forms; in vortices, as detached flow, and as a bubbly mixture. As cavitation is merely vaporization, it is the interaction with the flow conditions, which determines its eventual appearance. The governing non-dimensional parameter of cavitation is the cavitation number

$$\sigma = \frac{p_0 - p_v}{\frac{1}{2}\rho V_0^2} \quad (1.1)$$

with the ambient pressure p_0 , the vapor pressure p_v , density ρ , and velocity V_0 , or the pressure head to vaporisation over the dynamic pressure. The lower σ , the larger the risk or extent of cavitation.

1.1.1 Sheet cavitation

The attached or partial sheet cavity is a region of detached flow filled with vapor, typically forming downstream steep decreasing pressure gradients. When the length of the attached cavity exceeds the object upon where it originates, it is called super cavitation. An attached cavity can be described as a detached flow region, filled with vapor, with reattachment downstream on the same object (fig. 1.1). Due to its glossy and often (locally) steady appearance, it is mostly referred to as sheet cavitation.



1.1



1.2

Figure 1 At left, an attached cavity can be seen on a two-dimensional hydrofoil, as a stationary region filled with vapor. At right, the sheet cavity has been shed from the foil. This form of cavitation is designated as cloud cavitation and is often erosive.

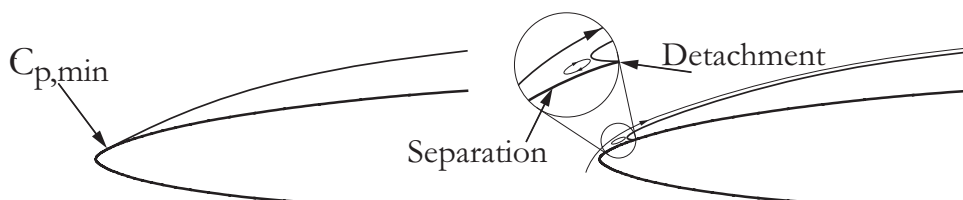


Figure 2 The detachment of the flow at the leading edge of a section. At left, the streamline detaches tangential to the hydrofoil surface, as described by the Brillouin-Villat detachment condition. At right, the actual situation is shown with a small recirculating region between the minimum pressure point and the actual detachment point. The pressure at the minimum pressure point was measured to be in tension.

The detachment point of the sheet cavity interface presents an interesting challenge. Note that there is a difference between fully-wetted boundary layer separation and sheet cavity interface detachment. When cavitating, the detached streamline defines the interface of the attached cavity (see fig.2). The Brillouin-Villat condition (Brillouin 1911, Villat 1914) is an early approach defining the detachment of the cavity streamline, stating that the streamline at the detachment point detaches tangentially to the surface (smooth detachment). Arakeri (1975)—using hemispherical head forms—observed that attached cavitation occurred only when laminar boundary layer separation was present at fully-wetted conditions and that the point of separation was downstream of the location of the predicted smooth-detachment location. When cavitating, however, the actual location of the detachment point was found downstream of the point of fully-wetted laminar boundary layer separation. The distance between boundary layer separation and cavity detachment depends on the Reynolds number and not on the cavitation number, but the location of

boundary layer separation was only dependent on the cavitation number; the extent of the attached cavitation influences the boundary layer upstream of the detachment.

It was previously assumed that the fluid could not support a pressure lower than the vapor pressure if nuclei are present offering a possibility for the fluid to evaporate—completely degassed water can resist a tension of 150 bar—and normally water is teeming with nuclei. But, if the flow is separated upstream of the incipient cavity, it must do so due to an adverse pressure gradient, meaning that the pressure upstream of the incipient cavity is below the vapor pressure. Farhat *et al.* (2002*b*) measured the pressure upstream of the boundary layer separation point with a miniature pressure transducers and concluded that the pressure at fully-wetted conditions was as low as -0.8 bar. With cavitation present the pressure upstream of the cavity interface detachment point was higher, but still negative and increased to the vapor pressure as the cavity covered the sensor when the cavitation number was progressively lowered.

Farhat & Avellan (2001) observed the influence of travelling bubble cavitation on a hydrofoil without laminar flow separation, leading to a attached sheet cavity as the angle of attack was increased. Laminar separation is not a requirement for the appearance attached cavitation as bubble cavitation can interact with the boundary layer. Farhat *et al.* suggested that sheet cavitation does not necessarily form downstream of the separation point, but may also be formed by traveling nuclei exploding after passing the low pressure regime at the leading edge forming a sheet cavity. This is a different mechanism from Arakeri (1975) and Katz (1984) who observed that a sheet cavity in laminarly separated flow starts by bubbles filling in the reattachment zone, expanding upstream toward the leading edge. The sheet cavity is not formed by nuclei traveling through the minimum pressure point, as the pressure gradient usually deflects nuclei away from that point, an effect called 'nuclei screening'.

Near the interface detachment point itself, a small recirculation zone was observed between the flow detachment point and cavity interface detachment point. Apparently, this small recirculation zone allows for the non-tangent detachment of the cavity interface streamline. The complex fluid dynamics at the leading edge occur on a very small scale. From the leading edge onward, the minimum pressure point is formed, followed by laminar separation and a region of recirculating liquid to the interface detachment point. These intricate dynamics are currently beyond the abilities of most numerical calculations and can present a challenge for viscous as well as potential flow methods. When using potential flow models, the tangential interface detachment criterion is often used although its exact location is determined a priori. The Brillouin-Villat condition is usually set at the minimum pressure point and subtle changes in its location influence the calculated cavity length (Vaz 2005).

Tangent reattachment, like tangent detachment, is not a possible flow situation. If the interface were to reattach smoothly, with the vapor pressure present along the interface,

the exact point of reattachment on the surface would be in a pressure imbalance. If the cavity interface streamline is reattaching non-tangent to the surface a stagnation point is formed, but the cavity streamline is also required to be at vapor pressure. Thus (stationary) boundary conditions prohibit a non-tangent reattachment that is both continuous in the velocity as well as in the pressure field near the wall. As a result, the streamline over the interface is directed back into the cavity by the pressure gradient.

A stagnation point forms behind the cavity locally increasing the pressure and a thin stream of liquid is forced into the cavity. This thin stream is called the re-entrant jet and is considered by many researchers as the precursor for the ensuing sheet instability. Impingement of this jet with the vapor-liquid interface results in a disturbance leading to a portion of the attached cavity to be pinched off and advected with the flow. This advected structure is termed cloud cavitation, as it quickly turns into a frothy and highly turbulent structure, as observed as early in 1955 by Knapp (1955) (fig. 1.2). This intrinsic system instability is the cause for cloud shedding. The role of the re-entrant jet as the main cause for shedding was proved conclusively by Kawanami *et al.* (1997), by blocking the re-entrant jet and altering the shedding behavior of the cavity. Le *et al.* (1993*b*) used dye injected near the cavity closure to visualize the re-entrant flow. Ink was observed near the leading edge, confirming an upstream flow component. Early computations by de Lange (1996)—using a potential flow paneling method—predicted the formation and development of the re-entrant jet.

For thick cavities a significant pressure increase or overshoot was measured by Le *et al.* (1993*a*) while for thinner sheets the pressure increases smoothly. The thickness of the re-entrant jet is thus coupled to the relative thickness of the cavity itself (Michel 1978, Dang & Kuiper 1999) and a very thin cavity has a re-entrant jet with a small momentum. Callenaere *et al.* (2001) observed attached cavitation behind a step and the ceiling above the step of the test section could be changed in height. Changing the angle and height of the ceiling changed the adverse pressure gradient and manipulated the re-entrant jet thickness. When the pressure gradient was small or non-existent, the cavity did not shed large structures but had a turbulent and unsteady closure that was termed 'open': small vortical structures were continuously formed. This behavior was also reported when the pressure gradient was large and the re-entrant jet thickness was as thick (or nearly so) as the cavity itself.

1.1.2 Vortex cavitation

Vortex cavitation occurs when vapor fills the core of a vortex. Such a vortex is usually present at tips of loaded wings or near propeller hubs and can be extremely noisy in the broadband range, typically between 4th to 7th order harmonics of a propellers blade passage frequency (van Wijngaarden *et al.* (2005)). Cavitating vortices interacting with the rudder can cause critical damage to the rudder. The vortex near the tip of the propeller is classified into three types by van Terwisga *et al.* (1999); trailing, leading-edge, and local tip vortex

cavitation

- The local tip vortex is generated by flow around a wing tip or propeller blade due to the pressure difference between suction and pressure side of the wing when the tip loading is very low. It appears as attached to or near the tip and its position of maximum strength is close to this region and appears after local boundary layer separation.
- The trailing vortex forms some distance behind the blade as the wake of the propeller rolls up and concentrates into regions of high vorticity. Additionally, as the slipstream of the propeller decreases in diameter downstream of the propeller, the vortices are stretched. These vortices are often seen to start cavitating at some distance behind the propeller.
- The leading-edge vortex is a vortex along the leading edge, typically for propellers with skew. It is similar to the leading-edge vortex on a delta wing and appears after flow separation at the leading edge.

All three vortices can mix, but may all appear simultaneously as three distinct structures. When sheet cavitation occurs near the propeller tip, the distinction between attached sheet and vortex cavitation is not clear due to the strong interaction of the vortex cavity with the attached sheet cavity. A solitary tip vortex does not necessarily lead to broadband noise but may interact strongly with fluctuating sheet cavities resulting in increased 1st harmonic pressure pulses. The diameter of the cavitating core of the vortex depends on the vortex strength, Reynolds number, and the rate of diffusion of dissolved gasses into the core. The trajectory of the developed tip vortex cavitation is insensitive to nuclei content or Reynolds number. Although vortex cavitation is beyond the scope of the present work, the interaction between sheet cavitation will be touched upon briefly.

1.2 An overview of previous work on cavitation

Measurement techniques

Detailed flow measurements are required in order to acquire an understanding of cavitating flows. As cavitation can be aggressive on inserted sensors, many of these measurement techniques are inevitably non-intrusive. Observation of the flow is the most straightforward method of experimenting. Due to a difference of index of refraction between vapor and liquid in water, cavitation is well visible and can be observed without any additional equipment (barring the need of illumination). With the advent of high-speed digital cameras visual observation remains a powerful tool (e.g., de Lange *et al.* 1993, Sato & Shimojo 2003 or Grekula & Bark 2001). For most types of cavitation, a framerate between 10^2 and 10^3 Hz is sufficient. Researchers studying the collapse of individual bubbles use a frame rate in the 10^5 to 10^8 Hz range (Lindau & Lauterborn 1999). More complicated forms of observations are for example holography (Kato *et al.* 1999, Yu & Ceccio 1996) or

stereoscopy (Mettin *et al.* 2001, Takahashi *et al.* 2003). Pereira (1997) used stereoscopy (termed as stereo tomography) to visualize the shedding vortices from the closure region of a sheet cavity into three-dimensional images and thus allowing for an estimation of the vapor volume in the vortex core.

Laser Doppler Velocimetry

Laser Doppler Velocimetry (LDV) has been used by various researchers. Kubota *et al.* (1989) used LDV to measure the flow velocity around cloud cavitation. Due to the inability of LDV to give a good time resolved signal, Kubota used the pressure signal as a trigger for periodic averaging. The mean velocity in the cloud was lower than the mean stream velocity and an increase in vorticity was measured. Brewer & Kinnas (1997) measured the velocity near a steady hydrofoil but noted that the measurement accuracy degraded near the cavity interface. Summarizing, LDV has been applied successfully, but cannot yield time-resolved measurements of the velocity field. It can also measure only at one location and has difficulties near the cavity interface.

Particle Imaging Velocimetry

Tassin Leger *et al.* (1995) used Particle Imaging Velocimetry (PIV) to measure the velocity field around traveling cavitating bubbles. Light scattering of the cavitation prevented the determination of velocity vectors close to the interface. Shridhar & Katz (2000) used fluorescent tracer particles and an optical filter to cancel all incident laser light and measured the velocity field in the wake of a cloud cavity. Reynolds shear stresses were found to have increased by 25 to 40% due to cavitation. Using fluorescent particles and optical filters, incident laser light and reflections of the cavity interface are removed. PIV has the benefit of resulting in both time-resolved and instantaneous measurements of the flow field and is a whole-field measurement technique as accurate as LDV.

Pressure measurements

A common form of a surface measurement is a pressure measurement. Due to the implosive force of a collapsing cavity exerted on the transducer, damage is often unavoidable. Le *et al.* (1993*b*) mounted an array of 9 pressure transducers in a rotatable disk in a plano-convex hydrofoil. The pressure pulses radiated by the collapsing cavity could be captured as the sensors had a very high natural frequency necessary to capture such a steep pressure gradient. Le concluded from pressure measurements that the pressure pulses from cloud cavitation were much higher than from attached cavitation—as cloud cavitation always collapses quickly—and that the location of the highest pressure amplitude was present at the center of the cloud. Similar results were obtained by McKenney & Brennen (1994) when the hydrofoil was oscillating. Reisman *et al.* (1998) mounted four piezo electric pressure transducers inside a hydrofoil and monitored the pressure transients of imploding cloud cavitation, which could be over 30 *bar* during a 10^{-4} s duration. The authors noted that less robust transducers were occasionally lost due to excessive pressure. Farhat *et al.*

(2002a) used miniature piezo-resistive transducers fitted into recesses but filled with a plastic compound in order to keep the hydrofoil surface smooth.

Cavity interior

The interior of the attached cavity remains difficult to probe other than with pressure transducers. Stutz & Reboud (1997) applied optical probes; Infra red light is emitted from the probe and partly reflected back depending on the index of refraction of the surrounding medium. Using a double optical probe at various locations resulted in a void fraction on average between 10 and 25 percent. Ceccio & Brennen (1991) inserted electric probes on the surface of axisymmetric head forms. A change in void fraction registers as a change of the impedance of the conductive medium. This setup was successfully used to locate individual bubbles. An array of either optical probes or electrodes can be used to measure the speed of the re-entrant jet front by cross correlation as it wets the sensors.

Shear layers

The structure of a shear layer is well-known for fully-wetted conditions (e.g., steps, jets), consisting of series of stream wise and span wise vortices (Jimenez 1983, Bernal & Rosko 1986, Lasheras *et al.* 1986, Lasheras & Choi 1988, Shridhar *et al.* 1999). At cavitating conditions and lower Reynolds numbers (smaller separated flow regions) cavitation inception occurs first in the span wise vortices. At higher Reynolds numbers (plane shear flow behind steps) cavitation inception occurs in the stream wise vortices and the larger span wise vortices cavitate at pressures estimated below the vapor pressure (O' Hern 1990, Belahadji *et al.* (1995)). The Reynolds stress in the wake of the cavitating shear layer is less than that of a fully-wetted shear layer. As a non-cavitating vortex line is stretched its rotation rate increases due to the conservation of vorticity. In case of a cavitating vortex, the core diameter also depends on the ambient pressure, changing the rotation rate. As a result, the stretching and rotation rate of cavitating vortex core are not fully coupled. (Belahadji *et al.* 1995, Iyer & Ceccio 2002).

1.2.1 Three-dimensionality

Crimi (1970) studied the effect of sweep (skew) and concluded the inception velocity increased with an increase in the skew angle. Hart *et al.* (1990) used an oscillating three dimensional hydrofoil. Hart *et al.* concluded that the cavity collapse was most violent when the natural shedding frequency of the cavity coincided with the oscillation frequency. de Lange & de Bruin (1998) studied three transparent hydrofoils in the cavitation tunnel at the University of Delft. One hydrofoil had a 23° sweep angle. de Lange & de Bruin concluded that the re-entrant jet of the two-dimensional hydrofoil was directed upstream, but in the three-dimensional case the re-entrant jet component normal to the closure line was reflected inward. As the pressure gradient is perpendicular to the closure line, it is to be expected that the tangential component remains unchanged. (Of course, the same is

true to the two-dimensional re-entrant jet, which has no transverse velocity component). Laberteaux & Ceccio (2001) studied a series of swept wedges. The cavity planform was significantly changed by the sweep and the re-entrant jet was directed into the cavity allowing for a steady sheet that only shed cloud cavitation at the far downstream edge. Dang & Kuiper (1999) studied the re-entrant jet on a hydrofoil with a span wise varying angle of attack numerically and found the re-entrant jet direction to be strongly influenced by the cavity topology. The change in the cavity shape was determined by span wise distribution of the loading and not by the sweep angle.

Shen & Gowing (1986) studied the relation between cavitation inception and laminar separation on an oscillating hydrofoil. The pressure measured inside the cavity was found to be frequency dependent. Franc & Michel (1988) studied the influence of the boundary layer on inception on an oscillating hydrofoil using dye injection. They concluded that—for the unsteady flow cases presented—the cavity was suppressed when the boundary layer was turbulent. Hart *et al.* (1990) studied cavitation on an oscillating three-dimensional hydrofoil and concluded that there is a strong interaction between the reduced frequency and the shedding cavitation formation, especially near the natural shedding frequency. Reisman *et al.* (1994) used oscillating hydrofoils to study cloud cavitation and found that radiated noise dropped when air was injected through the surface of the hydrofoil.

1.2.2 Physical modeling

The simulation of cavitation by mathematical models is currently an active field of research. Early attempts consist of analytical descriptions of bubble dynamics or linearized cavitation streamline equations, the latter is described in more detail by Wu (1972). Such analytical models do not predict the re-entrant jet as the closure model is a boundary condition, not a part of the solution. Panel methods in potential flow were used by de Lange (1996), to predict a re-entrant jet on a two-dimensional foil. The interface is considered as a dynamic surface without vaporisation or condensation. Potential flow methods are currently the industries standard, but more extensive methods are under development as paneling methods cannot predict shedding and the ensuing erosion. Computational methods using barotropic flow assumption calculate the vaporization by directly coupling the density to the pressure. Kubota *et al.* (1992) modeled the vapor production by calculating the rate of growth of bubbles in the flow and thus estimating the percentage of void per unit volume. Several methods use an empirical vapor production and destruction rate relation, (e.g., Senoçak & Shyy 2002, Kunz *et al.* 1999). These models empirically predict transfer of mass between liquid and vapor phases. The basis of such codes can be Euler, Reynolds-Averaged Navier-Stokes, or Large Eddy Simulation. Currently models are developed using thermodynamic equilibrium models to capture the vaporization and fully-compressible flow aspects of the liquid and gaseous states of the flow, without the need for a priori assumptions or empirical relations (Schnerr *et al.* 2006). With the advent of these numerical cavitation models, the availability of useful and detailed validation material is essential

1.3 Objectives

The present thesis addressed the lack of validation material indispensable for validating cavitation models in numerical flow calculations, considered an essential step in the process of deriving a reliable method for the prediction of cavitation erosion and radiated noise and for getting a better understanding of scale and interaction effects of unsteady cavitation. The objectives of this study are threefold:

- 1 To provide a better insight in the physical mechanisms that govern the dynamics and (internal) structure of a sheet cavity.
- 2 To provide a detailed and accurate database of benchmark tests of an unsteady cavity on various configurations that can be used for the validation of computational methods.
- 3 To interpret the results and to contribute to the development guidelines for propeller design

One could choose to study a rotating object, but this has several disadvantages. The area of interest may rotate out of the field of view, another propeller blade may block the field of view, the flow at the inner radii may be laminar, and so forth. Numerical simulation would require a rotating grid as the square test section is not axi-symmetric. Choosing a hydrofoil with a cavity plan form reminiscent to propeller cavitation greatly facilitates the experiment and utilizes the limited dimensions of the test setup to a maximum. The hydrofoils need to have a span wise change in loading and be subjected to a variable inflow in order to observe three dimensional cavitation in an unsteady inflow. Not only is this practical approach beneficial to the experiment, it will also assist the numerical modeler by having a stationary test subject, removing the need for a continuously changing or rotating mesh. The periodic inflow to the propeller blades is simulated by means of a flow oscillator.

The measurement setup will be discussed in chapter 3. The hydrofoil geometry will be presented including the flow oscillator positioned upstream of the hydrofoil. Special attention has been paid to the application of leading edge roughness. This chapter has several appendices with an detailed error analysis. Chapter 4 discusses the techniques used to adapt PIV to be used for cavitating flows. This chapter will demonstrate the importance of removing cavitation regions from PIV images to reduce the measurement error, for which image analysis is used. A brief introduction is presented first to get the reader acquainted with this technique. The results of the experiments are discussed in chapter 5 for steady and unsteady conditions, complemented with the results from the PIV and image analysis. The observed cavitation is described in detail. The conclusions and recommendations are presented in chapter 6

Chapter 2

Physical background

2.1 Introduction

The choice of a physical flow model for cavitation has its repercussions on the ability of a model to capture physical flow effects. The experiment must be set up so that only the relevant physical flow effects of unsteady attached sheet cavitation occur, flow effects that the numerical calculation must be able to capture. The experimental data used for validation of numerical calculations need to be free of other phenomena. This chapter will discuss the physical cavitation models briefly. It is not the goal to give a complete overview, nor to discuss their implementation.

The fundamental laws of fluids dynamics are conservation of mass, momentum and energy. The conservation of mass—or continuity—equation is a scalar conservation of the total mass of the flow. The conservation of momentum equation dictates that momentum is conserved along each possible vector in space and can be decomposed into three mutually independent directions. The conservation of energy equation conserves energy along a vector in time.

These three conservational laws—using constitutive relations for the viscous stresses and heat flux, and equations of state of the fluid—form a closed system of equations that are generally sufficient to determine the independent variables density, pressure, and all three velocity components. Cavitation adds the complexity of a two-fluid flow with phase transitions requiring additional constitutive relations to determine, e.g, constitutive relations of all fluid components, and evaporation and condensation conditions. These relations form a cavitation model.

The second part of this chapter derives the equations of the transport of vorticity for two-fluid models, in order determine if cavitation can act as a source of vorticity at the liquid-gas interface or merely acts to redistribute vorticity.

The notation used in this chapter—summation convention—is presented in appendix A.

2.2 Conservational relations

2.2.1 Reynolds Transport Theorem

Consider an arbitrary scalar or vector quantity $\xi(\mathbf{x}, t)$. The total amount of quantity can be obtained by integrating over a control volume $\Omega(t)$ with a boundary $\Gamma(t)$. Now, the rate of change of the total amount of $\xi(\mathbf{x}, t)$ within $\Omega(t)$ not only depends of its coordinates \mathbf{x} and time, t , but also on the rate of change of the $\Omega(t)$ with respect to the flux of $\xi(\mathbf{x}, t)$ over $\Gamma(t)$

$$\frac{d}{dt} \int_{\Omega(t)} \xi(\mathbf{x}, t) d\Omega = \frac{\partial}{\partial t} \int_{\Omega(t)} \xi(\mathbf{x}, t) d\Omega + \int_{\Gamma(t)} \xi(\mathbf{x}, t) (u_i - u_i^\Gamma) n_i d\Gamma \quad (2.1)$$

with \mathbf{n} the normal point out of $\Omega(t)$. Applying the Leibniz integration rule to the first term of the left-hand side

$$\frac{\partial}{\partial t} \int_{\Omega(t)} \xi(\mathbf{x}, t) d\Omega = \int_{\Omega(t)} \frac{\partial}{\partial t} \xi(\mathbf{x}, t) d\Omega + \int_{\Gamma(t)} \xi(\mathbf{x}, t) u_i^\Gamma n_i d\Gamma \quad (2.2)$$

results in

$$\frac{d}{dt} \int_{\Omega(t)} \xi(\mathbf{x}, t) d\Omega = \int_{\Omega(t)} \frac{\partial}{\partial t} \xi(\mathbf{x}, t) d\Omega + \int_{\Gamma(t)} \xi(\mathbf{x}, t) u_i n_i d\Gamma \quad (2.3)$$

Using the Gauss divergence theorem

$$\int_{\Omega(t)} \frac{\partial \xi_i}{\partial x_i} d\Omega = \int_{\Gamma(t)} \xi_i n_i d\Gamma \quad (2.4)$$

the boundary integral can be rewritten into a volume integral

$$\frac{d}{dt} \int_{\Omega(t)} \xi(\mathbf{x}, t) d\Omega = \int_{\Omega(t)} \left[\frac{\partial}{\partial t} \xi(\mathbf{x}, t) + \frac{\partial}{\partial x_i} \xi(\mathbf{x}, t) u_i \right] d\Omega, \quad \forall \mathbf{x}, t \quad (2.5)$$

and the Reynolds transport theorem is obtained. It states that the rate of change of the total amount of any quantity $\xi(\mathbf{x}, t)$ within $\Omega(t)$ is equal to the rate of change of $\xi(\mathbf{x}, t)$ in time plus the net flux of $\xi(\mathbf{x}, t)$ over the (dynamic) boundary $\Gamma(t)$, either due to convection or changes in the control volume $\Omega(t)$.

2.2.2 Continuity equation

The conservation of mass in the arbitrary control volume $\Omega(t)$ and boundary $\Gamma(t)$ in a velocity field $\mathbf{u}(\mathbf{x}, t)$, states that the change of total mass inside the control volume must equal the mass flux over the control boundary, or:

$$\frac{d}{dt} \int_{\Omega(t)} \rho d\Omega + \int_{\Gamma(t)} \rho (u_i - u_{i,\Gamma}) n_i d\Gamma = 0 \quad (2.6)$$

Applying eq.2.5 results in

$$\int_{\Omega(t)} \left[\frac{\partial \rho}{\partial t} + \frac{\partial \rho u_i}{\partial x_i} \right] d\Omega = 0 \quad (2.7)$$

As the above must be valid for any control volume $\Omega(t)$, the differential form of the continuity equation is obtained

$$\frac{\partial \rho}{\partial t} + \frac{\partial \rho u_i}{\partial x_i} = 0, \quad \forall \mathbf{x}, t \quad (2.8)$$

2.2.3 Conservation of momentum

Conservation of momentum states that the rate of change of momentum within $\Omega(t)$ and the flux of momentum through $\Gamma(t)$ must be equal to all forces exerted on and in the fluid in the control volume. These forces fall in two categories, volume forces (e.g., gravity and magnetism, but also coriolis and centrifugal forces in rotating frames of reference) and surface forces (pressure and viscous stress)

$$\mathbf{e}_i \frac{d}{dt} \int_{\Omega(t)} \rho u_i d\Omega + \mathbf{e}_i \int_{\Gamma(t)} \rho u_i (u_j - u_j^\Gamma) n_j d\Gamma = \mathbf{e}_i \int_{\Omega(t)} f_i^\Omega d\Omega + \mathbf{e}_i \int_{\Gamma(t)} f_i^\Gamma d\Gamma \quad (2.9)$$

Similar to the derivation of Reynold's transport theorem and the continuity equation, this equation is rewritten as

$$\int_{\Omega(t)} \mathbf{e}_i \left[\frac{\partial \rho u_i}{\partial t} + \frac{\partial \rho u_i u_j}{\partial x_j} \right] d\Omega = \int_{\Omega(t)} \mathbf{e}_i \left[f_i^\Omega - \frac{\partial p}{\partial x_i} + \frac{\partial}{\partial x_j} \sigma_{ij} \right] d\Omega \quad (2.10)$$

with $\boldsymbol{\tau}$ the stress tensor

$$\tau_{ij} = \mu \left(\frac{\partial u_i}{\partial x_j} + \frac{\partial u_j}{\partial x_i} \right) + \delta_{ij} \lambda \frac{\partial u_k}{\partial x_k} \quad (2.11)$$

with μ is dynamic viscosity of the fluid and λ a second viscosity term, such that the bulk viscosity, κ , equals $\kappa = \mu + \lambda$. From eq. 2.11 follows that λ is not consequential for incompressible flows. Stokes' hypothesis prescribes a zero bulk viscosity, or $2\mu + 3\lambda = 0$. Note that if the viscosity is assumed constant that the gradient of the stress tensor is equal to¹

$$\begin{aligned} \frac{\partial \tau_{ij}}{\partial x_j} &= \mu \frac{\partial}{\partial x_j} \left(\frac{\partial u_i}{\partial x_j} + \frac{\partial u_j}{\partial x_i} \right) + \lambda \frac{\partial}{\partial x_i} \frac{\partial u_k}{\partial x_k} \\ &= 2 \frac{\partial^2 u_i}{\partial x_j \partial x_j} + \varepsilon_{ijk} \frac{\partial}{\partial x_j} \left(\mathbf{e}_k \varepsilon_{klm} \frac{\partial u_m}{\partial x_l} \right) + \lambda \frac{\partial}{\partial x_i} \frac{\partial u_k}{\partial x_k} \end{aligned} \quad (2.12)$$

¹ $\nabla (\nabla \mathbf{u} + \nabla^T \mathbf{u}) = 2\nabla^2 \mathbf{u} + \nabla \times \boldsymbol{\omega}$

Similar to the continuity equation, the above is valid for any control volume $\Omega(t)$, and the Navier-Stokes equations are obtained

$$\mathbf{e}_i \left[\frac{\partial \rho u_i}{\partial t} + \frac{\partial \rho u_i u_j}{\partial x_j} \right] = \mathbf{e}_i \left[f_i - \frac{\partial p}{\partial x_i} + \frac{\partial}{\partial x_j} \left(\mu \left(\frac{\partial u_i}{\partial x_j} + \frac{\partial u_j}{\partial x_i} \right) + \delta_{ij} \lambda \frac{\partial u_k}{\partial x_k} \right) \right] \quad (2.13)$$

Note that the left-hand side, using the continuity equation, can be written as

$$\frac{\partial \rho u_i}{\partial t} + \frac{\partial \rho u_i u_j}{\partial x_j} = \rho \frac{\partial u_i}{\partial t} + \rho u_j \frac{\partial u_i}{\partial x_j} = \rho \frac{du_i}{dt} \quad (2.14)$$

with the material derivative defined as

$$\frac{d}{dt} = \frac{\partial}{\partial t} + \frac{\partial x_i}{\partial t} \frac{\partial}{\partial x_i} \equiv \frac{\partial}{\partial t} + u_i \frac{\partial}{\partial x_i} \quad (2.15)$$

Alternatively, the LHS of the Navier-Stokes equation can be written in the Lamb-Gromeka form

$$\begin{aligned} \mathbf{e}_i \rho \left[\frac{\partial u_i}{\partial t} + u_j \frac{\partial u_i}{\partial x_j} \right] &= \mathbf{e}_i \rho \left[\frac{\partial u_i}{\partial t} + \frac{1}{2} \frac{\partial u_j u_j}{\partial x_i} - \varepsilon_{ijk} u_j \left(\mathbf{e}_k \varepsilon_{klm} \frac{\partial u_m}{\partial x_l} \right) \right] \\ &= \mathbf{e}_i \rho \left[\frac{\partial u_i}{\partial t} + \frac{1}{2} \frac{\partial u_j u_j}{\partial x_i} - \varepsilon_{ijk} u_j \omega_k \right] \end{aligned} \quad (2.16)$$

where $\boldsymbol{\omega}$ —the curl of the velocity—is the vorticity vector.

2.2.4 Euler equations

The Euler equations are the inviscid-flow variant of the Navier-Stokes equations, so

$$\mathbf{e}_i \left[\frac{\partial \rho u_i}{\partial t} + \frac{\partial \rho u_i u_j}{\partial x_j} \right] = \mathbf{e}_i \left[f_i - \frac{\partial p}{\partial x_i} \right] \quad (2.17)$$

The Euler equations describe inviscid flows, but vorticity can be produced and advected. The application range of the Euler equations is high Reynolds number (non-)isentropic flows, naturally without viscous flow effects. The Euler equations can describe fully-compressible multiphase flows, requiring additional equations of state for the various phases, as well as additional relations describing the phase changes when applicable².

When the force field is conservative

$$f_i = -\frac{\partial F}{\partial x_i} \quad (2.18)$$

and if the flow is barotropic with

$$\mathbf{e}_i \frac{1}{\rho} \frac{\partial p}{\partial x_i} = \mathbf{e}_i \frac{\partial}{\partial x_i} \int \frac{dp}{\rho} \quad (2.19)$$

²as do the Navier-Stokes equations

and if the flow is steady, then the dot product of Euler equations—starting from the Lamb-Gromeka form in eq. 2.16—with the velocity \mathbf{u} can be written as

$$u_i \frac{\partial}{\partial x_i} \left[\frac{1}{2} u_j u_j + \int \frac{dp}{\rho} + F_i \right] - \underbrace{\varepsilon_{ijk} u_i u_j \frac{\partial \omega_k}{\partial x_j}}_{\equiv 0} = 0 \quad (2.20)$$

Bernoulli's equation for steady barotropic flow is recognized within the brackets and as this expression is tangent to the velocity vector it represents a streamline. If the sheet cavity interface is a streamline at the vapor pressure, the fluid is considered incompressible, and the forces are neglected, then the velocity at the interface is equal to

$$V_V = \sqrt{(1 + \sigma)} V_0 \quad (2.21)$$

with V_0 and σ as in eq. 1.1.

Large vaporous-structure shedding by re-entrant flow pinching off a part of the sheet cavity is an inertia dominated flow phenomenon and is captured by the Euler equations. For a proper validation of Euler-based calculations, it is essential that flow separation is not present on the test hydrofoils and that vorticity production in e.g., shear layers is absent or negligible. Intermittent vortex shedding is reported for cavities with turbulent reattachment and during cloud shedding. Still, Laberteaux & Ceccio (2001)—studying a series of cavitating swept wedges—found from their PIV measurements that the wake was free of vorticity. The vorticity in the wake of the cavity of the present hydrofoils has to be addressed in the experimental results.

2.2.5 Potential flow

The underlying assumption of potential flow is that the flow is irrotational. By defining the velocity as the gradient of a scalar field, this assumption is met as the curl of a gradient of a scalar is always zero. This scalar field is called the potential field, Φ . For this inviscid flow, equation 2.13 reduces to

$$\mathbf{e}_i \left[\rho \frac{\partial}{\partial t} \frac{\partial \Phi}{\partial x_i} + \frac{1}{2} \rho \frac{\partial u_j u_j}{\partial x_i} - f_i + \frac{\partial p}{\partial x_i} \right] = 0 \quad (2.22)$$

If the force field is conservative (eq. 2.18) and if the flow is barotropic (eq. 2.19) then eq. 2.22 can be written back into a surface integral using Gauss divergence theorem (eq. 2.4),

$$\int_{\Gamma(t)} \left(\rho \frac{\partial \Phi}{\partial t} + \frac{1}{2} \rho u_i u_i + p + F_i \right) n_i d\Gamma = 0 \quad (2.23)$$

Now the unsteady Bernoulli equation is recognized. For many applications of potential flow, the flow is considered incompressible so that the continuity equations reduces to the Laplace equation of the potential, or

$$\frac{\partial}{\partial x_i} \frac{\partial \Phi}{\partial x_i} = 0 \quad (2.24)$$

With this condition of divergence-free flow and with eq. 2.23 for streamlines intersection the flow domain, the entire flow domain is known from the boundary (The numerical implementation is hence termed a boundary-integral method). Note that the assumption of irrotationality in potential flow implies a no-slip boundary condition in the absence of shear in either compressible or incompressible flow. For incompressible potential flows, it is noted that the gradient of the stress tensor for a constant viscosity (eq. 2.12)

$$\frac{\partial \tau_{ij}}{\partial x_i} = 2 \frac{\partial}{\partial x_i} \frac{\partial^2 \Phi}{\partial x_j \partial x_j} + \varepsilon_{ijk} \frac{\partial}{\partial x_j} \left(\varepsilon_{ijk} e_k \frac{\partial^2 \Phi}{\partial x_l \partial x_m} \right) + \delta_{ij} \frac{\partial}{\partial x_i} \frac{\partial u_k}{\partial x_k} \quad (2.25)$$

Here the Laplacian of Φ , the rotation of Φ , and the divergence of the velocity are recognized; terms which defined zero for potential flow. The phase changes inherently present with cavitating flows cannot be described and the interface of the cavity must be considered as a part of the flow domain boundary. A pressure on that interface is prescribed—a required boundary condition—as being equal to the vapor pressure requiring that $V_V = V_0 \sqrt{1 + \sigma}$ for a *stationary* interface. The boundary element methods used for the prediction of cavitation can capture the re-entrant jet, but intersection of the re-entrant jet with the cavity interface is fatal to the solution as it isolates the cavity from the boundary.

Boundary element methods have a tendency to over-predict cavity lengths and the location of streamline detachment is pre-described. Despite the advent of more modern flow methods, potential flows methods are used—especially during the design phase—as they can be solved with a modest computer load and can give accurate result for flow problems such as the prediction of a wave pattern of a ship or a propeller loading. For validation studies, shedding of sheet cavitation or production cannot be present and the premise of the boundary condition on the cavity interface must be confirmed by measuring the velocity at that interface. Considering the unsteady nature of attached cavitation, these are stringent demands.

2.3 Cavitation models

Most RANS and Euler-based cavitation models are based on a continuum approach in the liquid-vapor distribution and introduce a fraction α , defined as the volume of fluid per specified control volume. For instance, the mixture density is written as a combination of several fluids, or

$$\bar{\rho} = \alpha_i \rho_i \quad (2.26)$$

For cavitation modeling the basic components are water and a number of contaminant gases. Neglecting gaseous contaminants, the fraction α can be taken as a *void-fraction* so that

$$\bar{\rho} = \alpha \rho_v + (1 - \alpha) \rho_l \quad (2.27)$$

Note that the void fraction is here defined as the *instantaneous* ratio of vapor per unit volume, while experimentalists use the void fraction as the *time-averaged* presence of vapor

in a measurement volume (e.g., the fraction of a measurement period when vapor bubbles are near a measurement probe). Substituting the above in the continuum equation and assuming no slip between phases results in

$$\left[\frac{\partial \alpha}{\partial t} + \frac{\partial \alpha u_i}{\partial x_i} \right] = \frac{\alpha}{\rho_l - \rho_v} \left[\frac{\partial \rho_v}{\partial t} + \frac{\partial \rho_v u_i}{\partial x_i} \right] + \frac{1 - \alpha}{\rho_l - \rho_v} \left[\frac{\partial \rho_l}{\partial t} + \frac{\partial \rho_l u_i}{\partial x_i} \right] + \alpha \frac{\partial u_i}{\partial x_i} \quad (2.28)$$

with ρ_v and ρ_l the vapor and liquid density, respectively. This equation is the transport equation of the void fraction. Note that for incompressible fluids the above reduces to

$$\left[\frac{\partial \alpha}{\partial t} + \frac{\partial \alpha u_i}{\partial x_i} \right] = \left[\frac{\bar{\rho}}{\rho_l - \rho_v} + \alpha \right] \frac{\partial u_i}{\partial x_i} \quad (2.29)$$

The RHS of eq. 2.29 is nonzero implying production or destruction of vapor when the flow is not divergence-free. The rate of change of the void fraction is determined by taking an empirical relation for the RHS, either a vapor production model or a vapor rate of production model.

A straightforward vapor production model is a barotropic model to directly link the density to the pressure, or $\rho = f(p)$ (Hoeijmakers *et al.* 1998, van der Heul *et al.* 2000, Koop *et al.* 2006). A smooth density transition is implemented near transition from vapor to liquid. The model captures the near-instantaneous evaporation of the liquid when a cavity is produced, but can predict a condensation shock at the closure of the cavity. No shock is observed in the experiments at the closure of the cavity when it smoothly reattaches with a re-entrant jet. Still, the speed of sound, c , in mixtures according to Wallis (1969) is equal to

$$\frac{1}{\rho c^2} = \frac{\alpha}{\rho_v c_v^2} + \frac{1 - \alpha}{\rho_l c_l^2} \quad (2.30)$$

From this relation it follows that the speed of sound for $\alpha = 0.5$ is as low of 5 *m/s*, a velocity that is certain to occur in cavitating flows, as a consequence supersonic speeds are easily obtained. van der Heul *et al.* 2000 used a barotropic production term with an Euler method, successfully predicting the re-entrant jet and the shedding of cavitation.

Empirical rate of vapor production models capture the evaporation and condensation rate by production and destruction rate functions. Such models have been used by e.g., Senoçak & Shyy (2002), Kunz *et al.* (1999), and are in the form of

$$\frac{\partial \alpha}{\partial t} + \frac{\partial \alpha u_i}{\partial x_i} = -\frac{\rho_v}{t_\infty} (C_{prod}(1 - \alpha)(p - p_v) H(p_v - p) + C_{dest}\alpha(1 - \alpha)^2) \quad (2.31)$$

with empirical constants for vapor production (C_{prod}) and destruction (C_{dest}), showing some variation among researchers. The production term is "switched on" by the Heaviside function H when the pressure falls below the vapor pressure. The production coefficient itself is large, as high as possible according to Wikström & Bark (2003), implying

near-instantaneous evaporation. The destruction term allows for some retardation in the condensation.

A different approach, based on cavitation inception, is the bubble model as developed by Kubota *et al.* (1992) who assumed that water is seeded with nuclei and that the growth of a nucleus is captured by the Rayleigh equation. Given a certain number of nuclei per unit volume, n_0 , the vapor fraction can then be estimated as:

$$\frac{\partial \alpha}{\partial t} + \frac{\partial \alpha u_i}{\partial x_i} = \rho_v \frac{n_0 4\pi R^2}{1 + n_0 \frac{4}{3}\pi R^3} \frac{dR}{dt} \quad (2.32)$$

and

$$\frac{dR}{dt} = \text{sgn}(p_v - p) \sqrt{\frac{2}{3} \frac{|p_v - p|}{\rho_v}} \quad (2.33)$$

with R the bubble radius. The elegant approach has the proper physical approach when estimating nuclei inception, but the physical interpretation inside sheet cavities with vapor fractions of 100% remains uncertain. To illustrate, at 100% vapor fraction, a fluid volume would be filled with bubbles partly overlapping with the overlapping volume equal to the volume of fluid between bubbles. The models requires a given number of nuclei with a radius distribution spectrum, a property known to change during cavitation tests in water tunnels, but has nonetheless been applied successfully and results are comparable with the model used by Kunz *et al.* (1999).

Schmidt *et al.* (2006) and Koop (2007) model cavitating flows by taking the fluid as a fully compressible medium capable of phase changes. Vapor production is not prescribed by empirical functions but controlled by conservation of energy at thermodynamic equilibrium conditions. The flow is a homogeneous mixture that is in thermodynamic and mechanical equilibrium, with temperatures and pressure equal for both the liquid and gaseous phase (in a control volume). A mean internal energy per unit volume is defined as

$$e = \epsilon e_v(T) + (1 - \epsilon) e_l(T) \quad (2.34)$$

with ϵ the *mass fraction*

$$\epsilon = \frac{\alpha \rho_v}{\bar{\rho}} \quad (2.35)$$

With this mass fraction the conservation of energy equation, for an inviscid flow, reads

$$\frac{\partial \bar{\rho} E}{\partial t} + \frac{\partial (\rho E + p) u_i}{\partial x_i} = 0 \quad (2.36)$$

with the total energy E equal to $E = e + \frac{1}{2} u_i u_i$.

By using the conservation of energy, a constitutive relation is substituted for the transport of void fraction equation and no a priori assumptions need to be made present in the

vapor rate of production models. The above should hold for any (inviscid) flow, so equations of state are required for the two phases of water and the mixture. Schmidt *et al.* and Koop use a modified Tait equation to describe the liquid phase and stiffened gas equation to describe the gas phase. For details the reader is referred to Koop (2007).

2.4 Transport of vorticity in two-phase flows

The production of vorticity has several origins. Boundary layers, forming from a no-slip boundary condition at the wall, produce a layer of vorticity, baroclinic torque is known to affect weather patterns, etcetera. Cavitation introduces large density and viscosity gradients in the flow, possibly introducing additional vorticity due to variations in shear stress and vapor distributions. A basic analysis is made of the transport of vorticity equation for flows with strong and non-negligible viscosity gradients. The derivation is presented below. Starting with the Navier-Stokes equations divided by ρ

$$\mathbf{e}_i \left[\frac{\partial u_i}{\partial t} + u_j \frac{\partial u_i}{\partial x_j} \right] = \mathbf{e}_i \left[\frac{f_i}{\rho} - \frac{1}{\rho} \frac{\partial p}{\partial x_i} + \frac{1}{\rho} \frac{\partial}{\partial x_j} \left(2\mu D_{ij} + \delta_{ij} \lambda \frac{\partial u_k}{\partial x_k} \right) \right] \quad (2.37)$$

with \mathbf{D} the symmetrical deformation or rate of strain tensor, so that

$$2\mathbf{D} \equiv \nabla \mathbf{u} + \nabla^T \mathbf{u} = \mathbf{e}_i \mathbf{e}_j \left(\frac{\partial u_i}{\partial x_j} + \frac{\partial u_j}{\partial x_i} \right) \quad (2.38)$$

Parenthetically, the rotation tensor \mathbf{R} is defined as

$$2\mathbf{R} \equiv \nabla \mathbf{u} - \nabla^T \mathbf{u} = \mathbf{e}_i \mathbf{e}_j \left(\frac{\partial u_i}{\partial x_j} - \frac{\partial u_j}{\partial x_i} \right) \quad (2.39)$$

The transport of vorticity equation can be now derived by taking the curl of equation 2.37

$$\mathbf{e}_i \varepsilon_{ijk} \frac{\partial}{\partial x_j} \left[\frac{D u_k}{Dt} \right] = \mathbf{e}_i \varepsilon_{ijk} \frac{\partial}{\partial x_j} \left[\frac{f_k}{\rho} - \frac{1}{\rho} \frac{\partial p}{\partial x_k} + \frac{1}{\rho} \frac{\partial}{\partial x_l} \left(2\mu D_{kl} + \delta_{kl} \lambda \frac{\partial u_m}{\partial x_m} \right) \right] \quad (2.40)$$

For single fluid flows one usually takes μ constants with negligible or zero derivatives. Here we will include their derivatives. The left hand side (LHS) and right hand side (RHS) of the above equation are treated separately

Left hand side I

The LHS of the equation equals

$$\mathbf{e}_i \varepsilon_{ijk} \frac{\partial}{\partial x_j} \left[\frac{\partial u_k}{\partial t} + u_l \frac{\partial u_k}{\partial x_l} \right] = \mathbf{e}_i \varepsilon_{ijk} \left[\frac{\partial}{\partial t} \left(\frac{\partial u_k}{\partial x_j} \right) + u_l \frac{\partial^2 u_k}{\partial x_j \partial x_l} + \underbrace{\frac{\partial u_l}{\partial x_j} \frac{\partial u_k}{\partial x_l}}_A \right] \quad (2.41)$$

and term A is written as

$$\begin{aligned}
 \varepsilon_{ijk} \frac{\partial u_l}{\partial x_j} \frac{\partial u_k}{\partial x_l} &= \varepsilon_{ijk} \frac{\partial u_k}{\partial x_j} \frac{\partial u_l}{\partial x_l} + \varepsilon_{ijk} \frac{\partial u_i}{\partial x_j} \frac{\partial u_k}{\partial x_i} \\
 &= \frac{\partial u_l}{\partial x_l} \varepsilon_{ijk} \frac{\partial u_k}{\partial x_j} - \varepsilon_{jkl} \frac{\partial u_i}{\partial x_j} \frac{\partial u_l}{\partial x_k} \\
 &= \omega_i \frac{\partial u_j}{\partial x_j} - \omega_j \frac{\partial u_i}{\partial x_j}
 \end{aligned} \tag{2.42}$$

Substituting in eq. 2.41

$$\mathbf{e}_i \varepsilon_{ijk} \frac{\partial}{\partial x_j} \left[\frac{\partial u_k}{\partial t} + u_l \frac{\partial u_k}{\partial x_l} \right] = \mathbf{e}_i \left[\frac{\partial \omega_i}{\partial t} + u_j \frac{\partial \omega_i}{\partial x_j} + \omega_i \frac{\partial u_j}{\partial x_j} - \underbrace{\omega_j \frac{\partial u_i}{\partial x_j}}_B \right] \tag{2.43}$$

Expanding term B

$$\omega_j \frac{\partial u_i}{\partial x_j} = \frac{1}{2} \left(\frac{\partial u_i}{\partial x_j} + \frac{\partial u_j}{\partial x_i} \right) \omega_j + \frac{1}{2} \left(\frac{\partial u_i}{\partial x_j} - \frac{\partial u_j}{\partial x_i} \right) \omega_j = D_{ij} \omega_j + \underbrace{R_{ij} \omega_j}_C \tag{2.44}$$

Note that elements of the rotation tensor \mathbf{R} can be written as

$$R_{ij} = -\frac{1}{2} \varepsilon_{ijk} \omega_k \tag{2.45}$$

or

$$\omega_i = \varepsilon_{ijk} R_{kj} \tag{2.46}$$

Term C now equals

$$\omega_j \left(\frac{\partial u_i}{\partial x_j} - \frac{\partial u_j}{\partial x_i} \right) = -\frac{1}{2} \varepsilon_{ijk} \omega_j \omega_k = 0 \tag{2.47}$$

The LHS is now written as

$$\mathbf{e}_i \varepsilon_{ijk} \frac{\partial}{\partial x_j} \left[\frac{D u_k}{D t} \right] = \mathbf{e}_i \left[\frac{D \omega_i}{D t} + \omega_i \frac{\partial u_j}{\partial x_j} - D_{ij} \omega_j \right] \tag{2.48}$$

or in vector notation

$$\nabla \times \frac{D \mathbf{u}}{D t} = \frac{D \boldsymbol{\omega}}{D t} + (\nabla \cdot \mathbf{u}) \boldsymbol{\omega} - \mathbf{D} \boldsymbol{\omega} \tag{2.49}$$

Right hand side I

The RHS is taken in two steps, as the force and pressure terms are straightforward

$$\mathbf{e}_i \varepsilon_{ijk} \left[\frac{\partial}{\partial x_j} \left(\frac{f_k}{\rho} \right) - \frac{\partial}{\partial x_j} \left(\frac{1}{\rho} \frac{\partial p}{\partial x_k} \right) \right] = \mathbf{e}_i \varepsilon_{ijk} \left[\frac{1}{\rho} \frac{\partial f_k}{\partial x_j} - \frac{f_k}{\rho^2} \frac{\partial \rho}{\partial x_j} - \frac{1}{\rho} \underbrace{\frac{\partial^2 p}{\partial x_j \partial x_k}}_{=0} + \frac{1}{\rho^2} \frac{\partial \rho}{\partial x_j} \frac{\partial p}{\partial x_k} \right] \quad (2.50)$$

The curl of the stress tensor is taken in its two parts

$$\begin{aligned} \mathbf{e}_i \varepsilon_{ijk} \frac{\partial}{\partial x_j} \left[\frac{1}{\rho} \frac{\partial}{\partial x_l} \left(2\mu D_{kl} + \delta_{kl} \lambda \frac{\partial u_m}{\partial x_m} \right) \right] &= \underbrace{\mathbf{e}_i \varepsilon_{ijk} 2 \frac{\partial}{\partial x_j} \left(\frac{1}{\rho} \frac{\partial \mu D_{kl}}{\partial x_l} \right)}_A \\ &+ \underbrace{\mathbf{e}_i \varepsilon_{ijk} \frac{\partial}{\partial x_j} \left(\frac{1}{\rho} \frac{\partial}{\partial x_l} \left(\delta_{kl} \lambda \frac{\partial u_m}{\partial x_m} \right) \right)}_B \end{aligned} \quad (2.51)$$

For term A, the chain rule of differentiation is applied

$$\mathbf{e}_i \varepsilon_{ijk} 2 \frac{\partial}{\partial x_j} \left(\frac{1}{\rho} \frac{\partial \mu D_{kl}}{\partial x_l} \right) = \mathbf{e}_i \varepsilon_{ijk} 2 \left[\underbrace{\nu \frac{\partial^2 D_{kl}}{\partial x_j \partial x_l}}_C + \underbrace{\frac{\partial \nu}{\partial x_j} \frac{\partial D_{kl}}{\partial x_l}}_D + \underbrace{\frac{1}{\rho} \frac{\partial \mu}{\partial x_l} \frac{\partial D_{kl}}{\partial x_j}}_E + \underbrace{\frac{1}{\rho} D_{kl} \frac{\partial^2 \mu}{\partial x_j \partial x_l}}_F + \underbrace{\frac{\partial \mu}{\partial x_l} D_{kl} \frac{\partial \rho^{-1}}{\partial x_j}}_G \right] \quad (2.52)$$

Note that the first and second derivatives of μ appear in the relation

Term C ³:

$$\begin{aligned} 2\mathbf{e}_i \varepsilon_{ijk} \nu \frac{\partial^2 D_{kl}}{\partial x_j \partial x_l} &= 2\mathbf{e}_i \varepsilon_{ijk} \nu \frac{\partial}{\partial x_l} \left(\frac{\partial D_{kl}}{\partial x_j} \right) = \mathbf{e}_i \varepsilon_{ijk} \nu \left[\frac{\partial^3 u_k}{\partial x_j \partial x_l^2} + \frac{\partial}{\partial x_l} \underbrace{\frac{\partial^2 u_l}{\partial x_j \partial x_k}}_{=0} \right] \\ &= \mathbf{e}_i \nu \frac{\partial^2}{\partial x_l^2} \left(\varepsilon_{ijk} \frac{\partial u_k}{\partial x_j} \right) = \mathbf{e}_i \nu \frac{\partial}{\partial x_l} \left(\frac{\partial \omega_i}{\partial x_l} \right) \end{aligned} \quad (2.53)$$

³ $2\nabla \times \mathbf{u} = \nu \Delta \omega$

Term D ⁴:

$$\begin{aligned} 2\mathbf{e}_i\varepsilon_{ijk}\frac{\partial\nu}{\partial x_j}\frac{\partial D_{kl}}{\partial x_l} &= \mathbf{e}_i\varepsilon_{ijk}\left(\frac{1}{\rho}\frac{\partial\mu}{\partial x_j}-\frac{\mu}{\rho^2}\frac{\partial\rho}{\partial x_j}\right)\frac{\partial D_{kl}}{\partial x_l} \\ &= \mathbf{e}_i\varepsilon_{ijk}\left(\frac{1}{\rho}\frac{\partial\mu}{\partial x_j}-\frac{\mu}{\rho^2}\frac{\partial\rho}{\partial x_j}\right)\left(\frac{\partial^2 u_k}{\partial x_l^2}+\varepsilon_{klm}\frac{\partial u_m}{\partial x_l}\right) \end{aligned} \quad (2.54)$$

Term E ⁵:

$$\begin{aligned} 2\mathbf{e}_i\varepsilon_{ijk}\frac{1}{\rho}\frac{\partial\mu}{\partial x_l}\frac{\partial D_{kl}}{\partial x_j} &= \mathbf{e}_i\varepsilon_{ijk}\left[\frac{1}{\rho}\frac{\partial\mu}{\partial x_l}\frac{\partial^2 u_k}{\partial x_j\partial x_l}+\frac{1}{\rho}\frac{\partial\mu}{\partial x_l}\underbrace{\frac{\partial^2 u_l}{\partial x_j\partial x_k}}_{=0}\right] \\ &= \mathbf{e}_i\frac{1}{\rho}\frac{\partial\mu}{\partial x_l}\frac{\partial}{\partial x_l}\left(\varepsilon_{ijk}\frac{\partial u_k}{\partial x_j}\right) = \mathbf{e}_i\frac{1}{\rho}\frac{\partial\mu}{\partial x_j}\frac{\partial\omega_i}{\partial x_j} \end{aligned} \quad (2.55)$$

Term F ⁶ is not rewritten. Term G ⁷ equals

$$2\mathbf{e}_i\varepsilon_{ijk}\frac{\partial\mu}{\partial x_l}D_{kl}\frac{\partial\rho^{-1}}{\partial x_j} = -2\mathbf{e}_i\varepsilon_{ijk}\frac{1}{\rho^2}\frac{\partial\mu}{\partial x_l}D_{kl}\frac{\partial\rho}{\partial x_j} \quad (2.56)$$

The curl of the second term of the stress tensor, term B ⁸, is equal to

$$\begin{aligned} \mathbf{e}_i\varepsilon_{ijk}\frac{\partial}{\partial x_j}\left[\frac{1}{\rho}\frac{\partial}{\partial x_l}\left(\delta_{kl}\lambda\frac{\partial u_m}{\partial x_m}\right)\right] &= \mathbf{e}_i\varepsilon_{ijk}\left[\frac{\partial}{\partial x_k}\left(\lambda\frac{\partial\rho^{-1}}{\partial x_j}\frac{\partial u_l}{\partial x_l}\right)+\frac{1}{\rho}\frac{\partial^2}{\partial x_j\partial x_k}\left(\lambda\frac{\partial u_l}{\partial x_l}\right)\right] \\ &= -\mathbf{e}_i\varepsilon_{ijk}\frac{\partial\rho}{\partial x_j}\left[\frac{1}{\rho^2}\frac{\partial\lambda}{\partial x_k}\frac{\partial u_l}{\partial x_l}+\frac{\lambda}{\rho^2}\frac{\partial^2 u_l}{\partial x_k\partial x_l}\right] \\ &= -\mathbf{e}_i\varepsilon_{ijk}\frac{\partial\rho}{\partial x_j}\left[\frac{1}{\rho^2}\frac{\partial\lambda}{\partial x_k}\frac{\partial u_l}{\partial x_l}+\frac{\lambda}{\rho^2}\frac{\partial\rho}{\partial x_j}\left(\frac{\partial^2 u_l}{\partial x_l^2}+\varepsilon_{klm}\frac{\partial\omega_m}{\partial x_l}\right)\right] \end{aligned} \quad (2.57)$$

⁴ $2\nabla\nu\times(\nabla\cdot\mathbf{D})=\left(\frac{1}{\rho}\nabla\mu-\frac{\mu}{\rho^2}\nabla\rho\right)\times(2\Delta\mathbf{u}+\nabla\times\boldsymbol{\omega})$

⁵ $\frac{2}{\rho}\nabla\mu\cdot\nabla\mathbf{D}=\frac{1}{\rho}(\nabla\mu\cdot\nabla)\boldsymbol{\omega}$

⁶ $2\mathbf{e}_i\varepsilon_{ijk}\frac{1}{\rho}D_{kl}\frac{\partial^2\mu}{\partial x_j\partial x_l}=-2\frac{1}{\rho}(\mathbf{D}\nabla)\times\nabla\mathbf{u}$

⁷ $2\nabla\rho^{-1}\times(\mathbf{D}\nabla\mu)=-2\frac{1}{\rho^2}\nabla\rho\times(\mathbf{D}\nabla\mu)$

⁸ $\nabla\times\left(\frac{1}{\rho}\nabla\cdot\lambda\mathbf{I}(\nabla\cdot\mathbf{u})\right)=-\frac{\nabla\rho}{\rho^2}\times((\nabla\cdot\mathbf{u})\nabla\lambda+\lambda(\Delta\mathbf{u}+\nabla\times\boldsymbol{\omega}))$

Combining all elements results in the transport of vorticity equation

$$\begin{aligned}
 \mathbf{e}_i \left[\frac{D\omega_i}{Dt} + \omega_i \frac{\partial u_j}{\partial x_j} - D_{ij}\omega_j \right] = & \mathbf{e}_i \varepsilon_{ijk} \left[\begin{aligned}
 & \frac{1}{\rho} \frac{\partial f_k}{\partial x_j} - \frac{f_k}{\rho^2} \frac{\partial \rho}{\partial x_j} + \frac{1}{\rho^2} \frac{\partial \rho}{\partial x_j} \frac{\partial p}{\partial x_k} \\
 & + \left(\frac{1}{\rho} \frac{\partial \mu}{\partial x_j} - \frac{\mu}{\rho^2} \frac{\partial \rho}{\partial x_j} \right) \frac{\partial D_{kl}}{\partial x_l} \\
 & + \frac{2}{\rho} \left(\frac{\partial^2 \mu}{\partial x_j \partial x_l} - \frac{1}{\rho} \frac{\partial \rho}{\partial x_j} \frac{\partial \mu}{\partial x_l} \right) D_{kl} \\
 & - \frac{\partial \rho}{\partial x_j} \left(\frac{\lambda}{\rho^2} \frac{\partial^2 u_l}{\partial x_k \partial x_l} + \frac{1}{\rho^2} \frac{\partial \lambda}{\partial x_k} \frac{\partial u_l}{\partial x_l} \right)
 \end{aligned} \right] \\
 & + \mathbf{e}_i \nu \left[\frac{\partial}{\partial x_j} \left(\frac{\partial \omega_i}{\partial x_j} \right) + \frac{1}{\rho} \frac{\partial \mu}{\partial x_j} \frac{\partial \omega_i}{\partial x_j} \right]
 \end{aligned} \tag{2.58}$$

The expression is now largely written in terms of the vorticity, $\boldsymbol{\omega}$, and viscosity and density gradients.

The liquid fraction

The viscosity and density of the mixture are expressed in terms of the vapor and liquid properties as a mixture function of the void fraction α

$$\begin{aligned}
 \mu &= \alpha \mu_v + (1 - \alpha) \mu_l \\
 \rho &= \alpha \rho_v + (1 - \alpha) \rho_l
 \end{aligned} \tag{2.59}$$

The expression for the viscosity of the mixture is a simple approach for an initial estimation of the transport equation. The classical Helmholtz-vorticity transport equation is often written in terms of $\bar{\omega} = \omega/\rho$, so eq. 2.59 is preferably written as a function of the liquid fraction $\gamma = 1 - \alpha$. If the additional condition for γ is added and $\rho_v \ll \rho_l$ and $\mu_l \ll \mu_v$ then

$$\frac{\rho_v}{\rho_l} \leq \gamma \leq 1 \tag{2.60}$$

then $\bar{\omega} = \omega/(\gamma\rho_l)$ is written as

$$\mu = \gamma \mu_l \tag{2.61}$$

$$\rho = \gamma \rho_l$$

with the additional condition for γ that

$$\frac{\rho_v}{\rho_l} \leq \gamma \leq 1 \tag{2.62}$$

With this condition both dynamic viscosity and density are linear in terms of γ and the kinematic viscosity is a constant. All its derivatives are therefore zero. Substitution of eq. 2.61 in eq. 2.58, applying Stokes' hypothesis that $\kappa = \mu + \lambda = 0$, and some minor rearranging results in

$$\mathbf{e}_i \left[\frac{D\omega_i}{Dt} + \omega_i \frac{\partial u_j}{\partial x_j} - D_{ij}\omega_j \right] = \mathbf{e}_i \varepsilon_{ijk} \left[\begin{aligned} & \frac{1}{\gamma \rho_l} \frac{\partial f_k}{\partial x_j} - \frac{f_k}{\gamma^2 \rho_l} \frac{\partial \gamma}{\partial x_j} + \frac{1}{\gamma^2 \rho_l} \frac{\partial \gamma}{\partial x_j} \frac{\partial p}{\partial x_k} \\ & + \frac{2\nu}{\gamma} \left(H_{\gamma,jl} - \frac{1}{\gamma^2} G_{\nabla\gamma,jl} \right) D_{kl} \\ & + \frac{2\nu}{3} \frac{\partial \gamma}{\gamma} \frac{\partial^2 u_l}{\partial x_j \partial x_k \partial x_l} \end{aligned} \right] \quad (2.63)$$

$$+ \mathbf{e}_i \left[\nu \frac{\partial}{\partial x_j} \left(\frac{\partial \omega_i}{\partial x_j} \right) + \frac{\nu}{\gamma} \frac{\partial \gamma}{\partial x_j} \frac{\partial \omega_i}{\partial x_j} \right]$$

or alternatively in vector notation

$$\begin{aligned} \frac{D\boldsymbol{\omega}}{Dt} + (\nabla \cdot \mathbf{u}) \boldsymbol{\omega} - \mathbf{D}\boldsymbol{\omega} &= \frac{1}{\gamma \rho_l} \nabla \times \mathbf{f} - \frac{f_k}{\gamma^2 \rho_l} \nabla \times \boldsymbol{\gamma} + \frac{1}{\rho_l \gamma^2} \nabla \boldsymbol{\gamma} \times \nabla p + \nu \nabla^2 \boldsymbol{\omega} \\ &+ 2 \frac{\nu}{\gamma} \left(\mathbf{H}_\gamma - \frac{1}{\gamma} \mathbf{G}_{\nabla\gamma} \right) \times \mathbf{D} \quad (2.64) \\ &+ \frac{2\nu}{3} \frac{\nu}{\gamma} \nabla \boldsymbol{\gamma} \times (\Delta \mathbf{u} + \nabla \times \boldsymbol{\omega}) + \frac{\nu}{\gamma} (\nabla \boldsymbol{\gamma} \cdot \nabla) \boldsymbol{\omega} \end{aligned}$$

The definitions of \mathbf{H} and \mathbf{G} follow from A.13 and A.14, respectively, and the tensor cross product from eq. A.16. For the next step, both the LHS and RHS will be written in terms of $\bar{\omega} = \omega/\rho$.

Left Hand Side - II

The transport of liquid equation can be derived by substituting eq. 2.59 in the continuity equation

$$\frac{\partial \gamma}{\partial t} + \frac{\partial \gamma u_i}{\partial x_i} = - \frac{\gamma}{\rho_l - \rho_v} \left(\frac{\partial \rho_v}{\partial t} + \frac{\partial \rho_v u_i}{\partial x_i} \right) - \frac{\gamma}{\rho_l - \rho_v} \left(\frac{\partial \rho_l}{\partial t} + \frac{\partial \rho_l u_i}{\partial x_i} \right) + \gamma \frac{\partial u_i}{\partial x_i} \quad (2.65)$$

where no a priori assumptions on the equations of state of either the vapor or gas phase are made. The RHS is usually substituted with a vapor production or destruction term S . The second term of the LHS of the above equation is differentiated in parts so that

$$\frac{\partial u_i}{\partial x_i} = \frac{1}{\gamma} \left(S - \frac{\partial \gamma}{\partial t} - u_i \frac{\partial \gamma}{\partial x_i} \right) = \frac{1}{\gamma} \left(S - \frac{D\gamma}{Dt} \right) \quad (2.66)$$

Second, note that

$$\mathbf{e}_i \frac{D\omega_i}{Dt} = \mathbf{e}_i \left[\gamma \frac{D\omega_i/\gamma}{Dt} + \frac{\omega_i}{\gamma} \frac{D\gamma}{Dt} \right]; \quad (2.67)$$

Substituting eqs. 2.66&2.67 in the LHS of eq. 2.63 yields

$$\mathbf{e}_i \left[\frac{D\omega_i}{Dt} + \omega_i \frac{\partial u_j}{\partial x_j} - D_{ij}\omega_j \right] = \mathbf{e}_i \left[\gamma \frac{D\omega_i/\gamma}{Dt} + \frac{\omega_i}{\gamma} S - D_{ij}\omega_j \right] \quad (2.68)$$

Right Hand Side - II

Note that the last two terms of the RHS of eq. 2.63 can be written as

$$\mathbf{e}_i \frac{\partial}{\partial x_j} \left(\frac{\partial \omega_i}{\partial x_j} \right) = \mathbf{e}_i \left[\frac{\omega_i}{\gamma} \frac{\partial}{\partial x_j} \left(\frac{\partial \gamma}{\partial x_j} \right) + \frac{1}{\gamma} \frac{\partial}{\partial x_j} \left(\frac{\partial \omega_i/\gamma}{\partial x_j} \right) + 2 \frac{\partial \gamma}{\partial x_j} \frac{\partial \omega_i/\gamma}{\partial x_j} \right] \quad (2.69)$$

and

$$\frac{1}{\gamma} \frac{\partial \gamma}{\partial x_j} \frac{\partial \omega_i}{\partial x_j} = \frac{\partial \gamma}{\partial x_j} \frac{\partial \omega_i/\gamma}{\partial x_j} + \frac{\omega_i}{\gamma^2} \frac{\partial \gamma}{\partial x_j} \frac{\partial \gamma}{\partial x_j} \quad (2.70)$$

Transport of vorticity equation

For the final results eqs. 2.68, 2.69, and 2.70 are substituted into eq. 2.63 and divided by γ .

$$\begin{aligned} \mathbf{e}_i \left[\frac{D\bar{\omega}_i}{Dt} + \frac{\bar{\omega}_i}{\gamma} S - D_{ij}\bar{\omega}_j \right] = & \mathbf{e}_i \varepsilon_{ijk} \left[\begin{aligned} & \left[\frac{1}{\gamma^2 \rho_l} \frac{\partial f_k}{\partial x_j} - \frac{f_k}{\gamma^3 \rho_l} \frac{\partial \gamma}{\partial x_j} + \frac{1}{\rho_l \gamma^2} \frac{\partial \gamma}{\partial x_j} \frac{\partial p}{\partial x_k} \right] \\ & + 2 \frac{\nu}{\gamma} \left(H_{\gamma,jl} - \frac{1}{\gamma^2} G_{\nabla\gamma,jl} \right) D_{kl} \\ & + \frac{2\nu}{3\gamma} \frac{\partial \gamma}{\partial x_j} \frac{\partial^2 u_m}{\partial x_k \partial x_m} \end{aligned} \right] \\ & + \mathbf{e}_i \frac{\nu}{\gamma} \left[\begin{aligned} & \bar{\omega}_i \frac{\partial}{\partial x_j} \left(\frac{\partial \gamma}{\partial x_j} \right) + \frac{1}{\gamma} \frac{\partial}{\partial x_j} \left(\frac{\partial \bar{\omega}_i}{\partial x_j} \right) \\ & + 3 \frac{\partial \gamma}{\partial x_j} \frac{\partial \bar{\omega}_i}{\partial x_j} + \frac{\bar{\omega}_i}{\gamma} \frac{\partial \gamma}{\partial x_j} \frac{\partial \gamma}{\partial x_j} \end{aligned} \right] \end{aligned} \quad (2.71)$$

or in vector notation

$$\begin{aligned} \frac{D\bar{\boldsymbol{\omega}}}{Dt} + \frac{\bar{\boldsymbol{\omega}}}{\gamma} S - \mathbf{D}\bar{\boldsymbol{\omega}} = & \frac{1}{\gamma^2 \rho_l} \nabla \times \mathbf{f} - \frac{\mathbf{f}}{\gamma^3 \rho_l} \nabla \times \gamma + \frac{1}{\gamma^2 \rho_l} \nabla \gamma \times \nabla p \\ & + \frac{\nu}{\gamma} \left[\begin{aligned} & 2 \left(\mathbf{H}_\gamma - \frac{1}{\gamma} \mathbf{G}_{\nabla\gamma} \right) \times \mathbf{D} + \frac{2}{3} \frac{\nabla \gamma}{\gamma} \times \nabla (\nabla \cdot \mathbf{u}) \\ & \bar{\boldsymbol{\omega}} \nabla^2 \gamma + \frac{1}{\gamma} \nabla^2 \bar{\boldsymbol{\omega}} + 3 (\nabla \gamma \cdot \nabla) \bar{\boldsymbol{\omega}} + \frac{\bar{\boldsymbol{\omega}}}{\gamma} (\nabla \gamma \cdot \nabla \gamma) \end{aligned} \right] \end{aligned} \quad (2.72)$$

The bulk of the terms are the result of the recurrent application of the chain rule for the derivatives on the viscosity. If we assume a constant viscosity and drop all gradients of the liquid factor, and recall that only the second term of the right hand side is a function of the density, then the above equation reduces to

$$\frac{D\bar{\omega}}{Dt} = (\bar{\omega} \cdot \nabla) \mathbf{u} + \frac{1}{\rho} \nabla \times \mathbf{f} + \frac{1}{\rho^3} \nabla \rho \times \nabla p + \nu \nabla^2 \bar{\omega} \quad (2.73)$$

which is the classical Helmholtz vorticity transport equation. The RHS consists of four terms namely the vortex stretching term, rotation due to external force fields, baroclinic torque, and viscous production.

The second term result in vorticity production of non-conservative force fields, such as electromagnetic forces or rotating coordinate systems. With cavitation flows, the only active force field is the gravity field with a curvature that is so large as to rendering its curl to practically zero. The baroclinic term acts whenever pressure and density gradients are not aligned. Large gradients in density and pressure do not lead to any vorticity production if the gradients are aligned, such as in a barotropic flow, or with any cavitation model with near instantaneous vapor production and destruction. The final term, viscous production, generates vorticity at a solid boundary and transports this vorticity into the flow. To identify production terms due to the viscosity gradients of the flow in eqs. 2.72, the incoming flow is set to $\bar{\omega} = 0$ so that

$$\begin{aligned} \frac{D\bar{\omega}}{Dt} = & \frac{1}{\gamma^2 \rho_l} \nabla \times \mathbf{f} - \frac{\mathbf{f}}{\gamma^3 \rho_l} \nabla \times \gamma + \frac{1}{\gamma^2 \rho_l} \nabla \gamma \times \nabla p \\ & + \frac{\nu}{\gamma} \left[2 \left(\mathbf{H}_\gamma - \frac{1}{\gamma} \mathbf{G}_{\nabla \gamma} \right) \times \mathbf{D} + \frac{2}{3} \frac{\nabla \gamma}{\gamma} \times \nabla (\nabla \cdot \mathbf{u}) \right] \end{aligned} \quad (2.74)$$

All remaining terms are inconsistent with a solution of zero vorticity production and are hence production terms. The terms on the first row of the RHS are resulting forces (usually zero for cavitating flows) and the baroclinic contribution. The term on the second line of the RHS is the remnant from taking a variable viscosity into account. This—for lack of a better term—viscoclinic torque is zero for isentropic flows or flows without any viscous dissipation. This term is non-zero if the interaction of the curvature in the liquid-fraction term and the deformation term is non-zero. In contrast to the viscous production term, viscoclinic torque can be generated away from a wall, in the flow domain, in regions of changing liquid fraction and high flow deformation. In order to estimate its contribution, detailed knowledge is required of both the velocity field and the liquid fraction field. From the experiments, the deformation tensor can only be partly resolved and the liquid fraction not at all, let alone its derivatives in all directions.

Vortical flow

An analysis of the above results for a vortical flow is made, using a simple rotation symmetrical and two-dimensional vortex model. Two basic motions are prescribed in cylindrical

coordinates. The first is uniform growth of the cavitating core so that

$$\begin{aligned} u &= U(r) \cos\theta & v &= U(r) \sin\theta \\ w &= 0 & \gamma &= f(r) \end{aligned} \quad (2.75)$$

basically acting as a source term, plus a radially variable tangential velocity distribution

$$\begin{aligned} u &= -U(r) \sin\theta & v &= U(r) \cos\theta \\ w &= 0 & \gamma &= f(r) \end{aligned} \quad (2.76)$$

corresponding to the swirling motion of the vortex. Any distribution function for γ and $U(r)$ can be chosen. Rewriting the viscoclinic equations for $\bar{\omega}_z = f(r, \theta)$ to polar coordinates result in

$$\frac{D\bar{\omega}_z}{Dt} = 0 \quad (2.77)$$

for the source motion and

$$\frac{D\bar{\omega}_z}{Dt} = 2\frac{\nu}{\gamma} \left(\frac{\partial^2 \gamma}{\partial r^2} - \frac{1}{r} \frac{\partial \gamma}{\partial r} - \frac{1}{\gamma} \left(\frac{\partial \gamma}{\partial r} \right)^2 \right) \left(\frac{\partial U(r)}{\partial r} - \frac{U(r)}{r} \right) \quad (2.78)$$

for the swirling motion. The contribution to the vorticity production is zero if

$$\frac{\partial U(r)}{\partial r} = \frac{U(r)}{r} \quad (2.79)$$

The solution $U(r)$ corresponds to solid core rotation of the vortex, for any distribution function of γ . As the interface of a cavitating vortex is often smooth, it appears that γ acts as a step function and may not contribute at all to the production term. So, with this simplified model, a vortex does not contribute to the viscoclinic torque, leaving the production to regions of high vorticity and deformation. Regions of high vorticity are not necessarily a vortex (Adrian *et al.* 2000), as shear flows can experience high shear. The low pressure inside the vortical core, isovortical lines and spiraling stream and path lines are an insufficient condition for finding a vortex (Jeong & Hussain 1995). When a vortex is cavitating, it can be readily be identified, but this is more difficult in the wake of a sheet cavity when the vortex core has condensed. In order to differentiate between vorticity due to a vortex or due to shear, the Q -criterion is introduced by Hunt *et al.* (1988), with the tensor \mathbf{Q}

$$Q_{ij} = \frac{R_{ij}^2 - D_{ij}^2}{2} \quad (2.80)$$

The eigen-values of \mathbf{Q} are λ_1 , λ_2 , and λ_3 with $\lambda_1 < \lambda_2 < \lambda_3$. The Q -criterion classifies a vortex as a region where $\lambda_1 + \lambda_2 + \lambda_3 < 0$. According to Jeong & Hussain (1995), a low pressure region corresponds to $\lambda_2 < 0$ and forms a more strict criterion. With the planar PIV, only the gradients within the PIV plane can be resolved. Note that even

stereoscopic PIV cannot resolve gradients perpendicular to the measurement plane so only 4 entries of e.g., the Reynolds stress tensor or rate of deformation tensor can be resolved. An alternative for two-dimensional turbulence is the Okubo-Weiss parameter (Pasquero *et al.* (2002)):

$$Q = \left(\frac{\partial u}{\partial x} - \frac{\partial v}{\partial y} \right)^2 + \left(\frac{\partial u}{\partial y} + \frac{\partial v}{\partial x} \right)^2 - \left(\frac{\partial u}{\partial y} - \frac{\partial v}{\partial x} \right)^2 \quad (2.81)$$

whereby a vortex core is typified by a strongly negative value of Q . Naturally, the velocity distribution is far from two-dimensional but may give some insight in the vorticity distribution. The vapor fraction cannot be determined with any accuracy with the experimental techniques used in the current research, but the rate of strain and vorticity can be found by means of detailed PIV analysis. Using the Okubo-Weiss parameter, regions of high vorticity due to shear can be found, distinguishable from regions of high vorticity near vortices.

Chapter 3

Measurement setup

3.1 Introduction

This chapter discusses the measurement setup in detail. Section 3.2 describes the basic setup: the cavitation tunnel at Delft University of Technology, modified to the needs of high-speed data acquisition. The water quality is discussed in terms of gas content, nuclei content, turbulence level, and the velocity profile of the test section. Leading edge roughness was applied to both ensure tripping of the boundary layer and the generation of flow nuclei. An extensive uncertainty analysis is presented in the appendices of this section. Section 3.3 discusses Particle Image Velocimetry (PIV). A brief introduction on the technique is followed by a discussion on its accuracy. As is known from literature, applying PIV to cavitating flows leads to over-exposure of the images leading in use of fluorescent particles and optical filters. A typical result of the empty test section is presented to ascertain the quality of the measurement technique as used.

This research is focused on three-dimensional hydrofoils and their geometry definition is given in sec. 3.4. Two parent forms are used, a finite span elliptical wing and a symmetric hydrofoil with a span-symmetric twist. The cross-section profile is a Naca0009 for the hydrofoils, except for one hydrofoil with an Eppler YS-920 profile. The Eppler hydrofoil has a flat pressure distribution on the suction side reminiscent to pressure distributions on propeller profiles and is expected to be sensitive to changes in loading. One hydrofoil is fitted with miniature pressure transducers, presented in s. 3.5. These pressure sensors are embedded in the foil as to reduce the risk of destruction by cavitation. The lift force on the hydrofoil is measured by a full 6 degrees of freedom load sensor on both sides of the tunnel wall (sec. 3.6). The result is a combined measurement of local pressures and directly measured lift force.

Section 3.7 discusses the flow oscillator. The flow oscillator is used to vary the loading on the hydrofoils in order to simulate the periodically changing inflow of a ship propeller. The difficulty with such a flow oscillator is keeping it free of cavitation and keeping the

forces on the setup low while generating a flow disturbance that will effect a change in the sheet cavity on the main hydrofoil.

3.2 The cavitation tunnel

The test facility used for the present research is the cavitation tunnel at Delft University of Technology. The tunnel was manufactured by Kempf und Remmers who supplied many laboratories with cavitation tunnels in the 1960's. During the 1970's, the sections of the tunnel were gradually replaced by stainless steel. The tunnel is driven by a 10 kW electric drive and uses a propeller from early propeller cavitation research by Kuiper (1981) as an impeller . The tunnel is a simple closed loop without a resorber or de-aeration chamber (fig. 1). The velocity in the empty test section can attain a maximum of 10 m/s , although for continuous running a speed of 7 – 8 m/s does not tax the tunnel drive to thermal shut-down.

At the start of the project the tunnel was fitted with mercury manometers and a plethora of tubes forming a continuous source of air leaks. The tunnel was renovated by removing all tubes and closing off all pressure taps, and was fitted with new pressure transducers, a thermocouple, and a new vacuum pump with an automated pressure valve to control the static pressure. The tunnel drive was replaced prior to the start of the current research but its control could not guarantee a completely constant water speed. The tunnel control system regulates on the rotation rate of the pump, resulting in a test section velocity depending on the water temperature as well as on the configuration of the test setup.

The test section has the dimensions $L \times B \times H$ 600mm \times 297mm \times 297mm. The advantages of a small test section are that the forces on the hydrofoils are comparatively small and the hydrofoils can span the entire water tunnel. The test section (fig 2) consists of four perspex windows allowing for optical access from all sides. The windows can be easily removed to change the test setup. The water tunnel is fitted with ten Keller PAA-15 transducers (fig. 1, point 2). Two sensors are placed in front of the contraction on the test section's central line. The inlet and outlet plane of the test section are fitted with four sensors each (fig. 2). The pressure in the outlet plane was purposely measured to be used as a boundary condition in numerical calculations. An example of a measurement is in fig. K4,p. 207 to show that the pressure within a measurement plane can be considered homogeneous. The determination of the velocity in the test section and the accompanying error analysis are discussed extensively in appendices B & C. *Note that the z -axis points downward and that all experiments were performed with the suction side of the test hydrofoils directed to the bottom of the test section.*

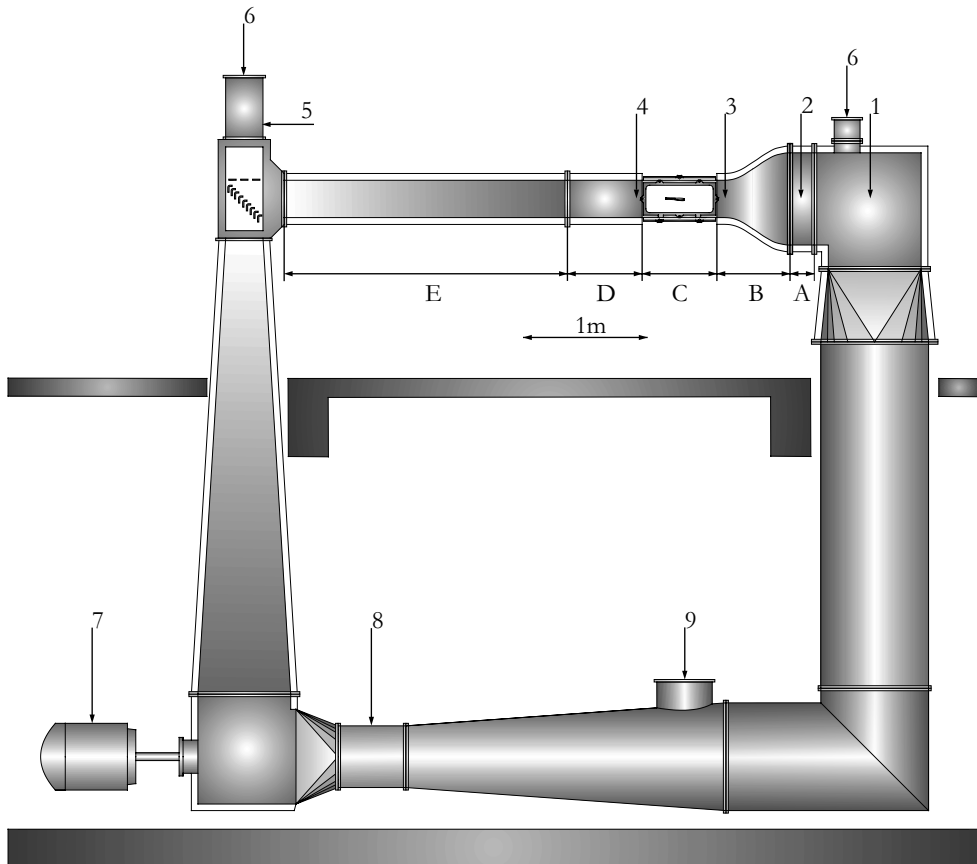


Figure 1 A sketch of the cavitation tunnel at Delft University of Technology. Flow is counter-clockwise. Indicated are the honeycomb grid (A), the contraction (B), the test section (C), a parallel section (D), and the diffuser (E). Numerals indicate: the location reference pressure transmitter (1), pressure transducers in front of the contraction (2), inlet (3) and outlet plane (4), a thermocouple (5), connections to the vacuum pump (6), the tunnel drive (7), impeller location (8), and a manhole with de-aeration tap (9)

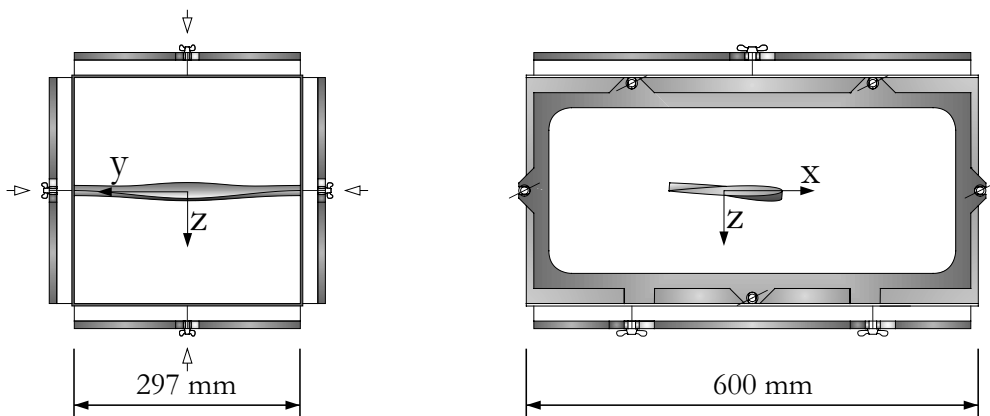


Figure 2 A sketch of the test section, flow right to left. The frame of reference is located at the center of the test section, shifted to $x = -40\text{mm}$ to coincide with the rotation point of the hydrofoils. The arrows indicate the position of the pressure transducers at the inlet and outlet plane. Note that the effective viewing area is reduced by the window frame.

3.2.1 Water quality and leading edge roughness

For limited Reynolds numbers—typical for small scale hydrofoils and propellers—the transition to turbulence of the boundary layer does not occur at the leading edge unless the boundary layer is locally disturbed. Four conditions are identified for fully-wetted flow; a) laminar flow without transition or separation, b) laminar flow with a natural transition to turbulence but remaining attached, c) laminar flow detaching with transition to turbulence in the separated region and d) flow with a natural transition to turbulence with separation in the turbulent region.

The flow does not cavitate when the boundary layer is laminar in the low pressure region and remains attached (a), as is observed at low Reynolds numbers. Laminar flow results in significant scale effects on both forces and cavitation inception. Natural transition to turbulence suppresses laminar leading-edge flow detachment. Experiments by Franc & Michel (1985) showed that when increasing the angle of attack on a hydrofoil, transition to turbulence occurred on the leading edge negating the formation of a separated laminar boundary layer and attached cavitation did not appear ¹

When laminar flow does separate, it has a transition to turbulence and reattaches downstream (c). When the flow is cavitating, the flow detaches some distance downstream of the separation point of the boundary layer. The location of boundary layer separation depends on the cavitation number but is independent of the Reynolds number. The distance from boundary layer separation to the cavity detachment point depends on the flow velocity but appears to be independent of the cavitation number (Arakeri 1975). The point of minimum pressure precedes both the point of flow detachment as well as boundary layer separation.

Attached cavitation can form in the turbulent boundary layer (d). On smooth hydrofoils without separation at the leading edge, the point of transition can be far downstream of the leading edge resulting in an suppression of inception at the leading edge. The natural transition on ship propellers occurs near the leading edge resulting in attached leading-edge cavitation, so transition to turbulence far downstream of the leading edge is not representative of full-scale propeller flow. Shen & Gowing (1986) and Caron & Avellan (2000) reported that for their oscillating hydrofoils with separation at the leading edge at steady conditions, the separated flow remained attached above a certain reduced frequency at fully-wetted conditions. The unsteady flow influences the boundary layer, which influences cavitation inception.

When the laminar boundary layer does separate at the leading edge, attached cavitation is formed at low pressures and its appearance is smooth and glassy. Experiments with axisymmetric headforms showed that for laminar cavity detachment, local indentations in the detachment line occur locally disturbing the interface (Tassin Leger *et al.* 1998). When the laminar boundary layer does not separate, transition occurs far downstream of

¹Bubbly cavitation can occur in attached turbulent regions, depending on the nuclei diameter spectrum and pressure (Katz 1984).

the leading edge and attached cavity appears on e.g., the aft section of the hydrofoil (Franc & Michel 1985).

Clearly, the boundary layer strongly influences the inception and appearance of the attached cavity. For this experiment three-dimensional hydrofoils are used at low velocities. The natural transition to turbulence will occur on different locations on the hydrofoil as the loading and local angle of attack of the hydrofoil changes in spanwise direction. The boundary layer will remain both laminar and attached at the sides of the sheet cavity on a smooth hydrofoil. If the boundary layer is tripped into transition by means of local leading-edge roughness elements, the scale effects on the inception of attached cavitation are avoided. Leading-edge roughness will effectively eliminate the laminar flow when the roughness is sufficiently large and if the pressure gradient is large.

Roughness elements of $100\ \mu\text{m}$ were applied at the leading edge (4% chord length) to force the transition to turbulence². The drag is increased but $\partial C_L/\partial\alpha$ does not change (Shen 1985). The roughness elements can lead to local streaks of cavitation appearing next to the main cavity. Either the roughness elements are too large resulting in inception on individual roughness elements, or the flow between roughness elements is insufficiently disturbed and remains laminar. The entire cavity region near the leading edge on the Twist hydrofoil resembled an agglomeration of such streaks at $5\ \text{m/s}$. This velocity was therefore deemed too low a velocity for quantitative validation measurements, but has been used for the observations as the individual streaks do merge into a single coherent attached cavity. A velocity of $7\ \text{m/s}$ resulted in a cavity with a much smoother appearance, see fig. 3.3. Note that the Reynolds number for this experiment was modest at $Re \approx 10^6$.

In a study on nuclei behavior, Liu *et al.* (1993) concluded that the number of nuclei in a tunnel changes with σ . At higher values for σ , the nuclei content decreases in time while it increases for lower σ . The time to change to a different nuclei concentration depends on the value of σ as well; concentrations may change over the course of hours. But, not only does the concentration change, the mean diameter and diameter distribution of the nuclei change as well. Clearly the occurrence of cavitation effects with the nuclei content for a closed system such as a water tunnel, resulting in a continuously changing nuclei diameter spectrum. This change in the spectrum depends in the cavitation extent, but also on the gas content due to diffusion of gas into the nuclei (Watanabe & Prosperetti 1994). An indication of nuclei content can be obtained with a so-called Cavitation Susceptibility Meter, by measuring the water's tensile strength. This device was not used and the nuclei content is not determined for these experiments, however, the gas content was measured by using a Van Slyke gas content meter. This device cannot distinguish between dissolved and free gases in the flow (Rood 1991).

²The hydrofoil tested at the Laboratoire Machine Hydraulique (LMH) at the École Polytechnique Fédérale de Lausanne (EPFL) was supplied with $60\ \mu\text{m}$ roughness

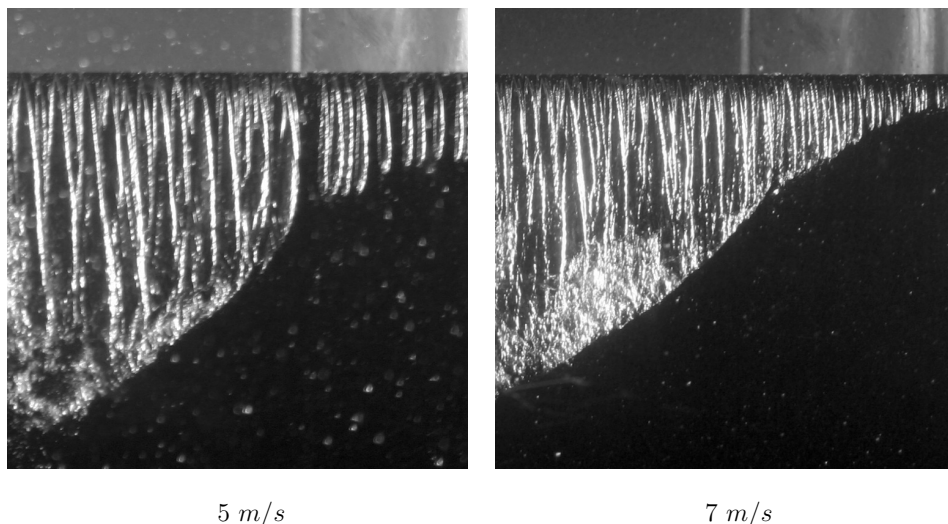


Figure 3.3 Close-ups of the leading edge, showing an area of 30% by 30% chord. The difference in the cavity appearance between a velocity of 5 m/s at left, and 7 m/s at right.

The default start-up procedure of the tunnel includes running for eight hours at very low values of σ with a cavitating hydrofoil in order to de-aerate the water. The total *volume* of the dissolved and free gas content was measured to be below 0.1%. The nuclei content was confirmed to be low on several occasions when the fully deaerated tunnel was activated after a few days of rest: the hydrofoil was observed to be free of cavitation at very low values of σ when suddenly a fully developed cavity appeared as a single nucleus entered the low-pressure region.

The gas content was not measured for most of the experiments, but the roughness elements applied to the leading edge will supply the degassed flow with ample nuclei for sheet cavitation to develop naturally (Kuiper (1982)). Without roughness, the nuclei concentration depends cubically on the ratio between full scale and model scale (Lecoffre & Bonnin 1979), so the concentration is too low at low Reynolds numbers. van der Meulen & Ye (1982) concluded that the application of roughness eliminates scale effects for bubble cavitation and was as effective as generating nuclei upstream by means of e.g., electrolysis. Bubble cavitation inception does not change due to the roughness elements as it is insensitive to the Reynolds number. However, this form of cavitation is not the goal of the current research. As incipient cavitation on roughness elements is typically observed when the value of $-\sigma$ equals the minimum pressure coefficient (Caron *et al.* 2000) it can be concluded that the nuclei content of the flow is no longer critical.

A velocity profile of the empty test section is given in fig. 3.4 for a nominal velocity of 7 m/s , measured using PIV (see s. 3.3). The inflow is not entirely uniform and varies within 2%. The velocity distribution is taken as $V = (V_0 + u', v', w')$. As the used setup results in a two-dimensional velocity field. Considering the symmetry in height and width of the cavitation tunnel, it is assumed that the turbulent fluctuations are homogeneous perpendicular to the mean flow direction so for the fluctuations v' and w' can be stated $\langle v' \rangle \approx \langle w' \rangle$. The turbulence level is calculated as

$$TL = \sqrt{\frac{\langle u' \rangle^2 + 2 \langle w' \rangle^2}{3V_0^2}} \quad (3.1)$$

to be 2-3% at the foil location.

Turbulent fluctuations in the test section remain constant within the field of view of the PIV measurements. The axial velocity was measured to rise by approx. 1% within the field of view of the PIV measurement.

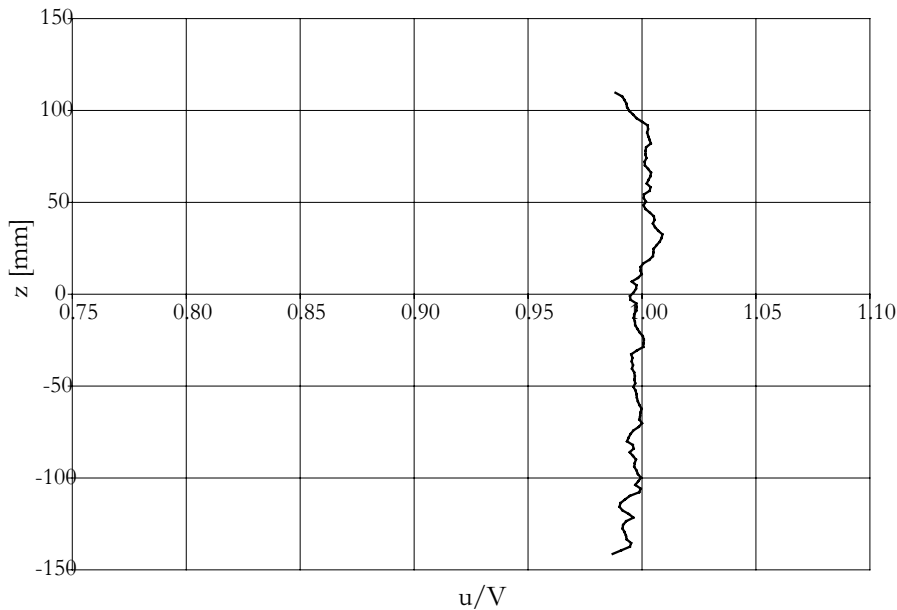


Figure 3.4 Normalized ensemble-averaged axial velocity profile measured during 0.341 s at the foil location ($x = 0$) as a function of test section height Z , see fig 2. The velocity is within 2%

3.3 Particle Image Velocimetry

3.3.1 Introduction

Particle Image Velocimetry (PIV) is an optical measuring technique for gaseous and liquid flows. The principle PIV is as follows. Seeding particles are added to the flow. If the particle density is close to that of the fluid and the particle size is not too large, they can be assumed to follow the flow perfectly and can be considered as fluid tracer particles: their velocity equals the fluid velocity. The particles are illuminated by laser light. This laser beam is expanded by means of lenses into a light sheet with a carefully specified width and thickness (see fig. D.1, p. 178). This light sheet illuminates a slice of the fluid domain. A camera—preferably placed perpendicular to the light sheet—captures the location of the tracer particles. The local particle displacement can be deduced from their location displacement from frame to frame. With a known image scaling and time between frames, the local velocity can be obtained to within 1% (Ullum *et al.* 1998).

The processing of the images in order to determine the velocity operates by dividing the image into smaller so-called interrogation windows, ranging from 16 to 128 pixels. These windows are cross-correlated with an interrogation window on the second image. A range of displacements of the interrogation window on the second image is tried in order to find the maximum correlation. This results in a correlation map based on pixel displacement, having a strong correlation peak at the matching displacement. It is important to understand that PIV interrogation does not match each individual particle from one image to the next, but correlates *particle patterns*. For instance, two photographs of a regular brick wall will show an equally strong cross-correlation at a multiples of brick displacements because the pattern is periodic. The correlation map often shows multiple correlation peaks and the strongest peak may be false, leading to a spurious result to be deleted in post-processing, e.g., by comparing it with its neighbors, checking its absolute value, or comparing its correlation peak value to the second correlation peak.

The result will be biased toward lower velocities when many particles leave the interrogation window between images due to their high velocity. In order to counter this bias error, a window shift can be applied equal to the expected particle displacement in order to keep the particle count relatively constant. More advanced algorithms use their initial solution to deform the interrogation window as well—applying the fluid’s strain rate—in order to increase the accuracy of the interrogation of the peak displacement further by capturing more matching particle pairs. Theoretically, deforming the entire first image with the correct deformation field will result in the second image, should no particle have left or entered the laser light sheet between images.

The velocity can be calculated dividing the displacement with the time between recordings and by applying an image deformation map. This image deformation map is the result of a calibration procedure, using an image of a grid with a known spacing as a scaling ref-

erence. This will (partly) remove deformation errors introduced by lens flaws or effects of looking through refracting materials (windows) at an oblique angle, introducing optical refractions and aberrations. One usually tries to place the camera perpendicular to the light sheet and tunnel wall, but even then the edges of the image are not perfectly perpendicular to the light sheet, resulting in some unavoidable deformation at the image edge. As the PIV images are often warped, curved, or otherwise distorted to some degree, a calibration function is required to "dewarp" the image back to the undeformed measurement plane. Note that the camera can only distinguish particles moving perpendicular to its viewing direction, so even if the image is dewarped, the error increases as the viewing direction deviates from orthogonal. For example, if the flow velocity would be perfectly perpendicular to the light sheet and directed toward the camera, particle displacement at the outer edges of the PIV frame seems to flow outward as a result of the perspective of the non-perpendicular viewing angle. This is interpreted as movement parallel to the light sheet by the two-dimensional PIV interrogation. With the setup used here, any out-of-plane velocity will influence the parallel velocity. This oblique viewing angle is about 4.3° at the image edges for the present experiments, resulting in a 0.3% error, which is considered acceptable.

The pulse delay of the laser used to expose two adjacent PIV frames is set so that the average particle displacement is around 10 pixels, so this delay depends on the flow velocity and size of the measurement area. With the use of high-speed cameras and lasers, a time-resolved PIV measurement can be made. It would be convenient if each frame could be correlated with its successor, so that the laser pulse delay dt would be equal to the time between frames. However, this is often not the case as the camera used for these experiments does not run at customizable frequencies (One can choose e.g., 2,000 or 3,000 frames per second and not the preferred $1/dt$). Two lasers are used so that the first laser flashes half the pulse delay before the end of frame #1 and the second laser flashes half the delay time after the start of frame #2. This will cut the effective frame rate of the camera in half.

The displacement of the tracer particles is only accurate if its trajectory follows the fluid path and if the curvature of this trajectory is negligible, resulting in a restriction of time between images, magnification and camera resolution. For most applications, the particle path is assumed to be a straight line, leaving the particle size on the image as a parameter. Very small particles will generally show up as a single pixel on the image. The interrogation program can then at most find displacements equal to discrete integer pixel values, an effect called peak-locking. With an average displacement of 10 pixels, this results in an unacceptable error of 10%. If a particle is so large that it is captured as several pixels, one can fit an e.g., three-point Gaussian distribution or bi-cubic polynomial to estimate its sub-pixel peak location (centroid) to within of 5 % of a pixel (Westerweel 1993). Note that one applies the fitting functions to the correlation map, not to individual particles. So the accuracy of PIV is much better than one would initially expect based on camera resolution. The particle size is preferably not smaller than 2 pixels, but no additional information is present if the particle is any larger (Westerweel 1997), most likely due to deteriorated correlation of centroid function on the larger particles. It is possible

to adapt centroid estimating functions to particle size, but such details within the interrogation routines are beyond the scope of the present work.

With a two-dimensional velocity field it is possible to calculate e.g., one vorticity component or a part of the Reynolds stress tensor or rate of deformation tensor. Note that stereo-PIV can resolve the third component of the velocity vector, but not the velocity gradient perpendicular to the light sheet unless two separate light sheets are used. Vorticity can be a useful parameter as it is not dependent on the frame of reference. Vorticity is a difference in velocity derivatives, usually calculated using finite difference schemes. The accuracy of the calculation depends on both the truncation error of these schemes as well as on the accuracy of the velocity measurement. The first error can be reduced by means of measurement grid refinement, the second error component cannot. Note that the interrogation windows during interrogation may partially overlap in which case velocity vectors are partially interdependent, sharing a portion on the raw PIV image. An increase in window overlap generally increases bias error in vorticity predictions (Raffel *et al.* 1998).

The reader is referred Adrian (1991), Raffel *et al.* (1998), or Westerweel (1993) for further reading.

3.3.2 Application to cavitating flows

The application of PIV to cavitating flows introduces several problems not present in fully-wetted flows. Particles do not mix with the vapor, and vaporous regions reflect the incident laser light. Tassin Leger *et al.* (1995) commented that strong reflections not only overexposed the images near the cavity interface, but also illuminated particles outside the light sheet. Bubbles and nuclei in the flow may also be interpreted as tracking particles by the interrogation routine. In fact, Wosnik *et al.* (2006) used bubbles exclusively as tracers in the wake of a cavity, however insufficient bubbles are present near the attached cavity and it is not immediately apparent if bubbles of various sizes will have a negligible slip or if shear will not deform the bubble between laser pulses to such a degree that the interrogation program will interpret it as a motion. If the bubbles are small, surface tension is sufficiently high to force the bubbles to retain their spherical shape, but even then contaminants on the bubble interface can cause a non-zero shear stress leading to deformations (Mei 1996). Early work by Johnson & Hsieh (1966) indicated that nuclei will be deflected by strong pressure gradients—such as in the vicinity of a stagnation point or regions of high vorticity—and move the nuclei away from the leading edge (delaying cavitation inception as well). The use of tracer particles with a density close to that of the liquid does not have such uncertainties. However, strong reflections by bubbles or cavitation are not negated by the use of such particles.

The problem of reflections can be easily solved by the application of fluorescent tracer particles, as used by Shridhar & Katz (2000) or Bachert & Stoffel (2003). All reflected laser light can be removed by placing an optical filter in front of the camera, removing the risk of overexposure or in worst cases damage to the optical chip of the camera itself

³. This technique is sometimes referred to as Laser Induced Fluorescent Particle Image Velocimetry (LIF-PIV), but the LIF prefix is not used further. The selected particles are PMMA particles coated with Rhodamine B, reflecting in the orange band at 590 nm. The particles used are not neutrally buoyant with a $\rho_p = 1.19 \cdot 10^3 \text{ kg/m}^3$. The net force of gravity minus buoyancy is

$$F = (\rho_p - \rho) g \frac{1}{6} \pi D^3 \quad (3.2)$$

and the oppositely directed drag force is

$$F_D = C_D \frac{1}{2} \rho V^2 \frac{\pi}{4} D^2 \quad (3.3)$$

With an expectedly small velocity ($Re \ll 1$), the drag coefficient of a sphere in Stokes' flow is

$$C_D = \frac{24}{Re} \quad (3.4)$$

Setting eq. 3.2 equal to eq. 3.3 for an equilibrium situations and substituting eq. 3.4 gives

$$V = g \frac{\rho_p - \rho}{18\mu} d^2 \quad (3.5)$$

which is less than 0.3 mm/s for the largest particle (50 μm) in water ⁴, too small to be detected considering the precision PIV can resolve. The frequency response of the particle depends on the ratio of particle and fluid densities. According to Mei (1996), when the particle/fluid density ratio is $0.56 < \rho_p/\rho_f < 1.62$, the response is very good. The particles will settle on the tunnel floor, but were quickly dispersed when starting the tunnel. The use of these particles and filters is often hampered by their high cost, but as the tunnel in Delft is small the expenses are limited.

However, two problems will not be solved by the use of fluorescent particles. First, diffraction of the light sheet by the cavity will continue to illuminate out-of-plane particles. If a camera is chosen with a very narrow depth of field, these particles will be out of focus, decreasing the possibility of forming a strong correlation peak. The diffraction of the light sheet could be clearly observed during the tests (fluorescent light from the particles also passes laser goggles, allowing for direct observation). Second, although direct illumination and overexposure is removed, the particles on their turn will illuminate the cavity and test section, resulting in background noise recorded by the camera. As any area of the PIV image may yield a strong correlation, the moving cavity cannot be interrogated and expected to produce an accurate displacement prediction because

- The cavity is a reflecting surface, so the recorded intensity depends on the direction of illumination. A subtle change in the cavity outline results in a change of the intensity of the reflection, leading to false correlation.

³The used filter has a transmission efficiency of 85% at 590 nm

⁴ $Re = 0.015$

- It is impossible to determine ⁵ if the recorded cavitation is inside or outside the light sheet. In fact, most of the time it is clearly outside the light sheet. The calibration is only valid in the measurement plane so interrogation of vapor is nearly always erroneous.
- Correlation of vapor does not lead to a correct prediction of the fluid velocity as one observes changes in the cavity interface, not changes in fluid velocity. For example, the interrogation of a smooth and stationary interface results in a zero-velocity prediction leading to strong gradients in the velocity field near the interface, which is simply not present in the actual flow.

It therefore must be removed using some form of pre-processing on the PIV images. This pre-processing is explained in detail in chapter 4.

3.3.3 Performance of the PIV system

In this section the evaluation of the performance of the PIV system is briefly described. The details of the setup are described in appendix D. The peak-locking error can be detected by plotting particle-displacement probability distribution functions (PDF's). When peak-locking is predominately present, strong peaks at integer pixel displacements are found. The effect of peak-locking can be reduced if the number of particle pairs in an interrogation window exceeds 4, the mean particle diameter is larger than one pixel (but preferably not larger than 2), and a good fitting algorithm is used for processing the correlation map. Note that the histogram can display a strong tendency toward an integer displacement value if that is the actual mean flow velocity. By keeping the flow conditions constant and varying the pulse delay time between PIV images, the histogram distribution should shift accordingly. Unfortunately the tunnel flow conditions could not be controlled to such a degree that the velocity was equal during each experiment, so the peak location does not always change linearly with the pulse delay. However, the presence of peak-locking can be determined by (random) sampling of several PIV conditions with varying pulse delays.

In a study by Christensen (2004), mean flow profiles were shown to be fully insensitive to peak-locking as the averaging of the error is similar in nature to the averaging of turbulent fluctuations, even in the case of absolute peak locking with zero sub-pixel accuracy. Of course, even when all elements of a data set collapse onto integer values, it is to be expected that the ensemble average equals the true mean for a sufficiently large set of data. Naturally, turbulence statistics, Reynolds stress terms, and vorticity are not insensitive to peak-locking, but the averaged flow field accuracy will not be affected by peak-locking errors. However, the instantaneous velocity field will be affected and when calculating ensemble averages the number of velocity fields cannot be considered large. Peak-locking errors should be avoided.

⁵with a single camera

The distribution in fig. 3.5 indicates peak-locking was not present for the fully-wetted case. One can also plot the fraction particle displacement, or difference from integer values; $x - \lfloor x \rfloor$. A low fraction distribution around 0.5 pixel may be indicative for peak-locking. The fractional displacement PDF is plotted in fig. 3.6. Note that the horizontal displacement is low around 0.0 to 0.5 pixel and vertical displacement is low around 0.5 pixel in fig. 3.6, even though from figs. 3.5 it is apparent that peak-locking was not present. Naturally, this is the result of the measurement gravitating around $(-8.3, 0)$ pixel for a horizontal flow.

3.4 Hydrofoil geometry

The basis for the hydrofoils is a three-dimensional hydrofoil, previously used by Dang (2000), with a chord length of $c = 150mm$ over the entire span. The span itself is $s = 300mm$ (spanning the entire test section). The hydrofoils have a span wise varying angle of attack giving the hydrofoils a characteristic twist. A local Cartesian coordinate system x, y, z is used with the x -axis in the undisturbed flow direction, the y -axis along the span, and the z -axis upward. The description of the hydrofoil follows in the normalized coordinates

$$\hat{x} = \frac{x}{c(y)} \quad \hat{y} = \frac{y}{s} \quad \hat{z} = \frac{z}{c(y)} \quad (3.6)$$

Note that $x = [0...1]$ always denotes the section from leading the trailing edge at any position \hat{y} , and z is normalized with respect to the local chord length. The hydrofoils are parametric in their description for sectional profile, chord length distribution, rake, skew, and twist distribution.

3.4.1 Sectional profile

NACA's description of the geometry is defining the camber as the mean division of the thickness of the foil, in such a way that the thickness is always perpendicular to the mean line. The distance between the NACA mean line and the chord line is called the camber (the mean line may also be called camber line). Such a definition can result in a sharp curvature of the camber line near the leading-edge nose with the added effect of the physical foil length sometimes exceeding the defined geometrical chord length. This definition is even more cumbersome if one wants to fit an existing foil of an arbitrary shape to this curvilinear description. The origin of this description can be found in the use of lifting surface theory, where only the camber line and a symmetric thickness distribution is used in the mathematical description for the foil geometry. The hydrofoils will be described using polynomials based on table of offsets or the exact analytical descriptions. An offset is the distance to the suction and pressure side to the chord line, following the definition of the International Towing Tank Conference.

Two sectional profiles are chosen for the hydrofoils. The first is a symmetric and uncambered NACA0009 section (Abbott & von Doenhoff 1959). The NACA0009 has a low-pressure peak at the leading edge and a continuously increasing pressure distribution from about 5% chord under a non-zero angle of attack. Such a pressure distribution results in a gradual increase in cavitation length when either σ decreases or the loading increases. This makes the NACA foil an ideal candidate for cavitation observations as it is relatively insensitive to small changes in the flow conditions. One may adopt such a section as a propeller blade section in regimes where cavitation cannot be avoided, although most sections will perform better than the NACA0009 section. A different approach is applying a pressure distribution that is flat along most of the chord length and does not have a distinct pressure peak at the leading edge when the angle of attack changes a few degrees. These hydrofoils are free of cavitation over a larger range of σ , but will immediately have a large attached cavity after cavitation inception. These hydrofoils are thus more sensitive to changes in flow conditions. The sections designed by Eppler & Shen have a flat pressure distribution and have been documented (Eppler 1981). The Eppler & Shen profile YS-920 is chosen as it has been subjected to verification experiments (Shen 1985) with 920 signifying a thickness-to-chord ration of 9%—identical to the NACA0009—and with the last 20% of the chord used for the pressure recovery. The $C_L = 0.22$ at its zero angle of attack. Jessup *et al.* (1994) presented application and full scale demonstration of Eppler type sections to a naval controllable-pitch propeller to increase the cavitation inception speed.

At this angle of attack, the minimum pressure and laminar separation points lie around $\hat{x} = 0.77$ and $\hat{x} = 0.78$, respectively, but will move to the leading edge when the angle of attack exceeds 1° . At $Re = 2.5 \cdot 10^6$, with leading roughness added, the zero lift angle is measured to be $\alpha_0 = -2.15^\circ$ and from visualization it was apparent that laminar separation was not present (Shen 1985).

The Eppler & Shen sections are designed to have the an attached boundary layer. The pressure recovery zone has been designed such that the turbulent boundary layer is least likely to separate. Such sections have a flat pressure distribution over 70 to 80 % of their chord length followed by a region of rapid pressure recovery. With the increase of the angle of attack to angles larger than $\alpha = 1.5 - 2.5^\circ$, the pressure exceeds its minimum pressure design requirement. As the method of Eppler & Shen is based on finding a table of offsets satisfying a specified pressure or velocity distribution, there is no parametric description. A polynomial is defined for both suction and pressure side to match the Eppler's coordinates in the form of

$$\hat{z}_{Eppler}(\hat{x}) = C_0\sqrt{\hat{x}} + \sum_i^N C_i\hat{x}^i + b \quad (3.7)$$

identical to the analytical description on the NACA0009 section and capturing the hydrofoil within milling accuracy (The square root is essential for capturing the curvature

of the leading edge). The coefficients for the NACA0009 and Eppler YS-920 are given in App. E. For the actual manufacturing of the foil, the trailing edge of a section must be sufficiently thick to prevent damage during the milling process and setting up of the experiments. The trailing edge of both the NACA0009 and Eppler YS-920 as thickened in accordance with the typical propeller manufacturing practice. A minimum trailing edge thickness of $t_{min} = 0.4mm$ was chosen in consultation with the manufacturer. See appendix E.2 for details of polynomial used to add additional thickness.

3.4.2 Geometric angle of attack of the Twist hydrofoils

The geometric angle of attack for the Twist hydrofoils increases toward the center of the foil, giving it a twist, to generate a three-dimensional cavity that only partially covers the span. The hydrofoil is free of cavitation at the walls in order to avoid the interaction of the cavity with the tunnel wall boundary layer. The twist distribution of the angle of attack $\alpha(\hat{y})$ is taken so that the angle of attack changes from 0 at the walls to α_M at the mid span position and have a zero-derivative at both points. A simple third-degree polynomial mirrored around $\hat{y} = \frac{1}{2}$ satisfies this condition.

$$\alpha(\hat{y}) = \alpha_M \left(16 \left| \hat{y} - \frac{1}{2} \right|^3 - 12 \left| \hat{y} - \frac{1}{2} \right|^2 + 1 \right) \quad (3.8)$$

with α_M the maximum angle of attack, see fig. 3.7.

The geometry description of the Ellipse hydrofoils is given in appendix E.5. The parameters of the hydrofoils of this study are listed in table E.3. A selection of the hydrofoil family is presented in fig. 3.9. The designation of the hydrofoils consists of the main type—Elliptical or Twist—followed by the maximum angle of attack, and hydrofoil type -NACA009 (N) or Eppler YS920 (E). The sections of the Twist-11N, Twist-11E, and Twist14N hydrofoils rotate around $\hat{x}_\alpha = .75$, taken at 75% chord. The Twist-8N and Ellipse-11N sections rotate at the mid-chord position at $\hat{x}_\alpha = .5$. The reason the center of rotation was moved further aft is that the hydrofoil at the sides is optically blocking the center plane when viewing from the sides during the PIV experiments. See figure 3.8.

3.5 Local pressure measurements

The measurement of pressures on the surface of the hydrofoil is required for validation of numerical results. The hydrofoils can be fitted with transducers—flush with the foil surface—at various locations. However, cavitation imploding at or near the location sensor can destroy it. Placing the sensor in a chamber in the hydrofoil with a small pressure tap to the surface reduces the risk of damage. This technique has been used successfully at the Laboratoire Machine Hydraulique (LMH) at the École Polytechnique Fédérale de Lausanne (EPFL) and has been implemented in the Twist-11N hydrofoil.

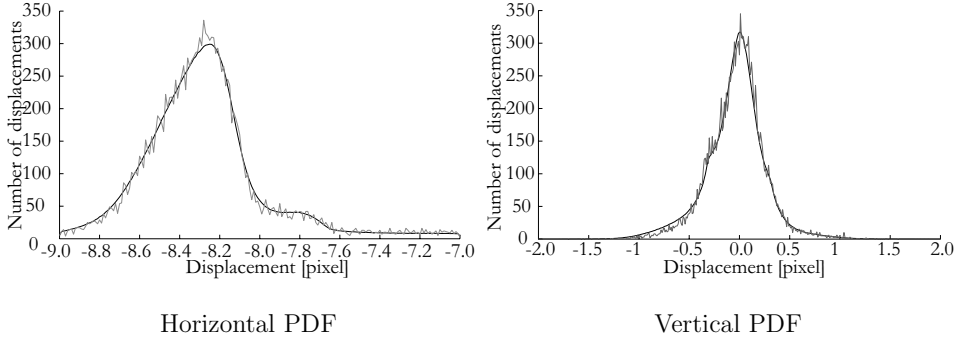


Figure 3.5 Histograms of horizontal and vertical pixel displacement values in steps of 0.01 pixel taken from the wake measurements of the flow oscillator. The smooth line is the normalized PDF of 1,024 displacement fields (not a PDF of the averaged displacement), the jagged line is a single displacement field. Note that the distribution does not peak near the integer value of -8 pixel. The right figure does peak around the integer value of 0 pixel, which is expected since the flow is horizontal.

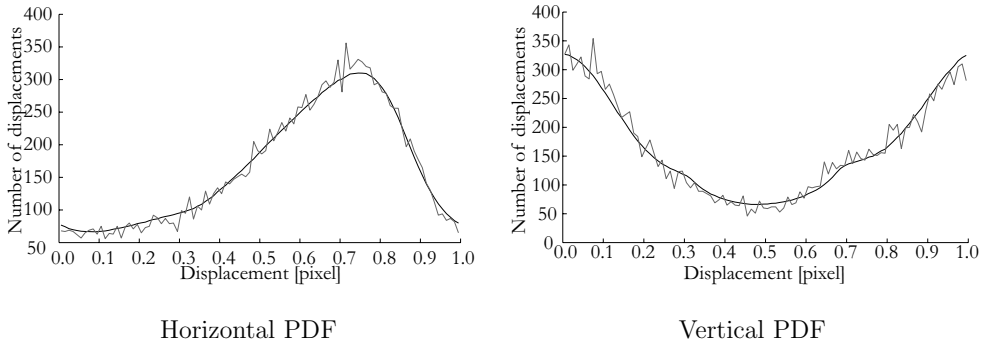


Figure 3.6 PDF's of fractional pixel displacement values in steps of 0.01 pixel as in fig. 3.5. Although the right figure shows a strong tendency toward integer values—suggesting a possible strong peak locking effect—it is the result of a measurement of a horizontal flow.

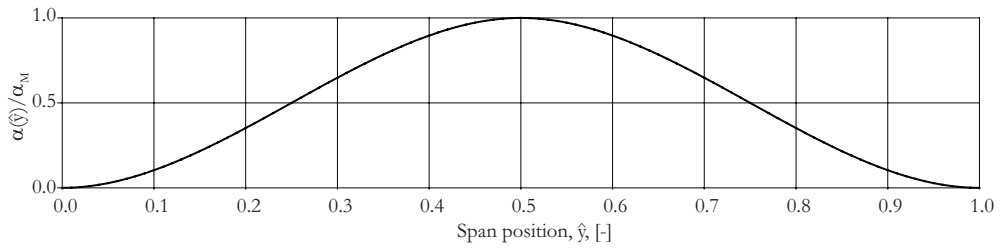


Figure 3.7 The angle of attack distribution function for the Twist series.

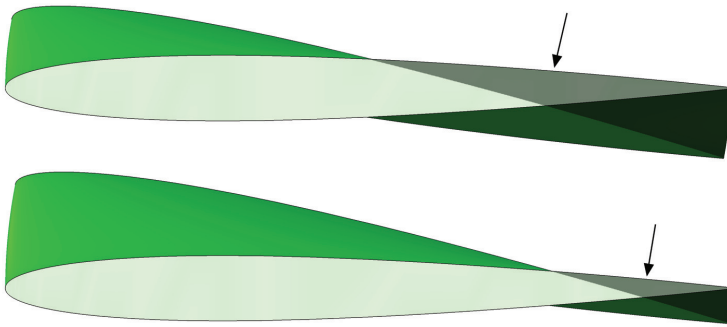


Figure 3.8 The center of rotation of the sections of the Twist series influences the optical blockage of the center plane during PIV measurements (top). Shifting the center of rotation aft reduced the blocked area (bottom).

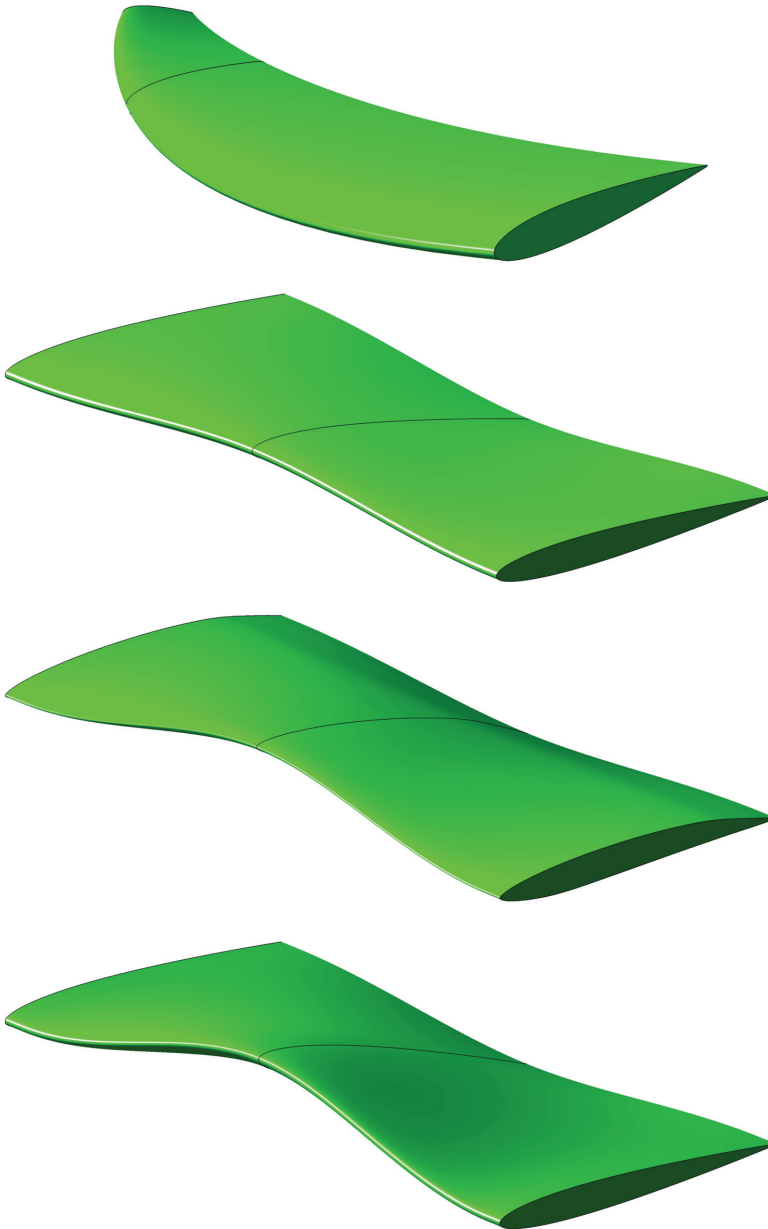


Figure 3.9 Renderings—from top to bottom—of the finite-span Ellipse-11N, and full-span Twist-8N, Twist-11E, and Twist-14N hydrofoils. The center of rotation of the sections is at 50% chord for the Twist-8N and at 75% for all other Twist hydrofoils, as is apparent by the leading edge offset of both the Twist-11E and Twist-14N.

3.5.1 Placement

The miniature pressure transducers are placed in small chambers with a $\varnothing 1\text{ mm}$ pressure tap toward the surface (see fig. 3.10). The sensor is placed in the chamber and glued to the hydrofoil. The chamber is filled with a resin (Epo-Tek 301-2), which has a very low viscosity before curing, allowing it to fill the chamber without entrapping air. When cured, the resin—sanded flush with the surface—has a density close to that of water with $\rho_{resin} = 1017.5\text{ kgm}^{-3}$. Two sets of sensors were used, Keller Series 2MI and Unisensor miniatures HP. The specifications are given in table 3.5.1. The fitting of the sensors and filling of the chambers is performed at Unisensor. Both sensors are temperature-corrected piezo-resistive sensors.

Sensor	Keller 2Mi	Unisensor HP
Height	1.9 mm	1.0 mm
Diameter	4.5 mm	3.0 mm
Range	10,000 kPa	6,896 kPa
Linearity	< 0.5%	< 0.2%

Table 3.1 Some specifications of the miniature pressure transducers.

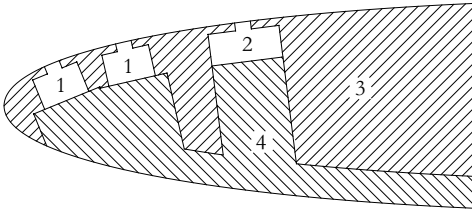


Figure 3.10 Schematic of the chambers of the miniature pressure transducers at the leading edge's suction side, with Unisensors (1) at 2.5% and 5% chord, Keller sensors at 10% chord, the hydrofoil (3) and the resin filling (4).

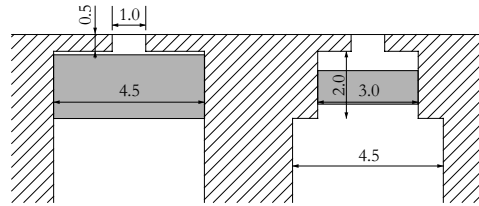


Figure 3.11 Detail of the chamber geometry for the Kellers (Left) and the Unisensors (right). The pressure taps are always perpendicular to the surface of the hydrofoil. The distance from sensor's top to the chamber's ceiling varies per sensor.

The static calibration of the transducers follows the same routine as for the wall transducers of the cavitation tunnel. The response of the sensors was confirmed to be fully linear by setting the pressure from 50 to 1000 mbar in steps of 50 mbar. Deviations are typically smaller than 0.5%. Normal operation calibration entails fitting a straight line through the two measured points at the extremes of the tunnel pressure range. The dynamic calibration

of a similar setup was performed by Pereira *et al.* (1993). The calibration used a spark generator—releasing 2.5 J between two immersed electrodes—and the response of the recessed miniature transducer is compared with the response of a reference sensor (Kistler 701) and an accelerometer. The spark creates a cavitation bubble and both its growth and collapse generate a pressure peak. The response is linear from 150 Hz to 25 kHz . As the bubble does not excite in the lower frequency band, a second calibration is performed by comparing the response of the sensor to the response of a reference sensor in a cylindrical pipe with a rotating valve. The response function is linear (Farhat *et al.* 2002a). Based on these results the miniature transducers were not dynamically calibrated and are assumed to have a linear response. After assembly, the hydrofoil was subjected to its pressure extremes, allowing for a brief break-in time of the resin. Measurements during this break-in period indicated an initial non-linearity in the resin behavior but after several pressure transients the response was confirmed to be fully (statically) linear. Since the chamber itself can act as a resonator, the Helmholtz resonator frequency of the pressure chamber can be estimated at

$$f \cong \frac{c}{2\pi} \sqrt{\frac{A}{tV_C}} \quad (3.9)$$

with the speed of sound c , a pressure tap area A & height t , and the chamber volume V_C . Although the diameter of the pressure tap is known, the exact height of the chamber differs from sensor to sensor. Typical values of the pressure tap resonance frequency are estimated in the order of 50 kHz to 70 kHz , far beyond the application range.

3.5.2 Sensor location

Due to the early availability of PIV data and high speed recordings, the Twist-11N was chosen to be fitted with the transducers. The hydrofoil is machined for both the cavitation tunnel at Delft and at the cavitation tunnel at EPFL, the latter having a test section with exactly half the dimensions of the Delft tunnel. Although the Twist 11N-EPFL is a 50% scale model of the Twist-11N, it has the same trailing edge thickness of 0.4 mm . The Twist 11N is fitted with 20 sensors, the Twist 11N-EPFL with 16. The location is given in table E.4 & E.5 (p. 185) and visualized in fig. 3.12.

Although the sensors are placed in recesses and have a range of several bars, any direct implosion of cavitation will destroy a sensor. Therefore, the measurement program has to be carefully planned to have the maximum number of available sensors left as the cavitation intensity increases. The Twist-11N-EPFL was tested at the same Reynolds number as the Twist-11N in Delft, as well as twice that number (28 m/s) The hydrofoil sensors lasted but a single afternoon with only 5 survivors at the end of the testing period, all at the leading edge. No sensors were damaged by cavitation with the Twist-11N at the cavitation tunnel at Delft.

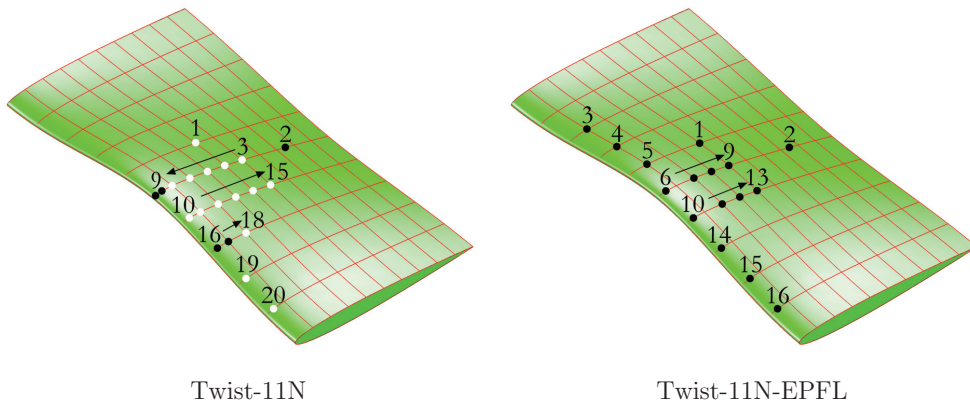


Figure 3.12 Location of the miniature pressure transducers with the TU Delft foil and the EPFL hydrofoil. The dots indicate the position of the Unisensors (black), Kellers, (white). All sensors are placed on the suction side, except sensor 1, which is placed on the pressure side, here indicated on the suction side.

3.6 Force balance

The forces and moments exerted by the hydrofoil on the flow are valuable to ascertain the effect of cavitation in unsteady flow conditions. Force measurements are common, but usually not all three force and moment components are measured due to the resulting complexity of the setup. The hydrofoil cannot touch the wall of the tunnel but the gap between the hydrofoil and tunnel wall must remain as small as possible. Measuring forces and moments in a water tunnel has difficulty of keeping the tunnel water-tight without disturbing the measurement. For this experiment commercially available load sensors are utilized. Details of the sensor and setup are in app. F.

3.7 Flow Oscillator

3.7.1 Introduction

From the point of view of the experimenter, one can choose between an oscillating hydrofoil (Shen & Gowing 1986, Franc & Michel 1988, Hart *et al.* 1990, McKenney & Brennen 1994, Reisman *et al.* 1994, Caron & Avellan 2000) or an oscillated flow (Hallander & Bark (1998)) to generate unsteady cavitation. The flow behind a ship is strongly non-homogeneous resulting in a periodic loading of the ship propeller. Cavitation is present in regions of either high loading or a very low to negative loading (resulting in pressure side cavitation). The effect of transient loading by periodic inflow variation is closely related to propeller flow so the current experiments were performed with a flow oscillator. The

oscillator itself should be completely free of cavitation, otherwise pressure measurements or PIV measurements will be subjected to noise. The bearing loads and oscillating torque exerted by the flow on the flow oscillator are preferably low to reduce both cost and weight. These requirements dictate that the combination of hydrofoil choice with the oscillating amplitude leans toward a large hydrofoil with a modest motion amplitude.

As cavitation on the oscillating foils has to be avoided, a hydrofoil specifically designed for delayed cavitation inception can be chosen or any other hydrofoil with a favorable (flat) pressure distribution. Still, Bark reported ⁶ cavitation on his flow oscillator at certain conditions. The use of foils such as the NACA 16 or 66 series, or those by Eppler (1979) offer some degree of protection by postponing the occurrence of a low pressure peak at the leading edge and thus delaying cavitation inception. The flow oscillator must not only have a minimum of cavitation, it must do so while generating lift and offer structural strength. The Eppler & Shen hydrofoils were designed to have an attached boundary layer. The pressure recovery zone is designed such that the turbulent boundary layer is least likely to separate. Such hydrofoils have a flat pressure distribution over 70 to 80 % of their chord length followed by a rapid pressure recovery region.

A deflectable trailing edge flap has a much smaller influence on the flow around the leading edge than changing the angle of attack of the entire hydrofoil. However, this deflectable trailing edge flap does create a low pressure region near the hinge as reported by Jacobs & Pinkerton (1931). This early work reports on the measurements of airfoil sections with deflectable flaps at several angles of attack and angles of deflection. It is clear from the measurements that the leading edge suction peak remains small for their section (NACA RAF30). However, the pressure near the trailing edge hinge can be low, as low as the leading edge pressure. The hinge of the flap must therefore be placed outside the flat pressure region and in the pressure recovery zone. This requirement disqualifies both the NACA 16, 66, and Eppler & Shen hydrofoils as suitable candidates.

A deflectable trailing-edge flap has the advantage that the wake will be reduced in height, wall effects are smaller and the geometry is simpler to represent in numerical simulations. It is expected that numerical simulations can be performed with static numerical mesh and that the perturbation of the deflection of the trailing edge flap can be implemented using disturbance functions. Also, the oscillating torque is smaller than an oscillating foil. So, a stationary foil with a deflectable trailing edge flap is ideally suited as an oscillator in a cavitation tunnel, provided that the foil is supported on either side of the tunnel wall. Krag & Wegner (1985) tested several types of flow oscillators in a wind tunnel ⁷ and concluded that the gust was constant in amplitude around the centerline over 80% of the span for gust generators spanning the entire test section (the effect of the gusts disappears toward the tunnel walls), and that the effect of the gusts diminishes quickly

⁶private communication

⁷flapping wings, deflectable trailing edges, jet flaps, and finite gust generators in the tunnel's contraction

behind the oscillators (two chord lengths).

The airfoil sectional profile and pressure distribution should have the following characteristics:

- 1 The airfoil should have sufficient thickness at the trailing edge hinge location in order to fit a hinge of sufficient strength
- 2 The pressure distribution near the leading edge should vary smoothly with the flap deflection in order to minimize the risk of leading edge cavitation
- 3 The pressure distribution should already be recovering at the trailing edge hinge location to reduce the risk of cavitation

The section for the oscillator is from the the NACA63A010 series. These hydrofoils have a gradual pressure recovery zone and a relatively high pressure at 80% chord and sufficient thickness from a structural point of view. The NACA 6-series were designed by Theodorsen's conformal mapping (Theodorsen & Garrick 1933) and an analytical description such as for the NACA 4-digit series is not available. However, a polynomial approximation based on a table of offsets made in the form of eq. 3.7 can be generated easily. The NACA 6-series mean lines have not been described, resulting in thickness distribution. Details are found in appendix E.3.

The tunnel top and bottom walls have a strong effect on the flow, so any velocity oscillation is expected to very quickly damp out. To reduce the risk that the effect of the flow oscillator is too small, it is placed a short distance upstream of the main hydrofoil. The vertical distance of the deflectable flaps to the main hydrofoil is preferably large to avoid the wake hitting the test hydrofoil, but not too close to the wall to prevent strong wall effect increasing the risk of cavitation. In order to avoid the flow oscillator to induce an asymmetric gust in the test section, two flow oscillator hydrofoils are chosen to be placed equidistant from the tunnel heart line at $z = 0$. The foils are positioned at $1/3$ and $2/3$ of the height of the test section, as sketched in fig. 3.13. The oscillating foils are manufactured as one complete foil. The trailing edge flap is sawed off and both ends are hollowed out with a spherical milling bit. A shaft is bolted to the trailing edge flap. The oscillation motion was generated by means of a simple crank shaft mechanism.

3.7.2 Ensemble averaging

In order to perform ensemble averaging over a period of the oscillation, the conditions from the measurements have to be sorted in order to match the correct instance during an oscillation. As the frequency of data acquisition and the frequency of the oscillator are often incongruous, a time lapse averaging is used, selecting those measurement points (i.e., PIV fields) that occur within a narrow time band during the oscillation period. The period

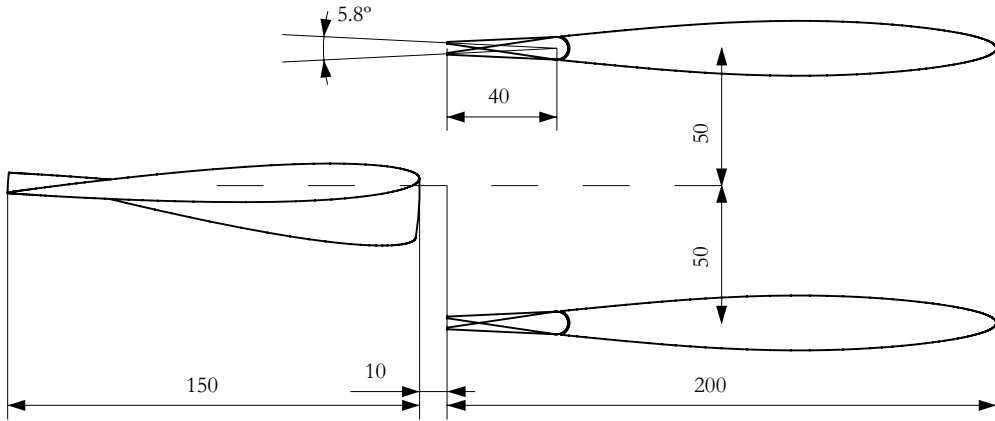


Figure 3.13 Schematic of the flow oscillator positioned upstream of the TWIST-11N hydrofoil. The trailing edge hinge position is set at 80% chord position. Note that all experiments were performed upside down. Distances in *mm*.

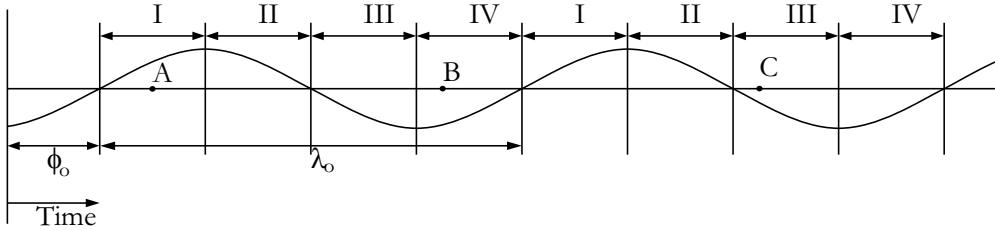


Figure 3.14 Time-resolved PIV measurements (*A, B, C*) are binned into time intervals of an oscillator period for selective ensemble averaging

of the oscillator, ($\lambda_0 = 1/f_0$), is divided into N discrete intervals, as visualized in fig. 3.14.

The (example) period is divided into $N = 4$ intervals with 3 points (*A, B, C*) representing the time when PIV measurements were made. From the graph is clear in what interval ($\Delta_i, i \in [1, 2, \dots, N]$) of the period they should be sorted. A 'binning function' is used to quickly sort the individual results t_j with a frequency f

$$\Delta_i = \left[\left(t_j f_0 - \frac{\phi_0}{2\pi} - \left[t_j f_0 - \frac{\phi_0}{2\pi} \right] \right) N \right] \quad (3.10)$$

where ϕ_0 is the phase delay at $t = 0$ s⁸. Some combinations of f and f_{FO} can result of certain bins containing for example only 5 measurements with the contiguous bin

⁸ $[x]$, $\lceil x \rceil$, nearest integer $< x$, $> x$ respectively

containing 75 measurements. For the best results, the 'degrees of freedom' distribution over the bins should be constant (at least 20-25 measurements per bin with 100 bins per period) to qualify for selection. An example is given in fig. K4, p. 207 for the measured pressure signals.

3.7.3 Frequency estimate

In order for the ensemble averaging to work, the phase and frequency must be determined accurately. For comparative purposes, the Twist14-N was tested for fully-wetted conditions at $\sigma \approx 1.7$ with the oscillator operating from 0 Hz to 34 Hz in steps of 2 Hz. Harmonic analysis of the lift and drag, as well as of all three moments, yielded frequencies agreement with the oscillator frequency to within 0.01%. Figure 3.15 shows the oscillator deflection angle, as well as the lift and moment plots (Note that these are reaction forces at the foil mounting and not the net lift forces). The phase delay of the lift and pitching moment is plotted in fig. 3.16 as a function of the reduced frequency

$$f_r = \frac{fc}{U} \quad (3.11)$$

based on the foil chord length and corrected for the distance $x_d = 85 \text{ mm}$ between the oscillator trailing edge flaps and the axis of rotation edge of the hydrofoil

$$\phi_0 = -\frac{x_d f}{U} \quad (3.12)$$

The frequency of the oscillator and tunnel velocity cannot be set to an accurate value and are always determined afterward. Given these variations from measurement to measurement and given that the phase delay collapses onto a single line in fig. 3.16, it can be concluded that the frequency and phase can be calculated accurately. The phase delay is observed going to a zero for infinitely long disturbances (i.e., $f_{FO} \rightarrow 0$). Note that the phase delay expectedly rises as the frequency increases.

3.7.4 Observations

The flow oscillator has been tested at several cavitation numbers with one of the test hydrofoils (Twist-11N). As is known from the research of Franc & Michel (1988), laminar flow without leading edge separation can temporarily suppress cavitation. Leading edge roughness should not be added to the leading edges of the flow oscillator hydrofoils. This was later confirmed with early tests with leading edge roughness applied to the flow oscillator and the cavitation behavior was improved after removal of the roughness elements. Inception of cavitation on the flow oscillator appeared nearly simultaneously at the leading edge and at the hinge. Also, due to the flat pressure distribution of the section, the sheet cavity had a length of about 75% of the chord after inception. The cavitation number for inception was much lower than the standard operational conditions for testing. The wake of the oscillator has been measured by PIV at eleven conditions for validation purposes.

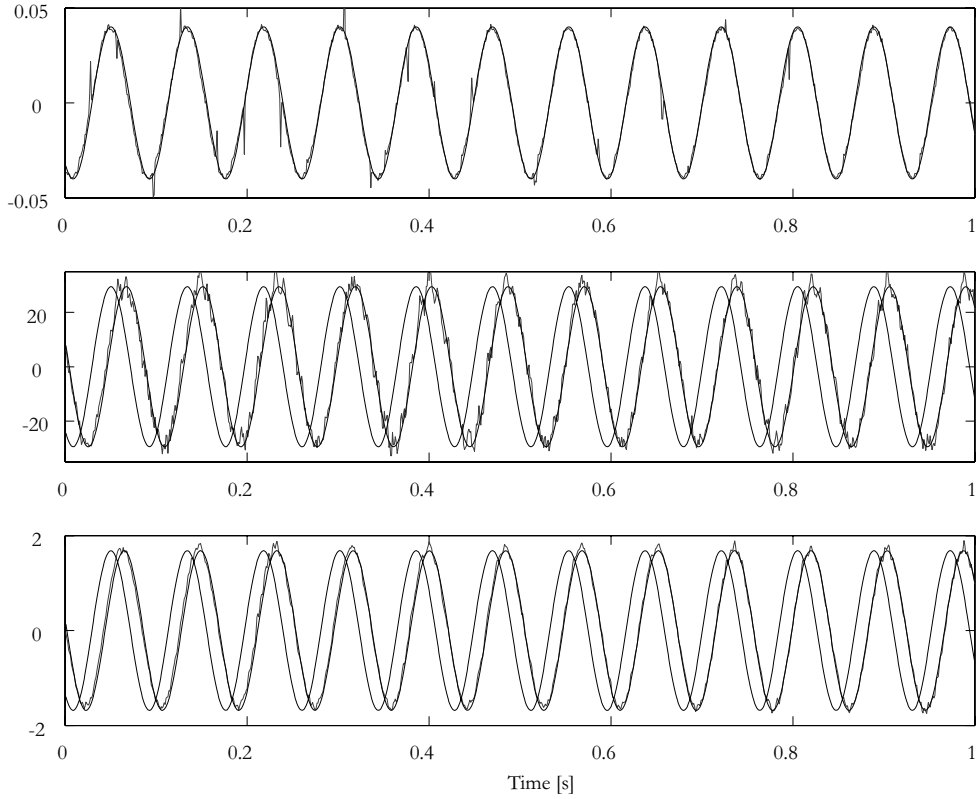


Figure 3.15 Flow oscillator deflection angle (top), lift (center), and pitching moment (bottom) signals for the Twist14-N at $f_{FO} \approx 12 \text{ Hz}$. Note that the sinusoidal approximation through the lift ($[N]$) and moment ($[Nm]$) captures the frequency, amplitude, and phase perfectly.

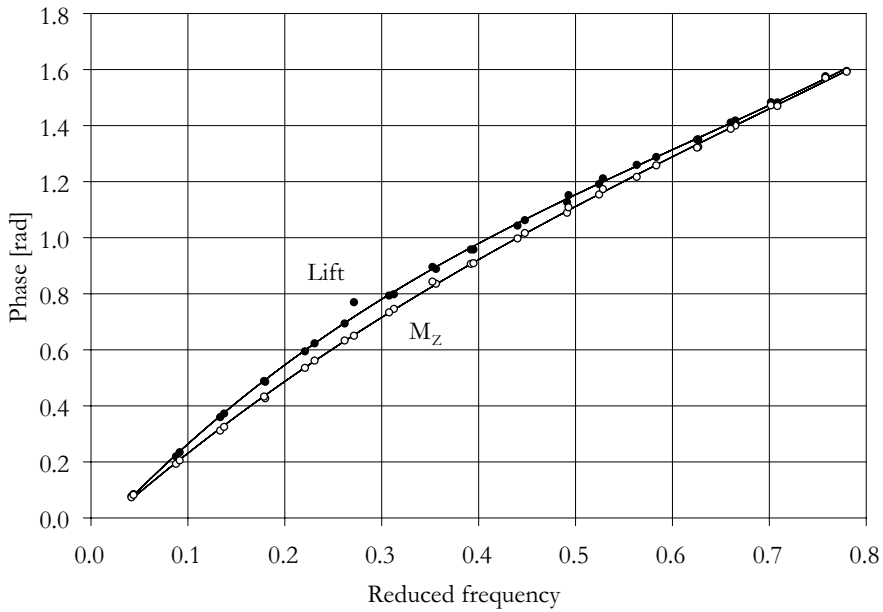


Figure 3.16 Phase delay plot of the lift and spanwise moment with regard to the trailing edge deflecting angle versus the reduced frequency for two independent measurements using the Twist-14N at fully-wetted conditions. The two measurements collapse onto a single line, indicating the phase is determined accurately.

Chapter 4

Applying Time resolved PIV to cavitating flows

4.1 Introduction

A brief introduction to the application of PIV to cavitating flows was given in section 3.3. When measuring in multi-phase flows, simultaneous PIV correlation between the various phases leads to correlation errors and one must discriminate between the phases Deen *et al.* (2002) for either simultaneous interrogation on both phases or suppression of interference between phases. Kosiwczuk *et al.* (2005) used two fluorescent dyes for two phases which were recorded by two separate cameras. Delnoij *et al.* (1999) distinguished between phases in a bubbly column by comparing the correlation peaks, depending on a priori knowledge of the velocities of vapor and liquid phases. Lindken & Merzkirch (2002) used Laser-Induced Fluorescence (LIF) and shadowgraphy to distinguish between liquid and bubbles, separating the phases digitally. Khalitov & Longmire (2002) discriminated on both local intensity and size of bright areas using second-order gradients filters. Gui *et al.* (2003) integrated the phase discrimination directly into the PIV algorithm itself.

Particles do not mix with the vapor, and vaporous regions reflect the incident laser light. Tassin Leger *et al.* (1995) commented that strong reflections not only overexposed the images near the cavity interface, but also illuminated particles outside the light sheet. Bubbles and nuclei in the flow may also be interpreted as tracking particles by the interrogation routine. Incident laser light, bubbles, and vapor can be partially removed by the application of fluorescent tracer particles and optical filters (Adrian (1991) Shridhar & Katz (2000) Bachert & Stoffel (2003)). However, two problems will not be solved by the use of fluorescent particles and optical filters. First, diffraction of the light sheet by the cavity will continue to illuminate out-of-plane particles. Second, although direct illumination and overexposure is removed, the particles on their turn illuminate both the test section and the cavity, resulting in background noise registered by the camera. Static objects can be identified effectively by applying a minimum filter over all images in time, but as any area

of the PIV image may yield a strong correlation during interrogation, the moving cavity cannot be interrogated for an accurate flow displacement prediction as;

- it is not possible to determine—with a single camera—if the recorded cavitation or bubble is inside or outside the light sheet (and calibration area).
- the correlation of vapor or bubbles leads to the displacement of the phase interface, not the velocity of the fluid.
- the cavity and bubbles are reflecting surfaces so the recorded intensity depends on the direction of illumination. A change in the phase outline results in a displacement of reflection intensity, not the velocity of the liquid.

The cavity must therefore be removed using some form of pre-processing on the PIV images. This chapter will explain the removal process of background noise, or the identification of particles. In order to gather information from all particles—including those partially covered by vaporous regions on the image—image analysis is used to actively identifying all tracer particles. Particle reflection by the cavitation is not a problem, as the vaporous is highly turbulent and diffusive and does not yield a distinct reflection. The preprocessing of the PIV images can be performed by applying a local median function. However, both Kiger & Pan (2000) and Deen *et al.* (2001) comment that artifacts of this processing remain possibly leading to erroneous correlation. The emphasis in this chapter is on presenting a generic phase-separating filtering technique that can identify the tracer particles and discard background noise in order to increase the measurement accuracy of PIV interrogation near vaporous interfaces. A brief introduction to image analysis is given in s. 4.2. The image analysis used is a combination of matrix multiplications on local areas of the PIV image, interpreting the image as a matrix. An overview is given—with examples—of several basic image analysis tools.

In section 4.2.3, a special operator is presented that was developed specifically for identifying particles on the PIV images. The operator—termed a modified standard deviation filter—captures both low and high intensity particles and is not sensitive to larger regions. A sequence of filter actions is presented that was used to pre-process the PIV images to filter out all cavitation in section 4.2.4.

Image analysis can be used to filter out the cavity, but the same operators can also be used to filter out the particles and to actively track the cavity interface. In s. 4.2.5 it is explained how the cavity interface was determined from the PIV images. The result is that both the velocity field can be evaluated and the cavity outline can be determined yielding valuable information on the cavity thickness during a shedding period.

The last section will discuss the performance of the pre-processing and its effect on the solution. It will be shown that the presence of vapor within an interrogation window can result in a large error in the velocity. It is concluded that if an accurate velocity measurement near the cavity interface is required it is not sufficient to use fluorescent particles and optical filters. The cavity must be removed from the image as well.

4.2 Image Analysis

4.2.1 Introduction

The images obtained during the experiment must be pre-processed prior to PIV interrogation. Erroneous correlation will degrade the results near the cavity interface, as will be shown below. Background noise can result in positive correlation and the attached cavity and shed vortices can be considered background noise. The images must be processed such that all particles will remain unharmed and all cavitation is removed from the image. It is possible to get close to the interface without preprocessing or the use of filters and fluorescent particles, but cloud cavitation is not captured as a sharp region by the camera.

no sharp interface is offered visually by cloud cavitation. The cavity interface needs to be determined on each individual frame but the sheer number of frames necessitates the use of a robust image analysis algorithm that is insensitive to all forms of noise typically recorded during the experiments. One solution is to try to capture as many PIV particles as possible, usually isolated bright spots (hot spots) of several pixels, while ignoring large regions of high intensity. However, from fully-wetted flow results it was apparent that weak particle illuminations—nearly dissolved in back ground noise—yield valuable data and are preferably retained after pre-processing.

4.2.2 An overview of existing image analysis tools

The image \mathbf{I} used for these experiments are 10 bit images, consisting of pixels with values between zero and 1023. The image can be seen as a large matrix containing pixel intensity values reducing the imaging algorithm to basic matrix operations. However, most operations are only effective if local image information is used—when determining the local mean intensity—meaning that only a portion of the image or matrix information is used. Local values can be determined using convolution kernel functions. The local convolution kernel isolates a region of the matrix with the same size as the kernel and applies a Hadamard product, $(\mathbf{A} \cdot \mathbf{B})_{ij} = a_{ij}b_{ij}$, multiplying matrix elements per entry. These elements are then summed and returned as a single value to the resulting matrix. This operation is repeated for each entry of the original matrix \mathbf{R} . Mathematically, the multiplication of an $M \times N$ kernel with an $I \times J$ matrix results in an $I \times J$ matrix \mathbf{R} :

$$R_{i,j} = \sum_{n=1}^N \sum_{m=1}^M I_{i-\frac{M}{2}+m,j-\frac{N}{2}+n} K_{m,n} \quad (4.1)$$

The kernel slides through each individual element of \mathbf{I} . Preferably, the kernel multiplication does not change the dimensions of the initial matrix so boundary conditions must be given if the kernel passes the matrix edge. Mirroring the image is usually quite effective for smaller kernels. This operation is the core of the image analysis presented.

In order to calculate the average value around a pixel within a $N \times N$ area the following kernel can be used:

$$\bar{\mathbf{I}} = \frac{\mathbf{I}K_N}{N_{K_N}} \quad (4.2)$$

with K_N a $N \times N$ unity kernel. The sum of all kernel elements, N_K , is defined as

$$N_K \equiv \sum_{i=1}^N \sum_{j=1}^N K_{N,ij} \quad (4.3)$$

One can also set all entries within a certain radius of the kernel center to unity—the rest to zero—resulting in a circular kernel of size w so that

$$K_{C,ij}(w, c) = 1 \quad , \quad \left(\frac{1}{2}w + \frac{1}{2} - i\right)^2 + \left(\frac{1}{2}w + \frac{1}{2} - i - j\right)^2 < \frac{1}{4}c(w+1)^2 \quad (4.4)$$

$$K_{C,ij}(w, c) = 0 \quad , \quad \textit{else}$$

with c some tuning constant for the radius. For low values of w , K_C is coarse; varying c allows for some shape regulation. In order to blur an image, a smoothing filter can be applied, for example by means of a Gaussian kernel

$$K_{G,ij}(w, c) \equiv e^{-10c \left[\left(\frac{i-1}{w-1} - \frac{1}{2} \right)^2 + \left(\frac{i-1}{w-1} - \frac{1}{2} \right)^2 \right]} \quad (4.5)$$

with c a tuning constant.

Median filtering, or determining the local maximum, requires a different operation. The local values around a smaller $M \times N$ kernel need to be sorted and an element of choice returned to the resulting matrix. The sorting function is denoted S in this chapter

$$S(\mathbf{I}, K, i) \equiv \textit{sort}_i(\mathbf{I} \cdot K) \quad (4.6)$$

with *sort* the (non-mathematical) notation of a vector or matrix elements sorted from lowest to highest entry. For example, with $i = 1$, the above is a minimum filter and with $i = \frac{1}{2} \lfloor N_K \rfloor^1$ a median filter.

The image can be modified by multiplying it point-for-point with another matrix. For example, if one wants to set all values below 10 to zero in a matrix, this is written as $\mathbf{R} = \mathbf{I} \cdot (\mathbf{I} < 10)$ with $(bmI < 10)$ a boolean matrix.

¹ $\lfloor x \rfloor$, nearest integer $< x$

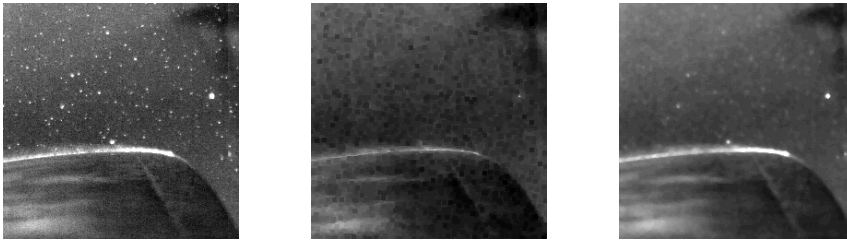


Figure 4.1 This example shows the original image at left. The central image is a minimum filter result; the least intense pixel within a certain area is retained, which can be useful when a background is deleted from an image. Static objects can be identified effectively by applying a minimum filter over all images in time Lindken *et al.* (2005). The right image shows retention of the median pixel. Minimum and median filtering is an effective tool to remove outliers from the image. However, artifacts remain after filtering as reported by Kiger & Pan (2000) and Deen *et al.* (2001)

Peak Detection

The local maxima in an image can be detected by using a Laplacian filter. The Laplacian $\nabla^2 \mathbf{I}$ in kernel form is

$$K_{LA} = \begin{bmatrix} 0 & -1 & 0 \\ -1 & +4 & -1 \\ 0 & -1 & 0 \end{bmatrix} \quad K_{LS} = \begin{bmatrix} -1 & -1 & -1 \\ -1 & +8 & -1 \\ -1 & -1 & -1 \end{bmatrix} \quad (4.7)$$

This kernel is called a spatial filtering kernel, and is especially useful to track noise. In image analysis, one often applies a Gaussian smoothing kernel first to remove noise and then adds the Laplacian to find high derivatives to be enhanced later. In our case, noise or particles are the subject of interest. The Laplacian kernel identifies all peaks in the image.



Figure 4.2 This example shows the original image at left and two results from a Laplacian kernel; the K_{LA} (center) and K_{LS} (right). The gradients in the image are captured.

Edge Detection

Intensity transition can be captured by means of an edge detection kernel. A well-known and effective approach is the use of Sobel's 3×3 Kernels

$$K_{hor} = \begin{bmatrix} -1 & 0 & +1 \\ -2 & 0 & +2 \\ -1 & 0 & +1 \end{bmatrix} \quad K_{ver} = \begin{bmatrix} +1 & +2 & +1 \\ 0 & 0 & 0 \\ -1 & -2 & -1 \end{bmatrix} \quad (4.8)$$

The two kernels calculate the local horizontal and vertical gradients of an image and have the advantage of being insensitive to the mean intensity value. The total gradient is determined by

$$|\mathbf{R}_{Sobel}| = \sqrt{(\mathbf{I}K_{hor})^2 + (\mathbf{I}K_{ver})^2} \quad (4.9)$$

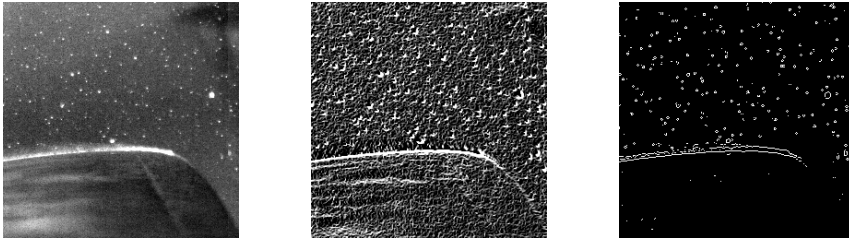


Figure 4.3 Sobel's kernel effectively captures gradients (center). A threshold value—e.g., local maximum—can be taken (right). The filter can capture most particles at the cost of picked up noise, but generally performs similarly to the Laplacian filters on the PIV images.

Local Image Statistics

Kernel operations can be used to great effect to determine e.g., the local standard deviation of a picture. The expression for the standard deviation is (see app. B.13)

$$\hat{\sigma}_{N-1}(x) = \sqrt{\frac{N \sum_i x_i^2 - \left(\sum_i x_i \right)^2}{N^2 - N}} \quad (4.10)$$

The standard deviation of the picture is now

$$\mathbf{I}K_{\hat{\sigma}}(K_N) = \sqrt{\frac{K_{K_N}(\mathbf{I} \cdot \mathbf{I}) K_N - (\mathbf{I}K_N)^2}{N_{K_N}^2 - N_{K_N}}} \quad (4.11)$$

Note that the image is multiplied with the unity K_N , but can also be multiplied with any binary kernel K , such as the circular kernel K_C . This relation closely resembles the

(unnormalized) correlation coefficient, which is the numerator of $\hat{\sigma}^2$.



Figure 4.4 The standard deviation gives a good indication of activity in the image and yields a result that is close to the Sobel filter, but the result is less sharp.

The standard deviation is defined above for a region of interest of arbitrary shape within an image. A kernel function ϕ is introduced to be mapped onto the kernel that can, e.g., exclude regions from participating in the calculation by containing ones and zeros only, or reduce the participation weight by setting an element from $\phi_{i,j} = 1$ to $\phi_{i,j} = 2$ effectively using the same element twice. With this definition N becomes the sum of the elements of the kernel containing ϕ and x are the elements in the image.

$$\hat{\sigma}_{N-1}(x, \phi) = \sqrt{\frac{\sum_{i=1}^N \phi_i \sum_{i=1}^N \phi_i x_i^2 - \left(\sum_{i=1}^N \phi_i x_i\right)^2}{\left(\sum_{i=1}^N \phi_i\right)^2 - \sum_{i=1}^N \phi_i}} \quad (4.12)$$

Note that 1) this function is neither the cross-correlation between ϕ and x , nor the standard deviation of ϕx and 2) that the bias-correction standard deviation is used—containing $N^2 - N$ and not N^2 in the denominator—resulting in minor deviations if $\phi \notin \mathbb{N}$. This does not affect the result of the presented preprocessor.

4.2.3 Custom filtering

A new variant of the standard deviation kernel is introduced that is uniquely suited for the PIV images. In our image analysis, the first term of the numerator of eq. 4.12 is changed from

$$\sum_{i=1}^N \phi_i \sum_{i=1}^N \phi_i x_i^2$$

to

$$\sum_{i=1}^N \phi_i \sum_{i=1}^N (\phi_i x_i)^2$$

so that the expression for the modified standard deviation $\hat{\sigma}_M$ becomes

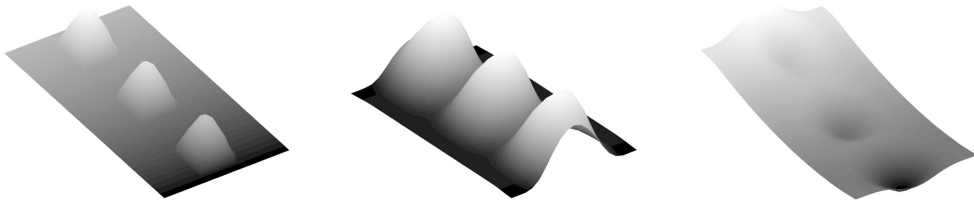
$$\hat{\sigma}_M(x, \phi) = \sqrt{\frac{\sum_{i=1}^N \phi_i \sum_{i=1}^N (\phi_i x_i)^2 - \left(\sum_{i=1}^N \phi_i x_i\right)^2}{\left(\sum_{i=1}^N \phi_i\right)^2 - \sum_{i=1}^N \phi_i}} \quad (4.13)$$

For our preprocessor, a normal distribution $\phi = e^{-c\zeta^2}$ —purposely similar to the intensity distribution of a particle—is mapped on the symmetric kernel K^ϕ of size $M \times M$, with ζ the distance to the kernel center and c a constant to tune the shape of the distribution. The constant c is chosen as $c = 5$ so that the values of the entries in the corners of the kernel are less than 0.1.

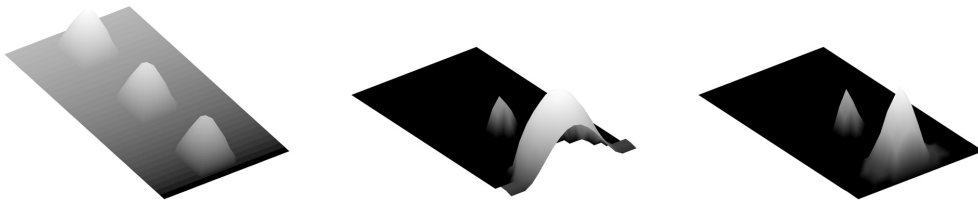
As the first term in the numerator of eq. 4.13 contains ϕ^2 and since $\phi < 1$ for our choice of ϕ , the influence of high pixel values at the outer edge of the kernel is reduced with respect to the second term in the numerator. The numerator of eq. 4.13 is negative and the resulting image will be locally imaginary due to the square root in the expression. Only when no neighboring high values are present around a particle, the result of $\hat{\sigma}_M$ will be real and a particle is identified. This also means that 1) the particle density should be low to medium (e.g. Okamoto, 2001, case A) and 2), in order to identify tracer particles the background level of the image should be very low. In order to sift out the background, one can apply a minimum or median filter. Smoothing this minimum image and subtracting it from the original image effectively sifts most of the background, resulting in an image $\tilde{\mathbf{I}} = \mathbf{I} - \bar{\mathbf{I}}$. Now $\hat{\sigma}_M(\tilde{\mathbf{I}})$ will effectively determine the position of the tracer particles. The result of $\hat{\sigma}_M(\tilde{\mathbf{I}})$ can be used as an adaptive mask by interrogating the sifted image $\tilde{\mathbf{I}}$ only where $\hat{\sigma}_M(\tilde{\mathbf{I}})$ is real and PIV interrogation can be performed on particles only.

For the image analysis, this $\hat{\sigma}_M$ is written as

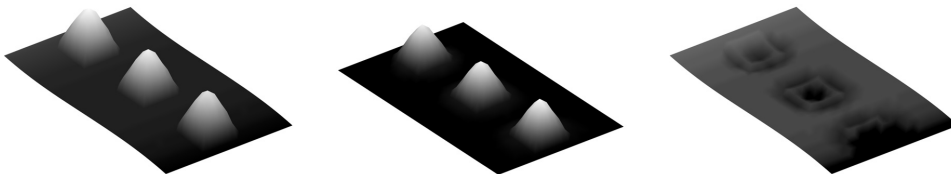
$$\mathbf{I}K_M(K_\phi) = \sqrt{\frac{N_{K_\phi}(\mathbf{I} \cdot \mathbf{I})K_\phi^2 - (\mathbf{I}K_\phi)^2}{N_{K_\phi}^2 - N_{K_\phi}}} \quad (4.14)$$



A synthetic image is created (left), consisting of background with increasing intensity and three PIV particles. The central and right image are the squared result of the standard deviation and **negative** $\hat{\sigma}_M$. The standard deviation captures a large region around the particles. The $\hat{\sigma}_M$ shows a completely different result. A dip in the distribution is seen near the particle in the low background level, most of the area around the particles is negative.



The real part of $\hat{\sigma}_M$ (center) is seen to fully capture the particle in the low background and partially in the background noise. At right, the Hadamard product with the original image is seen. No remnants of the background intensity remain, but no particles are captured in the high background region either.



By subtracting the mean image from the original—a minimum filter of the original image—an image is created with a low background intensity (left). Applying the $\hat{\sigma}_M$ results in the capturing of all particles (center). The ability of the $\hat{\sigma}_M$ to capture particles in high intensity backgrounds draws heavily on the quality of the subtracted mean image, or conversely, the nature of gradients in the original image. The right image shows the residue after subtraction of the $\hat{\sigma}_M$ result (contrast increased for clarity).

4.2.4 Preprocessing the PIV images

Now that some filters have been defined, the PIV image can be preprocessed in order to remove the sheet cavity from the images. This preprocessing is performed with an algorithm combining several filters and excludes regions of the image where cavity can not

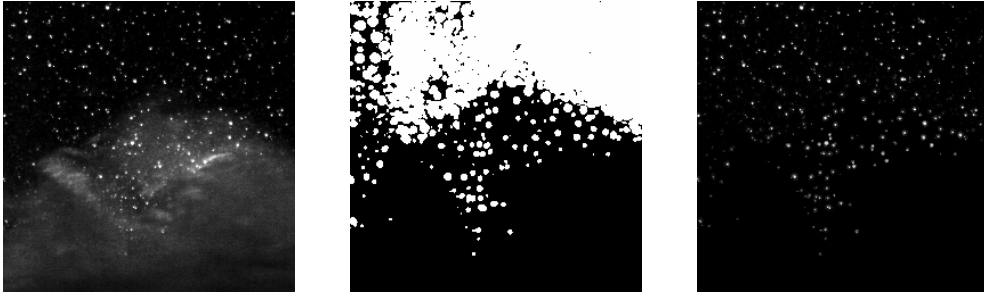


Figure 4.5 The left image is a raw close-up showing both particles and cavitation. The result of the $\hat{\sigma}_M$ filter (center) shows the real (white) and imaginary (black) regions of the image. Splitting the original image results in the image at right. The particles are separated from the original image and no part of the cloud visible in the image at left remains.

exist (e.g., the hydrofoil location). Although the $\hat{\sigma}_M$ (eq. 4.13) comes close, no single filter can perform this task. It is imperative that the filter does not change the result in the fully-wetted domain and only affects regions near the cavity.

The Laplacian filter is strong at identifying noise and thus pixels but also capture regions within the sheet. By using a threshold value for this filter, the sheet cavity is excluded, but so are many low-intensity particle images, leading to a degraded interrogation result. The modified standard definition captures all particles outside the cavity but does not capture all particles within the shed cavity. Hence, a combination of both filters is needed. The resulting filters are used as a passage filter, allowing regions to be passed to the preprocessed image and leaving the rest black (zero pixel count). The recipe used for the pre-processing is given in appendix H.

4.2.5 Finding the cavity interface

Now that the particles have been identified, a second search can be performed: that of the outline of the cavity. The shape is clearly defined on the PIV images and contains valuable information on the cavity outline during shedding. From the previous exercise it was already noticed that particles are present both in the fully-wetted flow region as in parts of the cavity. The $\hat{\sigma}_M$ of the original image was able to find particles in a low background noise, thus finding the fully-wetted flow. The cavity is nearly the opposite of the modified filters of the preprocessed images. If the high-intensity particles are filtered from the wetted flow regions, the remainder of the image can be put through a high-pass filter and the result is vapor, as visible in fig. 4.6. The recipe is given in appendix I

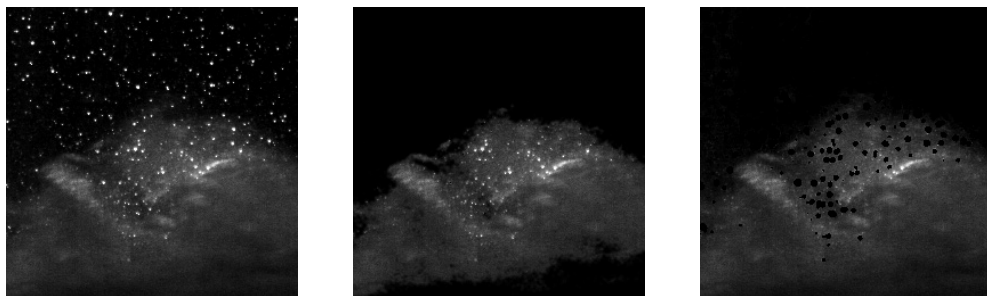


Figure 4.6 The left image is a raw close-up showing both particles and cavitation. The central image shows the results after the Hadamard product with the imaginary part of $\hat{\sigma}_M$ of the original image. Note that there is no particular interest in finding particles inside the cloud. On the contrary, the exclusion of these particles would appear as gaps in the cavity (right). Therefore, the $\hat{\sigma}_M$ filter (eq. 4.13) is applied to the original image \mathbf{I} and not to the averaged image $\bar{\mathbf{I}}$ (eq. H.3, p. 194)

4.2.6 Time series

As a time-resolved PIV data set consists of many images, a three dimensional image can be constructed in which the cavity can be seen to develop as time passes. Each PIV image contains two frames separated by the laser pulse delay. The PIV images themselves are taken at an effective frequency of $f = 1500 \text{ Hz}$ resulting in a time of $\simeq 666.\bar{6} \mu\text{s}$ from one PIV image to the next. The second frame of a PIV image follows after the laser pulse delay (ranging from 185 ms to 285 ms for the current experiments) This mismatched time axis between odd and even frames is small and using both frames yielded better results. Should the pulse delay be relatively small compared with the time between frames, the change in cavity outline would be comparatively small. In order to visualize the dynamics of the cavity in time, the individual cavity outlines are combined into a three-dimensional array. The individual frames containing the cavity are reduced in size. This will remove some of the spatial detail but keeps the general outline. Also, this is necessary considering the high memory demands of the routines used to determine the three-dimensional image. The computation of the cavity surface uses an isosurface routine and is handled by Matlab R14 imaging tools. Results are presented in chapter 5.

4.3 Performance of the Pre-Processing

A synthetic PIV image was created to test the kernel function $\hat{\sigma}_M$ as a preprocessor. Two frames were built with both background noise (i.e., cavitation) and particles present. The second frame was created in which the particles are shifted ten pixels to the left but the background noise only seven pixels. These two frames—together with two frames that

were preprocessed using $\hat{\sigma}_M$ —were passed to LaVision’s Davis 7 and cross-correlated with 16×16 windows with 50% overlap. The results are shown in fig. 4.7.1 and 4.7.2. The results are shown in fig. 4.7.3 and 4.7.4, with the regions outlined where particles, vapor, or both exist. From this synthetic image it is clear that the influence of background noise significantly deteriorates the measurement with a strong transition between regions of ten pixels and seven pixels, while the preprocessed image clearly shows a displacement of ten pixels for nearly the entire solution (84% of the vectors are within a 1% uncertainty vs. less than 40% for the raw image). It is concluded that application of PIV with fluorescent particles and optical filters is insufficient for accurate PIV measurements near the cavity interface if that cavity interface is captured by the camera.

The probability distribution function (PDF) of the synthetic image is plotted in fig. 4.8 and 4.9 for both the horizontal and vertical velocity component. The ‘noise floor’ in the horizontal component was removed and the error in the vertical component reduced. The PDF of a single non-synthetic PIV image of fully-wetted flow is shown in fig. 4.10. The distribution was largely equal with and without pre-processing, with a concentration around a zero-pixel displacement due to background noise correlation (hydrofoil) from which it can be concluded that the pre-processing does not alter the solution in the flow domain. The number of zero-pixel displacements increases significantly for the cavitating flow, see fig. 4.11. Note that the distribution showed a significant increase of probability between -8 and -3 pixels and that the distribution has changed over its entire range.

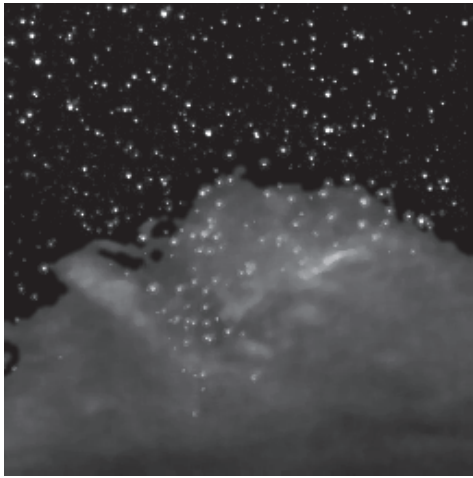
The velocity fields as determined by PIV interrogation were compared in figs. 4.12 and 4.13 for the fully-wetted flow. The results were *identical* in the flow regime, except near the hydrofoil location. Note that reflections in the hydrofoil surface result in a velocity vector that was always tangent to the hydrofoil. Although it is to be expected that the fluid ran tangent to the wall, it is not necessarily true that the averaged value within the interrogation window of a certain size is parallel to the wall as well. Figures 4.14 and 4.15 show an example with cavitation. Here the influence of the preprocessing is clearly visible as many positive correlations in the raw image were deleted. Figures 4.16 and 4.17 show the raw PIV image and velocity field with an outline of the identified vaporous region. Here, it is well visible that many particles were within the vaporous region. By actively filtering the image, and not masking the vaporous region, all particles that are visible were used to generate information.

4.4 Conclusions

PIV of cavitating flows without fluorescent particles and optical filters causes overexposure near the cavity interface. Although using fluorescent particles and optical filters will remove the overexposure, the solution still deteriorates due to correlation of illuminated vapor. This vapor is often outside the measurement plane. It is crucial that this source of background noise is properly dealt with if the location of the cavity interface is not known.

The preprocessing removes cavitation from the PIV images while leaving the solution of the flow unaffected. Upon close inspection of the result of pre-processed and unprocessed images, it can be concluded that the solutions are identical in the fully-wetted region. The measurement error increases near vaporous regions for the unprocessed images. The removal of reflections using fluorescent particles and optical filters is an insufficient condition for accurate PIV measurements near the cavity interface. The image processing removed most of this uncertainty and retains mostly particles. The combined use of laser induced fluorescence and optical filters, and image pre-processing allows for the interrogation of velocity vectors close to the vaporous regime with good accuracy.

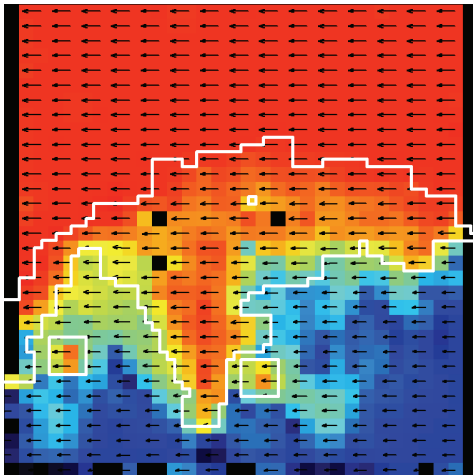
For some experiments, the cavitation was not visible without additional illumination. With the use of image pre-processing, the cavity can be purposely lit and tracked. Both the velocity field and cavity outline could be determined from a single camera without the need of a more complicated setup using several cameras and filters.



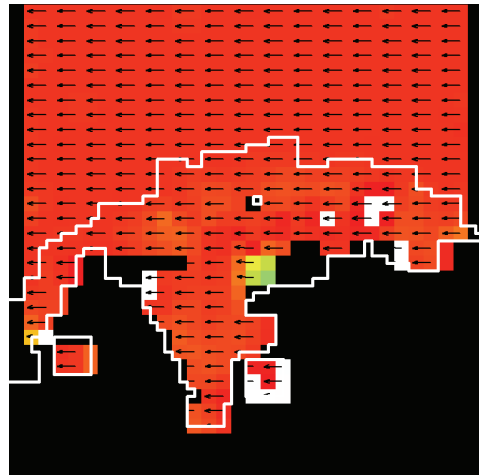
4.7.1 Synthetic image



4.7.2 Pre-processed image



4.7.3 Result of the unprocessed image



4.7.4 Result of the pre-processed image

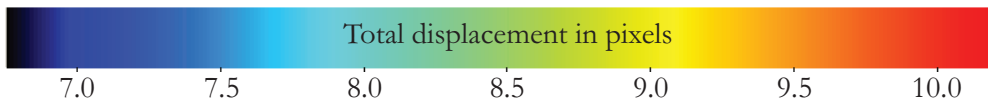


Figure 4.7 A synthetic image is created (1) and filtered (2). Particle shift is 10 pixels, cloud shift is 7 pixels. The bottom pictures show the solution both without (3) and with pre-processing (4). The solution after pre-processing results in near-uniform pixel displacement of -10 pixels.

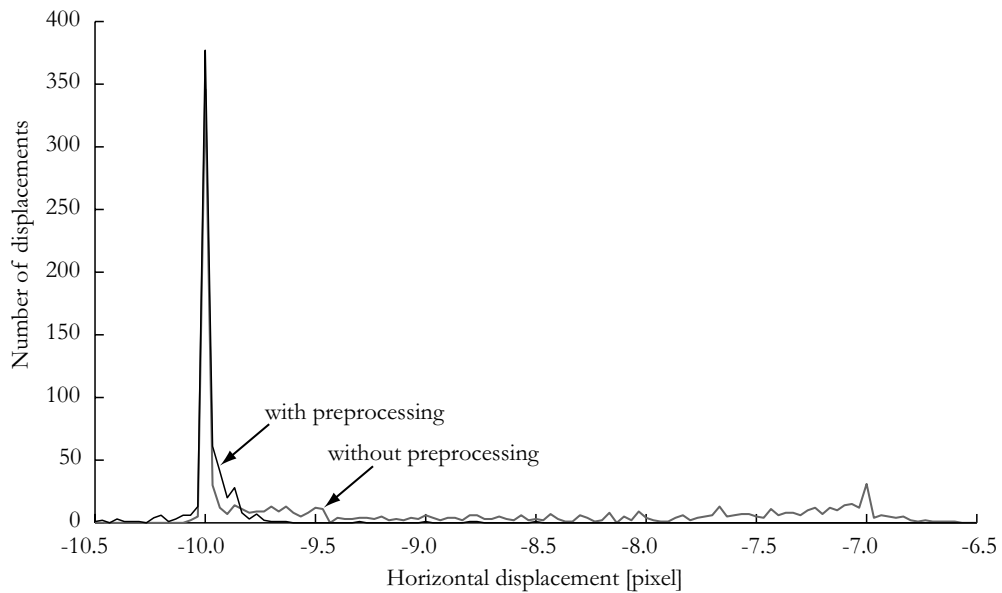


Figure 4.8 PDF of the horizontal velocity component of the synthetic PIV image with and without preprocessing, plotted at a resolution of $1/30$ pixels. Note that the PDF after preprocessing has concentrated toward the actual displacement of -10 pixel and no data remains between -6.5 and -9.75 pixels.

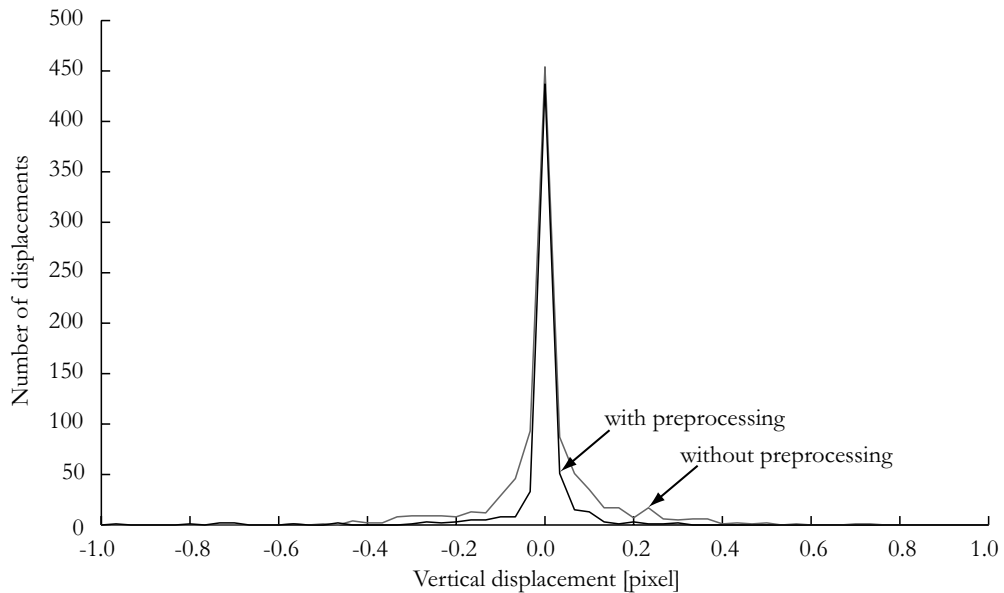


Figure 4.9 PDF of the vertical velocity component of the synthetic PIV image with and without preprocessing, plotted at a resolution of $1/30$ pixels. The correct solution is a zero-pixel vertical displacement. The vertical displacement after preprocessing remains within ± 0.1 pixel.

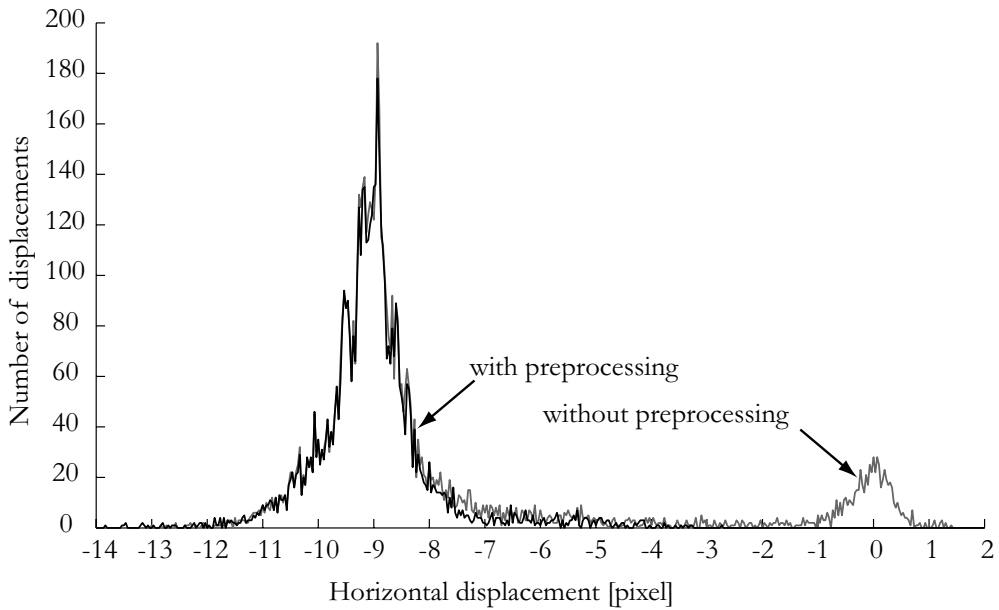


Figure 4.10 PDF of the horizontal velocity component of fully-wetted flow with and without preprocessing, plotted at a resolution of $1/30$ pixels. The solution is virtually identical at displacements between -14 and -8 pixel displacement. The influence of the preprocessing is well visible between -8 and 0 pixel displacement. Normally a fixed masking region is used to remove vectors outside flow regions.

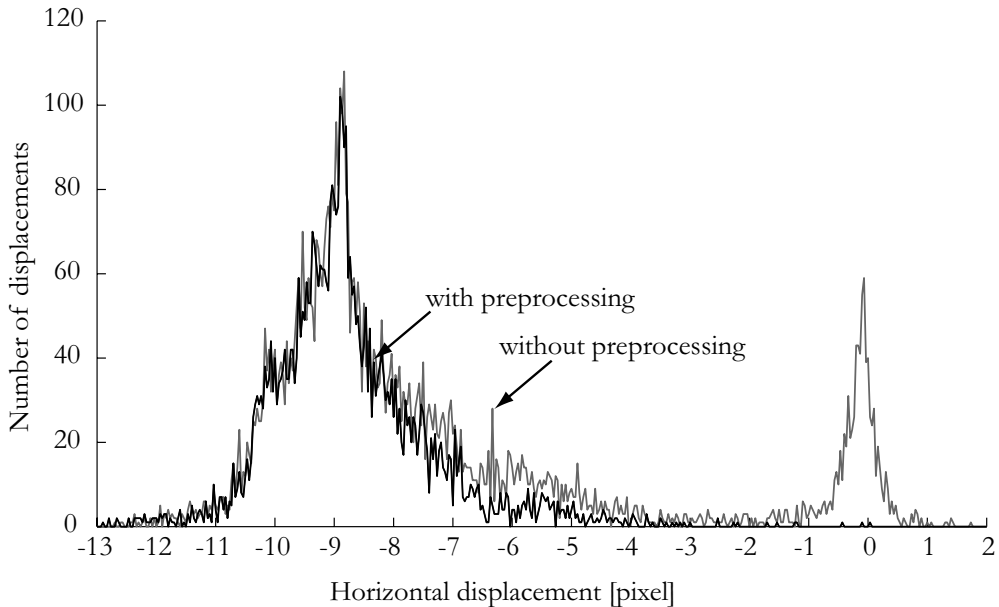


Figure 4.11 PDF of the horizontal velocity component of cavitating flow with and without preprocessing, plotted at a resolution of $1/30$ pixels. The influence of the preprocessing is more pronounced.

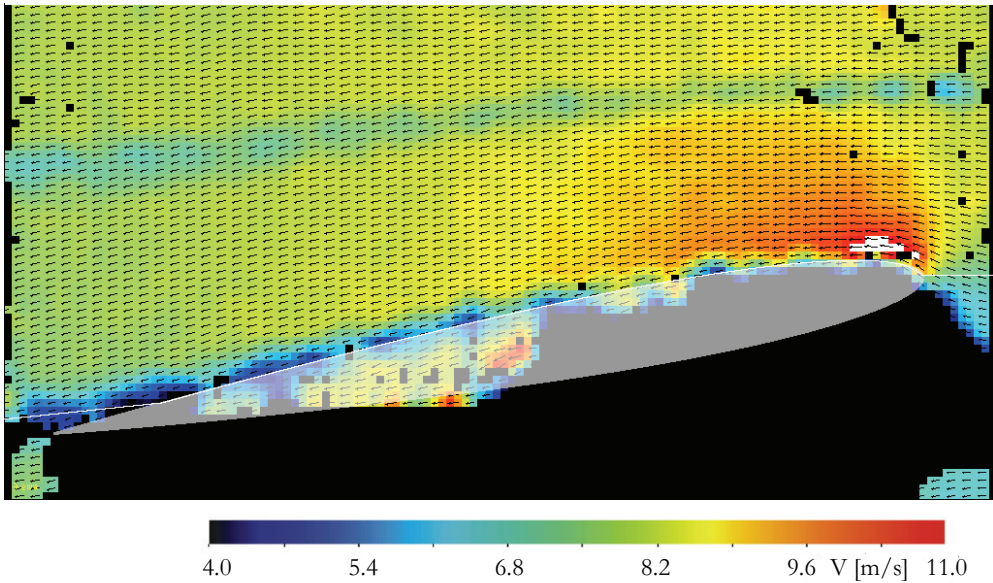


Figure 4.12 Fully-wetted flow, flow from right to left with the indicated outline of the section location at the measurement plane. An individual PIV velocity field showing the absolute velocity as a background color and direction as vectors. A solution is found in this mask area, due to the correlation of particles reflected in the hydrofoil. Normally a fixed masking region is used to remove vectors outside flow regions.

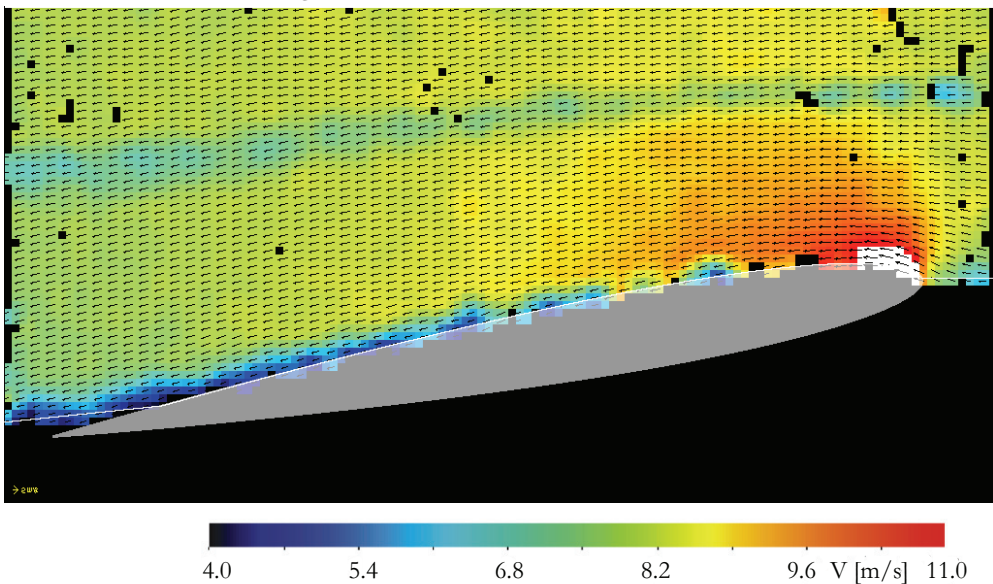


Figure 4.13 The same situation as above after image preprocessing and application of a fixed masking region. The influence of the static mask is clear, particularly near the leading edge (at right). The solution in the flow is identical after preprocessing, except for a few vectors now considered spurious, leaving gaps in the flow field. This is not considered a problem.

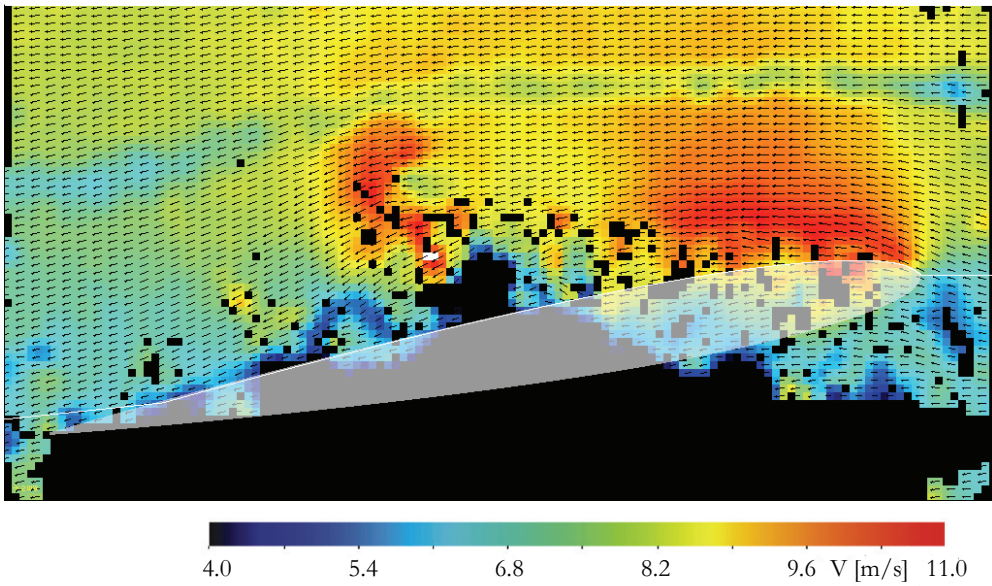


Figure 4.14 Cavitating flow, flow from right to left with the indicated outline of the section location at the measurement plane. With cavitation present, the distinction between the static mask and cavitating regimes is less clear. The solution, however, does not seem to contain hotspots of 'obviously wrong' vectors. Note the large solution region at the bottom right of the image, the result of the correlation of the cavity (see fig. 4.16).

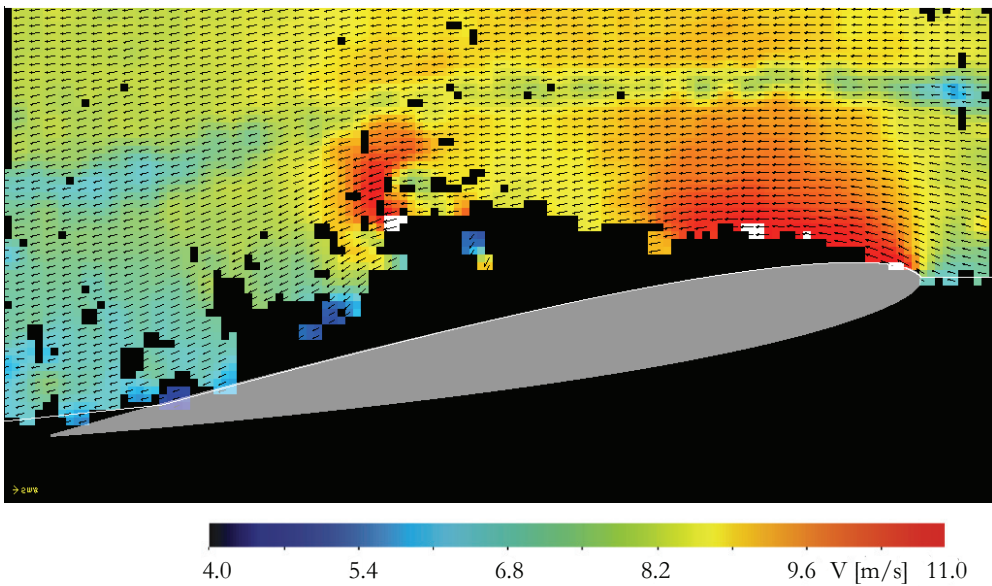


Figure 4.15 Cavitating flow, flow from right to left. This images shows the result after preprocessing the cavitating regime, clearly having avoided a large selection of vectors based on the interrogation of vapor, not particles

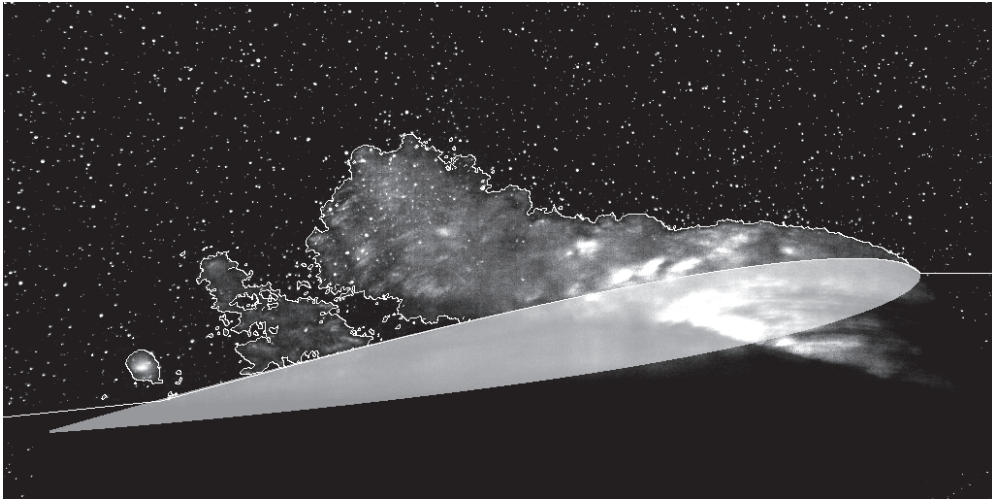


Figure 4.16 Cavitating flow, flow from right to left with the indicated outline of the section location at the measurement plane. Tracing the vaporous region shows that in the shed cloudy structure at center left, particles are visible. This vapor region is most likely not in the measurement plane.

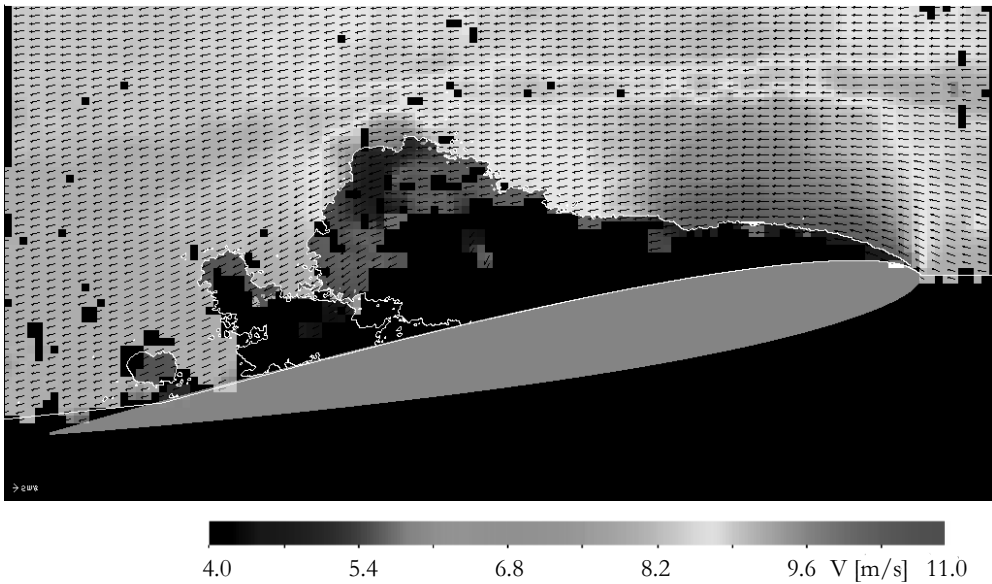


Figure 4.17 Plotting the cavity outline on the PIV solution shows that the preprocessing does not act as a mask, but actively identifies particles inside the vaporous regions on the image.

Chapter 5

The structure of attached cavitation

5.1 Introduction

This chapter discusses the results from the experiments. The focus will be on the effect of three-dimensionality of the hydrofoils on cavitation, and its effect on the cavitation shedding behavior.

Early work on three-dimensional hydrofoils was performed by Crimi (1970) on the effect of sweep (called skew for propeller blades) and it was concluded that the inception velocity increased with an increase in the skew angle. Hart *et al.* (1990) investigated an oscillating three-dimensional finite-span hydrofoil and concluded that the cavity collapse was most violent when the oscillating frequency coincided with the natural shedding frequency of the cavity. de Lange & de Bruin (1998) studied three transparent hydrofoils in the cavitation tunnel at the University of Delft and concluded that the re-entrant jet of the two-dimensional hydrofoil was directed upstream, but in the three-dimensional case the re-entrant jet velocity component normal to the cavity closure line was reflected into the cavity. As the pressure gradient is perpendicular to the closure line, the flow is deflected perpendicularly to the cavity closure line. This is also true for the two-dimensional re-entrant jet, which has no velocity component tangential to the cavity closure. Laberteaux & Ceccio (2001) studied a series of swept wedges. The cavity planform was observed to change significantly compared with two-dimensional planforms. The re-entrant jet was directed into the cavity allowing for a stationary sheet that only shed cloud cavitation at the far downstream edge. The flow behind the stationary cavity regions was measured by means of PIV to be free of vorticity. Dang & Kuiper (1999) studied the re-entrant jet on a hydrofoil with a spanwise varying angle of attack numerically and found that the direction of the re-entrant jet to be strongly influenced by the cavity topology. In their case the change in cavity shape was determined by loading and not by the sweep angle.

From the above is clear that the direction of the re-entrant jet is governed by the cavity closure and that changes to that closure can be effectuated by choosing hydrofoils with

swept edges or spanwise variation in pressure distribution. On a ship propeller the cavity is always three-dimensional, due to its three-dimensional geometry, the non-uniform inflow, and its rotation. In the present work the effect of three-dimensional pressure distribution on the shedding behavior of attached cavitation was studied on a series of hydrofoils with a spanwise change in loading. The effect on a non-uniform inflow was studied using a flow oscillator, which generated gusts in the test section. The sections used were a NACA0009 section with a low pressure peak near the leading edge at an angle of attack, and an Eppler YS-920 section with a flat pressure distribution over 70% to 80% of its chord. This allowed for the observation of the effect of the pressure distribution on the sheet cavitation behavior.

The chapter is split up in the study of the cavitating flow around hydrofoils in a uniform inflow (s. 5.2) and in a flow with gusts (s. 5.3).

Shedding behavior at steady inflow conditions

The finite-span hydrofoil with an elliptical planform is presented first in s. 5.2.1. The influence of the three-dimensionality of an attached cavity with tip vortex is visualized. The following section (s. 5.2.2) presents the shedding mechanism obtained from the results of the Twist-8N hydrofoil with an isolated sheet cavity. This case has previously been tested as a validation case for boundary element methods developed by Dang (2000) and Vaz (2005). A first case study is presented for a flow condition where a collapsing cavity did not detach itself from the leading edge but collapsed in a cascade of spanwise vortices. In a second case, a typical three-dimensional cavity and its shedding mechanism is discussed in detail. The shedding of the cavity was predominantly governed by its topology and was shedding large structures from the closure region of the cavity and not from the leading edge. The term 'side entrant jet' is introduced to distinguish the three-dimensional re-entrant flow from the classical two-dimensional flow where the re-entrant flow reaches the leading edge. It is shown that this side-entrant flow is the main cause for the cloud shedding and not the re-entrant jet reaching the leading edge as is the case in two-dimensional flow.

After having identified several flow structures, the flow over a hydrofoil with a flat pressure distribution is described in section 5.2.3. While the Twist-8N is a hydrofoil with a low pressure peak on the suction side near the leading edge region, describes the cavity-shedding behavior of the Twist-11E hydrofoil, with an Eppler YS-920 section with a pressure distribution that is (nearly) constant over most of its chord. From this case it becomes clear that a re-entrant jet of low momentum impinging with the sheet cavity interface does not lead to the shedding of the sheet cavity. This difference in shedding behavior underscores the importance that if stability of a sheet cavity is to be calculated accurately, than the cavity and the re-entrant flow must be represented accurately .

Shedding behavior at unsteady inflow conditions

The influence of an unsteady inflow on the cavity shedding behavior is presented for a Twist-11N hydrofoil in s. 5.3.1. It is shown that the cloud shedding frequency will lock in with the incoming flow when the frequency of the disturbance approaches the natural shedding frequency. In s. 5.3.2, the unsteady inflow effects on the shedding on the Twist-11E are discussed with conditions closest to actual propeller cavitation. Using the results from the PIV measurements, several distinct vortices in the wake of the cavity are recognized while the rest of the in-plane vorticity is zero.

Conclusions drawn from both steady and unsteady conditions are presented in s. 5.4.

5.2 Shedding behavior at steady inflow conditions

5.2.1 The Ellipse-11N hydrofoil

The Ellipse-11N is a finite-span hydrofoil designed to have a high loading at the tip, so that the interaction of sheet cavitation with the tip vortex could be observed. This hydrofoil was used for a feasibility study of the application stereoscopic PIV to cavitating flows¹. Skew was applied to avoid the interacting of the re-entrant flow with the sheet cavity at the leading edge. When subjecting the hydrofoil to low cavitation numbers, a small sheet and tip vortex appeared. The vortex can be seen to start from the leading edge of the tip in fig. 5.1. The cavity topology is similar to attached cavitation on swept wedges as reported by Laberteaux & Ceccio (2001) with the re-entrant flow directed into the cavity with a large spanwise velocity component. This cavitation pattern resembles propeller cavitation by having re-entrant flow directed at the tip that is advected by the tip vortex, see fig. 5.2. The sheet was stable and steady at most conditions, forming a basic example of a steady three-dimensional cavity without any shedding.

When sheet cavitation is present at very low σ along the entire span it is no longer predominantly three-dimensional and starts shedding in regions away from the tip, where the hydrofoil and the cavitation can be considered to be nearly two-dimensional. The vortex is identified as a leading edge vortex, containing vorticity at the leading edge. Leading edge vortices are typically observed on highly skewed propellers and can be easily avoided by applying a straight leading edge or even forward skew (Kuiper 2001). A very low cavitation numbers a local cavitating tip vortex was observed starting at the trailing edge of the tip of the Ellipse-11N.

From figure 5.2 it can be observed that the re-entrant flow is directed toward the tip of the hydrofoil. The front of the jet is visible as a line between A and B . The jet reaches the leading edge at B and from that point onward toward the tip the cavity no longer detaches

¹The stereoscopic PIV is not presented, see van der Hout (2007)

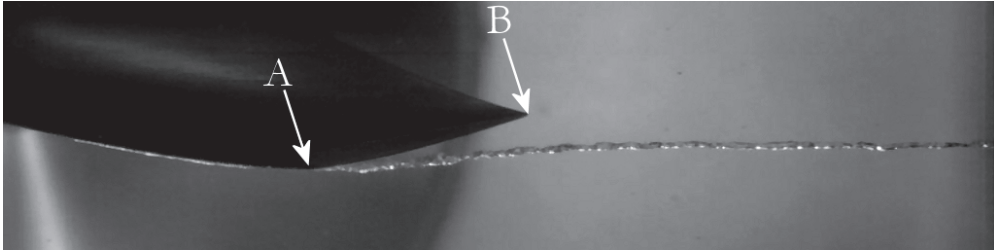


Figure 5.1 Side view of the Ellipse-11N, flow from left to right, $V_0 = 7.05 \text{ m/s}$, $\sigma = 0.80$, $\alpha = +1^\circ$. The leading (A) and trailing edge (B) of the tip chord are clearly visible, as well as the cavitating core. Note that the vortex starts at the leading edge of the tip.

from the leading edge. The detachment line visibly moves downstream. The re-entrant flow is advected by the leading edge vortex and does not cause any unstable behavior. For this example, the impact of the re-entrant flow near the detachment point of the attached sheet cavity is insufficient to cause the sheet to become unstable and start shedding.

On full-scale propellers the shedding of several cavitating vortices from the leading edge is often observed, showing a trail of vaporous vortices. It is hypothesized that re-entrant flow in the radial direction can impact on the detachment point of the attached cavitation and cause separation into a trailing vortex.

Increasing the loading of the Ellipse-11N using the flow oscillator clearly had an effect on the diameter of the cavitating core of the vortex, as can be seen in figure 5.3 with the first frame corresponding to the minimum lift where the cavitating core diameter was smallest (i.e., not cavitating). The thickness of the cavitating core was determined optically from the high-speed video frames, 1cm behind the trailing edge of the tip and plotted in fig. 5.4, from two orthogonally placed cameras. Comparing the tip vortex diameter with the measured lift clearly shows a direct relationship. A small phase delay is observed. The cavity and tip vortex clearly respond to the flow oscillator.

5.2.2 The Twist-8N hydrofoil

The shedding process of the attached cavity is classified into three regimes. At high cavitation numbers ($\sigma > 1.1$), the attached cavity was short in length and present over a wide part of the leading edge and hence mainly two-dimensional. This cavity was shedding vortices intermittently, no large cloudy structures were identified. Such a closure is termed 'open' by Laberteaux & Ceccio (2001). At moderate cavitation numbers, ($0.65 > \sigma > 1.1$), large structures were shed regularly. This intermediate regime is dominated by the three dimensionality of the cavity. Lowering the pressure further ($\sigma < 0.65$) created an attached

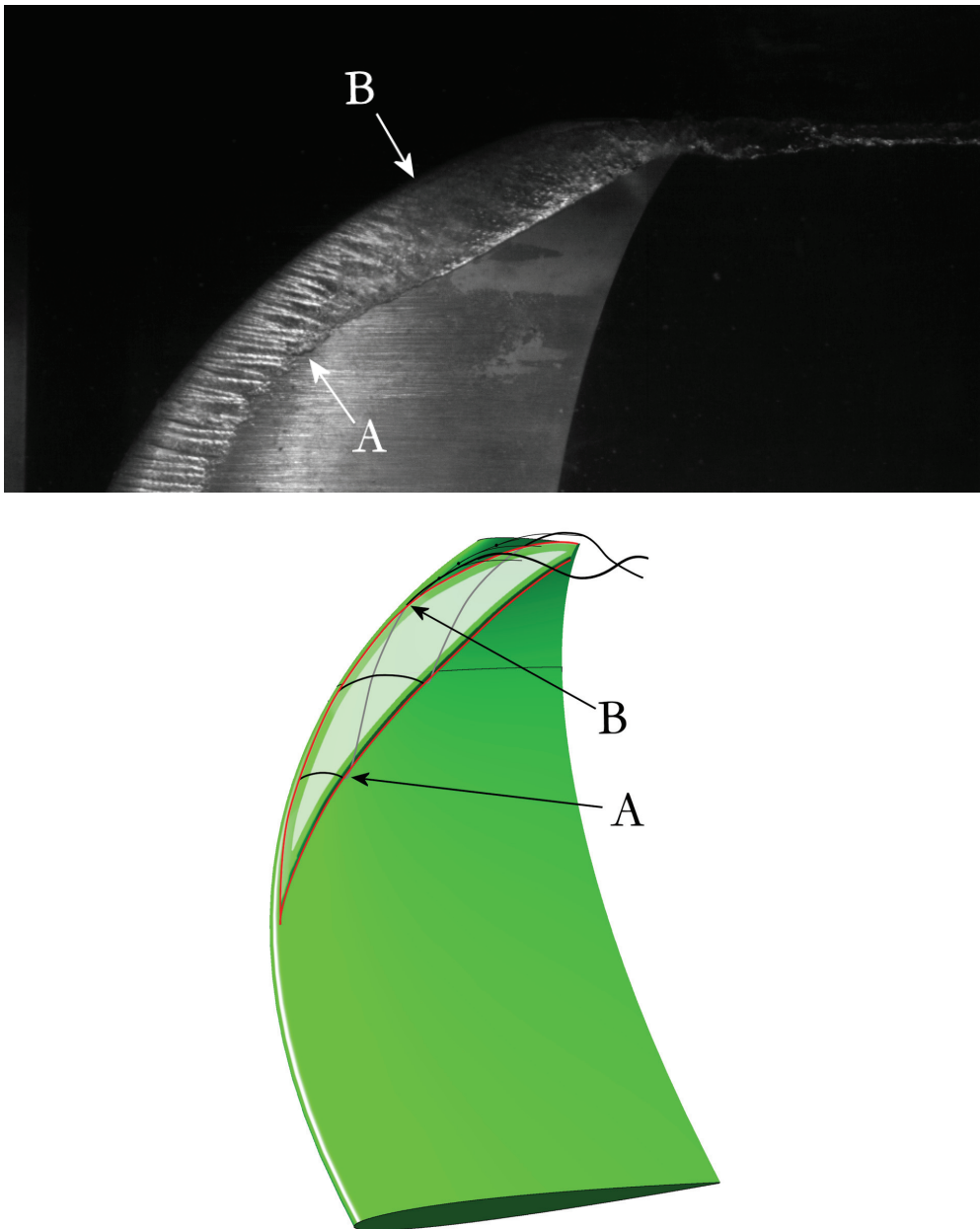


Figure 5.2 Top view of the Ellipse-11N, $V_0 = 7.00 \text{ m/s} \pm 3.76\%$, $\sigma = 0.73 \pm 7.27\%$, $\alpha = +1^\circ$. The sheet cavity is seen to merge with the tip vortex. The hydrofoil is cavitating over most of its span, but below the point denoted as A a distinct sheet is not present. The cavity consists of streaks from roughness elements that do not merge into a single structure. The re-entrant flow reaches the leading edge at B, from whereon the cavity detachment point moves downstream.

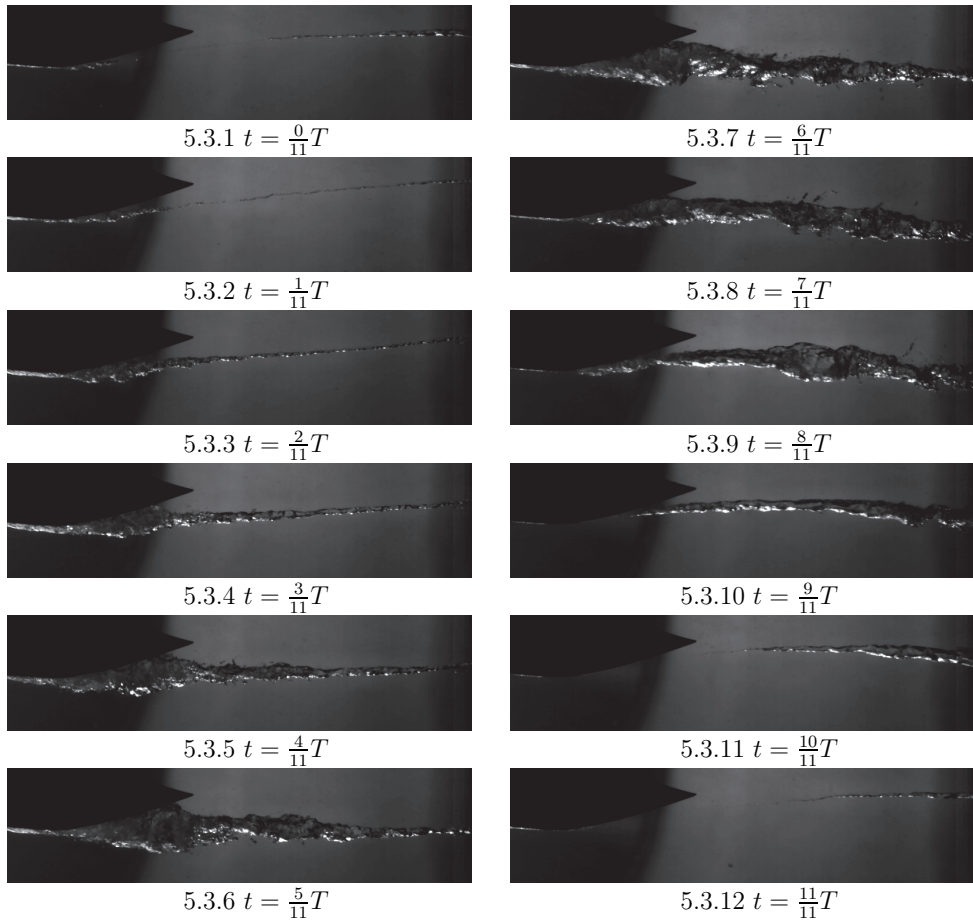


Figure 5.3 Side view of the tip vortex on the Ellipse-11N at $\alpha = +1^\circ$ during one period of the oscillator ($T = 64 \text{ ms}$, $V_0 = 7.29 \text{ m/s} \pm 3.57\%$, $\sigma = 0.67 \pm 7.13\%$, $f_{FO} = 15.61 \text{ Hz}$). The first frame coincides with the minimum lift of the hydrofoil.

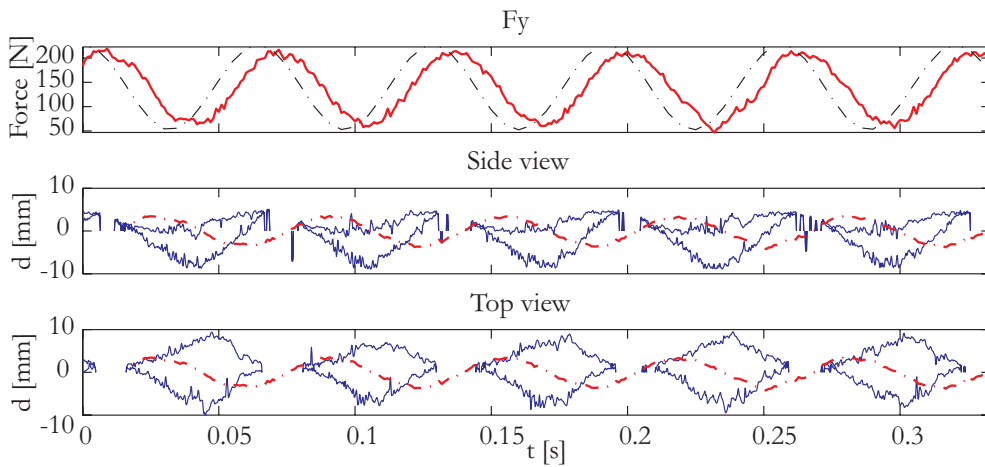


Figure 5.4 Conditions as in fig. 5.3. The top graph shows the phase delay between the oscillator position and measured lift (red). The diameter of the tip vortex, d , is measured using image analysis, $x_d = 6\text{cm}$ behind the leading edge of the tip. The phase between the lift and flow oscillator position, ϕ has been corrected with $\phi_c = fx_d/U$, taking the mean flow velocity and distance from the leading edge of the tip to the measurement position into account. The tip vortex position and diameter are seen to be repeatable over several periods of the flow oscillator.

cavity reaching a length comparable with the chord length of the hydrofoil. Shedding was then intermittent and irregular. The cavity spanned the entire foil and was once more mainly two-dimensional.

Visual analysis of the high speed video recordings indicated that the Strouhal number

$$St = \frac{fl}{V} \quad (5.1)$$

based on cavity shedding frequency f —determined by frame-by-frame analysis of the high-speed video over ten sheddings—and cavity length l was around $St = 0.185$ when $0.65 < \sigma < 1.1$. Strouhal numbers of $St = 0.25 - 0.40$ —based on the same parameters as above—were reported or specified by Arndt *et al.* (1995) as:

$$St = \frac{1}{4}\sqrt{1 + \sigma} \quad (5.2)$$

Coutier-Delgosha *et al.* (2005)—observing the shedding of cloud cavitation on two-dimensional plano-convex hydrofoils—reported Strouhal numbers near $St=0.25$ for $\sigma < 1.3$. The Strouhal number was around $St = 0.11 \pm 0.01$ only when cavities larger than 80% chord were observed. Both the cavity length and frequency were determined from the visualization, marking the frame when shedding was observed and the length of the cavity at that time instant, over a range of 12-15 sheddings. The standard deviation on frames is typically 1-1.5 frames. Some modulation is observed in the shedding frequency, but the shedding itself is regular. No frequency could be obtained from the outlet pressure signals. The cavity length shows a standard deviation of 5% at $\sigma > 1.2$ increasing to 15% at $\sigma=0.7$. From the observations—by examining the Strouhal number—can be concluded that due to the three-dimensional geometry of the foil the resulting shedding of the sheet of the present work differed significantly from a two-dimensional cavity shedding. In fig. 5.5 the Strouhal number is plotted versus the cavitation number, σ as well as the Strouhal number following from eq. 5.2. There was no indication that the Strouhal number was dependent on the cavitation number for the angles of attack considered in the present work.

Case study at a low cavitation number

Figure 5.6 presents example of a (super) cavity showing the shedding in detail. In fig. 5.6.1-5.6.6 the location of the front of the re-entrant jet is given by the arrow in the center. Although difficult to identify on photographs, on the recordings it is clearly seen to move slowly forward. The breaking-up of the sheet in fig. 5.6.1-5.6.10 starts from the end, moving upstream.

The shed flow structure in fig. 5.6.7-5.6.8 consists of primary spanwise and secondary streamwise vortices, similar to the turbulent shear flow structure observed behind steps and other mixing layers (O' Hern 1990). Figure 5.7 shows the formation of a spanwise vortex from fig. 5.6.5-5.6.5 (showing intermediate images as well). Such a spanwise vortex

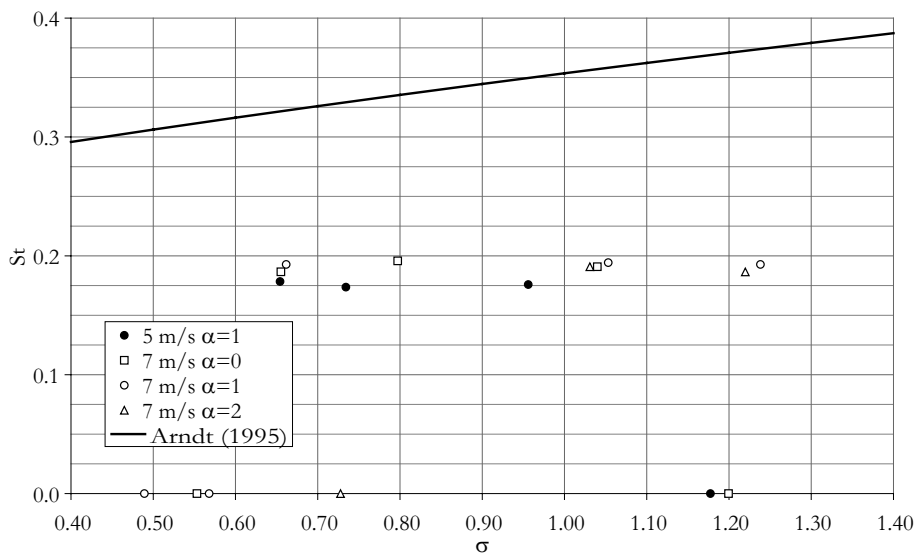


Figure 5.5 Strouhal number as a function of σ at two different velocities based on maximum cavity length with an average value of the Strouhal number of $St = 0.185$, significantly lower than for a two-dimensional foil. Several points at $St = 0$ are visible indicating either irregular shedding ($\sigma < 0.65$) or the absence of the shedding of large structures resulting in an 'open' cavity ($\sigma > 1.1$). The continuous line is the eq. 5.2 from Arndt *et al.* (1995) for cavity shedding on two-dimensional hydrofoils.

system can be a result of a Kelvin-Helmholtz instability of the shear layer forming at the cavity interface with the re-entrant flow, with a street of vortices with a positive strength (where the vorticity has the same sign as the hydrofoil's circulation). This vortex system is different from alternating Kármán-Bérnard vortices, consisting of counter rotating vortices. A close-up of fig. 5.6.6-5.6.9 is given in fig. 5.8, including all intermediate images. Bernal & Rosko (1986) describe a structure that greatly resembles the presented shedding structure of span wise and stream wise vortices, describing the structure of a helium-nitrogen mixing layer.

The observed streamwise vortices originated as small spanwise vortices, quickly warped around the primary spanwise vortices. These secondary vortices are formed from perturbations in the primary two-dimensional Kelvin-Helmholtz instability (Meiburg & Lasheras (1988)). The secondary vortices can be seen to be stretched around the periphery of the primary structures. As these secondary vortices are stretched, conservation of angular mo-

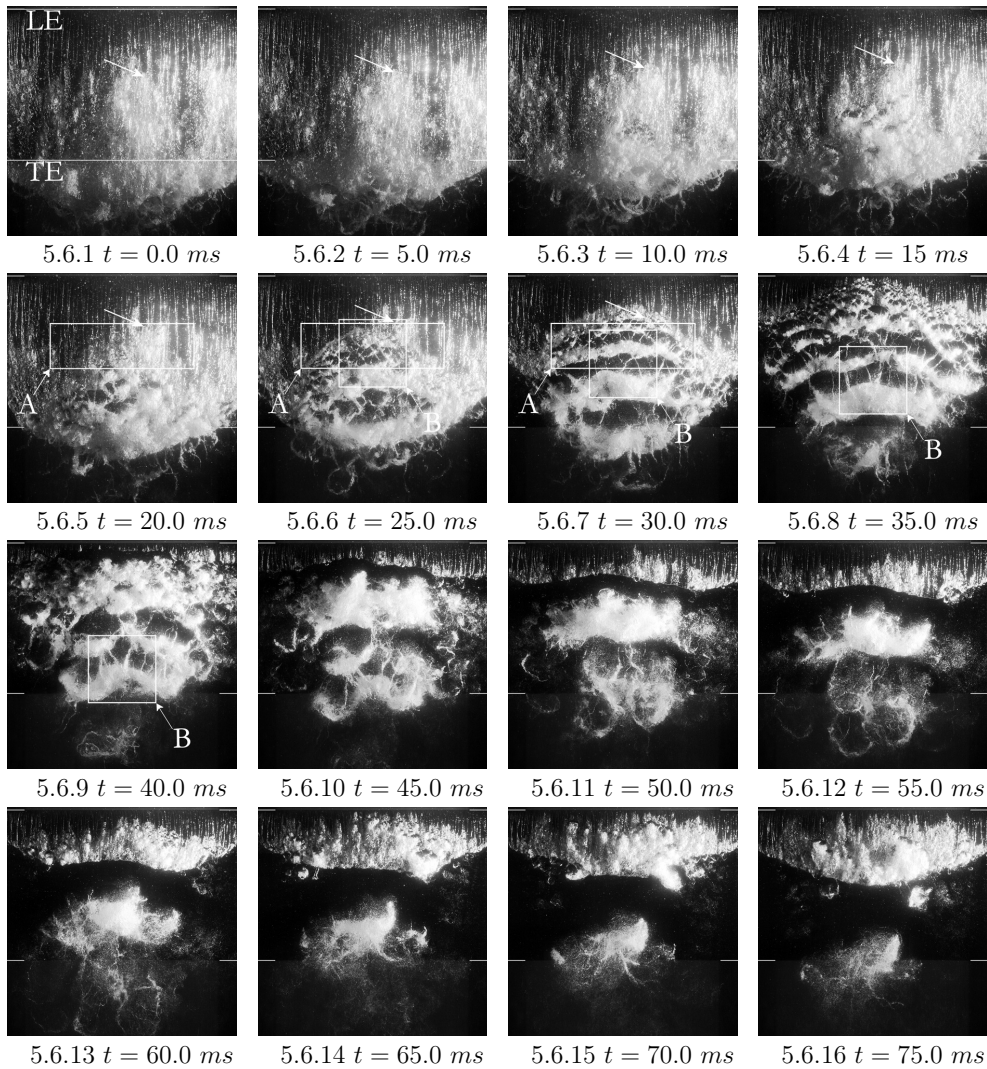


Figure 5.6 Visualization at $V_0 = 6.89 \text{ m/s} \pm 7.70\%$, $\alpha = +1^\circ$, $\sigma = 0.49 \pm 28.4\%$, recorded at $f = 2000 \text{ Hz}$, showing every fifth frame. White outlines indicate areas A and B enhanced in figs. 5.7 & 5.8, respectively

mentum dictates that their rate-of-rotation increases. When a non-cavitating vortex line is stretched its rotation rate increases due to the conservation of moment of momentum. In case of a cavitating vortex, the pressure in the core is lowered leading to an increase in the cavitating core diameter. This larger cavitating-core diameter again reduces the rotation rate but the influence of vortex stretching is the dominating factor. As a result, the stretching and rotation rate of cavitating vortex core are not directly related as the core diameter depends on the ambient pressure as well. Due to the high rate of rotation, cavitation inception is first observed in these secondary vortices in plane shear layers (O' Hern 1990, Belahadji *et al.* 1995, Iyer & Ceccio 2002), but here vapor is trapped in the initial formation and inception is not applicable.

From figure 5.6.4-5.6.8 it is visible that the front of the mixing moved forward and the collapse was cascading toward the leading edge. The collapse of the sheet started out as concave but the front drew parallel to the span as it progressed upstream. The front of the disturbance accelerated at a constant rate up to the mean stream velocity when it reached the leading edge, as determined from frame-by-frame analysis. The approximate location of the front at the central plane was identified and plotted in fig. 5.9.

The re-entrant jet momentum depends on the pressure gradient in the closure region (Le *et al.* 1993a). The increase in collapse speed may be explained as follows. At the start of the collapse cycle the cavity is a well-defined spatial structure with a convex closure. Due to the three-dimensional geometry with a symmetry plane, a stagnation point is present in the closure region only (fig. 10.1). After the first pinch-off the closure region of the cavity has changed from a convex into a concave or straight shape and the reattachment region has widened (fig. 10.2) and widening further with each pinch off (fig. 10.3) as the cavity loses its three dimensionality. From observations at higher values of σ —presented below—it is observed that on a three-dimensional cavity the re-entrant jet diverges radially from the closure into the sheet when the cavity is fully grown.

Case study at a higher cavitation number

In figure 5.11 a full shedding cycle at 5 m/s , $\sigma = 0.66$, and $\alpha = +1^\circ$ of a regularly-shedding cavity is shown, with the flow from top to bottom. The shedding was repeatable, constant in its shedding frequency, and always followed the same macro structural collapse.

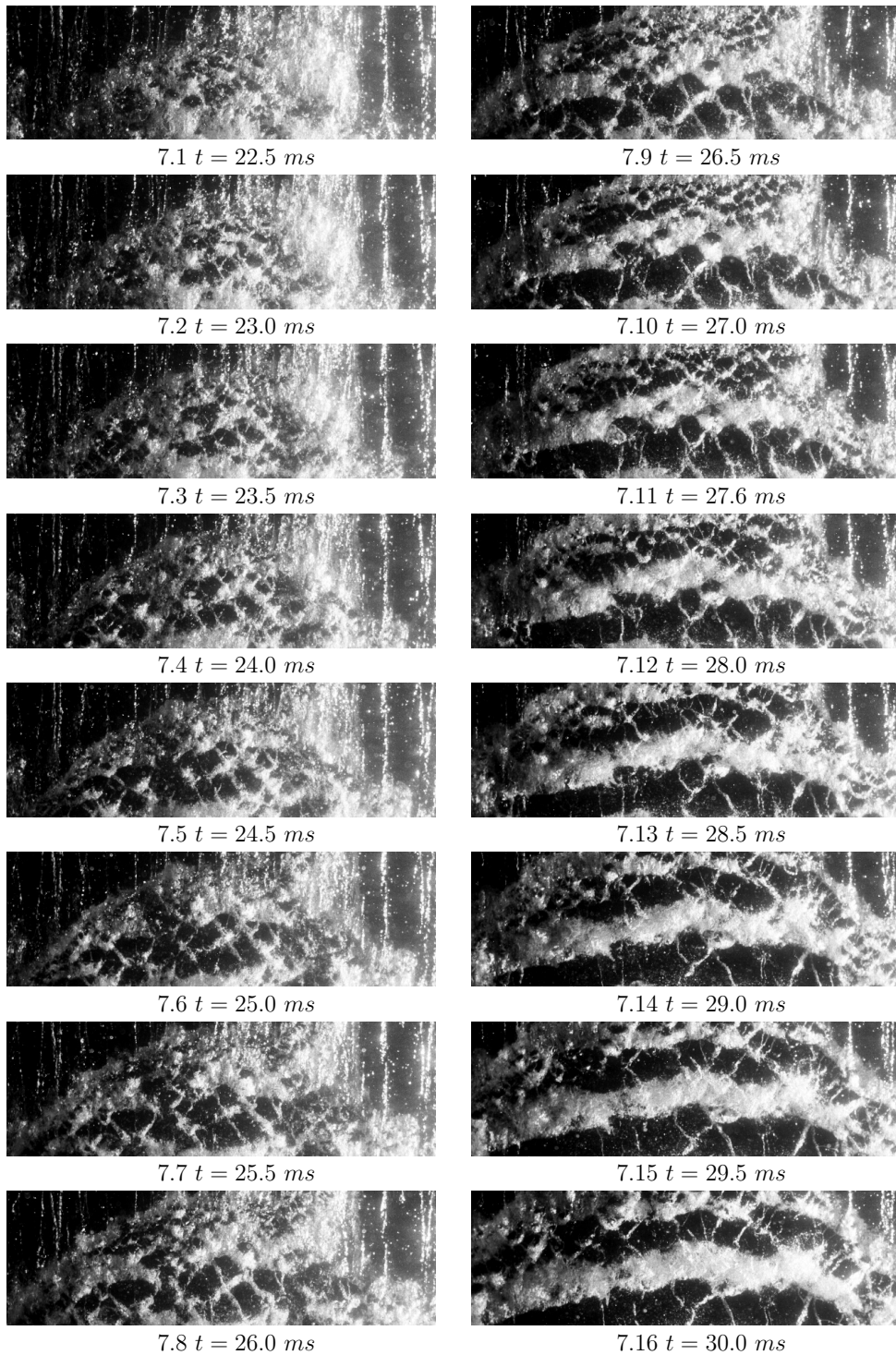


Figure 5.7 A close-up of figure 5.6 (marked A) shows the formation of a large spanwise vortex at $f = 2000 \text{ Hz}$. As the main sheet collapses, a trail of very small spanwise vortices is created, merging in several distinct larger structures

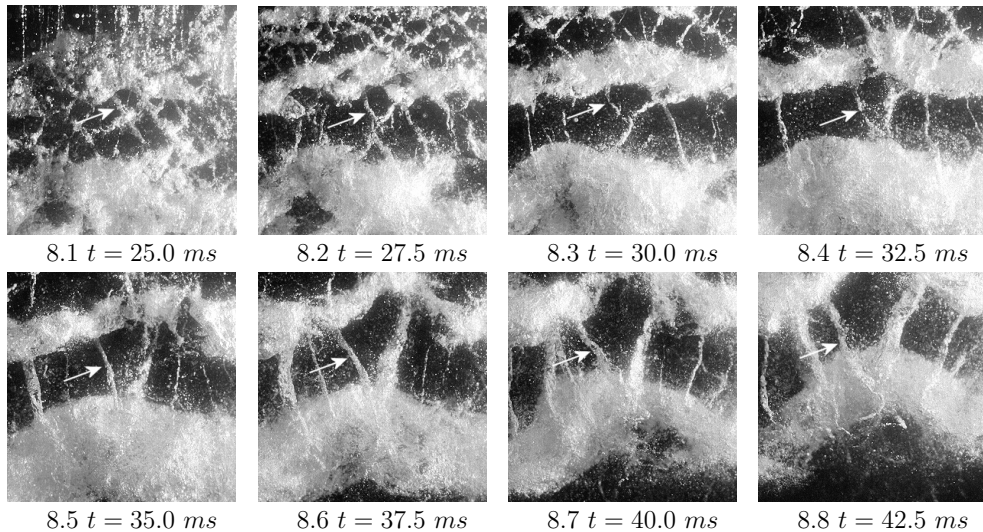


Figure 5.8 Close-ups of fig. 5.6.6-5.6.9 (marked B) including intermediate images. The streamwise cavitating vortices originate perturbations near the primary spanwise vortices are stretched around the primary spanwise vortices.

The shedding cycle of the cavity in figure 5.11 is divided into four phases: destabilization, primary and secondary shedding, followed by growth into its initial condition. There is a short overlap between primary and secondary shedding (and growth). The primary shedding is located at the mid plane of the hydrofoil, the secondary shedding is visible at the sides of the region of the primary shedding as two distinct smaller vortices.

Phase 1	5.11.1-5.11.4	<i>Initial disturbance</i>
Phase 2	5.11.5-5.11.12	<i>Primary Shedding (cavity center)</i>
Phase 3	5.11.9-5.11.16	<i>Secondary Shedding (cavity sides)</i>
Phase 4	5.11.17-5.11.20	<i>Growth</i>

Initial disturbance

Figures 5.11.1-5.11.4 show the convex cavity, here considered fully grown. The lower part of the cavity interface was turbulent, while the cavity at the sides and near the leading edge was glassy and transparent. It is in the closure region where the cavity became turbulent first, not near the leading edge, as is typical of large structure shedding on two-dimensional hydrofoils. The reasons are two-fold.

1. The closure region in a two-dimensional flow would normally be followed by a stagnation line (parallel to the leading edge), here it was a stagnation point at the mid plane

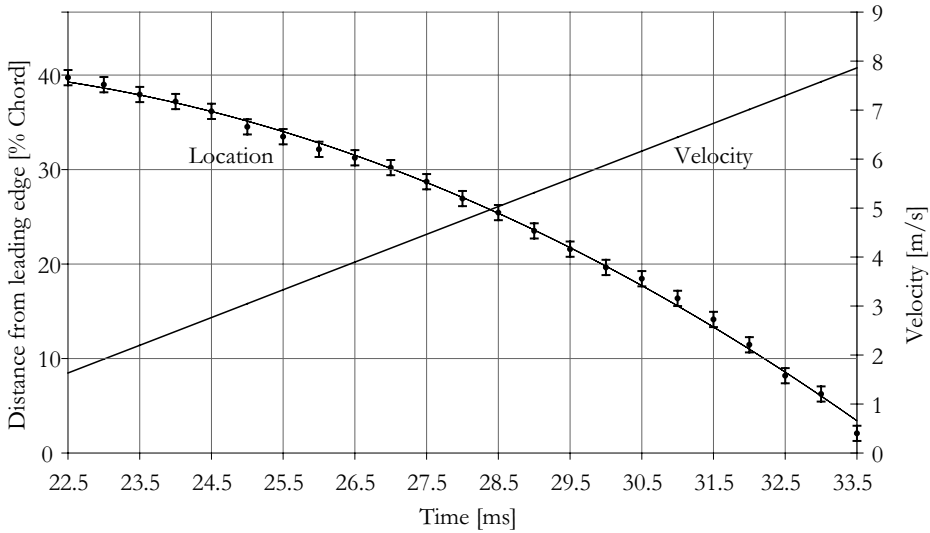


Figure 5.9 The location (and its quadratic fit) and velocity of the visible collapse front in the central plane as visible in figs 5.6.5-5.6.10 determined from frame-by-frame analysis. Error bars indicate a 10 pixel error in the location of the collapse front. The front seems to accelerate at a constant rate.

implying the local pressure gradient was weakened. As indicated above, the momentum in the re-entrant jet depends on the pressure gradient in the closure region, so the three-dimensional shape of the cavity resulted in a re-entrant jet diverging radially into the cavity from its closure at the mid span position. Therefore, its forward momentum was diminished as it progressed into the cavity.

2. The pressure gradient at the sides of the sheet forced the flow over the sheet into the cavity roughly "mirroring" the streamlines at the interface contour as sketched in figure 5.12. De lange & de Bruijn concluded that the re-entrant jet of the two-dimensional hydrofoil was directly upstream, but in the three-dimensional case the re-entrant jet component normal to the closure line was reflected inward. As the pressure gradient was perpendicular to the closure line, the component tangential to the closure line remained unchanged. At the sides of the cavity, re-entrant flow had a very small span-wise component and was directed downstream. The spanwise component was largest when the cavity closure contour was at about 45° with the incoming flow where the velocity component in downstream direction of the re-entrant flow was zero. At larger angles, the re-entrant

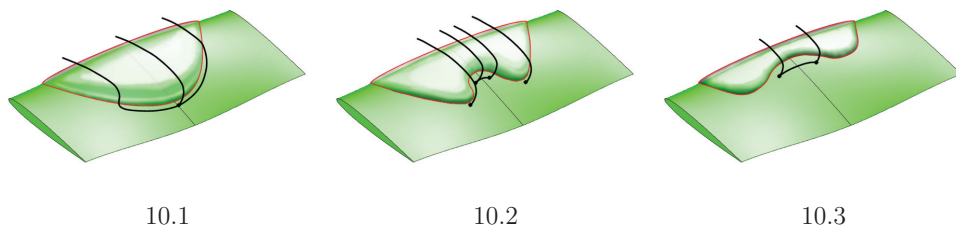


Figure 5.10 Flow lines converge at the central plane with re-attachment and re-entrant flow emanating from this central plane point (as later observed in fig. 5.14 and sketched fig. 5.13). With each pinch-off the re-attachment region widens and the closure of the cavity becomes increasingly more two-dimensional.

jet had an upstream component (fig. 5.12). As the pressure gradient is perpendicular to the closure line, the flow is deflected perpendicular to the cavity closure line. At larger angles, the re-entrant jet had an upstream component (fig. 5.12). When the sheet cavity was growing, flow from the sides was not obstructed, nor was it directed at the leading edge.

To distinguish between various directions of the re-entrant flow, the term side-entrant jet is introduced. This term refers to that part of the re-entrant flow that has a strong spanwise velocity component. The term re-entrant jet is reserved for the re-entrant flow that has a velocity component that is mainly streamwise. The re-entrant flow is thus split up in re-entrant and side-entrant jet components, even though at certain points of the flow both terms may apply. Note that the side-entrant jet component, in contrast to the re-entrant jet component, is not necessarily directed upstream. The term side-entrant is introduced to emphasize the three-dimensional character of the flow. For presented cases, the side-entrant jets from both sides were flowing into the closure region of the sheet where they collided. Side-entrant jets of the re-entrant flow do not reach the leading edge but also lead to shedding.

Any fluid ejected upward through the cavity interface creates a significant disturbance, isolating a small portion of vapor and creating a bubbly flow consisting of jet-entrained vapor. The velocity of a streamline at the cavity surface is measured at $V_V = V_0\sqrt{1 + \sigma}$ (Foeth *et al.* 2006). Although the velocity of the re-entrant flow is difficult to measure, the velocity of the jets is unlikely to be appreciably smaller. Also, if we assume that during the shedding cycle the two side-entrant jets were converging for about a third of the shedding cycle (15 Hz), the amount of fluid through a square millimeter—taking a homogeneous velocity distribution—at this velocity of 6.4 m/s was about 285 mm³ per mm² cross-section of the re-entrant flow. At this rate the cavity closure is collecting fluid quickly even if the jets are thin.

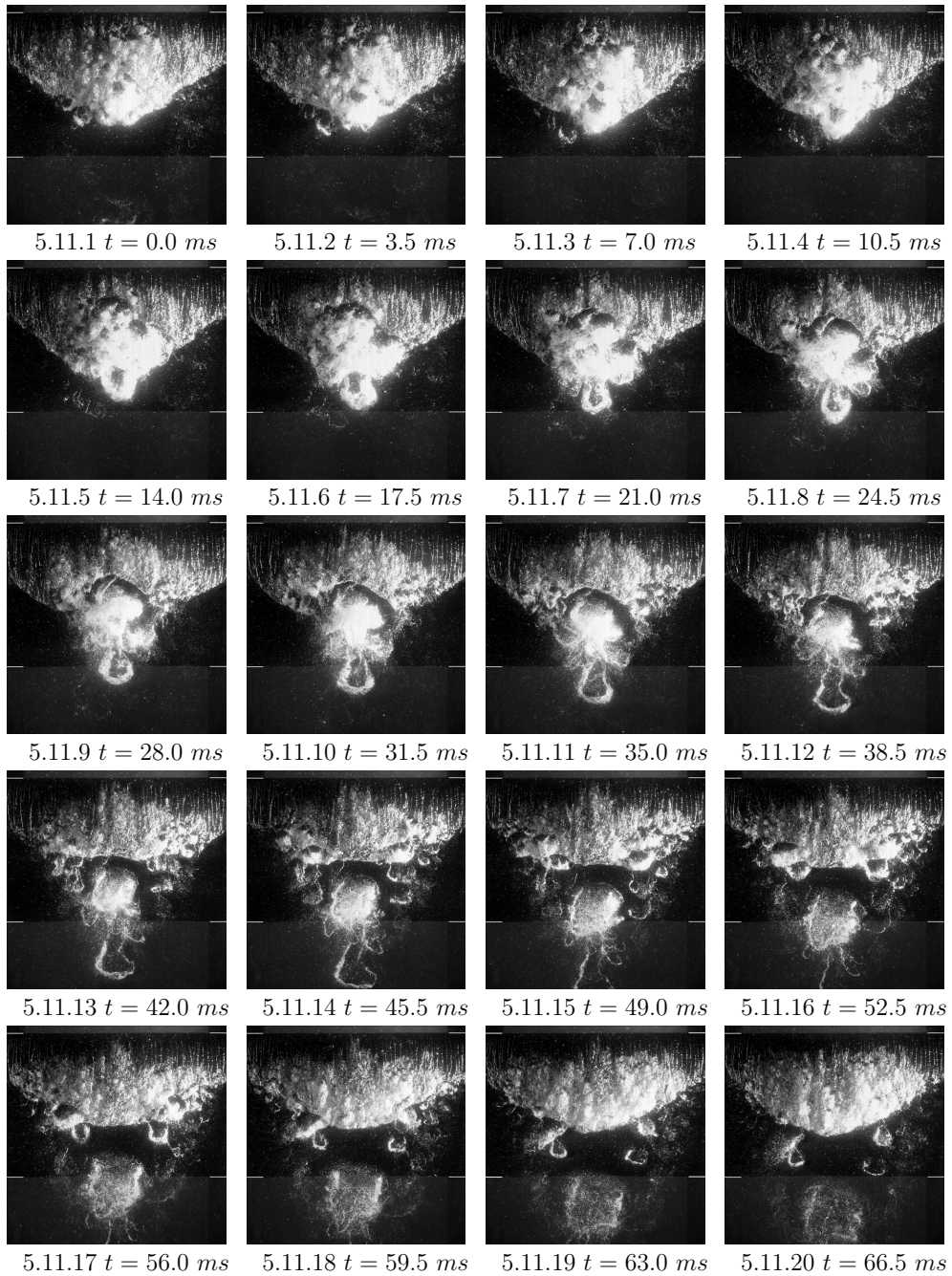


Figure 5.11 Visualization at $4.96 \text{ m/s} \pm 6.4\%$, $\alpha = +1^\circ$, $\sigma = 0.66 \pm 7.94\%$, recorded at $f = 2000 \text{ Hz}$, showing every seventh frame. Flow from top to bottom.

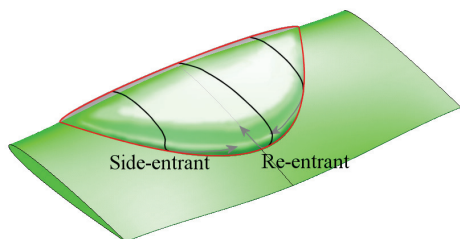


Figure 5.12 Streamlines over the cavity interface are directed inward

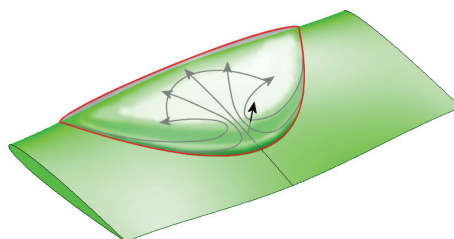


Figure 5.13 Observed direction of re-entrant flow focusing causing the primary pinch-off. The re-entrant flow is radially diverging into the cavity.

Primary Shedding (cavity center)

The primary shedding originated at the collision region in the center of the sheet, see figs. 5.11.5-5.11.12. However, only a portion was broken off from the main sheet and advected with the flow. Most of the cavity remained attached. This shed structure could be seen to roll up quickly in figs. 5.11.5-5.11.8 by self-induction into a hairpin vortex. This structure grew significantly in height, on the order of the cavity length (Foeth *et al.* 2006). The cavity closure after the cut-off of the hairpin vortex was temporarily turbulent—shedding a large cloudy structure—but reattached smoothly shortly thereafter. In order to visualize the re-entrant flow more clearly, a series of additional images of the transparent hydrofoil is presented in figs. 5.14 & 5.15. The cavitation is filmed through the pressure side of the transparent hydrofoil showing the internal flow structure of the cavity. The radially diverging re-entrant flow is clearly visible in fig. 5.14 (denoted as A) as waves on the jet surface reflected the laser light.

The re-entrant flow directed upstream in a two-dimensional situation would be constrained in its lateral movement. The vapor interface at the leading edge was not visibly disturbed upon contact with this re-entrant flow; its apparently low momentum did not lead to immediate shedding. As the side-entrant jets were aimed at the closure, it was here that the fluid first impinged on the interface. Therefore, the main cause for the detachment of the main structure was the side-entrant jet and not the re-entrant jet.

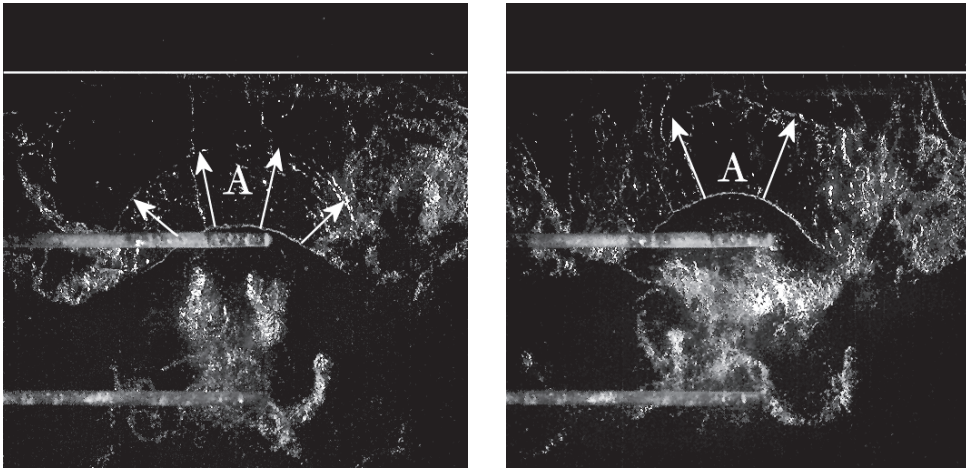


Figure 5.14 The re-entrant flow was filmed through a transparent hydrofoil, corresponding approximately to figs.5.11.7-5.11.10. The images show the re-entrant jet after cleaning up the pictures (despeckle, color & histogram enhancement). These figures show the radially diverging re-entrant jet (A) emanating from the center of the foil at two different shedding cycles as sketched in fig. 5.17. The two horizontal lines are holes for ink injection (not presented)

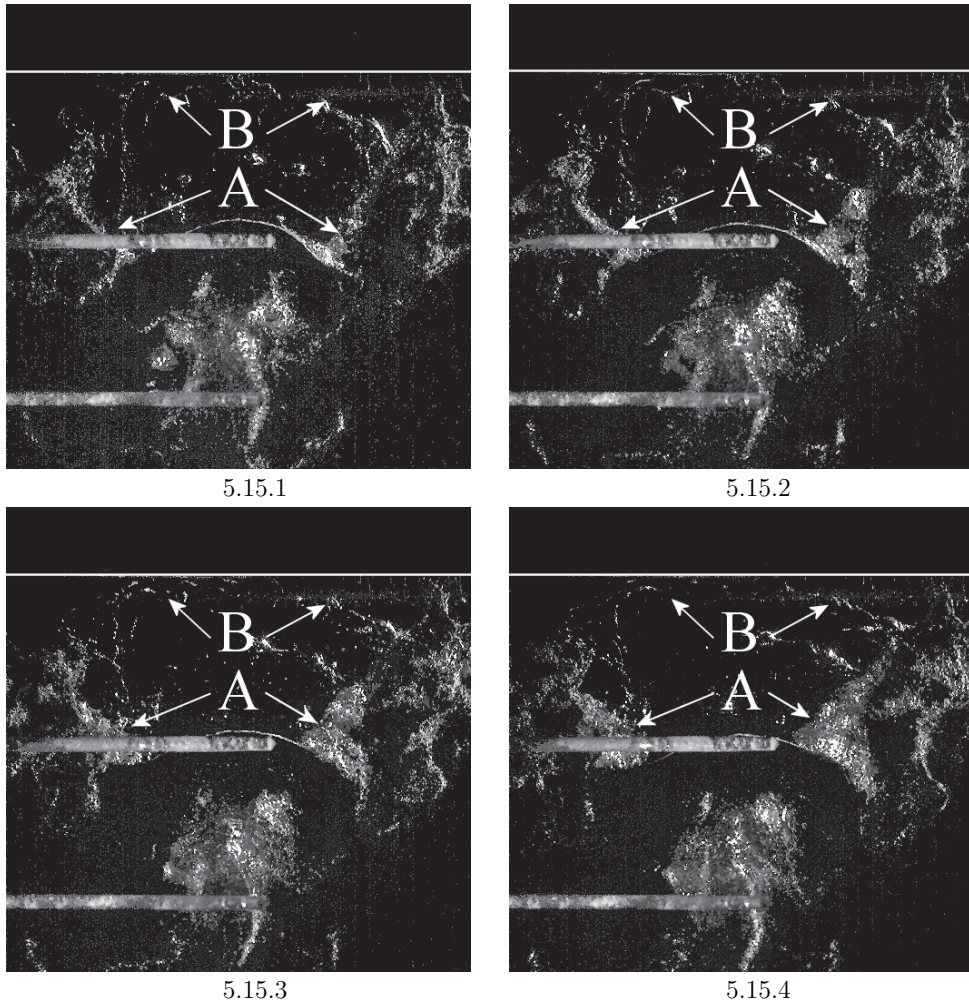


Figure 5.15 This series shows the cavity at the end of its secondary shedding corresponding to figs 5.11.15-5.11.17. The side-entrant jet is seen to develop at both corners of the sheet (A) as visualized in fig. 5.18. The re-entrant jet is visible near the leading edge (B)

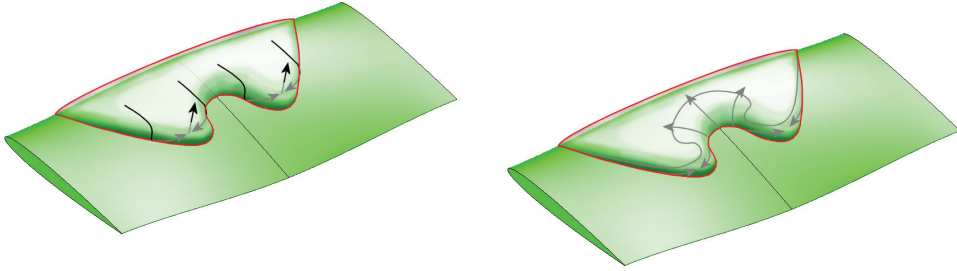


Figure 5.16 The streamlines at the side planes in the concave part are partly directed away from the central plane, corresponding to fig. 5.11.7-5.11.8

Figure 5.17 Observed direction of re-entrant flow in fig. 5.16 converging in the lobes causing a second pinch-off

Secondary shedding (cavity sides)

The remaining topology of the sheet closure line in figs. 5.11.5 to 5.11.12 was concave. The locally convex regions of the cavity are seen to shed a series of larger vortices, followed by a turbulent flow region. From observation, the secondary shedding greatly resembled the primary shedding. The secondary shedding disappeared when the closure was no longer concave.

The re-entrant flow direction in the center was still directed radially outward after the shedding of the first cloudy structure. The main side-entrant jets and radially diverging re-entrant jet were now converging in both downstream lobes of the remaining cavity shape (fig. 5.16 & 5.17). The secondary shedding was caused by the collision of these two flows. Basically, the main shedding as visible on figs. 5.11.5-5.11.12 was repeated at both sides of the central plane as visible in figs. 5.11.9-5.11.18.

After the secondary shedding the remaining cavity had a near-convex shape with two concave regions, denoted H in fig. 5.18, corresponding to fig. 5.11.18. From these regions the re-entrant flow entered the cavity sideways, similar to the re-entrant flow in fig. 5.17 after the primary shedding. The re-entrant flow from the closure of the cavity at the midplane and from the sides on the cavity—denoted B and C, respectively, in fig. 5.18—remained present and collided with the side-entrant jets from H. Figure 5.15 shows this situation on the transparent hydrofoil. The movement of the front of the side-entrant flow (A) from these regions at fig. 5.18-H can be seen, as re-entrant flow forced into the cavity collided with re-entrant flow from the plane of symmetry (B) and a frothy turbulent region was created upon impact at the lower corners. At the outer side, a continuous mixing is

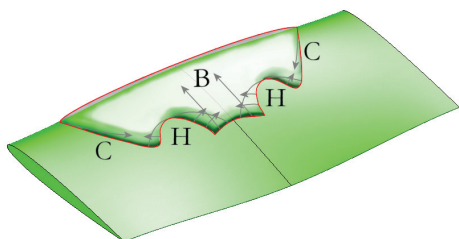


Figure 5.18 The streamlines at the side planes in the concave part are partly directed away from the central plane. Corresponding to figs 5.11.15-5.11.17.

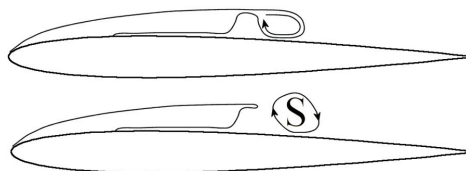


Figure 5.19 Side-entrant jets converge in the closure region and cut off the first vortical structure. The remaining cavity closure is now "open".

observed as re-entrant flow from the main flanks of the cavity (5.18.C) continued to collide with the re-entrant flow from (H). No large-scale shedding was observed at this point of the shedding cycle, as with each subsequent shedding the scale and hence total jet momentum decreased, while the inflow and its momentum from the sides of the cavity remained constant. Without any further major disturbances allowing for a sheet topology change in the closure region, the cavity grew back into its original convex shape and side-entrant jets at the central plane collided once again repeating the process. The cavity never reaches a constant length.

The shedding of the sheet cavity in the three-dimensionality case is similar to a two-dimensional shedding, having its origin as a disturbance of its interface, except that the disturbance occurs at the aft part of the sheet. The fluid impinging on the interface isolates a region of vapor as sketched in fig. 5.19. If the interface is considered a streamline with a tangential velocity $V_V = V_0\sqrt{1 + \sigma}$, it is immediately apparent from contour integral of that velocity over the boundary of S , that circulation is detached and advected with the flow. The re-entrant flow may continue upstream and cut off a next structure, leading to a cascade type of break-up. The impingement and detachment of the vapor structures appears to be inertial in nature. This agrees with work by Stutz (2003) who concluded that roughness of the hydrofoil surface did not influence shedding behavior on attached cavitation. If the re-entrant flow does not cut off a subsequent vapor structure from the cavity closure, a contact surface between the main sheet interface and impinging fluid forms a mixing layer, leading to a continuous shedding of small cavitating vortices.

5.2.3 The Twist-11E hydrofoil

The Twist-11E utilizes the Eppler & Shen YS-920 section (Shen 1985), which has a near-constant pressure distribution over the first 80% of its chord at a modest angle of attack at both suction and pressure side (see fig. 5.20), specifically designed to delay cavitation inception. Once below its critical σ , cavitation will quickly cover the entire low-pressure plateau. This hydrofoil is chosen for its expected thin cavity and with a weak pressure recovery in the closure region of the attached cavity, leading to a weak re-entrant jet and strong sensitivity to the flow oscillator.

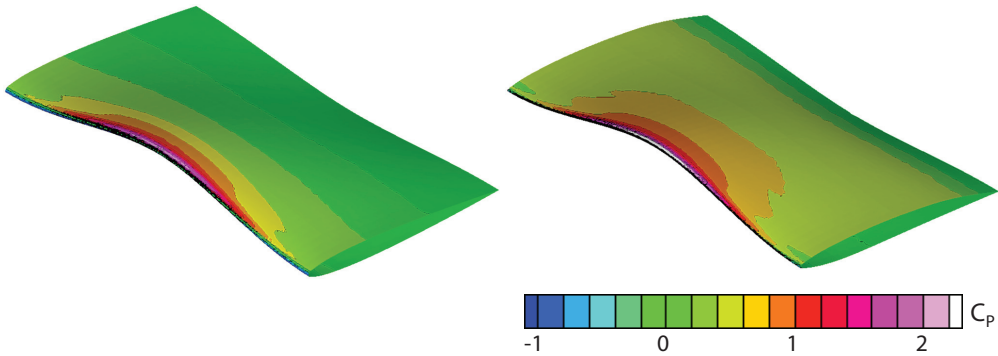


Figure 5.20 Pressure distributions on the Twist-11N (left) and Twist-11E (right) at $\alpha = 1^\circ$ from an Euler-based calculation. The low pressure plateau on the Twist-11E is clearly reflected in the plot. Calculations by Koop *et al.* (2006).

The Twist-11E is shown cavitating at an angle of attack of $\alpha = -3^\circ$ in fig. 5.21 in steps of 50 *ms*. The extent of the sheet cavity is more narrow and more concentrated than the cavity on the Twist-11N hydrofoil at similar conditions, as is expected from the more uniform pressure distribution of the Twist-11E. What is remarkable for a cavity of this length (75% chord) is that for the images presented there is no change in the cavity topology and that large structure shedding does not occur. This cavity is steady. As intended by its design, the side-entrant flow is directed in the closure region where the shedding of small-scale cavitating vortices can be observed. Due to its elongated shape, the side-entrant jets are now directed entirely into the close region (fig. 5.22), barely folding around the edges. The interface at the center of the cloud is visibly turbulent.

afterpage

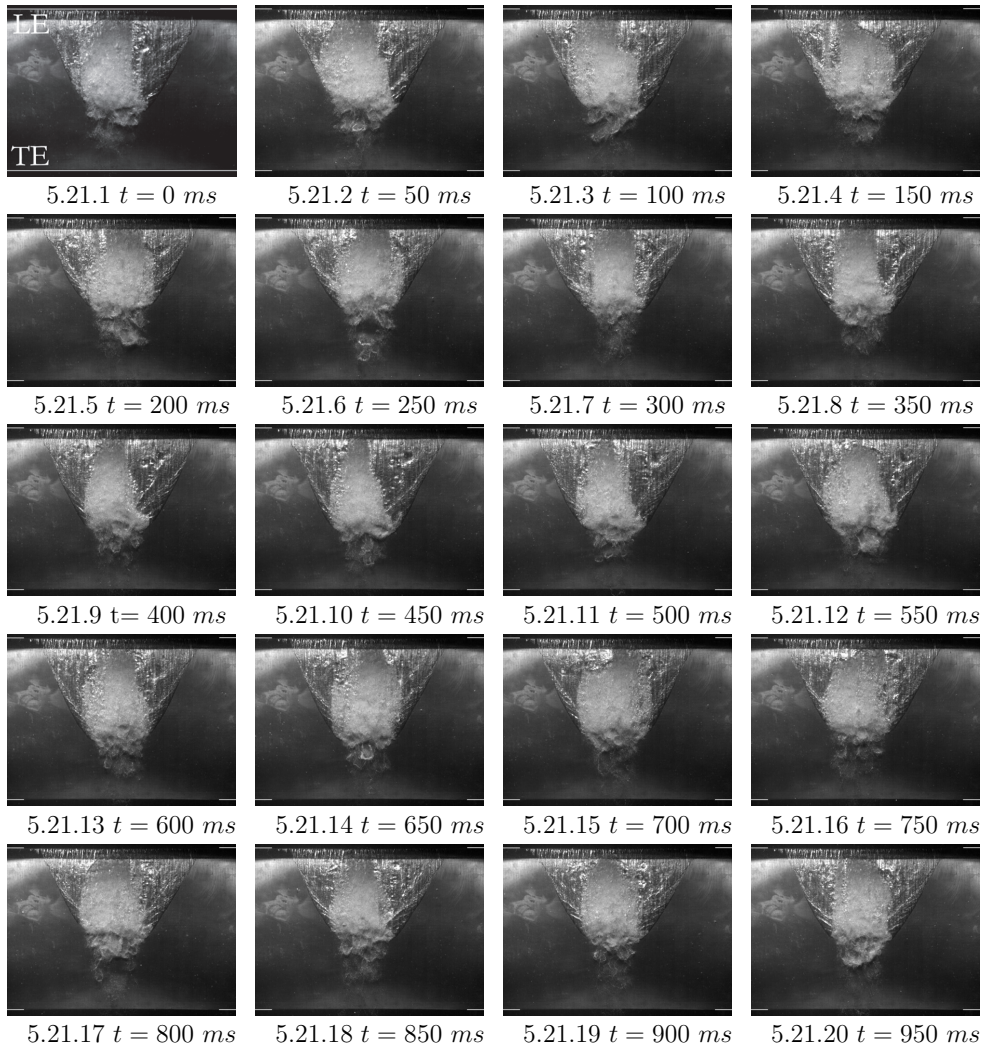


Figure 5.21 The Twist-11E hydrofoil at $\alpha = -3^\circ$, $V_0 = 6.6 \text{ m/s} \pm 4.1\%$, $\sigma = 0.75 \pm 7.8\%$, steady-inflow conditions. The twenty images shown were taken at 50 ms intervals. Note that the major part of cavity was stationary and its topology constant. Some variation in location of the turbulent interface is observed and small-scale vortices were continuously shed in the closure region.

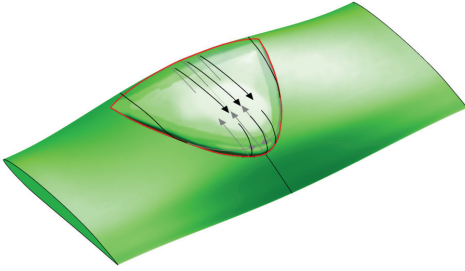


Figure 5.22 Streamlines over and inside the cavity on the Twist-11E

Figure 5.23 Cavity outline as experimentally determined (conditions as in fig. 5.21)

Due to the elongated shape, the region where the re-entrant jet is formed is narrow and is continuously disturbed by the side-entrant flow. The momentum of the jet flowing upstream is small. It can be concluded that the origin of the turbulent flow region on the otherwise-glassy sheet interface was caused by the re-entrant jet impinging on the interface. Its presence is inconsequential as far as main structure shedding is concerned. If the attached cavity is steady and the re-entrant flow is directed upstream, re-entrant flow must be advected out of the cavity. As sketched in fig. 5.22, the re-entrant jet is recirculated over the sheet interface (this is presented more clearly in 5.3.2). On the Twist-8N and Twist-11N hydrofoils, the re-entrant jet was concluded not to be the main cause of the shedding. For the Twist-11E it is observed that the re-entrant jet hitting the leading edge of the sheet is an insufficient condition for the detachment of the attached cavity. When the loading of the hydrofoil was increased by changing the angle of attack from $\alpha = -3^\circ$ to $\alpha = -1^\circ$ and to a σ leading to a similar cavity planform, the cavity thickness was increased and the periodic shedding behavior appeared.

The results from the PIV measurements were used to reconstruct the cavity interface as it changed in time, see fig. 5.25 where a period of 0.1 s is presented. The image shows that the sheet thickness distribution was clearly constant during the measurements, as was clear from the visualizations in fig. 5.21. Disturbances are present on the interface as the re-entrant jet is recirculated, visible as perturbations on the cavity surface traveling downstream. A close-up is presented in fig. 5.24. The velocity is estimated to be equal to the fluid velocity at the cavity interface, or $V_V = V_0\sqrt{1 + \sigma}$ and drawn as the line A. In an attempt to estimate the wave length of surface tension waves on the interface a brief Kelvin-Helmholtz instability analysis is presented in appendix J. This leads to leading to a theoretical wave length of approx. $\lambda = 1.71 \text{ cm}$. This wave length is drawn at four location, connecting a few wave crests, and shows good agreement but this correlation may

be entirely fortuitous. For this predicted wave length follows that the velocity difference between liquid and vapor at the interface is zero to be stable. Note that when the disturbances reach the end of the cavity at B , they coincide with small cavitating vortices that are shed at the closure of the sheet (with two examples at C).

The second image in fig.5.25 shows a velocity isosurface rendered at 99% of $V = V_0\sqrt{1+\sigma}$, indicating that the velocity $V = V_0\sqrt{1+\sigma}$ is present over the entire attached cavity.

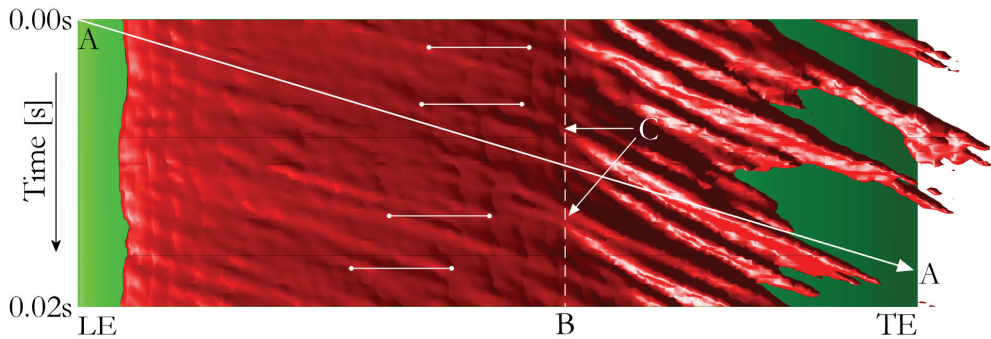


Figure 5.24 Top view of the attached cavity corresponding to the conditions fig. 5.21 in with the leading edge at left, time progressing from top to bottom for a period of 0.02s. Small disturbances travel downstream on the cavity surface along the line AA , with a velocity $V_V = V_0\sqrt{1+\sigma}$. Note that when the disturbances reach the end of the cavity at B , they coincide with the shedding of small cavitating vortices traveling at roughly half the speed (with two examples at C).

5.3 Shedding behavior at unsteady inflow conditions

5.3.1 The Twist-11N hydrofoil

The response of the cavity to the periodically changing inflow has been investigated on the Twist-11N, Twist-11E, and Twist-14N hydrofoils. The frequency of the flow oscillator was varied at a constant amplitude at several angles of attack of the Twist hydrofoils and several values of σ . The location of the cavity interface was determined from the PIV images as described in section 4.2.5.

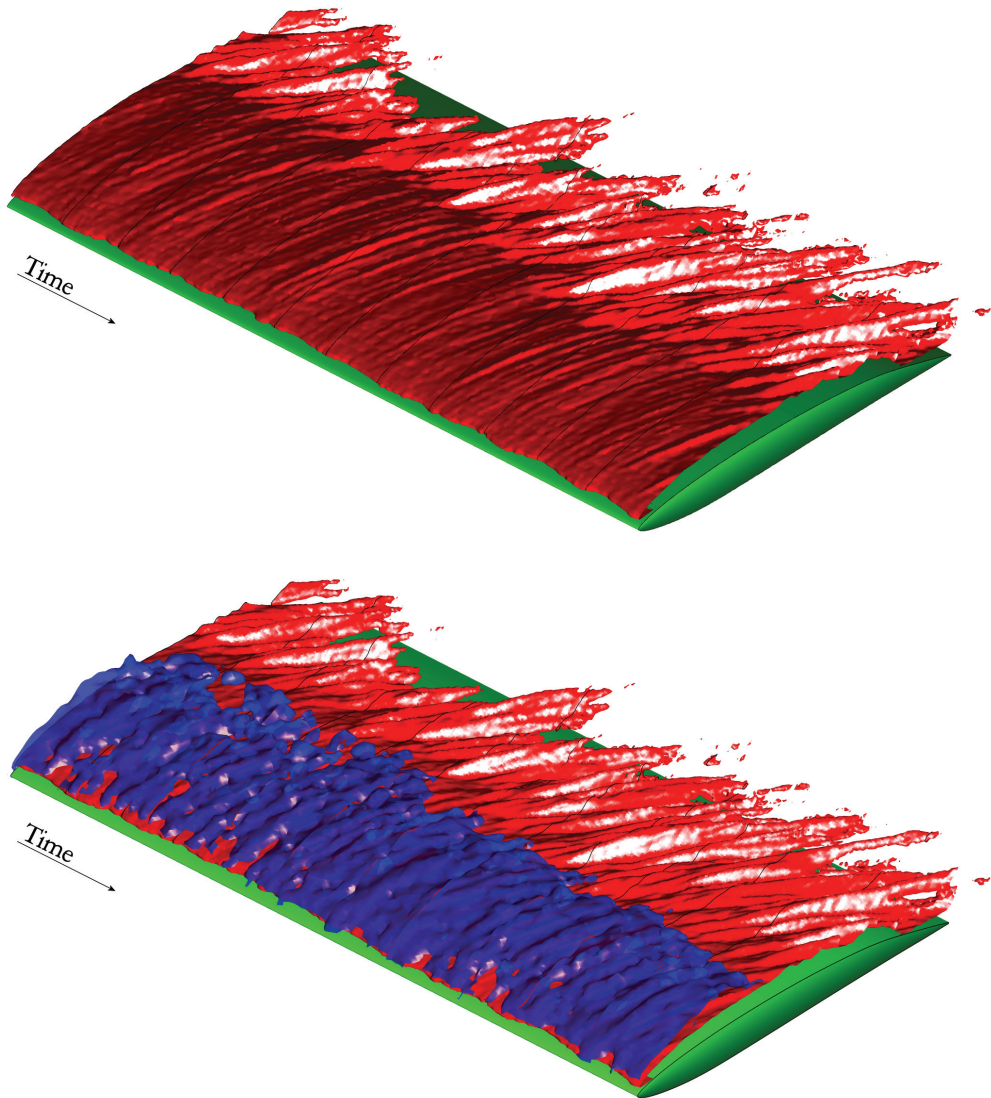


Figure 5.25 Three-dimensional reconstruction of the vapor-interface outlines (as determined as in App I) of the Twist-11E at $\alpha = -3^\circ$, $V_0 = 6.69 \text{ m/s} \pm 4.0\%$, $\sigma = 0.76 \pm 7.6\%$ (similar to fig. 5.21) during a period 0.1 s , time from left to right. The top image presents the cavity interface and shows that the cavity interface is stationary and is only shedding vortices at its closure. The result of the re-entrant flow impinging on the leading edge can be seen as perturbations traveling downstream on the interface. The bottom image has an isovelocity surface drawn at 99% of $V = V_0\sqrt{1+\sigma}$ (blue). The isosurface shows signs of flow turbulence as well as the disturbances are seen to travel downstream. For stationary situations, the boundary condition that $V = V_0\sqrt{1+\sigma}$ on the interface is valid for the attached cavity.

Results for the Twist11-N hydrofoil at an angle of attack of $\alpha = -2^\circ$ and at a default value of $\sigma = 1.11$ and $V_0 = 6.6-6.9 \text{ m/s}$ are presented in figure 5.26. In this figure, a three-dimensional top view of the cavitation visualization is given together with the oscillator position. The natural shedding frequency of the cavity was determined at the oscillator frequency $f_{FO} = \pm 32.55 \text{ Hz}$. From the visualization, it is apparent that the cavity is regularly shedding large structures.

At lower oscillator frequencies (figs. 5.26.2-3), the general cavity volume was clearly seen to fluctuate with the oscillator frequency, as the cavity length depended directly on the position of the flow oscillator. This situation was clearly quasi-steady only. From figs. 5.26.3 to 5.26.10, the oscillator frequency steadily approached $f_{FO} = 32 \text{ Hz}$. From fig. 5.26.09 onward, the shedding is fully locked-in at $f_{FO} = 24 \text{ Hz}$ with the flow oscillator frequency and its intrinsic behavior at $f_{FO} = 32 \text{ Hz}$ is fully suppressed.

This lock-in behavior was observed at all observed angles of attack and for all three hydrofoils. An increase in the phase between the cavity shedding and oscillator position was observed as the frequency increased. This is similar to the measured frequency-dependent phase delay between the lift of the Twist-14N and flow oscillator deflection angle (fig. 3.16). The maximum lift was measured prior to the cavity shedding its main structure (from the leading edge onward). This is expected because when part of the cavity is cut off from the main cavity, circulation is advected with the flow resulting in a direct decrease of the bound circulation of the hydrofoil. Hence the decrease in lift.

Harmonic analysis of the outlet-plane pressure signal showed that the dominant frequency in the outlet-plane pressure was within 0.1% of the flow oscillator frequency for both $f_{FO} = 28 \text{ Hz}$ and $f_{FO} = 32 \text{ Hz}$, confirming the lock-in of the shedding occurs for frequencies below the natural shedding frequency. When the cavitation was shedding irregularly or at non-cavitating conditions, the measured frequency of the outlet-plane pressure was between 43.5 Hz and 48.0 Hz , close to the tunnel drive impeller's blade passage rate at 46.7 Hz . This indicates that the shedding frequency modulates with the position of the flow oscillator as the cavity length and hydrofoil loading change quasi-statically (figs. 5.26.2-3).

From these observations it can be concluded that the shedding behavior of the cavity is sensitive to the flow oscillator and reacts strongly to the periodically changing inflow. The shedding frequency will lock in to the incoming flow variations if the frequency of the inflow variations approaches the natural shedding frequency. This forced sheet cavitation shedding is directly coupled to the incoming flow and will suffer no modulation in shedding frequency or phase, such as was observed at natural cavitation shedding in a uniform flow. With the dominant flow features under control, the forced shedding is repeatable and therefore more suited for validation purposes. Small scale instabilities observed in the closure region of the cavity occur on a much faster time scale and were not affected by the oscillator.

In fig. 5.27 two views of a three-dimensional rendering show the shedding of a sheet cavity during a period of 0.1 s. Although the interface shows periodicity, it also shows a large variation in its details, such as the vortex shedding in the closure region. The ensemble averaged data—fig. 5.28—does not show these variations. The shed structure and closure region captured by the ensemble-averaged cavity outline encompasses all variations of the shed structures of many shedding periods and therefore overestimates the shed volume. Note that in each individual frame the captured cavity outline itself is an envelope of vapor or a liquid-vapor mixture (see App. I where an example is given using the data as presented in fig. 5.28). The shedding is not the solid vapor structure suggested by the renderings.

Nevertheless, the attached cavity prior to shedding is a 'solid' vapor structure and repeatable from cycle to cycle. The ensemble averaging removed the variations due to turbulence in the incoming flow or disturbances caused by the re-entrant flow impinging on the interface. Clearly, the quality of the cavity outline and velocity measurement is improved by the ensemble averaging.

5.3.2 The Twist-11E hydrofoil

A full oscillation cycle is given in fig. 5.29 of the Twist-11E hydrofoil at $\alpha = 3^\circ$, $V_0 = 6.59$ m/s, $\sigma = 0.743$ with the flow oscillator was at $f_{FO} = 31.69$ Hz. The first image coincides with the neutral position of the oscillator and the cavity length was smallest. The cavity was longest when the lift was at the beginning on its oscillation period (i.e., zero up-crossing). The lift and cavity length were nearly $\pi/2$ rad out of phase. The closure region of the cavity was turbulent during the entire shedding period. The sheet interface was not always turbulent. The cavity was seen to be glassy in fig. 5.29.17-5.29.20 when the cavity was receding in length as the loading of the foil decreased. During this period, the re-entrant jet was not visibly present, but reappeared when the cavity length was at its minimum, fig. 5.29.1-5.29.4. The cavity shed a larger structure when its growth stagnates around fig. 5.29.13-5.29.16. This structure appeared to be similar to the primary shedding on the Twist-8N hydrofoil, caused by the collision of side-entrant flow. For the Twist-11E, a rebound in the vortex collapse could be observed.

The side-entrant flow remained focused into the cavity closure during the entire shedding, as it did on all Twist hydrofoils. Only the central region was visibly turbulent. A sequence of close-ups of the re-entrant jet reaching the detachment point of the attached cavity is given in fig. 30. The re-entrant jet was seen to move toward the leading edge and leave a turbulent streak on the interface upon contact. It did not lead to shedding. As for the stationary condition, the re-entrant flow was advected over the cavity interface. Liquid was observed on the hydrofoil surface on either side of the turbulent region, creeping slowly forward. The velocity of this near-stationary liquid was clearly well below the velocity $V_V = V_0\sqrt{1 + \sigma}$ one would prescribe using potential flow boundary conditions.

A similar condition to that of fig. 5.29 is measured using PIV. The interface and a velocity isosurface at 99% of $V_V = V_0\sqrt{1+\sigma}$ is given in fig. 5.31. In contrast to the results for the Twist-11N hydrofoil (fig. 5.27) the (blue) velocity isosurface scarcely covers the sheet. As the Eppler hydrofoils have a uniform pressure distribution over most of their chord, the cavity length reacts strongly with lift variations. It is hypothesized that the unsteady flow behavior is responsible for the velocity attaining a lower value on the interface. The ensemble averaged data and three (identical) shedding periods are presented in fig. 5.32. From this side view it is apparent that the shed structure increases in height from the leading edge. On average, the velocity on the interface is lower than 99% of $V = V_0\sqrt{1+\sigma}$ as can be concluded by the absence of the (blue) velocity isosurface. Similarly to the results of the ensemble-averaged data for the Twist-11N, the ensemble-averaged cavity location of the Twist-11E hydrofoil is a vapor envelope and less precise due to variations in the location of the shed vortices of individual sheddings.

A central plane frame corresponding to fig. 5.29.19-5.29.20 is isolated from the PIV series and presented in figs. 5.33 to 5.36. The shed vortical structure—visible in figs. 5.29.13-5.29.16 rolling up into a hairpin vortex—is close to its collapse, so it is nearly devoid of vapor and about to pass the trailing edge of the hydrofoil. Figure 5.33 shows the raw PIV frame. The shed structure—as visible in figs. 5.29.13-5.29.16—is denoted as A . The cavity length is shortest at this time instance and the closure of the attached cavity is denoted B . Most of the vaporous vortices shed by the receding cavity can be seen as vapor downstream of B , as well as PIV tracer particles.

After filtering out all vapor, the result—minus the incoming flow velocity—is given in fig. 5.34. The wake of the flow oscillator is visible in the top half of the vector field. Note that even at an oscillator frequency 32 Hz the wake does not yet show any rolling up within the field of view. It is stressed that all gaps in the velocity field have been filled either by interpolation or by extrapolation, including the gap left by the sheet cavity. A vortical motion is identified at A . Note that for the proper localization one should subtract the traveling velocity of the vortex core and not the inflow velocity (Adrian *et al.* 2000) but the location of the vortex is generally sufficiently correctly determined. A strong induced velocity from the vortex—rolled up into a hairpin vortex—is measured below A , on the order of an upstream velocity 5 m/s near the foil surface. The region below the core of the vortex and upstream of the upwash, C , has a larger-than-average out-of-plane component, as can be concluded from the loss of most particle pairs. The correlation map of the PIV interrogation deteriorated significantly in the area and most vectors were spurious. For nearly all PIV results, the region of high induced velocity due to the presence of the vortical structure showed many erroneous vectors. By applying more strict vector selection parameters during post-processing² these vectors can be removed. This inherent

²Increasing the minimum required ratio of the first to second peak value within the correlation map and/or removing vectors with 1 STD of their neighbors without reinserting a second or third choice vector

error is apparently caused by the velocity of the hairpin vortex induced in the direction perpendicular to the plane of observation resulting in the loss of particle pairs. The erratic behavior of the PIV flow measurement near C was not observed near B .

Figure 5.35 shows a plot of the vorticity perpendicular to the measurement plane. Regions of high vorticity are found near the vortex at A , in the region with many spurious velocity vectors C and in the wake of the attached cavity. The receding cavity is known to shed vortices (D), but one has to keep in mind that the size of a PIV interrogation window is large compared with these vortices. A trail of vorticity is seen in the wake of the flow oscillator (E).

Figure 5.36 shows the local Okubo-Weiss parameter (eq. 2.81). Strongly negative values of the parameter are found at the location of the regions of high shear, suggesting or confirming that the regions of high vorticity are a vortex structure. No other regions of high shear were found in the closure of the attached cavity for the Twist-11E. As the current experiments only capture the height of the cavity within three or four interrogation windows, the small vortices in the wake of the cavity closure are not captured by the resolution of the measurements of the current work.

5.4 Discussion

From the experiment investigations with the three-dimensional cavities follows that re-entrant flow from the sides dictates the behavior of the shedding cycle. The re-entrant flow from the sides depends on the cavity shape. Thus, the cavity topology largely dictates the re-entrant flow direction.

The convex cavity planform leads to converging re-entrant flow and that flow convergence leads to shedding in the cavity closure region. Re-entrant flow was observed to reaching the leading edge did not result in shedding. The re-entrant flow can be moving both upstream and in spanwise direction. The spanwise component of the re-entrant flow is denoted as the side-entrant jet. For any convex cavity shape, the side-entrant components of the re-entrant jet converge in the closure region of the sheet, creating a disturbance that causes local break-off of the aft part of the main sheet structure. This converging of side-entrant flow is suggested as a second shedding mechanism for attached sheet cavitation, in addition to the well-known mechanisms of re-entrant flow impinging on the cavity interface near or on sheet cavity detachment point. The cause of the shedding is the same: impingement of a high-momentum flow on the surface of the hydrofoil on the cavity interface.

With a convex cavity closure line, side-entrant jets converge in the cavity closure region leading to a pinch off of the aft part of the cavity. The observed (cavitating) vortices in the wake of the remainder of the attached cavity are similar to the spanwise and streamwise vortices in a planar mixing layer. It is concluded that the wake of an attached cavity

shedding small-scale vortices is in fact a mixing layer with its characteristic wake structure. Thin cavities have a smooth pressure recovery zone in the cavity closure region generating re-entrant flow with a minimum of momentum. These cavities typically shed small vortices at their closure region. The collision of side-entrant jets of thick cavities of a large length (near 100% chord), can form a continuous disturbance leading to continuous shedding of vortices, preventing the shedding of large cavity structures.

For all observed shedding mechanisms—from full-length cavity shedding, to local sheet break-off due to re-entrant flow impingement on the cavity interface, and eventually the mixing layer on the liquid-vapor interface due to re-entrant flow disturbances—the basic mechanism is sheet cavity interface impingement. The scale of the shedding is determined by the topology of the re-entrant flow.

For the Twist-11E hydrofoil with a near-constant pressure distribution on the suction side—using the Eppler YS-920 section—, a long and slender cavity was created, covering 70% of the chord at the mid plane, and that was relatively thin at moderate angles of attack. The slenderness of the cavity resulted in side-entrant jets continuously aimed toward the closure region in the central plane resulting in the shedding of small cavitating vortices. The thin cavity has a weak re-entrant flow that did not disturb the sheet cavity upon contact at the leading edge. The re-entrant jet that impinged on the cavity interface was advected with the flow over the cavity interface, so that the cavity was stable in length for the entire observed period. From the investigations of the Twist-8N and Twist-11N hydrofoils it could be concluded that the side-entrant jets could form an equally important mechanism of sheet instability. From these observations it follows that impingement of a re-entrant jet at the cavity streamline detachment point itself is an insufficient condition for shedding. This did not change for unsteady inflow conditions as the leading edge was visibly cavitating during the entire shedding period, although the scale of shed vortices did increase for lower cavitation numbers. The steady behavior of the cavitating flow around the Twist-11E hydrofoil disappeared when the angle of attack was increased from $\alpha = -3^\circ$ to $\alpha = -1^\circ$, leading to a shedding behavior similar to that observed for both the Twist-8N and Twist-11N hydrofoils. Apparently, by increasing the angle of attack and thus the cavity thickness, the resulting increase in the pressure in the closure region at a higher angle of attack increased the re-entrant jet momentum sufficiently to cause large-scale shedding of the attached cavity.

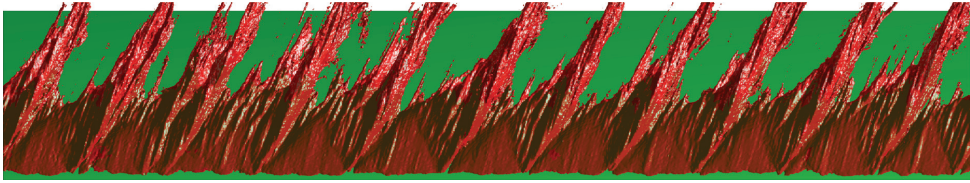
For a hydrofoil with a given pressure distribution, the cavity topology determines the direction and momentum of the re-entrant flow and that re-entrant flow determines the shedding behavior of the cavity. In order to accurately predict the shedding behavior, to eventually predict the risk of cavitation erosion, the re-entrant flow must be predicted accurately.

Quantitative analysis of the flow by means of PIV measurements showed that regions of high vorticity appear at the expected location of shed vortices—as found on the high speed video—and the Okubo-Weiss parameter confirmed the existence of vortices in these regions. The experiments in the present were aimed at resolving the whole flow field. Therefore the

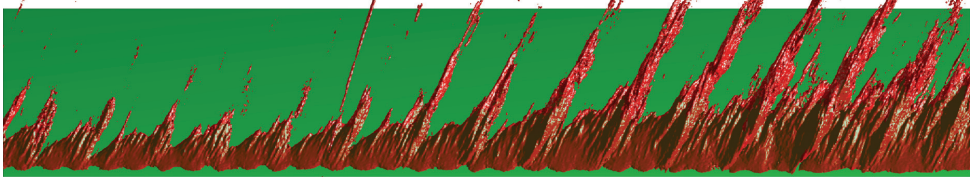
magnification was insufficient to resolve the closure of the cavity. No appreciable vorticity was measured at locations other than a vortex. The velocity at the interface of the attached cavity was measured to be $V_V = V_0\sqrt{1 + \sigma}$.

The shedding mechanism of the cavity is inertial in nature, so viscosity most likely plays a minor role. Stutz (2003) indicated that the shedding behavior of attached cavitation was insensitive to the roughness of the hydrofoil surface. However, Coutier-Delgosha *et al.* (2005) observes a notable dependency of the cavitation length and shedding frequency of the attached cavity on a plano-convex hydrofoil for an equivalent roughness of the surface of 100 to 400 μm , but only when their smooth hydrofoil was shedding large structures and not for light loadings. Apparently, only when both the re-entrant jet momentum and surface roughness is large can the behavior be affected by the excessive surface roughness. Roughness elements in the range of 100 to 400 μm are much thicker than the viscous sublayer of the boundary layer. Full-scale propellers—operating at higher Reynolds numbers—have an equivalent roughness of 20 to 30 μm so that the effect of roughness of the blade surface of the cavity does not effect the re-entrant jet or the shedding behavior.

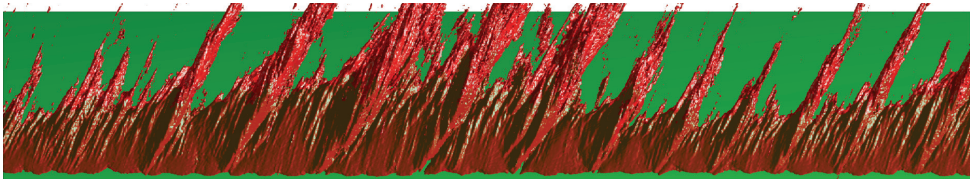
The alternating shedding seen on the hydrofoils results in a distinct cycle. However, the two-dimensional hydrofoil lacks the spanwise variation in pressure distribution in the center, resulting in the seemingly random local shedding along its cavity closure. Any disturbance at its closure will redirect the re-entrant flow into converging side-entrant flow resulting in local shedding. The two-dimensional cavity has a highly three-dimensional structure making it more difficult to study, either numerical or experimental, with re-entrant flow constantly changing direction and continuously converging in other locations along the span. The three-dimensional cavity is shown to have a repeatable collapse making it a more proper candidate for numerical validation studies of cloud shedding. The shedding frequency shows minor variations in time, variations that are smaller when the cavity is excited by an oscillating inflow with a frequency close to or larger than the natural shedding frequency of the cavitating hydrofoil.



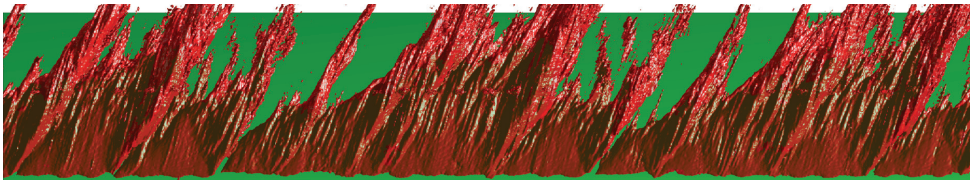
5.26.2 $f_{FO} = 0 \text{ Hz}$, $V_0 = 6.83 \text{ m/s}$, $\sigma = 1.11$



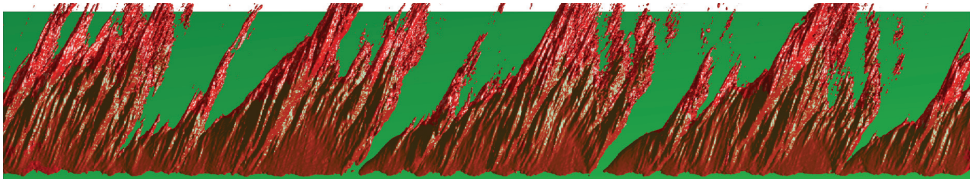
5.26.3 $f_{FO} = 1.96 \text{ Hz}$, $V_0 = 6.58 \text{ m/s}$, $\sigma = 1.28$



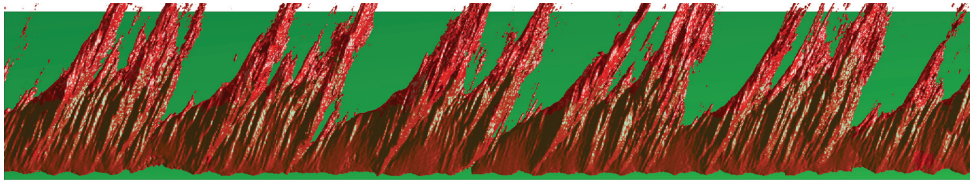
5.26.4 $f_{FO} = 3.89 \text{ Hz}$, $V_0 = 6.82 \text{ m/s}$, $\sigma = 1.14$



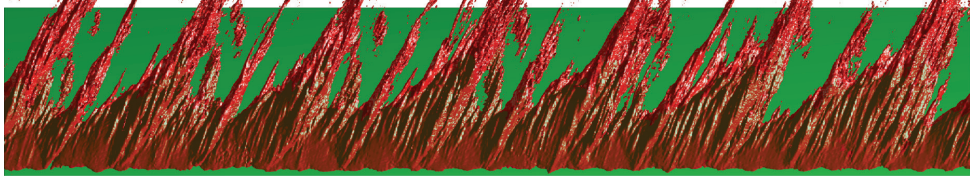
5.26.5 $f_{FO} = 7.88 \text{ Hz}$, $V_0 = 6.93 \text{ m/s}$, $\sigma = 1.09$



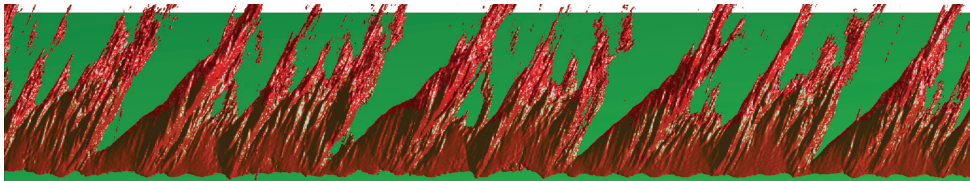
5.26.6 $f_{FO} = 11.94 \text{ Hz}$, $V_0 = 6.64 \text{ m/s}$, $\sigma = 1.23$



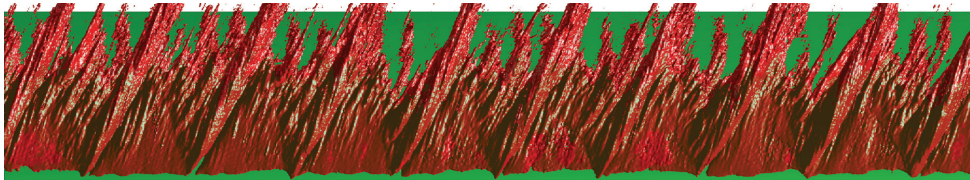
$$5.26.7 \quad f_{FO} = 15.89 \text{ Hz}, V_0 = 6.72 \text{ m/s}, \sigma = 1.18$$



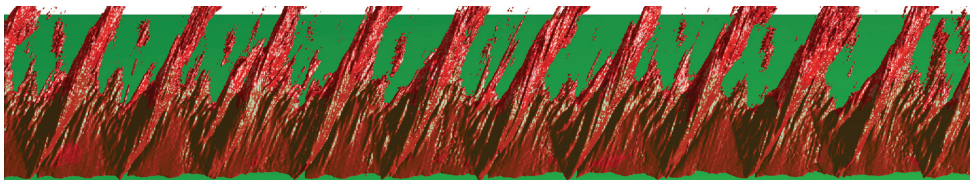
$$5.26.8 \quad f_{FO} = 19.84 \text{ Hz}, V_0 = 6.79 \text{ m/s}, \sigma = 1.15$$



$$5.26.9 \quad f_{FO} = 23.77 \text{ Hz}, V_0 = 6.59 \text{ m/s}, \sigma = 1.26$$



$$5.26.10 \quad f_{FO} = 27.71 \text{ Hz}, V_0 = 6.96 \text{ m/s}, \sigma = 1.06$$



$$5.26.11 \quad f_{FO} = 31.48 \text{ Hz}, V_0 = 6.93 \text{ m/s}, \sigma = 1.09$$

Figure 5.26 Top view of the development of cavitation on the Twist-11N hydrofoil at $\alpha = -2^\circ$ at increasing flow oscillator frequencies $1.06 < \sigma < 1.28$. Flow from bottom to top, with time progressing from left to right for a period of 0.3417 s . The influence of the flow oscillator (the black sine) is seen to affect the shedding of the attached cavitation.

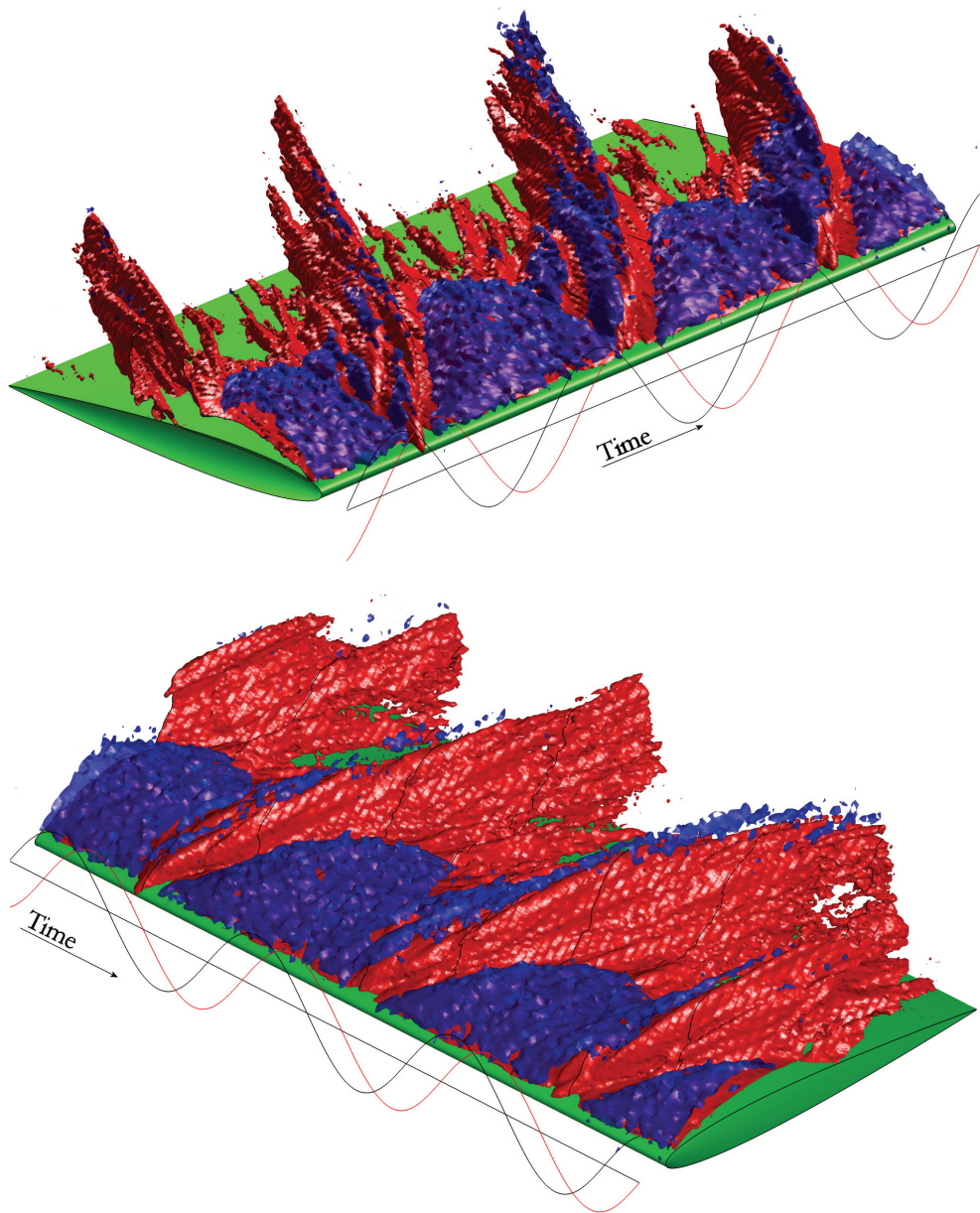


Figure 5.27 Cavitation development (red) in time at the midplane of the Twist-11N hydrofoil at $\alpha = -1^\circ$, $V_0 = 6.9 \text{ m/s} \pm 3.9\%$, $\sigma = 1.26 \pm 6.5\%$, $f_{FO} = 31.64 \text{ Hz}$. Velocity isosurface (blue) drawn at 99% of $V = V_0\sqrt{1 + \sigma}$, clearly covering the entire attached cavity between sheddings. The black sine indicates the flow oscillator's position, the red line the variation of the hydrofoil lift force (no scale). The lift has its maximum just before the cavity sheds its primary structure.

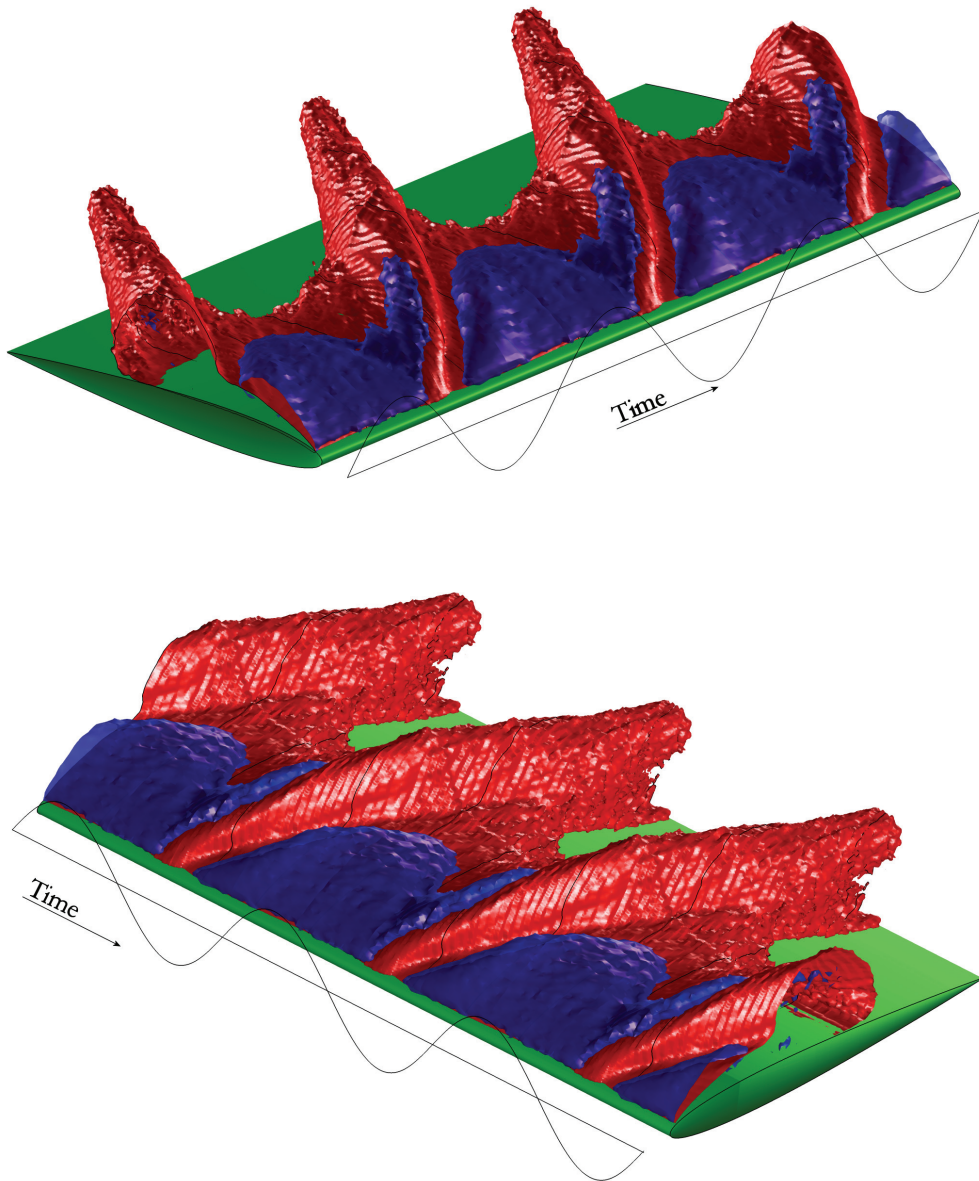


Figure 5.28 Cavitation development (red) in time at the midplane of the Twist-11N hydrofoil at $\alpha = -1^\circ$, $V_0 = 6.9 \text{ m/s} \pm 3.9\%$, $\sigma = 1.26 \pm 6.5\%$, $f_{FO} = 31.64 \text{ Hz}$, showing three periods of ensemble-averaged data. The cavity is a coherent structure showing a more pronounced repeatability when compared with the unaveraged data. Fluctuations on the cavity interface and velocity isosurface average out, only the main structure remains present. The turbulent closure region—showing more variation between sheddings—averages out to a vapor envelope.

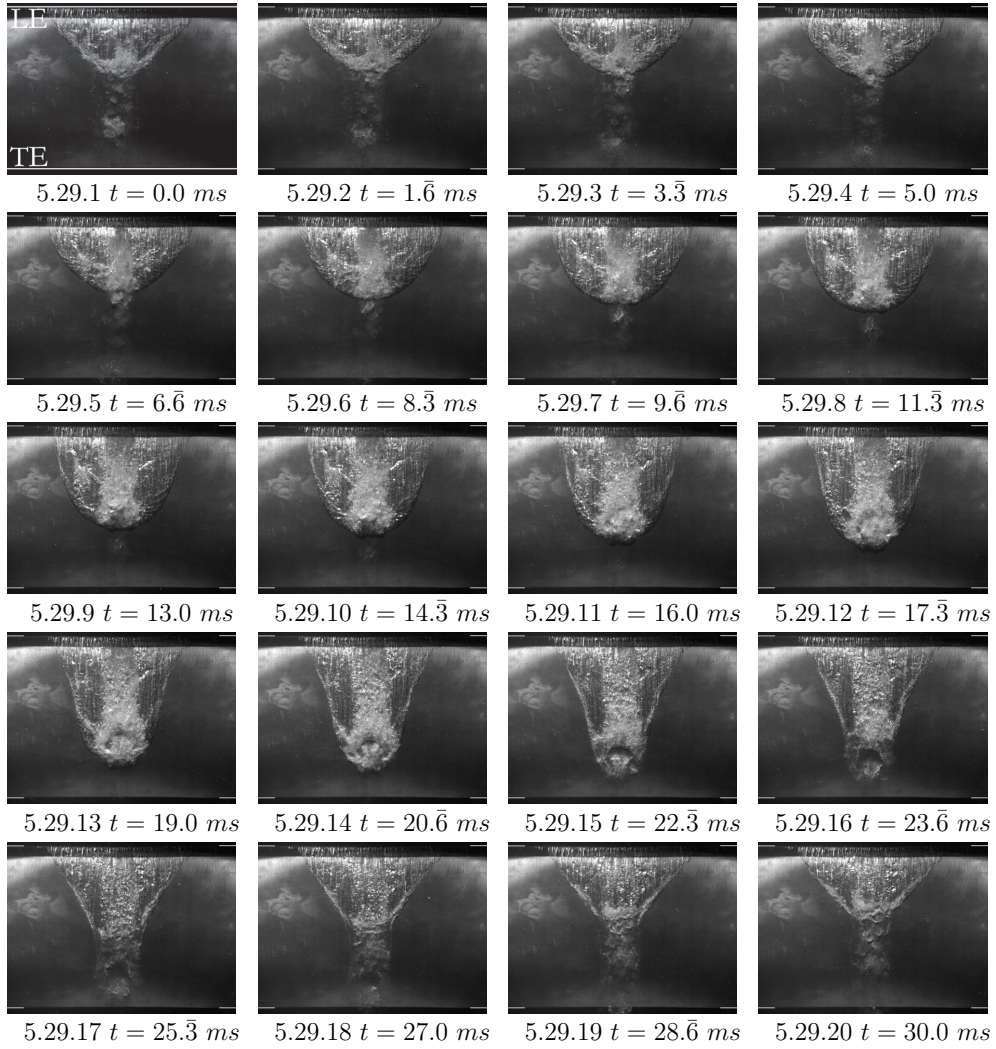
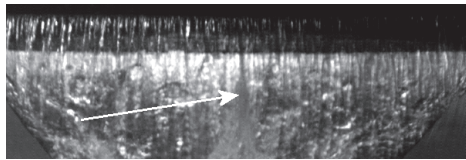
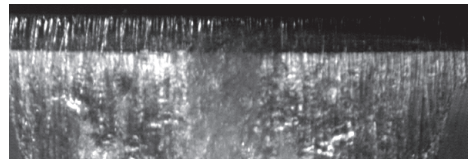


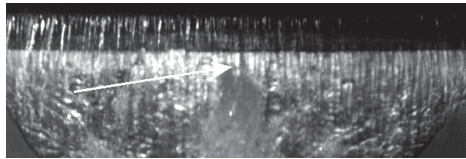
Figure 5.29 The Twist-11E hydrofoil at $\alpha = -3^\circ$, $V_0 = 6.59 \text{ m/s} \pm 4.12\%$, $\sigma = 0.743 \pm 7.85\%$, $f_{FO} = 31.69 \text{ Hz}$. The twenty images show a full oscillation period.



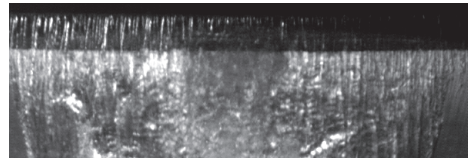
5.30.1 $t = 3.\bar{3} \text{ ms}$



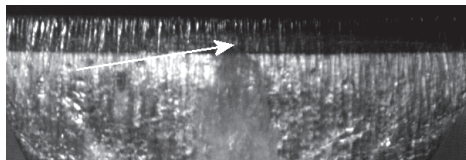
5.30.6 $t = 11.\bar{3} \text{ ms}$



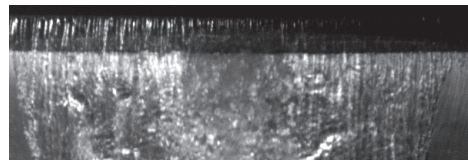
5.30.2 $t = 5.0 \text{ ms}$



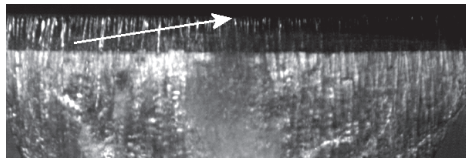
5.30.7 $t = 13.0 \text{ ms}$



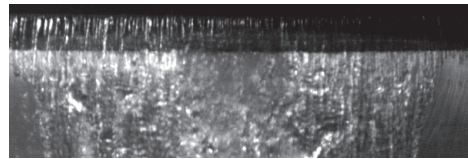
5.30.3 $t = 6.\bar{6} \text{ ms}$



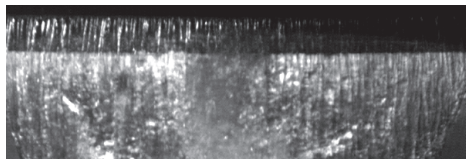
5.30.8 $t = 14.\bar{3} \text{ ms}$



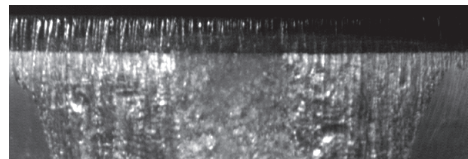
5.30.4 $t = 8.\bar{3} \text{ ms}$



5.30.9 $t = 16.0 \text{ ms}$



5.30.5 $t = 9.\bar{6} \text{ ms}$



5.30.10 $t = 17.\bar{3} \text{ ms}$

Figure 30 Close-ups from figs. 5.29.3-5.29.13. The re-entrant jet is visible and indicated in the first four frames and is seen not to cause any shedding of the cavity.

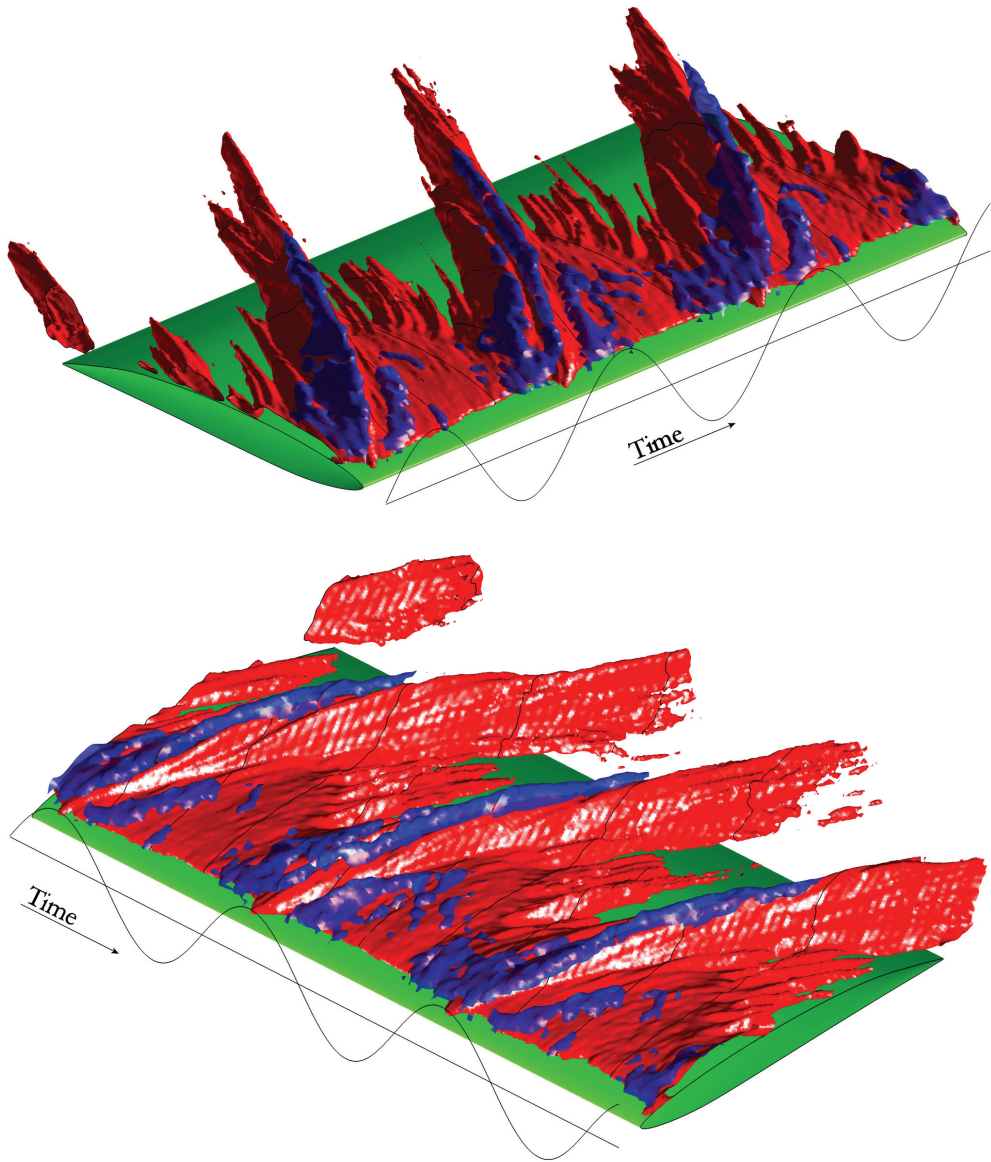


Figure 5.31 Visualization of the cavity outline on the midplane of the Twist-11E at $V_0 = 6.5 \text{ m/s} \pm 4.2\%$, $\sigma = 0.85 \pm 7.6\%$, $f_{FO} = 31.56 \text{ Hz}$, similarly to fig. 5.29, showing three cycles. The visualizations indicate the small shed structure at the midspan increases the cavity from the moment the re-entrant jet impinges on the leading edge. The blue outline is the velocity isosurface taken at 99% of $V = V_0\sqrt{1 + \sigma}$. In contrast with the Twist-11N hydrofoil, the velocity on the interface is lower. Note that the cavity continues to the leading edge, but this was not captured due to insufficient illumination.

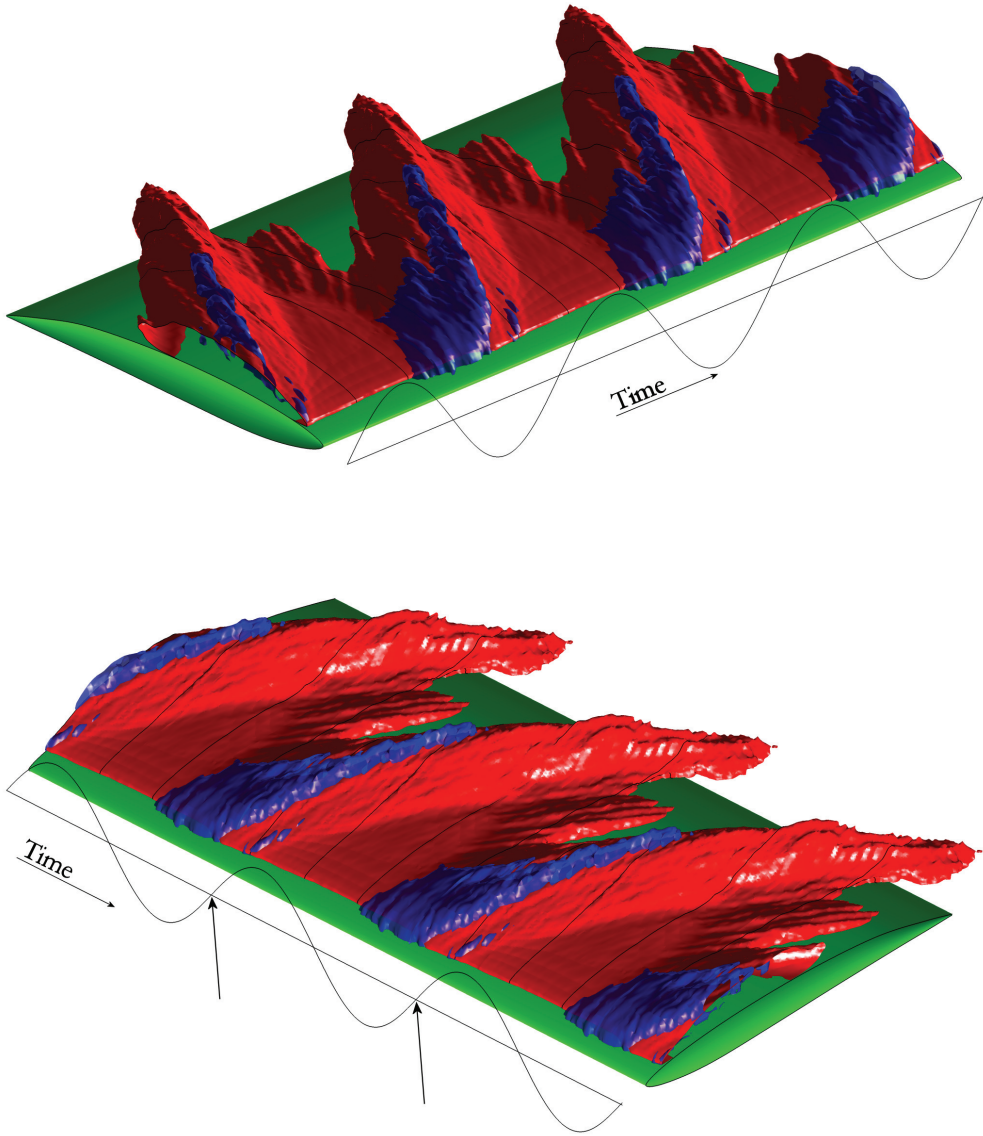


Figure 5.32 Visualization of the ensemble-averaged cavity outline on the midplane of the Twist-11E at $V_0 = 6.5 \text{ m/s} \pm 4.2\%$, $\sigma = 0.85 \pm 7.6\%$, $f_{FO} = 31.56 \text{ Hz}$, similarly to fig. 5.29, showing three cycles. Most of the smaller vortical structures collapse during the averaging giving an overestimate of the cavity length compared with the original data.

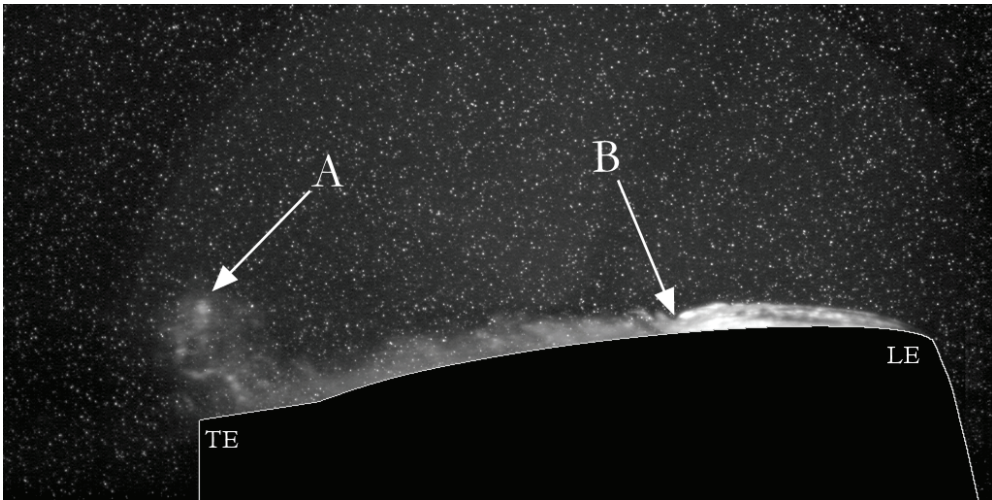


Figure 5.33 PIV frame on the midplane of the Twist-11E at $V_0 = 6.5 \text{ m/s} \pm 4.2\%$, $\sigma = 0.85 \pm 7.6\%$, $f_{FO} = 31.56 \text{ Hz}$. Flow right to left, leading edge at right. The shed structure as visible in figs. 5.29.19-fig:T11E-s2.20 is denoted as *A*. The cavity length is shortest at this time instance and the closure of the attached cavity is denoted *B*. Most of the vaporous vortices shed by the receding cavity can be seen as vapor downstream of *B*, as well as PIV tracer particles.

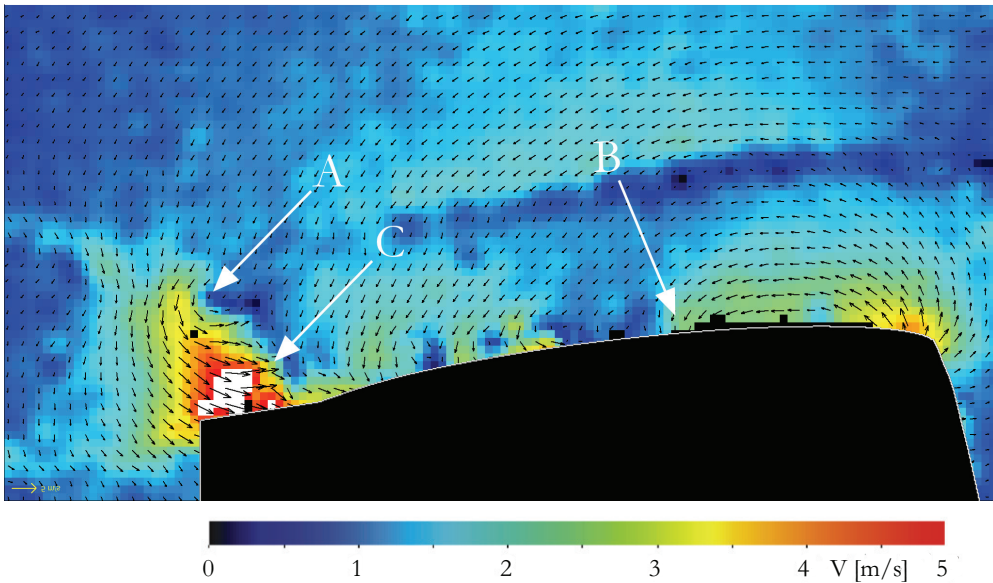


Figure 5.34 Velocity field and magnitude from the PIV image in fig. 5.33, incoming flow velocity subtracted. Note that all gaps in the velocity field have been interpolated, including those inside the cavity. The hairpin vortex is identified (*A*) as well as a strong induced upstream velocity within the hairpin vortex (*C*), on the order of 5 m/s near the foil surface, where many spurious vectors occurred due to a loss of most particle pairs. The correlation map of the PIV interrogation deteriorated significantly in the area.

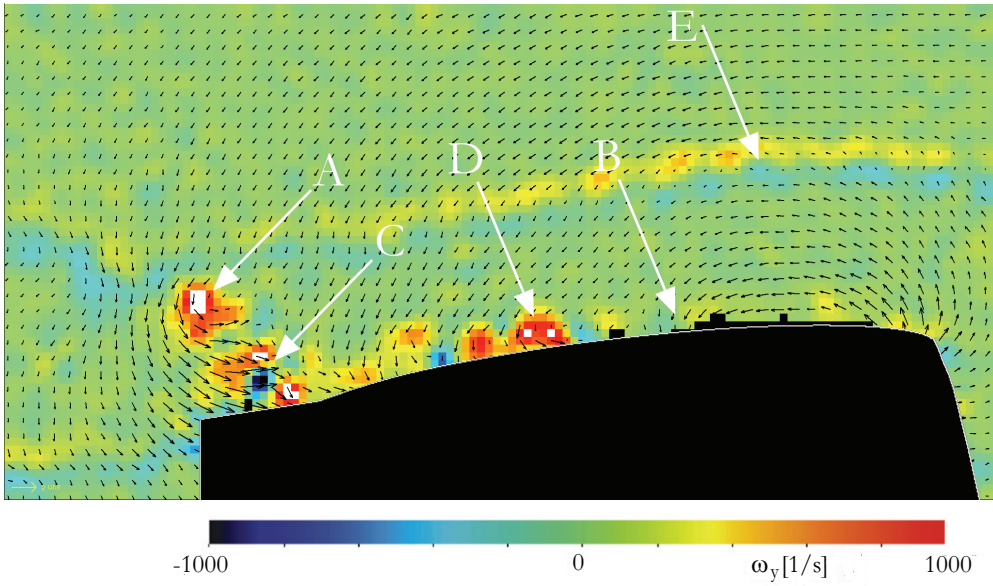


Figure 5.35 Velocity field and vorticity magnitude from the PIV image in fig. 5.33. A region of high vorticity is seen at the location of the vortex core and at several regions close to the hydrofoil surface (*D*). Some vorticity is observed in the wake of the flow oscillator (*E*)

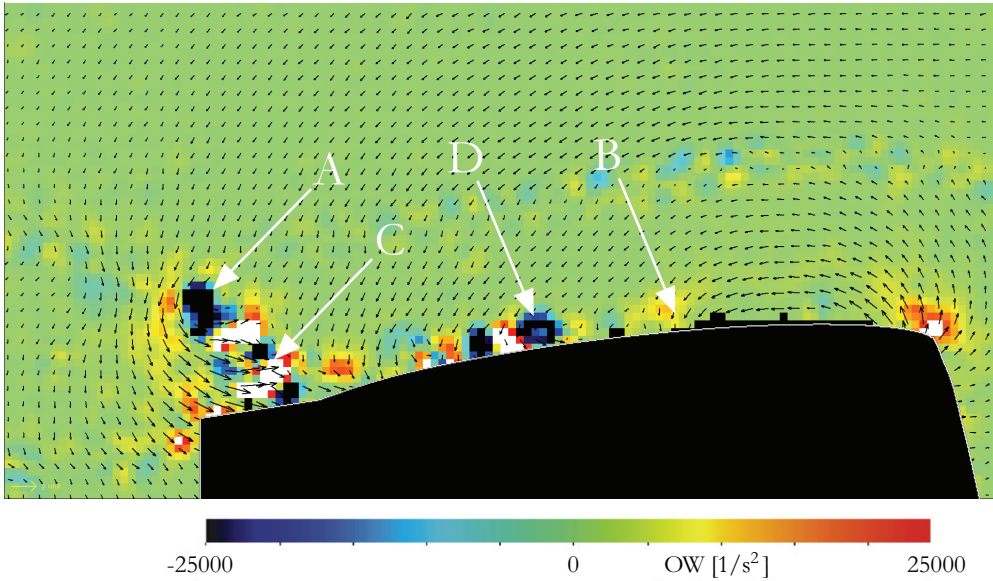


Figure 5.36 Velocity field and magnitude of the Okubo-Weiss parameter (eq. 2.81). Strongly negative values of the parameter—signifying a vortex core in two-dimensional flow—are found at the location of regions of high shear, suggesting that most regions of high vorticity correspond to a vortex structure. No other regions of high shear were found in the closure region of the attached cavity on the Twist-11E.

Chapter 6

Conclusions and Recommendations

6.1 The application of PIV to cavitating flows

The use of Laser Induced Fluorescence is insufficient for accurate Particle Image Velocimetry measurements in cavitating flows. Incident laser light reflected from the cavity can overexpose and saturate the camera, and even damage it. The use of laser-induced fluorescent particles and optical filters is an easy and effective method to solve the problem of over-exposure by removing all laser light and recording particles only. Nevertheless, two problems remain.

- *Out-of-plane particles are illuminated by the reflection and refraction of the light sheet by the vapor-liquid interface.* This can be partially solved by purposely applying a very small focal depth—obtained by a large aperture of the lens—so that the focus on out-of-plane particles is quickly lost and resulting in lower and wider peaks on the PIV correlation map. With the application of high speed PIV, the energy per pulse of the lasers is low giving a modest light budget, so high apertures are already common.
- *An error is introduced by the unintended correlation of illuminated vapor captured by the camera.* Two cameras were used with different sensitivities and no vapor was recorded when using the less sensitive—but faster—camera, so the correlation of vapor is not always a problem of the application of PIV measurements to cavitating flows. nevertheless, one would prefer to opt for a sensitive camera to capture more information from the light sheet, increasing the risk of capturing illuminated vapor by the camera.

Whenever vapor is visible, the PIV measurement will deteriorate due to correlation of illuminated vapor for several reasons:

- *The cavity liquid-vapor interface is a reflecting surface, so the recorded intensity depends on the direction of illumination.* A subtle change in the cavity outline results in a change of the intensity of the reflection, leading to false correlations.

- *It is impossible to determine*¹ *if the recorded cavitation is inside or outside the light sheet.* In fact, most of the time it is clearly outside the light sheet. The calibration is only valid in the measurement plane so interrogation of vaporous flows is nearly always erroneous.
- *Correlation of vapor does not lead to a correct prediction of the fluid velocity as one observes changes in the cavity interface, not changes in fluid velocity.* For example, the interrogation of a smooth and stationary interface results in a prediction of zero-displacement leading to strong gradients in the velocity field near the interface, gradients which are simply not present in the actual flow.

It is crucial that this source of background noise is removed—e.g., using image analysis—in order to avoid correlation errors. The image-analysis presented in chap. 3 offers a possible solution to remove the cavity while leaving the measurement of the flow displacement unaffected. Upon close inspection of the result of pre-processed and unprocessed images, it can be concluded that the solutions are identical in the fully-wetted region. With the use of synthetic PIV images it was shown that the error is reduced significantly when applying the pre-processing. In order to apply PIV effectively and accurately in cavitating flows, the combined use of laser induced fluorescence and image pre-processing is required. The modified standard deviation function as presented in s. 4.2.3 performs well for the identification of particles, but the order of applied kernel operations, their sizes and settings require some degree of optimization differing per experiment and should not be interpreted as a generic approach.

6.2 The structure of three-dimensional cavitation

An isolated sheet cavity was studied occurring in the flow on three-dimensional hydrofoils with different sections and spanwise loading distributions. From the experiments with the three-dimensional attached cavities it follows that re-entrant flow from the sides dictates the behavior of the shedding cycle and the re-entrant flow from the sides depends on the cavity closure line. Thus, the cavity topology largely dictates the re-entrant flow direction.

Side-entrant flow

The re-entrant flow from the side of the cavity dictates the behavior of the shedding cycle and the flow from the sides depends on the cavity closure line. The instationary cavity closure line governs the cavities shedding behavior. The convex cavity shapes on the Twist hydrofoils are intrinsically unsteady. The re-entrant flow direction is mirrored on the cavity closure line, so the re-entrant flow can be moving upstream and also in spanwise direction, the latter denoted as a side-entrant component. For any convex cavity closure line, side-entrant components of the re-entrant flow focus in the aft region of the sheet. The side-entrant flow impinges on the cavity interface causing a local break-off of a part of

¹with a single camera

the main cavity. Side-entrant components often collide before the re-entrant flow reaches the leading edge. The convergence of side entrant jets is a second shedding mechanism for attached sheet cavitation in addition to the re-entrant flow reaching the leading edge and impinging the sheet vapor interface near the sheets detachment line.

Re-entrant flow

The impingement of a re-entrant jet on the vapor-liquid interface near the cavity detachment location is an insufficient condition for cloud shedding. By using a hydrofoil with a near-constant pressure distribution on the suction side—the Eppler YS-920 section—in a Twist-11 configuration, a cavity was created that was slender, covered 70% of the chord at the mid plane, and was relatively thin at moderate angles of attack. The slenderness of the cavity and its closure line resulted in side-entrant jets continuously aimed at the very end of the cavity closure region, causing the continuous shedding of small scale vortices from the closure region. The thin cavity with its low pressure gradient had a weak re-entrant jet that did not disturb the sheet cavity interface upon contact. The re-entrant jet was recirculated over the cavity interface upon contact so that the cavity was constant in length. This is distinctly different from the classical point of view that re-entrant flow always causes shedding, as is observed for two-dimensional hydrofoils.

The closure of the attached cavity

With all observed shedding mechanisms—from full-length cavity shedding, to local sheet break-off, and eventually to small-scale vortex shedding—the basic mechanism is sheet cavity interface impingement by re-entrant flow. With the experiments for the Twist-8N and Twist-11N primary and secondary sheddings were identified to be the same collapse mechanism on different scales (s. 5.2.2). The scale of the eventual shedding is determined by topology of the cavity closure line. The importance of the (local) jet momentum was shown by the hydrofoils with a near-constant suction-side pressure distribution. *It is therefore essential that the direction and momentum of the re-entrant flow are captured in numerical simulations in order to accurately simulate cloud shedding.*

The shedding mechanism observed after side-entrant jet convergence at the center plane is a pinch-off of the aft part of the attached cavity. A part of the attached cavity at the central plane is pinched off after the collision of side-entrant flow. The observed (cavitating) vortices of the remainder of the attached cavity are similar to the spanwise and streamwise vortices in a mixing layer. It is concluded that the wake of an attached cavity shedding small-scale vortices is in fact a mixing layer with its characteristic vortical structure that is clearly visible on the images presented for a large scale cavity.

Cloud cavitation

The seemingly aptly named term cloud cavitation is a misnomer. From photographs the shed structure indeed resembles an indefinite and opaque region, collapsing into bubbly

remains, but from the present experiments it follows that the shed structure mainly consists of cavitating vortices. The low nuclei content in the water tunnel allows for the observation of the structure without bubbles clouding the view and at no time a pure bubbly cluster or cloud was observed. From the results obtained for the Twist-8N hydrofoil, it was demonstrated that the wake of the sheet cavity consists of smaller streamwise vortices stretched around the main co-rotating spanwise vortices. The entire wake of the attached cavity quickly rolled up and concentrated in the central plane by the time it passed the trailing edge. As a result, the wake of the cavity is highly turbulent and this made it difficult to perform PIV as many particles left the measurement plane due to a large out-of-plane velocity component.

The two dimensional cavity

The attached cavitation on a two-dimensional hydrofoil has a highly three-dimensional structure making it a more difficult study object, both numerically as experimentally, as re-entrant flow is constantly changing direction and converging at different locations. The periodic shedding seen on the present hydrofoils results in a distinct cycle. However, the two-dimensional hydrofoils used for most cavitation research lack the spanwise pressure distribution with a well-defined low-pressure region. The results is the seemingly random local shedding along the cavity closure line. Any disturbance at its closure line will redirect the re-entrant flow into a side-entrant flow resulting in local convergence of re-entrant flow and subsequently into local shedding. The three-dimensional cavity is shown to have a repeatable collapse cycle. This makes it more accessible as a validation case for numerical studies. Also, the cavity on the hydrofoils from the present work does not interact with the boundary layer of a tunnel wall, interactions that are not captured when simulating cavitating flow using inviscid flow models.

Unsteady inflow

The shedding of the sheet cavity fully locks in with the perturbation generated by the oscillator when the oscillators frequency approaches the natural shedding frequency. The naturally shedding cavity is shedding reasonably periodically, the frequency and phase show some modulation. This modulation complicates the ensemble averaging of the measurements. This modulation is removed when using the flow oscillator at a frequency for which the cavity locks in at the oscillation frequency. The quality of the measurements to be used as validation data for numerical computations is improved at the cost of having to include the flow oscillator. As the amplitude of the flow oscillator was small. It was designed to be able to be simulated by using a fixed mesh with a transpiration boundary condition. In that case the additional computational cost is thought to be low. The Twist hydrofoil with the Eppler section and its stationary cavity with its small scale vortex shedding is exempt from this recommendation. The shedding of the small structures of this cavity occurs at a time scale not feasible by the flow oscillator and the main cavity topology was steady.

Cavitation erosion is linked to vapor structures rebounding near a surface after a collapse. These were observed during the experiments for unsteady inflow conditions but not during natural shedding. The natural collapse is enhanced by the increase in cyclic pressure as the foil loading decreases. It is hypothesized that if the natural shedding frequency is lower than the frequency of the oscillating inflow field, the risk of erosion is reduced. This will have to be verified by erosion-oriented experiments.

Transport and production of vorticity

From an analysis of the transport equation for vorticity it follows that gradients in the void fraction can interact with the rate of deformation tensor and can produce vorticity. This 'viscoclinic' production is additional to the known production terms due to external forces (e.g., a rotating frame of reference), baroclinic torque, and generation of vorticity in boundary layers. The interaction of the gradient of the void fraction and the rate of deformation tensor could not be measured by means of PIV.

Regions of high vorticity were not measured using PIV, except near the core of vortices. The smaller-scale vortices in the wake of the cavity could not be detected as the experiments were aimed at measuring the entire flow field. The resolution was insufficient to resolve the closure of the cavity and no appreciable vorticity was measured in the wake. For the interrogation of the wake of the cavity, a much smaller field of view—combined with smaller particles—would be required, which was beyond the scope of the present work.

In viscous flow calculations, gradients in an insufficiently-resolved void-fraction distribution interacting with the rate-of-deformation of the flow could possibly introduce an additional artificial vorticity production term. The production of vorticity requires further study, preferably by means of simple test cases.

Design consequences

Ship propellers are usually designed to avoid isolated sheet cavities—i.e., attached cavities not connected to the tip vortex—since they are commonly associated with erosion. For this reason, a propeller designer attempts to design sheet cavities that increase in length toward the tip. Application of inception-delaying sections—such as an Eppler section—can be used to keep the propeller free of cavitation, but operating conditions can exceed the inception conditions. At these conditions, a large cavity can appear that can grow explosively and can generate high pressure transients. The experiments with the Twist-11E hydrofoil at $\alpha = -3^\circ$ indicate that the thin sheet cavity on the Eppler section is not shedding at moderate loadings and can be an acceptable form of sheet cavitation with regard to noise, erosion, and vibration by virtue of its minimal volume fluctuations. The cavity extent is large, but the shedding and volume fluctuations are small. So, a chordwise-large attached cavity is not a cause for concern if it is thin and does not shed large structures. However, experiments for the case of the unsteady inflow indicate that the cavity will start

shedding larger structures as the frequency increases, so load variations of the propeller blade should be preferably small. Unfortunately, the variations in loading are a result of the flow pattern caused by the upstream ship hull and the frequency of the variation depends on the propeller rate of revolution. These constraints are nearly always design conditions and rarely design parameters.

Accurate prediction of the direction of the re-entrant flow forms the basis of an accurate prediction of cloud shedding. For (potential flow) boundary element methods, an accurate non-linearized re-entrant flow is computationally very expensive. Also, potential flow models cannot easily model the impingement of the re-entrant jet on the cavity interface. Hence, potential flow methods have difficulty in predicting cavitation erosion.

From the experiments for the elliptical hydrofoil it is concluded that the side-entrant flow reaching the leading edge influences the detachment point in the region where the attached cavity merged with the tip vortex. As the cavity closure-line shape determines the direction of the side-entrant jet and the side-entrant jet determines the local detachment criterion, the cavity closure-line shape affects the point of detachment. Potential flow calculations usually fix the point of detachment on or near the leading edge. It is not expected that boundary element methods can capture the flow aspects predominantly present near the propeller tip, at least, without special treatment of the interaction of re-entrant flow and the sheet cavity detachment.

Numerical methods calculating the whole flow field do not have this restriction. The described shedding mechanisms are largely based on convergence points of re-entrant flow and impingement on the cavity interface. These effects are all thought to be inertia driven so it is expected that Euler simulations are able to capture most if not all of the major structures observed during the experiments in the Twist hydrofoils.

When simulating the behavior of cavitation shedding e.g., using volume-of-fluids methods, it is often difficult to capture the interface of the sheet cavity. From observations it follows that the interface of the sheet is a discontinuity step from liquid to vapor. For cloud cavitation, the numerically diffuse interface is often justified from the numerical point of view in order to capture the optically diffuse structure of the cloud. The cloud structure in the present work has been identified as a structure of vortices, not an agglomeration of bubbles. It is expected that for correctly simulating the cloud one must preserve a sharp interface in order to prevent diffusion—either numerically or physically.

From a physical point of view, the medium can exist as pure vapor or pure liquid (that is, below the critical point where the distinction between the gas and liquid phase no longer exists). The cloud cavitation is a mixture of liquid, vapor, vaporous bubbles, and droplets. The vapor fraction does not really have a meaning other than to capture a complicated two-phase flow pattern in a continuum approach. It is hypothesized that the choice of vapor production models is of subsidiary importance to capturing the physics of the flow

with a sharp interface.

Recommendations

The interaction between attached cavitation and the tip vortex, both steady and unsteady, has only been briefly explored in the present thesis. Tip vortex cavitation can generate pressure transients between the 4th to 7th blade harmonics that can be as loud as collapsing cloud cavitation resulting in on-board noise and vibration. Tip vortex cavitation can be experimentally studied using the same techniques as outlined in the present work. The induced velocities of a tip vortex constitute a strongly three-dimensional flow field so the use of stereoscopic PIV is indispensable.

The application of stereoscopic PIV in the cavitation tunnel of Delft is feasible as outlined in the Master thesis by van der Hout (2007). The use of a hydrofoil with a zero tip chord is recommended. The Ellipse-11 suffered from the leading-edge vortex detaching from the leading edge and with local tip vortices detaching from the trailing edge, visible when the cores of these vortices cavitated. For the design of a wing with a controlled lead-edge and tip vortex system, optimization using numerical methods is recommended.

Appendix A

Notation

A brief explanation of the notation used for chapter 2. Einstein summation convention is used during derivations. This notation results in brief expressions, and it often greatly facilitate deduction and complicated permutations such as those of compounded chain rules. However, the notation can sometimes be so terse that it is defeating the purpose of accessible notation. A combination of three or four tensor operators in succession can result in a complicated combination of derivatives as is the case with Chapter 2. The summation convention is kept within the derivations, and occasionally dropped in favor of vector operator notation.

The summation convention is simple. Whenever an index appears twice in an expression it is to be summed so that for any vector or tensor ζ , ξ

$$\zeta_i \xi_i \equiv \sum_{i=1}^N \zeta_i \xi_i \quad \zeta_{ij} \xi_{ik} \equiv \sum_{i=1}^N \zeta_{ij} \xi_{ik} \quad (\text{A.1})$$

Whenever a pair of suffices appear, they are both summed, *in any order*

$$\zeta_{ij} \xi_{ik} \zeta_{jm} \equiv \sum_{i=1}^N \sum_{j=1}^N \zeta_{ij} \xi_{ik} \zeta_{jm} \quad (\text{A.2})$$

So, a single free suffix indicates an element of a set, vector, or tensor. Double suffices are automatically summed¹. Note that these suffices are always *dummy suffices* and can be interchanged indiscriminantly. The number of suffices of a variable is a direct indicator of its tensor order.

A.1 Operators

The Kronecker Delta, δ_{ij} , is a second order tensor defined as

$$\delta_{ij} = \mathbf{e}_i \cdot \mathbf{e}_j \begin{cases} 1 & i = j \\ 0 & i \neq j \end{cases} \quad (\text{A.3})$$

¹no part of an equation can hold more than two identical suffices

with \mathbf{e}_i the unit vector and $\delta_{ii} = 3$. A shorter Kronecker Delta is sometimes encountered

$$\delta_i = \mathbf{e}_i \cdot \mathbf{e}_1 \begin{cases} 1 & i = 1 \\ 0 & i \neq 1 \end{cases} \quad (\text{A.4})$$

The gradient and divergence operators of a scalar (f), vector (ζ), or matrix (ξ) are

$$\begin{aligned} \nabla f &= \mathbf{e}_i \frac{\partial f}{\partial x_i} \quad ; \quad \nabla \zeta = \mathbf{e}_i \mathbf{e}_j \frac{\partial \zeta_j}{\partial x_i} \\ \nabla \cdot \zeta &= \frac{\partial \zeta_i}{\partial x_i} \quad ; \quad \nabla \cdot \xi = \mathbf{e}_i \frac{\partial \xi_{ij}}{\partial x_j} \end{aligned} \quad (\text{A.5})$$

Note that the divergence reduces and the gradient increases the order of the tensor by one. The permutation symbol of Levi-Civita, ε_{ijk} , is introduced to properly describe the cross-product and curl²

$$\varepsilon_{ijk} = \begin{cases} 0 & i = j \wedge j = k \wedge i = k \\ 1 & (i, j, k) \in \{[1, 2, 3], [2, 3, 1], [3, 1, 2]\} \\ -1 & (i, j, k) \in \{[1, 3, 2], [2, 1, 3], [3, 2, 1]\} \end{cases} \quad (\text{A.6})$$

The symbol is positive for a cyclic and negative for an anti-cyclic combination of $[i, j, k]$ and zero for equal suffices. This operator is not a tensor. The rotation of vectors can be written as

$$\zeta \times \xi = \begin{vmatrix} \mathbf{e}_1 & \mathbf{e}_2 & \mathbf{e}_3 \\ \zeta_1 & \zeta_2 & \zeta_3 \\ \xi_1 & \xi_2 & \xi_3 \end{vmatrix} = \mathbf{e}_i \varepsilon_{ijk} \zeta_j \xi_k \quad (\text{A.7})$$

and the curl as

$$\nabla \times \zeta = \begin{vmatrix} \mathbf{e}_1 & \mathbf{e}_2 & \mathbf{e}_3 \\ \frac{\partial}{\partial x_1} & \frac{\partial}{\partial x_2} & \frac{\partial}{\partial x_3} \\ \zeta_1 & \zeta_2 & \zeta_3 \end{vmatrix} = \mathbf{e}_i \varepsilon_{ijk} \frac{\partial \zeta_k}{\partial x_j} \quad (\text{A.8})$$

When applying e.g., a double curl, the result is

$$\begin{aligned} \nabla \times \nabla \times \zeta &= \mathbf{e}_i \varepsilon_{ijk} \frac{\partial}{\partial x_j} \left(\varepsilon_{klm} \frac{\partial \zeta_m}{\partial x_l} \right) = \mathbf{e}_i \varepsilon_{ijk} \varepsilon_{klm} \frac{\partial^2 \zeta_m}{\partial x_j \partial x_l} \\ &= \mathbf{e}_i (\delta_{ij} \delta_{jm} - \delta_{im} \delta_{jl}) \frac{\partial^2 \zeta_m}{\partial x_j \partial x_l} \\ &= \mathbf{e}_i \left(\frac{\partial^2 \zeta_j}{\partial x_i \partial x_j} - \frac{\partial^2 \zeta_i}{\partial x_j \partial x_j} \right) = \nabla (\nabla \cdot \zeta) - \nabla^2 \zeta \end{aligned} \quad (\text{A.9})$$

² $\varepsilon_{ijk} \equiv \mathbf{e}_i \cdot (\mathbf{e}_j \times \mathbf{e}_k)$

From the definition of the Levi-Civita symbol follows that

$$\boldsymbol{\zeta} \times \boldsymbol{\xi} = \varepsilon_{ijk} \zeta_j \xi_k = -\varepsilon_{ijk} \xi_j \zeta_k = -\boldsymbol{\xi} \times \boldsymbol{\zeta} \quad (\text{A.10})$$

and for a scalar f (or vector element ζ_i)

$$\varepsilon_{ijk} \frac{\partial^2 f}{\partial x_j \partial x_k} = 0 \quad (\text{A.11})$$

A.2 Tensor operators

Several tensor operators are introduced to facilitate a compact notation, including two custom-defined products. The Jacobian \mathbf{J} of a vector $\boldsymbol{\zeta}$ is defined as

$$\mathbf{J} = \mathbf{e}_i \mathbf{e}_j \frac{\partial \zeta_i}{\partial x_j} = \nabla^T \boldsymbol{\zeta} \quad (\text{A.12})$$

The Hessian \mathbf{H} of a scalar f is defined as

$$\mathbf{H}_f = \mathbf{e}_i \mathbf{e}_j \frac{\partial^2 f}{\partial x_i \partial x_j} = (\nabla \otimes \nabla^T) f \quad (\text{A.13})$$

or the dyadic product of gradient operators. Note that $\mathbf{H} = \mathbf{H}^T$. A (custom) dyadic product tensor \mathbf{G} of a vector $\boldsymbol{\zeta}$ is introduced as

$$\mathbf{G}_{\boldsymbol{\zeta}} = \mathbf{e}_i \mathbf{e}_j \zeta_i \zeta_j = \boldsymbol{\zeta} \otimes \boldsymbol{\zeta}^T \quad (\text{A.14})$$

with $\mathbf{G} = \mathbf{G}^T$. The dyadic product of the gradient of a scalar f is written as

$$\nabla f \otimes \nabla^T f = \mathbf{G}_{\nabla f} \quad (\text{A.15})$$

A custom tensor cross product is used operating on (3×3) matrices \mathbf{A} and \mathbf{B}^T

$$\begin{aligned} \mathbf{A} \times^M \mathbf{B} &= \begin{bmatrix} a_{11} & a_{12} & a_{13} \\ a_{21} & a_{22} & a_{23} \\ a_{31} & a_{32} & a_{33} \end{bmatrix} \times^M \begin{bmatrix} b_{11} & b_{12} & b_{13} \\ b_{21} & b_{22} & b_{23} \\ b_{31} & b_{32} & b_{33} \end{bmatrix} \\ &= A_1 \times B_1^T + A_2 \times B_2^T + A_3 \times B_3^T = \mathbf{e}_i \varepsilon_{ijk} A_{jk} B_{lk} \end{aligned} \quad (\text{A.16})$$

with A_i the i -th column of \mathbf{A} . Although the expression is compact in the summation convention, no vector notation was found and hence a short hand symbol is introduced. Basically, the tensor cross product is the sum of the cross product of the columns of \mathbf{A} and \mathbf{B}^T . The tensor cross product is not commutative as

$$\mathbf{A} \times^M \mathbf{B} = -\mathbf{B}^T \times^M \mathbf{A}^T \quad (\text{A.17})$$

Other properties on the tensor curl are

$$\mathbf{A} \times^M \mathbf{A} \neq 0 \quad (\text{A.18})$$

$$\mathbf{A} \times^M \mathbf{A}^T = 0 \quad (\text{A.19})$$

The tensor cross product of the gradient of a vector ζ and the dyadic tensor \mathbf{G} of ζ are

$$\zeta_{\nabla} \times^M (\zeta \otimes \zeta^T) = \mathbf{J}_{\zeta} \times^M \mathbf{G}_{\zeta} = -\frac{1}{2} \zeta \times \nabla |\zeta|^2 \quad (\text{A.20})$$

Appendix B

Uncertainty analysis and error propagation

Any measurement is certain to contain some measurement error. The regions can be legion, but in order to quantify or estimate the error bounds, one must use a formal procedure. In this section, the definitions are given with several methods used in order to estimate the confidence interval. A measurement is nearly always a discrete set of data points, often taken from an analogue signal. This signal is called x . A cumulative probability function $F(x)$ of a variable x is defined such that the probability function f of an event x equals

$$F(\xi \leq x) = \int_0^x P(\xi) d\xi \quad (\text{B.1})$$

This function F is monotone and from the definition of the probability function of f it follows that $F(-\infty) = 0$ and $F(\infty) = 1$. The probability function $f(x)$ is defined as $f(x) = dF(x)/dx$. The mean or expectation is equal to

$$\hat{\mu} = \bar{x} \equiv \int_0^{\infty} x f(x) dx \quad (\text{B.2})$$

Any n-th moment around the mean for $n \neq 1$ can be defined as

$$\hat{\mu}_n(x) \equiv \int_{-\infty}^{\infty} (\xi - \bar{x})^n f(\xi) d\xi \quad (\text{B.3})$$

or as a raw moment

$$\hat{\mu}_n(x) = \bar{x}^n \equiv \int_{-\infty}^{\infty} \mu^n f(\xi) d\xi \quad (\text{B.4})$$

When $n = 2$, we obtain the variance or, the square of the standard deviation. The standard deviation is a good indicator of the spread of data around the mean value.

$$\hat{\sigma}(x) = \sqrt{\hat{\mu}_2(x)} \quad (\text{B.5})$$

Skewness ($\hat{\gamma}_1$) and kurtosis ($\hat{\gamma}_2$) are defined as the raw moments with $n = 3, 4$ divided by the standard deviation to the power n

$$\hat{\gamma}_1 \equiv \frac{\hat{\mu}_3(x)}{\hat{\sigma}^3(x)} \quad \hat{\gamma}_2 \equiv \frac{\hat{\mu}_4(x)}{\hat{\sigma}^4(x)} \quad (\text{B.6})$$

The skewness indicates whether the distribution contains an asymmetry. For $n = 4$, we obtain the Kurtosis, the degree of peakedness of a distribution, indicating the concentration of a distribution or to what degree the standard deviation is dependent on extreme outliers (its peakedness or flatness). High kurtosis means that the probability distribution has long "tails". Note that the kurtosis of the normal distribution equals 3. Both skewness and kurtosis are a good quality indicator of the measured signal and can be used to validate the use of a normal distribution for a measured signal. These integrals are nearly always evaluated in a discretized form and the demands on the number of points increases rapidly with increasing values of n . For any discrete set of N samples of x_i , the (sample) mean reads

$$\bar{x} = \frac{\sum_{i=1}^N x_i}{N} \quad (\text{B.7})$$

Note that for a discrete sample, $\bar{x} \neq \hat{\mu}$. The second moment is

$$\bar{x}_{N,2} = \frac{\sum_{i=1}^N (x_i - \bar{x})^2}{N} \equiv \sigma_N^2(x) \quad (\text{B.8})$$

or

$$\bar{x}_{N-1,2} = \frac{\sum_{i=1}^N (x_i - \bar{x})^2}{N-1} \equiv \hat{\sigma}_{N-1}^2 \quad (\text{B.9})$$

Note that in the above the so-called sample moment (eq. B.8) and bias-corrected sample moment (eq. B.9) are given. In literature both definitions are used ambiguously, but here the bias-corrected variant is always meant unless explicitly stated otherwise and the subscript $N-1$ is dropped. Furthermore, the standard deviation σ is defined as the square root of the bias-corrected sample moment and is frequently encountered. The standard uncertainty is defined to

$$u = \frac{\hat{\sigma}}{\sqrt{N}} \quad (\text{B.10})$$

For the numerator of both eq. B.8 and B.9

$$\sum_{i=1}^N (x_i - \bar{x})^2 = \sum_{i=1}^N x_i^2 - 2\bar{x} \sum_{i=1}^N x_i + N\bar{x}^2 \quad (\text{B.11})$$

substituting eq. B.7 gives

$$\sum_{i=1}^N (x_i - \bar{x})^2 = \frac{1}{N} \left(N \sum_{i=1}^N x_i^2 - \left(\sum_{i=1}^N x_i \right)^2 \right) \quad (\text{B.12})$$

The standard deviation is rewritten as

$$\hat{\sigma}_{N-1}(x) = \sqrt{\frac{N \sum_{i=1}^N x_i^2 - \left(\sum_{i=1}^N x_i \right)^2}{N^2 - N}} \quad (\text{B.13})$$

This saves the effort of calculating \bar{x} , saving considerable time and memory when applying image analysis. A slight modification of the standard deviation is also used with a weighing function ϕ . The function ϕ can be a function acting as a mask, excluding regions or variables from participating in the calculation of the standard deviation. The function ϕ can also be any function, adhering more importance to specific values. Using this function ϕ the standard deviation becomes

$$\hat{\sigma}_{N-1}(x, \phi) = \sqrt{\frac{\sum_{i=1}^N \phi_i \sum_{i=1}^N (\phi_i x_i^2) - \left(\sum_{i=1}^N \phi_i x_i \right)^2}{\left(\sum_{i=1}^N \phi_i \right)^2 - \sum_{i=1}^N \phi_i}} \quad (\text{B.14})$$

and is later used for calculating local image statistics and is mentioned for completeness' sake. A series of moments is further defined as

$$\hat{\sigma}_N(x) N = ss_{xx} = \sum_{i=1}^N (x_i - \bar{x})^2 \quad (\text{B.15})$$

$$COV(x, y) N = ss_{xy} = (x_i - \bar{x})(y_i - \bar{y}) = x_i y_i - \bar{x} \bar{y} \quad (\text{B.16})$$

the second expression is the covariance of x and y , expressing a measure of strength of the correlation between two sample variables.

Distribution functions

There is a wide range of choices for the probability functions f . A common distribution is the normal (or Gaussian) distribution

$$f_N(x) = \frac{1}{\hat{\sigma} \sqrt{2\pi}} e^{-\frac{(x - \hat{\mu})^2}{2\hat{\sigma}^2}} \quad (\text{B.17})$$

and it is most frequently encountered in physical processes. And even though some processes have different distributions, central limit theory states that their errors and deviations often are again (approximately) normal distributed. As a result the normal distribution is a primary choice for f . Still, more realistic functions are required when the mean value is close to a limiting factor or the deviations are distributed asymmetrically. When the distribution is skewed, due to some asymmetric tolerance limit x_L , a log-normal function can be used where the logarithm of x is normally distributed around population mode $\hat{\mu}_M$ and mean $\hat{\mu}$ (The population mode is the peak of the probability function, equal to the mean for a symmetric distribution)

$$f_{LN}(x) = \frac{1}{\hat{\sigma}\sqrt{2\pi}|x-x_L|} e^{-\left(\frac{1}{2\hat{\sigma}} \ln \frac{x-x_L}{(\hat{\mu}_M-x_L)\hat{\mu}}\right)^2} \quad (\text{B.18})$$

In case of a digital read-out or instrument bias, the uniform distribution is applicable over the resolution (x_L). The uniform distribution has full containment over its limited range $\pm x_L$,

$$f(x) = \begin{cases} \frac{1}{x_L}, & -1/2x_L < x < 1/2x_L \\ 0, & \text{otherwise} \end{cases} \quad (\text{B.19})$$

with a standard deviation $\hat{\sigma} = x_L/2\sqrt{3}$. For example, the quantization standard deviation of an A/D conversion present on the data acquisition hardware can then be expressed as

$$\sigma_{A/D} = \frac{\text{range}}{2^{n+1}\sqrt{3}} \quad (\text{B.20})$$

with n the digital resolution (in bits) of the measurement equipment. Other distributions with 100% containment limits are triangular, quadratic, cosine, half cosine, and the U distribution (Castrup 2001). But, establishing 100 % containment limits is not a trivial matter as these limits often do not exist.

The mean can be determined for a sampled measurement within a certain uncertainty. But, this uncertainty has been determined with a limited number of samples giving it its own uncertainty based on its limited number of samples. Assuming that the sample values are distributed normally, uncertainty limits can be calculated for the uncertainty itself. For the (log) normal distribution, the true standard deviation is inherently unknown as only a *sample standard deviation* can be determined. The uncertainty of the uncertainty can be estimated using a sample-based probability function $f(t)$. This function determines a confidence interval where the true standard deviation resides in. The width of this confidence interval decreases as the number of samples increases. This is called the expanded uncertainty and approaches the standard deviation in ideal cases. Students t -distribution is a classic example of such a containment probability function. Students variable t is defined as

$$t \equiv \frac{\bar{x} - \hat{\mu}}{\hat{\sigma}_2/\sqrt{N}} \quad (\text{B.21})$$

with a probability density function $f(t)$

$$f_{N-1}(t) = \frac{\Gamma\left(\frac{1}{2}(r+1)\right)}{\sqrt{\pi r} \Gamma\left(\frac{1}{2}r\right) \left(1 + \frac{t^2}{r}\right)^{N + \frac{1}{2}}} \quad (\text{B.22})$$

with Γ the gamma function and the degrees of freedom, r , equal to $r = N - 1$. This function approaches the normal distribution for $n \rightarrow \infty$. Usually a 95 % confidence interval is used in which $f_{95}(n-1) = t_{95}(n-1) \approx 1.96$ for an infinite number of samples. From a practical point of view it must be noted that for one hundred samples the difference between $t_{95}(100)$ and $t_{95}(\infty)$ is smaller than 1 %. For a signal with data in abundance—such as a measured pressure—this is hardly a stringent demand. nevertheless, for singular data of a limited number of calibration points the expanded uncertainty can result in a wide confidence interval.

If several components are available each with its own number of degrees of freedom, an effective value of r can be estimated -a representative mean degree of freedom- using the approximation of Welch-Satterthwaite

$$r_{eff} = \frac{\left(\sum_{i=1}^N \hat{\sigma}_i^2\right)^2}{\sum_{i=1}^N \frac{\hat{\sigma}_i^4}{r_i}} \quad (\text{B.23})$$

This averaging expression is an ISO norm, but it must be noted that the above expression can overestimate r_{eff} : when additional error terms are added to a low uncertainty component with limited degrees of freedom (say r between 3 and 6), t_{95} actually decreases (Ballico 2000). The expression indicates that a combination of measurement errors will be dominated by the error with the lowest degree of freedom.

Bias and precision error

For any experiment, all known sources of error must be identified. Barring systematical errors, the difference between a measurement and the actual value is a combination of bias errors (ϵ_B) and precision errors (ϵ_F) and the real mean

$$x = \bar{x} + \epsilon_B + \epsilon_f \quad (\text{B.24})$$

Bias errors include factors such as uncertainties in calibration or sensor location, while precision errors contain e.g., scatter and data reduction artifacts. If we have a reference value and a measured statistical distribution then *accuracy* indicates the error between the reference value and the measured mean value. *Precision* is the spread in the measured values. Precision entails the reproducibility or repeatability of a test. Note that accuracy and precision are independent. If both are present, the measurement (or calculation) is

valid. Precision errors are often referred to as random error or random noise, the subscript f refers to a certain distribution function. Bias errors can—at least theoretically—be quantified and removed from the measurement but this requires significant experience with the measurement setup. If not, they can be a troublesome source of error. If an uncertainty can be evaluated statistically, it is referred to as a Type A uncertainty and Type B if otherwise. Note that both precision error (P) and bias (B) can be classified type A or type B.

Examples of Type A uncertainty sources can be

- Differences between similar sensors (P & B)
- Errors introduced by different operators (B)
- Reference standards calibrated internally (P & B)
- Reproducibility error (B)
- Inhomogeneties of the sample material (B)

Examples of Type B uncertainty sources can be

- Reference standards calibrated externally, unless stated. (P & B)
- Physical constants used in the calculation (P & B)
- Misalignment (B)
- Resolution (P)
- Errors in A/D conversion (P)

Estimating the degrees of freedom of a type-B uncertainty

As a type B uncertainty cannot be adequately sampled it requires experience to ascertain. The degrees of freedom for a type B uncertainty often equals infinity, but this is not necessarily so. Estimating containment limits and coverage facts is often not sensible as these uncertainties can be based on e.g., third party statistical tests or predetermined calibration intervals (Castrup 2000). An approximation can be written as

$$r \simeq \frac{1}{2} \frac{\bar{x}^2}{\hat{\sigma}^2(x)} \quad (\text{B.25})$$

but for most type-B data $\hat{\sigma}^2$ is not known. But, the degrees of freedom can be estimated if the error limits are given and if we assume those errors to lie in an estimated containment limit. One could state: out of n observations of x , p % lie within $x \pm L$. Following Castrup (2000), the degrees of freedom can be estimated at

$$r_B \simeq \frac{3L^2\Phi^2(p)}{2\Delta_L^2\Phi^2(p) + \pi L^2\Delta_p^2e^{\Phi^2(p)}} \quad (\text{B.26})$$

with $\Phi(p)$

$$\Phi(p) = f_N^{-1}\left(\frac{1+p}{2}\right) \quad (\text{B.27})$$

based on the inverse normal distribution

$$f_N^{-1}(x) = \sqrt{\frac{1}{2\pi x^3}} e^{-\frac{(x - \hat{\mu})^2}{2x\hat{\mu}^2}} \quad (\text{B.28})$$

The containment limit L is often given as an error percentage by the manufacturer. If the confidence level p needs to be estimated the uncertainties ΔL en Δp need to be estimated as well but this is even more difficult to do. The error L is often given; the limit is not and taken as zero, so that the estimate depends on Δp only. This value is estimated using a binomial distribution

$$\Delta p = \frac{p(1-p)}{n} \quad (\text{B.29})$$

based on a certain number of n measurements (also unknown, but taken as a minimum at $n = 1$). The estimate is now

$$r_B \simeq \frac{3n^2\Phi^2(p)}{\pi p^2(1-p)^2 e^{\Phi^2(p)}} \quad (\text{B.30})$$

For a 95 % confidence interval, the DOF for a type-B estimate is 61, with $t_{95} \approx 1.9996$ and $n = 1$. For $n = 2$ this value already equals $t_{95} \approx 1.9697$ and approaches $t_{inf} \approx 1.9600$ for a 99 % confidence interval. The degrees of freedom for type-B uncertainties in calibration analysis will therefore be taken as infinite. This results in the most conservative limit when estimating a standard deviation from a manufacturer-reported uncertainty. When using the Welch-Satterthwaite formula it is taken as 61, resulting in the widest expanded uncertainty limits when reporting measurement error.

Propagation of error

The bias error ε_B must be estimated to within a (for instance) 95% confidence interval, based on the sensitivity and calibration accuracy of a sensor as determined by the manufacturer. The random error ε_f will be determined from statistical analysis. Any relation combining several measurements will be subject to an interaction of each components error. The sensitivity of the result $f(x)$ to error in x can be expressed using non-dimensional Taylor series

$$\frac{\partial f}{\partial x} = \frac{f(x + E_x) - f(x)}{E_x} + O(E_x) \quad (\text{B.31})$$

The above relation is often written as a non-dimensional sensitivity coefficient θ of a parameter f to x_i

$$\theta_x^f = \frac{\partial f}{\partial x} \frac{\bar{x}}{\bar{f}} \quad (\text{B.32})$$

The total linearized error of a single component is

$$E_i = \theta_i(\varepsilon_{B,i} + \varepsilon_{f,i}) = E_{B,i} + E_{f,i} \quad (\text{B.33})$$

The estimation of the total error propagation of a relation f is

$$E = \sqrt{\theta_1^2 \varepsilon_{B,1}^2 + \theta_1^2 \varepsilon_{f,i}^2 + 2\theta_i \varepsilon_i \theta_j \varepsilon_j} = \sqrt{\theta_i^2 \hat{\sigma}_{B,i}^2 + \theta_i^2 \hat{\sigma}_{f,i}^2 + 2\hat{\rho}_{ij} \theta_i \hat{\sigma}_i \theta_j \hat{\sigma}_j} \quad (\text{B.34})$$

with a factor ρ called the correlation coefficient

$$\hat{\rho}_{ij} = \frac{\varepsilon_i \varepsilon_j}{\hat{\sigma}_i \hat{\sigma}_j} \quad (\text{B.35})$$

determining the cross correlation between covariant sources of error and is zero if measurements are independent. For example, when determining the difference between two close-by pressure transducers, the correlation coefficient is most likely non-zero.

The error in linear regression

In some cases a simple $y_p = ax + b$ relation suffices to describe a data set with points (x_i, y_i) . The least squares method determines the coefficients

$$a = \frac{SS_{xy}}{SS_{xx}} \quad b = \bar{y} - a\bar{x} \quad (\text{B.36})$$

An estimated error for a prediction for points y_p at x_i is given as

$$\hat{\sigma}(y) = \sqrt{\frac{\hat{\sigma}_{res}^2}{n-2}} \sqrt{\frac{1}{m} + \frac{1}{n} + \frac{(x_i - \bar{x})^2}{SS_{xx}}} \quad (\text{B.37})$$

for m repetitions of n points, with $\hat{\sigma}_{RES}$ an estimator in the variance in the error in the predicted value y_p . Using the above definitions for y_p the uncertainty can be written as:

$$\hat{\sigma}_{RES} = \frac{1}{N-1} \left[\frac{SS_{xy}}{SS_{xx}} \sum_{i=1}^N (x_i - \bar{x}) + \sum_{i=1}^N (\bar{y} - y_i) - \underbrace{\frac{SS_{xy}}{SS_{xx}} \sum_{i=1}^N (x_i - \bar{x}) + \sum_{i=1}^N (\bar{y} - y_i)}_0 \right]^2 \quad (\text{B.38})$$

Note that the last term of the right the expression averages out to zero. Furthermore:

$$\begin{aligned} \left(\frac{SS_{xy}}{SS_{xx}} \sum_{i=1}^N (x_i - \bar{x}) + \sum_{i=1}^N (\bar{y} - y_i) \right)^2 &= \frac{SS_{xy}^2}{SS_{xx}^2} \sum_{i=1}^N (x_i - \bar{x})^2 - 2 \frac{xx_{sy}}{SS_{xx}} \sum_{i=1}^N (x_i - \bar{x})(y_i - \bar{y}) \\ &\quad + \sum_{i=1}^N (y_i - \bar{y})^2 \\ &= SS_{yy} \left(1 - \frac{SS_{xy}^2}{SS_{xx} SS_{yy}} \right) \\ &= (N-1) \hat{\sigma}^2(y) (1 - \hat{r}^2) \end{aligned} \quad (\text{B.39})$$

The term r is the coefficient of correlation frequently encountered in statistical functions, going to unity for a better "goodness of fit". The expanded uncertainty based on the predicted value y_p to x_i is now

$$\hat{\sigma}(y_p) = t_{95}(N-2) \sqrt{\frac{N-1}{N-2} \hat{\sigma}^2(y) (1 - \hat{r}^2) \left(\frac{1}{M} + \frac{1}{N} + \frac{(x_i - \bar{x})^2}{SS_{xx}} \right)} \quad (\text{B.40})$$

The number of replicate determinations M is practically between 2 and 5, but often one for a daily calibration. This equation is generally used for evaluating the calibration of the pressure sensors, expressing their uncertainty directly as a function of their calibration quality.

Appendix C

The uncertainty in the velocity and cavitation number

C.1 Calibration uncertainty

The sensors in the test section are calibrated with a Keller PAA-33 pressure transmitter. Table C.1 summarizes the identified error sources. Note that manufacturing errors are interpreted as an exact $2\hat{\sigma}$ limit, with a 95.45 % confidence interval. The combined degrees of freedom is determined by the Welch-Satterthwaite formula, resulting in a DOF that is for all practical purposes equal to infinity, so $t_{95} = 1.96$ leading to a calibration error of 158 *Pa* in a 95 % confidence interval. Note that the resulting uncertainty is not a measure of statistical uncertainty during an experiment, but the compounded uncertainty due to calibration and sensor uncertainties.

		Distribution	Limits	Coverage	$\hat{\sigma}$	DoF
Calibration error	150 <i>Pa</i>	Normal	95.45	2	75	∞
Resolution	6P <i>Pa</i>	Rectangular	100	$\sqrt{3}$	3.46	∞
Standard deviation	0.61 <i>Pa</i>	Normal	95.45	2	0.306	149
				Sum	78.77	

Table C.1

The reference sensor can be used to calibrate the pressure transducers fitted throughout the test section. For this procedure, the pressure is measured for 30 seconds with the tunnel at rest. This results in roughly 1250 measurements by the reference sensor and 30,000 by all pressure transducers. The vacuum pump is set at 0.1 *bar* increments from 0.1 *bar* to 1.0 *bar*. Using eq. B.40 results in an uncertainty of 0.04 *Pa* over the entire range. Addition errors include: the resolution error (minimum sensitivity), the temperature drift (approx. 0.025%/° resulting in an offset of 250 *Pa* for a 4° *K* error in temperature. This temperature difference is not of the fluid, but of the laboratory conditions), the DAQ error (offset as given by the manufacturer in volts times the calibration factor), and the jitter (noise).

		Distribution	Limits	Coverage	$\hat{\sigma}$	DoF
Calibration error	158 Pa	Normal	95.45	2	78.77	∞
Regression error	0 Pa	Normal	95.45	2	0	30000
Resolution	7.7 Pa	Rectangular	100	$\sqrt{3}$	4.43	∞
Temperature	250 Pa	Normal	95.45	2	125	30000
DAQ error	65 Pa	Normal	95.45	2	32.5	∞
Jitter					7.54	30000
Sum					248.24	

Table C.2

As the number of degrees of freedom is infinite for all practical purposes, the expanded uncertainty of the bias error in the static calibration is 487 Pa with $t = 1.96$ within a 95% confidence interval. This value is taken as 500 Pa, or 0.5% of the measurement range of 1 bar. The static calibration of the pressure transducers is accurate to within 0.5% in a 95% confidence interval. Also, calibrating the pressure sensors can be performed by using only two points as the sensors are fully linear, as can be concluded from the low regression error, nearly zero due to the very low value of Pearson's correlation coefficient $1 - \hat{r}^2 < 10^{-7}$. From experience it is known that the sensitivity of the sensors (a) is constant, but that the offsets (b) may vary within several hours. The sensors are therefore recalibrated before and after each measurement or after 4 hours, whichever came sooner.

C.2 Effects of temperature and contaminants

The temperature of the water is measured by a PT-100 thermocouple. The accuracy of the thermocouple plus signal conditioning is specified at $0.3^\circ K$. The vapor pressure is described over a temperature range between $0^\circ C$ and $80^\circ C$ to within 0.01% by the Goff-Gratch-equation (Goff 1957),

$$\begin{aligned}
 \log_{10} p_V = & -7.90298 \left(\frac{T_S}{T} - 1 \right) + 5.02808 \log_{10} \left(\frac{T_S}{T} \right) \\
 & - 1.3816 \cdot 10^{-7} \cdot \left(10^{11.344 \left(1 - \frac{T}{T_S} \right)} - 1 \right) \\
 & + 8.1328 \cdot 10^{-3} \cdot \left(10^{-3.49149 \left(\frac{T_S}{T} - 1 \right)} - 1 \right) + \log_{10} 1013.246
 \end{aligned} \tag{C.1}$$

with T the absolute temperature and T_S the steam temperature at 1 atmosphere (373, 16K).

This expression is approximated to within 0.1% by a polynomial in the form of

$$p_V(T) = \sum_{i=0}^N C_i T^i \quad (\text{C.2})$$

and is used to determine the vapor pressure. The density of water is calculated using the expression by Patterson & E.C. (1994)

$$\rho(T) = \rho_0 \left(1 - \sum_{i=1}^5 C_i (T - T_0)^i \right) \quad (\text{C.3})$$

with $\rho_0 = 999.97358 \text{ kg/m}^3$ the maximum water density at $T_0 = 3.9818^\circ\text{C}$. The expression for water density and vapor pressure are plotted in fig. 3.1, values for the polynomials are in table C.3.

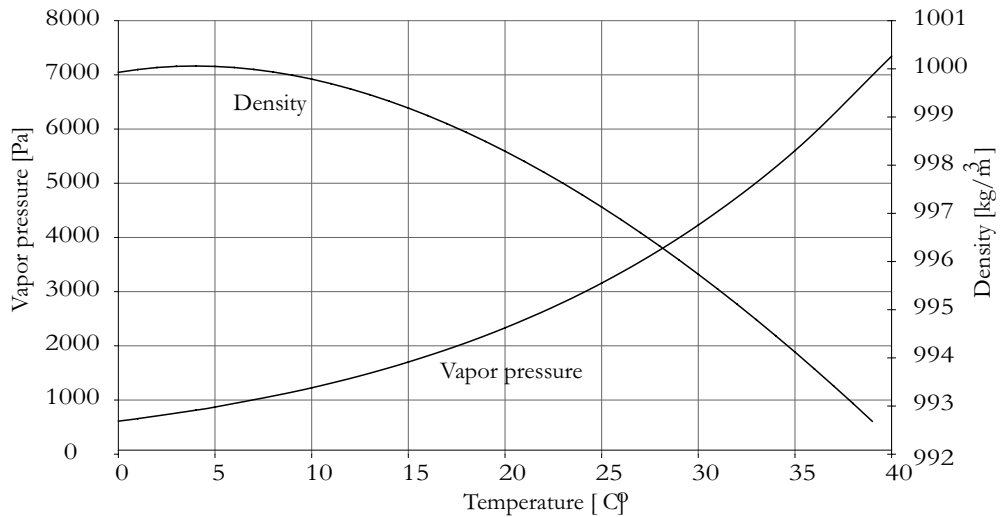


Figure 3.1 Vapor pressure (Goff 1957) and water density (Patterson & E.C. 1994) versus temperature.

Chemical impurities raise the evaporation point with

$$\Delta T = K_B m_B \quad (\text{C.4})$$

with K_B the ebullioscopic constant of water (0.51 K kg/mol) and m_B the molality of the chemical impurities (mol/kg), about 6 mmol/kg for fresh water near Delft. This results in a boiling point increase of $\Delta T \approx 0.003 \text{ K}$, a negligible influence. Dissolved gasses form a much larger component because of their partial gas pressure. A concentration difference of

i	$C_{i,\rho}$	$C_{i,pV}$
0	0	$9.09647963 \cdot 10^2$
1	$7.013400 \cdot 10^{-8}$	$4.44018819 \cdot 10^1$
2	$7.926504 \cdot 10^{-6}$	$1.40067514 \cdot 10^0$
3	$-7.575677 \cdot 10^{-8}$	$2.81795445 \cdot 10^{-2}$
4	$7.138940 \cdot 10^{-10}$	$2.34639662 \cdot 10^{-4}$
5	$-3.596458 \cdot 10^{-12}$	$3.18237150 \cdot 10^{-6}$
6	0	$-3.06840000 \cdot 10^{-9}$

Table C.3 Polynomial coefficient values for the density (eq. C.3) and vapor pressure (eq. C.1).

the dissolved gasses occurs when liquid evaporates and gas will diffuse into the cavity. This can be of particular importance to bubble dynamics for a process termed rectified mass diffusion (Brennen 1995). During the expansion phase of the bubble, the concentration of gasses in the bubble will decrease while the bubble's surface area increases. Gasses will flow into the bubble. During the collapse the concentration increases but the effective surface area decreases, reducing the gas mass flux out of the bubble compared with the influx during expansion. Also, the radial concentration distribution in the liquid shows a thinner 'concentration boundary layer' at the bubble interface during the expansion phase. Diffusion effects are therefore not linear. Bubbles are several orders of magnitude smaller than attached cavities and bubble collapse is a much faster phenomenon. In general, the effect of dissolved gasses appears to be more important to desinent cavitation¹.

C.2.1 Velocity in the test section

One of the most important parameters is the velocity in the test section. The easiest way to determine the velocity is calculating it by the pressure drop over a known contraction. Three planes have been chosen around the test section: upstream of the contraction (C), downstream the contraction (the inlet of the test section) (I) and downstream of the test section (O). Continuity for an incompressible medium states that

$$\int_{S_C} V_C dS = \int_{S_I} V_I dS = \int_{S_O} V_O dS \quad (C.5)$$

At the moment this velocity profile is assumed to be constant, so $S_i V_i = \text{constant}$. Using Bernoulli's relation for the conservation of momentum and denoting cross-section tunnel areas as A , the velocity is expressed as

$$V = c_V \sqrt{\frac{A_C^2}{A_C^2 - A_O^2} \frac{p_C - p_T}{\frac{1}{2}\rho(T)}} \quad (C.6)$$

¹desinence is the opposite of inception, i.e., the conditions where cavitation disappears by e.g., increasing the value of σ

This relation may be inaccurate, as the effective cross sectional area is smaller due to the displacement offset of the boundary layer. Also, the velocity is assumed to be constant over the cross section but as the pressure sensors of the inlet are just downstream the contraction, the velocity is not necessarily uniform. The above relation is calibrated by means of PIV to determine the value of the correction constant c_V . The ratio of area's is incorporated into a small new constant c_A

$$c_A = c_V \sqrt{\frac{A_C^2}{A_C^2 - A_O^2}} \quad (\text{C.7})$$

The above expression's sensitivity components are

$$\theta_{c_A}^V = 1 \quad ; \quad \theta_{p_T}^V = \frac{-p_T}{p_C - p_T} \quad ; \quad \theta_{p_C}^V = \frac{p_C}{p_C - p_T} \quad ; \quad \theta_\rho^V = -\frac{1}{2} \quad (\text{C.8})$$

The propagated uncertainty in velocity V is

$$\hat{\sigma}_V = \sqrt{\theta_{c_A}^2 \hat{\sigma}_{c_A}^2 + \theta_{p_T}^2 \hat{\sigma}_{p_T}^2 + \theta_{p_C}^2 \hat{\sigma}_{p_C}^2 + 2\hat{\rho}_{p_T p_C} \theta_{p_T} \theta_{p_C} \hat{\sigma}_{p_T} \hat{\sigma}_{p_C} + \theta_\rho^2 \hat{\sigma}_\rho^2} \quad (\text{C.9})$$

Note that the pressure sensors both measure fluctuations in the tunnel with a resulting covariance close to unity, a covariance denoted $\hat{\rho}$, see eq. B.35 on p. 168. The error in the density is mainly due to measurement error in the temperature, albeit small:

$$\hat{\sigma}_\rho = \frac{\partial \rho}{\partial T} \frac{\langle T \rangle}{\langle \rho \rangle} \hat{\sigma}_T \quad (\text{C.10})$$

with the water fluid density taken from eq. C.3.

C.2.2 Cavitation number in the test section

The cavitation number is defined as

$$\sigma = \frac{p_\infty + \rho(T)gh - p_v(T)}{\frac{1}{2}\rho(T)V_\infty^2} \quad (\text{C.11})$$

with V_∞ , p_∞ the conditions at the test section entrance. The above can be rewritten by substituting eq. C.6 and eq. C.7

$$\sigma = \frac{1}{c_V^2} \frac{A_C^2 - A_O^2}{A_C^2} \frac{p_T - p_v}{p_C - p_T} = \frac{1}{c_A^2} \frac{p_T - p_v}{p_C - p_T} \quad (\text{C.12})$$

with sensitivity components

$$\begin{aligned} \theta_{c_A}^{\hat{\sigma}} &= -2 \quad ; \quad \theta_{p_I}^{\hat{\sigma}} = \frac{p_C - p_v}{p_I - p_v} \frac{p_I}{p_C - p_I} \\ \theta_{p_C}^{\hat{\sigma}} &= -\frac{p_C}{p_C - p_I} \quad ; \quad \theta_{p_v}^{\hat{\sigma}} = \frac{-p_v}{p_I - p_v} \end{aligned} \quad (\text{C.13})$$

The propagated uncertainty in the cavitation number is

$$\hat{\sigma}_\sigma = \sqrt{\theta_{c_A}^2 \hat{\sigma}_{c_A}^2 + \theta_{p_T}^2 \hat{\sigma}_{p_T}^2 + \theta_{p_C}^2 \hat{\sigma}_{p_C}^2 + 2\hat{\rho}_{p_T p_C} \theta_{p_T} \hat{\sigma}_{p_T} \theta_{p_C} \hat{\sigma}_{p_C} + \theta_{p_v}^2 \hat{\sigma}_{p_v}^2} \quad (\text{C.14})$$

The error in vapor pressure is mainly caused by the error in the temperature measurement

$$\hat{\sigma}_\rho = \frac{\partial p_v / \langle T \rangle}{\partial T / \langle p_v \rangle} \hat{\sigma}_T \quad (\text{C.15})$$

C.3 Example

The error is given in an example for a value of $\sigma = 0.74$, with a shedding sheet cavity and active flow oscillator. Note that the pressure sensors at the entrance and at the exit can be taken to calculate the test section conditions and both are shown. The predicted values for the velocity and cavitation number—after calibration by PIV—are

	Velocity	σ
Inlet	6.59 m/s	0.7425
Outlet	6.64 m/s	0.7852

The sensitivity components of the velocity prediction are

	$\theta_{c_A}^V$	$\theta_{p_T}^V$	$\theta_{p_C}^V$	θ_ρ^V	$\theta_{\hat{\rho}(p_T, p_C)}^V$
Inlet	1.00	0.8485	-1.8458	-1.00	0.0571
Outlet	1.00	0.9508	-1.9508	-1.00	0.044

The uncertainties of all the measured and derived quantities are:

	$\hat{\sigma}_c$	$\hat{\sigma}_{p_T}$	$\hat{\sigma}_{p_C}$	$\hat{\sigma}_\rho$	$\hat{\sigma}_{\hat{\rho}(p_T, p_C)}$
Inlet	1.00%	1.37%	0.63%	-0.01%	0.01%
Outlet	1.00%	1.35%	0.63%	-0.01%	0.01%

The uncertainties p_T , p_C include the error due to a standard deviation in the pressure signal as well as the calibration uncertainty of 250 Pa. The errors in ρ and p_V are due to a temperature bias of $0.3^\circ C^a$. As the number of samples is more than 10,000 for the pressure signals, they give only a very small uncertainty in the estimate of the mean. The following table presents the number of the degrees of freedom from the the Welch-Satterthwaite formula (eq. B.23), as well as the contribution of each of the components.

	DOF	$\epsilon(V)_c$	$\epsilon(V)_{p_T}$	$\epsilon(V)_{p_C}$	$\epsilon(V)_{\hat{\rho}(p_T,p_C)}$	$\epsilon(V)_\rho$
Inlet	192.67	27.19%	36.59%	36.22%	0%	0%
Outlet	205.41	24.14%	40.00%	35.90%	0%	0%

^amanufacturer specification

It can be concluded that there is no appreciable contribution of the covariance between pressure signals, nor any influence of the temperature error. The calibration error of the constant c_A and test section pressure are dominant, the latter consisting of the bias error in calibration and noise.

For σ , the sensitivity components are

	$\theta_{c_A}^\sigma$	$\theta_{p_T}^\sigma$	$\theta_{p_C}^\sigma$	$\theta_{\hat{\rho}(p_T,p_C)}^\sigma$	$\theta_{p_V}^\sigma$
Inlet	-2.00	2.01	-1.84	0.09	-0.16
Outlet	-2.00	2.10	-1.95	0.066	-0.15

with uncertainties

	$\hat{\sigma}_c$	$\hat{\sigma}_{p_T}$	$\hat{\sigma}_{p_C}$	$\hat{\sigma}_{\hat{\rho}(p_T,p_C)}$	$\hat{\sigma}_{p_V}$
Inlet	1%	1.37%	0.63%	0.01%	2.24%
Outlet	1%	1.35%	0.63%	0.01%	2.24%

and the degrees of freedom from the Welch-Satterthwaite formula (eq. B.23) and component break-down. The DOFs of the pressure signal are typically 10,000, the DOF in the bias error is estimated as explained in the appendices, section B.

	DOF	$\epsilon(\sigma)_c$	$\epsilon(\sigma)_{p_T}$	$\epsilon(V)_{p_C}$	$\epsilon(\sigma)_{\hat{\rho}(p_T,p_C)}$	$\epsilon(\sigma)_{p_V}$
Inlet	148.52	30.71%	58.08%	10.23%	0%	0.98%
Outlet	170.13	29.3%	59.10%	10.90%	0%	0.80%

Similar to the error analysis in V , there is no influence of the temperature uncertainty and covariance. The calibration error by PIV and the bias error in the pressure calibration determine the final error. The value of σ and V appeared to be insensitive to which sensor array was used, but the uncertainty with the outlet plane incremented the error ranging from a few percentage points. Taking the degrees of freedom into account and using the DOFs to calculate the expanded 95% uncertainty limits (typically expanding the uncertainty by a factor of 1.96), the conditions reported for this example as

	Velocity	σ
Inlet	6.59 m/s \pm 4.12%	0.74 \pm 7.85%
Outlet	6.64 m/s \pm 4.26%	0.79 \pm 8.00%

Note that both estimates are well within each others confidence intervals. As noted, this is an example of a situation with the flow oscillator active and extensive cavitation. For non-cavitating conditions, the errors are near 2.7% in the inlet velocity and 5% in σ . Naturally, the inlet plane is chosen as the reference plane for the inflow conditions, as the wake of the cavitating hydrofoil passes the outlet pressure sensors.

Appendix D

PIV setup

D.1 Light sheet

The light sheet is constructed using a series of cylindrical lenses. Several combinations have been used, to control both the width and thickness of the lightsheet. The thickness should be sufficient so that between illumination pulses, most particles do not move out of the light sheet. The light sheet width has to illuminate the entire field of view, but the intensity distribution peaks at the center and the illumination at the sides of the field of view is reduced. This can affect the accuracy of the results, but as the images will be pre-processed before interrogation—as explained in chapter 4—the intensity distribution is preferably uniform and is therefore chosen to be much wider than strictly necessary for PIV. The optics are placed such that the laser beam does not converge at a point, as it may locally ionize the air, or that reflections of the lenses are directed into the laser source. Two sets of cylindrical lenses were used—details in table D.1- so that the width and thickness could be set independently, as sketched in figure D.1

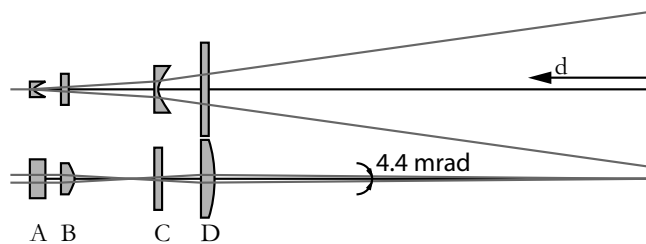


Figure 4.1 Sketch of the setup of the lenses in order to create light sheet (not to scale). See table D.1 for information on the lenses *A* to *D*.

	type	$L \times B$	f	d
A	concave	25×10	-12.7	1000
B	convex	20×20	100	950
C	concave	40×30	- 80	784
D	convex	60×50	100	734

Table D.1 Lenses used in the PIV setup. Indicated are lens height L and width B , focal distance f , and distance to center of the test section d . All dimensions in mm .

With this setup, the thickness variation of the light sheet over the field of view is minimized. The thickness of the sheet was about 1 mm , the width 500 mm so that the field of view ($200 \times 200mm$) was lit reasonably uniformly.

D.2 Setup

The PIV setup consisted of a Pegasus Laser and Photron cameras controlled by LaVision's DaVis 7.0, a PIV measurement and interrogation program. Two sets of cameras have been used, the Photron Ultima APX and the Photron Ultima APX-RS, denoted Flowmaster HSS4 and HSS5 by LaVision, a developer of—amongst other—PIV systems. Both cameras have a 1024×1024 pixel CCD and can be used at full resolution at 2,000 fps for the HSS4 and 3,000 fps for the HSS5. The frame rate can be increased at a decreased resolution. The details of both cameras are in table D.2. The HSS4 was used for initial feasibility studies for the application of PIV measurements to cavitating flows, later replaced by the HSS5.

Camera	HSS4	HSS5
Resolution	1024×1024	1024×1024
Frame rate @ max resolution	2,000	3,000
Frame rate @ half resolution	4,000	10,000
Frame rate @ min resolution	120,000	250,000
Shutter time	$4 \mu s - 16.7 ms$	$2 \mu s - 16.7 ms$
Memory (RAM)	2.6 Gb	16 Gb

Table D.2 Cameras used in the PIV setup

The laser used for the illumination is a New Wave Pegasus containing two ND-YLF lasers with a beam wave length of 527 nm (quite close to the wave length of a Nd-YAG laser at 532 nm). The first laser flashes half the pulse delay before the end of frame #1 and the second laser flashes half the delay time after the start of frame #2. The advantage of two lasers instead of a double pulsing single laser is the quality of the beam profile and uniformity of the pulse duration. The laser has a constant 10 $mJ/pulse$ output over a wide frequency range and a pulse duration of 180 ns .

The calibration serves two purposes; it determines both the scale and the deformation of the image. A calibration plate with an accurately spaced dotted grid was positioned in the light sheet (fig. 4.2). A correction polynomial was calculated by DaVis to warp the image into a fully regular pattern. Even when the camera is placed perpendicular to the light sheet, the viewing angle will gradually decrease from 90 degrees to the edges of the image. Some errors due to limited oblique viewing, barrel or cushion distortion, or other lens aberrations can be partially corrected. As the calibration procedure uses peak detection algorithms similar to those used during PIV interrogation, it is subject to similar sources of error.

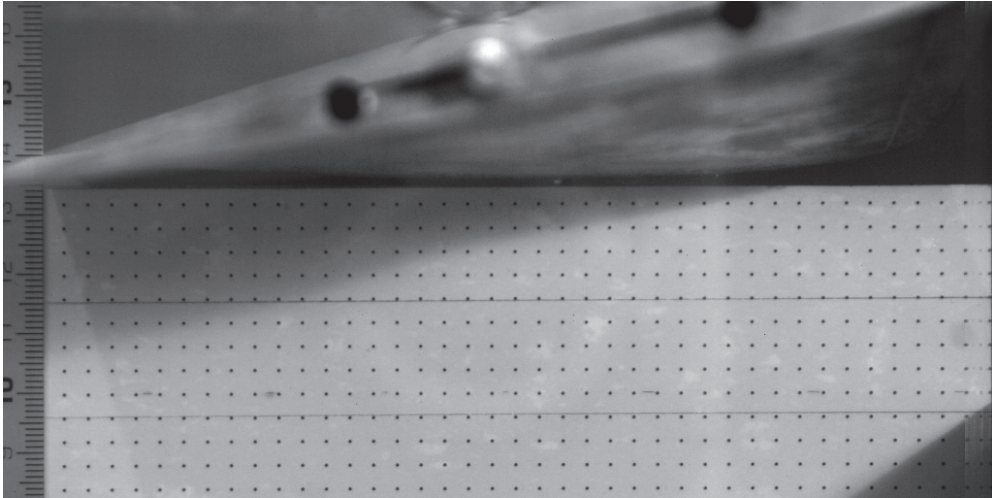


Figure 4.2 A typical calibration image, showing a ruler to determine the height from the test section bottom.

Appendix E

Details of the hydrofoil geometry

E.1 NACA0009 section

The expression for the NACA0009 section is

$$\hat{z}_{NACA0009}(\hat{x}) = \frac{t}{0.20} \left(0.2969\sqrt{\hat{x}} - 0.126\hat{x} - 0.3516\hat{x}^2 + 0.2843\hat{x}^3 - 0.1015\hat{x}^4 \right) \quad (\text{E.1})$$

with $t = 0.09$ for the NACA0009 section.

E.2 Eppler YS-920 section

The exact coordinates of the Eppler YS-920 are plotted in fig. 5.1 including the derivative based on both the exact coordinates and the custom polynomial approximation. The former is calculated with a central difference scheme for a non-uniform mesh:

$$\frac{d\hat{z}}{d\hat{x}}(\hat{x}_i) = \frac{\hat{x}_i - \hat{x}_{i-1}}{\hat{x}_{i+1} - \hat{x}_i} \frac{\hat{z}_{i+1} - \hat{z}_i}{\hat{x}_{i+1} - \hat{x}_{i-1}} + \frac{\hat{x}_{i+1} - \hat{x}_i}{\hat{x}_i - \hat{x}_{i-1}} \frac{\hat{z}_i - \hat{z}_{i-1}}{\hat{x}_{i+1} - \hat{x}_{i-1}} \quad (\text{E.2})$$

using the offsets from Shen (1985) The derivative shows some deviation near the trailing edge, but that detail will be lost on the machined hydrofoil. Its effect on the flow is expected to be negligible.

E.3 NACA63A010 section

A 7th order polynomial (i=7) proved to be sufficiently accurate to define the geometry of the NACA63A010 section with the coefficients in table E.2.

The trailing edge of the oscillator hydrofoils is thickened to a minimum of 0.6 *mm*—using the same procedure as for the NACA and Eppler cross sections—as given in the next section(eq. E.3). The chord length is taken at 200 *mm*, in order to further reduce the loading, with the trailing edge flap at the last 20%.

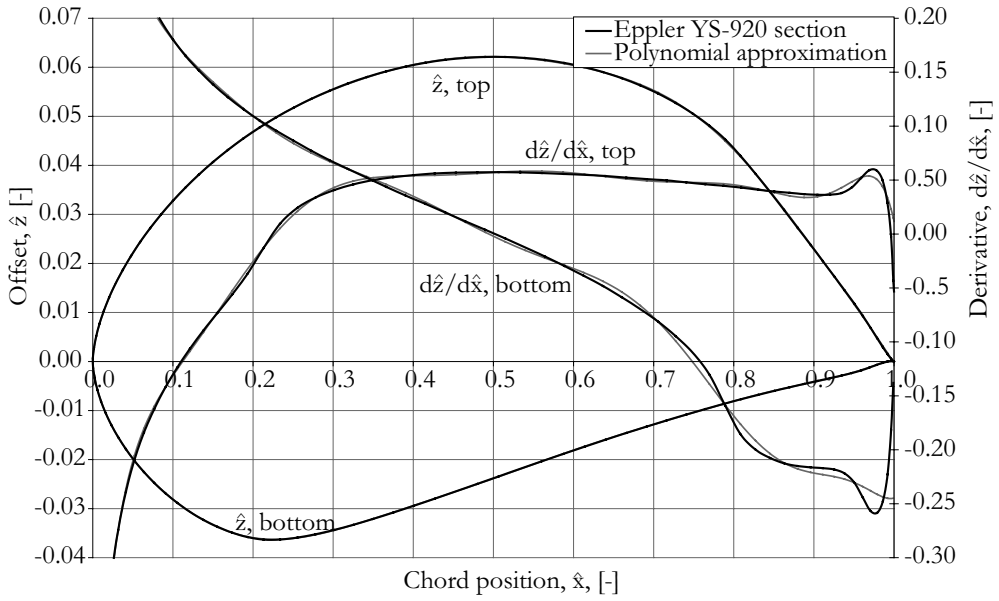


Figure 5.1 The exact coordinates of the Eppler YS-920 and its custom polynomial approximation. The trailing edge of the hydrofoil has some waviness that is not exactly captured by the polynomial approximation.

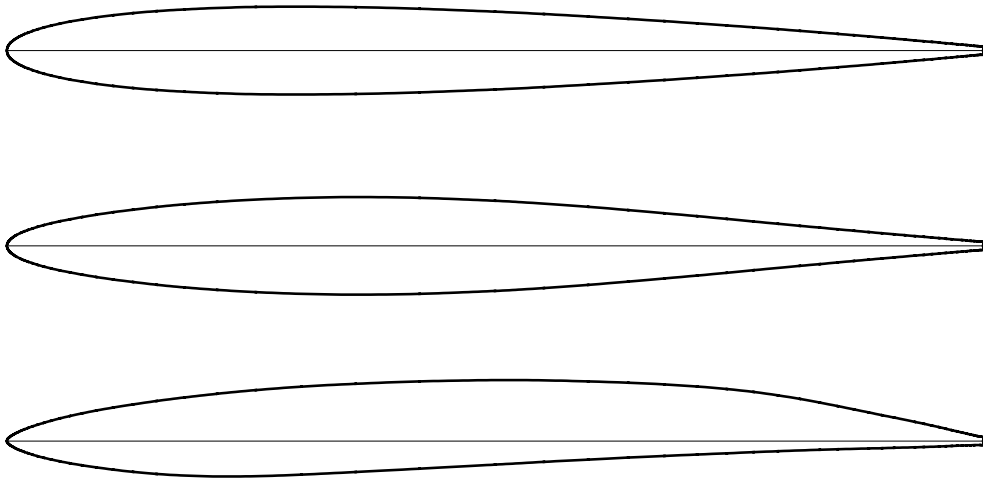


Figure 5.2 From top to bottom, plots of the NACA009, NACA63A010 (for the flow oscillator), and Eppler YS-920 sections with the trailing edge thickness addition.

	Top	Bottom
C_0	$+6.32842885463017 \cdot 10^0$	$-5.87570501167541 \cdot 10^0$
C_1	$+2.33849654895556 \cdot 10^1$	$-2.23982153284351 \cdot 10^1$
C_2	$-2.17216837411403 \cdot 10^2$	$+2.72557497494152 \cdot 10^2$
C_3	$+1.82934159830747 \cdot 10^3$	$-2.47400016278531 \cdot 10^3$
C_4	$-9.90277942740479 \cdot 10^3$	$+1.41971721794002 \cdot 10^4$
C_5	$+3.17221227381530 \cdot 10^4$	$-4.59094620266695 \cdot 10^4$
C_6	$-5.77473464324118 \cdot 10^4$	$+8.19377207576040 \cdot 10^4$
C_7	$+5.00847049863250 \cdot 10^4$	$-6.89177163601913 \cdot 10^4$
C_8	0	0
C_9	$-2.73140052464736 \cdot 10^4$	$+3.54049711842593 \cdot 10^4$
C_{10}	0	0
C_{11}	$1.74125601856616 \cdot 10^4$	$-2.17683515603658 \cdot 10^4$
C_{12}	0	0
C_{13}	$-7.26585937783280 \cdot 10^3$	$+9.00702430949563 \cdot 10^3$
C_{14}	0	0
C_{15}	$+1.36873930846369 \cdot 10^3$	$-1.72163204802988 \cdot 10^3$
b	0	0

Table E.1 Eppler & Shen YS-920 hydrofoil offset polynomial

C_0	+0.12162190
C_1	-0.05664884
C_2	+0.15585952
C_4	+1.37528714
C_3	-0.82179654
C_5	-0.15236506
C_6	+1.08896977
C_7	-0.33900325
b	-0.00047289

Table E.2 Coefficients for the NACA63A010 polynomial

E.4 Trailing edge thickness function

To increase the thickness of the foil at the trailing edge, a correction function was chosen with a zero first derivative at the point of initialization.

$$\Delta \hat{z}(\hat{x}, \hat{y}) = \left(\frac{\hat{x} - \hat{x}_{sp}}{1 - \hat{x}_{sp}} \right)^2 \left(\frac{t_{min}}{2c(\hat{y})} - \hat{z}(1) \right) H(\hat{x}_{sp}) \quad (\text{E.3})$$

with $\hat{x} = [0, \dots, 1]$, $\hat{x}_{sp} = 0.35$ the starting point of the thickness correction function, H the Heaviside function, and $\bar{z}(1)$ the original thickness of the section at the trailing edge. This function effectively increases the symmetrical offset of the NACA0009 hydrofoil (continuously) smoothly from 35% to 100% chord. The NACA0009 hydrofoil is plotted in fig. 5.3 with the added thickness for $c = 150 \text{ mm}$ and $c = 50 \text{ mm}$ (Tip Ellipse). A minimum trailing edge thickness of $t_{min} = 0.4 \text{ mm}$ was chosen in consultation with the manufacturer.

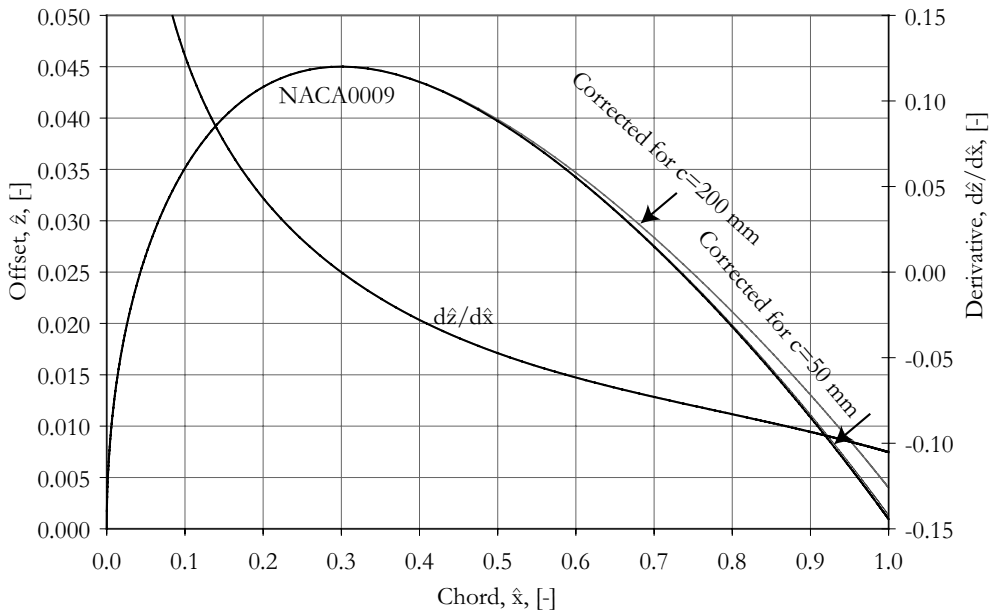


Figure 5.3 The thickness correction is added and plotted for the NACA0009 section. For the chord length of $c = 150 \text{ mm}$ the correction is negligible and modest for $c = 50 \text{ mm}$. No appreciable change in the derivative of the section is present.

E.5 Geometry of the Ellipse hydrofoils

The Ellipse hydrofoil has an angle of attack distribution increasing toward to tip.

$$\alpha(\hat{y}) = \alpha_M \frac{e^{\alpha_\gamma \hat{y}} - 1}{e^{\alpha_\gamma} - 1} \hat{y} \quad (\text{E.4})$$

with α_γ a constant. This function is chosen to have a zero derivative at the root staying low for small values of \hat{y} so that the root of the foil will remain unloaded, correcting for the upwash from the wake as calculated specifically for these hydrofoils by Koop *et al.* (2006).

The amplitude α_M determines the eventual maximum geometric angle of attack for both hydrofoils. Note that the entire hydrofoil—as a rigid body—always rotates around $(\hat{x}, \hat{z}) = (0.5, 0)$, the origin of the frame of reference of the test section. The chord distribution for all Twist hydrofoils is constant at $c = 300 \text{ mm}$. The chord distribution for the Ellipse hydrofoil is elliptic. The chord distribution is not allowed to become zero at $\hat{y} = 1$ but to a length c_T - truncating the ellipse to avoid the thickness becoming zero. The expression for the chord distribution is

$$c(\hat{y}) = \sqrt{(1 - \hat{y}^2) c_R^2 + \hat{y}^2 c_T^2} \quad (\text{E.5})$$

The Ellipse hydrofoils have a chord length $c_R = 200 \text{ mm}$ at the root and a chord length $c_T = 50 \text{ mm}$ at the tip for all Ellipse type hydrofoils.

For a propeller, the generator line is an axis radiating outward from the propeller hub (the root). Skew is defined as the offset of the foils mid chord point from the generator line along its mean line. Unfortunately this will result in a curvilinear system as the chord lines are rotated with $\alpha(\hat{y})$. Here, skew is taken as a translation of the local section along the undisturbed flow direction, x . The skew of the Ellipse is given as

$$s(\hat{y}) = c(\hat{y}) - c_R \quad (\text{E.6})$$

The mid chord point of the top aligns with the trailing edge of the chord at the wall. The rake follows a similar description as the angle of attack distribution, taken perpendicular to the skew

$$r(\hat{y}) = r_T \frac{e^{r_\gamma \hat{y}} - 1}{e^{r_\gamma} - 1} \hat{y} \quad (\text{E.7})$$

E.6 Miniature pressure transducer location

The following tables present the locations of the miniature pressure transducers for the Twist-11N and Twist-11N-EPFL hydrofoils.

Name	Section	α_M [°]	α_γ [-]	$\alpha_{\hat{x}}$ [-]	r_T [mm]	r_γ [-]	P
Twist-8N	NACA0009	8	-	0.50	0	-	y
Twist-11N	NACA0009	11	-	0.75	0	-	n
Twist-11E	Eppler YS-920	11	-	0.75	0	-	y
Twist-14N	NACA0009	14	-	0.75	0	-	y
Ellipse-8N	NACA0009	8	7	0.50	0	-	n
Ellipse-11N	NACA0009	11	7	1.00	20	1	n

Table E.3 Definition of the tested hydrofoils with parameters according to eq. 3.8 and E.7. The last column indicates whether or not a hydrofoil is also manufactured in transparent perspex.

Twist-11N								
	c	s	c			s		
1	40%	40%	8	5%	50%	15	50%	40%
2	75%	50%	9	2.5%	50%	16	5%	30%
3	50%	50%	10	5%	40%	17	10%	30%
4	40%	50%	11	10%	40%	18	20%	30%
5	30%	50%	12	20%	40%	19	5%	20%
6	20%	50%	13	30%	40%	20	5%	10%
7	10%	50%	14	50%	40%			

Table E.4 Position of the pressure taps of the sensor chambers of the Twist-11N in percent chord and span. All sensors are placed on the suction side, except sensor 1, which is placed on the pressure side.

Twist-11N EPFL					
	c		s		
1	40%	70%	9	40%	50%
2	75%	50%	10	5%	40%
3	10%	90%	11	20%	40%
4	10%	80%	12	30%	40%
5	10%	60%	13	40%	40%
6	5%	50%	14	5%	30%
7	20%	50%	15	5%	20%
8	30%	50%	16	5%	10%

Table E.5 Position of the pressure taps of the sensor chambers of the Twist-11N-EPFL in percent chord and span. All sensors are placed on the suction side, except sensor 1, which is placed on the pressure side.

Appendix F

Force balance

The sensors used are *ATI-industrial automation's* FT-Delta SI-660-60 and FT-Delta SI-330-30 (see table F.1). With a cross section of 92 mm, the sensor should have a range of at least 600 N in the y -direction when the tunnel is at 100 mbar. The lift and drag of the hydrofoil are much lower. The sensor is a monoblock wheel with three spokes with the inner part connected to a measurement adapter plate and each spoke fitted with two pairs of opposing strain gauges. The sensor is factory calibrated by applying a variety of loads in several (26) combinations, resulting in a calibration matrix for the combined 12 channels. Crosstalk is thus implicitly corrected for by the calibration within its specified range. The sensor is mechanically protected against overloading. The sensor is not water-tight and is therefore placed outside the cavitation tunnel complicating the setup.

	Range	Sensitivity	Stiffness	Overload	Error
$F_{x,z}$	$\pm 660\text{ N}$	$1/32\text{ N}$	$37 \cdot 10^6\text{ N/m}$	515%	0.76%
F_y	$\pm 1980\text{ N}$	$1/16\text{ N}$	$61 \cdot 10^6\text{ N/m}$	606%	0.23%
$M_{x,z}$	$\pm 60\text{ Nm}$	$3/1600\text{ Nm}$	$52 \cdot 10^3\text{ Nm/rad}$	367%	0.38%
M_y	$\pm 60\text{ Nm}$	$3/1600\text{ Nm}$	$94 \cdot 10^3\text{ Nm/rad}$	700%	0.14%

Table F.1 Specifications of the load cell, type FT-Delta SI-660-60. The FT-Delta SI-330-30 has identical characteristics but half the range at twice the sensitivity.

Two $\varnothing 180\text{ mm}$ stainless steel disks were inserted in the windows holding the sensor and the hydrofoil (see fig. 6.1). The entire disk can be rotated to change the angle of attack of the hydrofoil. A flexible seal is used to keep the setup water-tight. The flexibility of the seal should be low enough not to influence the measurement but high enough that it does not deform too much with changes in pressure, clearly conflicting demands. The forces and moments versus pressure are plotted in fig. 6.2 for the load sensor. For pressures above 80 kPa the influence of the seal is clearly visible in F_X and F_Z . For low pressures the seal is seen to be pulled into the slit between parts 1 and 4, fig. 6.1, lowering the effective area the pressure acts upon by 6.2 %. Below this value—as is always the case during cavitation tests—the values are nearly linear.

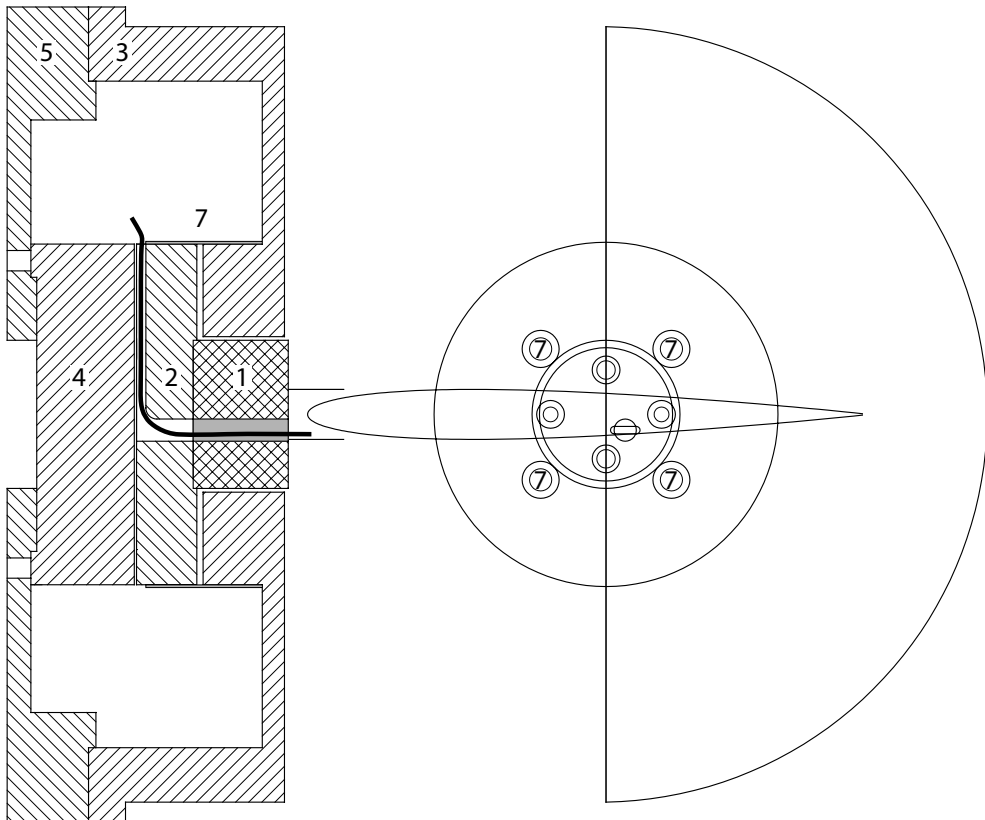
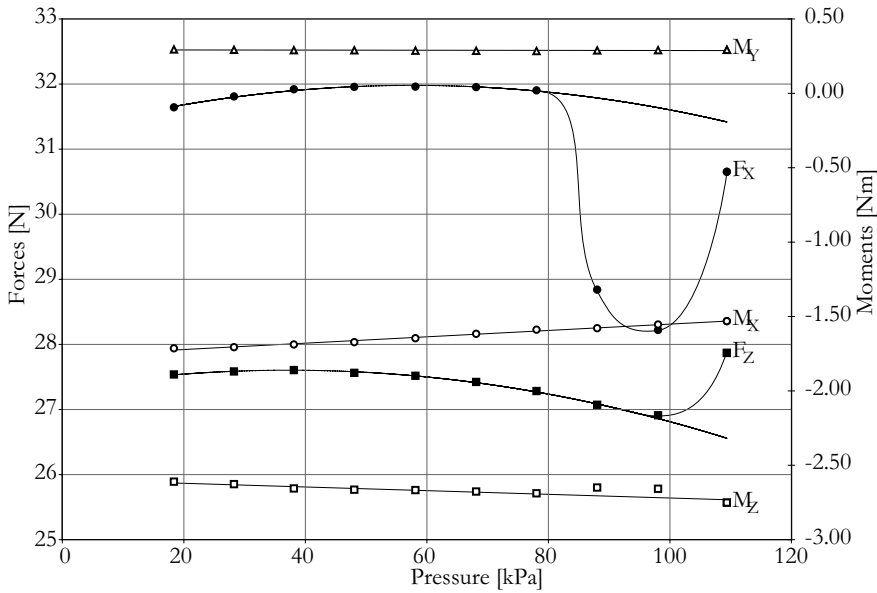


Figure 6.1 Cross section and front view of the mounting of the hydrofoil. When preparing this setup, the hydrofoil is first connected to its mounting block (1), then bolted to an adapter plate (2) through the main disk (3) fitted in a tunnel window. Next, the force sensor (4) is bolted to the cover plate (5). The sensor is bolted to the adapter plate from inside the test section through a series of access ports (6). Finally, the seal (7) is put into place. Note that the foil mounting (1) and adapter plate (2) do not touch the main disk (3). O-rings are placed between all parts exposed to water, including all bolt heads. The wiring of the miniature pressure transducers (black line) is routed through the mounting block.

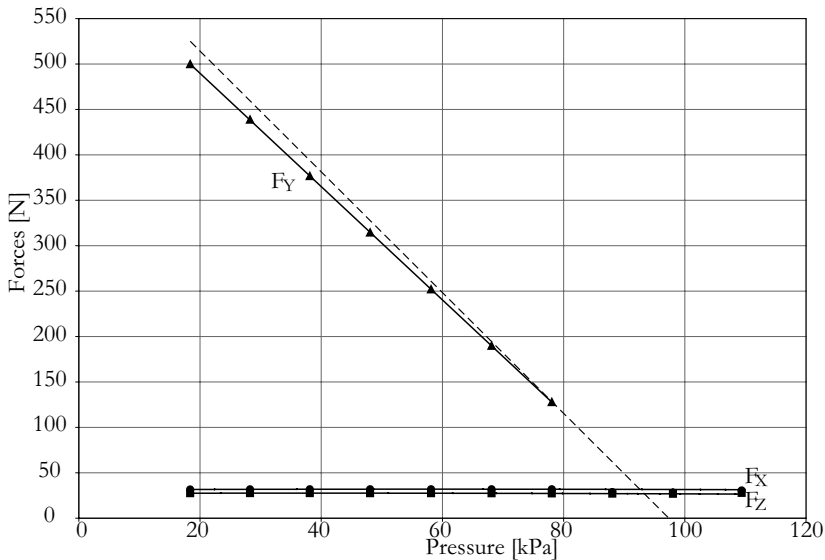
The lines as drawn in fig. 6.2 are used for a pressure-dependent calibration. The pressure during calibration is not equal to the pressure in outlet plane during testing due to the induced velocity of the hydrofoil. For the symmetric hydrofoil, it is assumed that the force component F_Y is caused only by the effective pressure on the wall and that the hydrofoil itself does not experience a net F_Y . The force F_Y is thus interpreted as an indirect pressure measurement. From fig. 6.2 can be seen that the dependency on pressure of the other signals is small.

Since the load cell optically blocks one tunnel window, it cannot be used during PIV measurements at both sides of the test section at the same time. One load cell was present during all measurements as the changes in loading can be used to determine the frequency and phase response of the hydrofoil during tests with the flow oscillator (See s. 3.7).

Due to availability constraints of the second load cell, two load cells were used only when the hydrofoil was fitted with the miniature pressure transducers. When using two load cells, the hydrofoil was firmly bolted to one load cell, and the other end of the hydrofoil was fitted with a pin inserted into the mounting block. This pin restricted horizontal and vertical movement only. Note that the setup is not statically indeterminate in the classical textbook exercise sense as all reaction forces are measured, and not derived from static equilibrium equations. Misalignment, and the seal and test section deformation will result in a change in most measured channels. nevertheless, net force measured at the load cells must be equal to the net load on the hydrofoil in addition to the influence of the seals. Calibration tests confirmed that the net force measured by applying weights to the hydrofoil was fully linear in its response and did not change when the weights were shifted over the hydrofoil. Other forces and moments were not checked, as it is the lift force that is primary interest.



F_X , F_Z , M_X , M_Y , and M_Z as a function of pressure in the test section at rest



All force and moment components as a function of pressure in the test section at rest.

Figure 6.2 The top figure shows the influence of the seal above 80 kPa in F_X , F_Z , and M_Z . The bottom figure plots all three force components. The dashed line is the integrated force acting on the sensor area (fig. 6.1, item 4) due to the tunnel pressure indicating the influence of the seal on F_Y reducing the effective area by 6.2%. Note that the crosstalk is visibly low in F_X and F_Z .

Appendix G

Oscillator motion

The crank shaft mechanism enforces a non-symmetrical motion on the flow oscillator deflectable trailing edge flaps. If ensemble averaged results are to be calculated, the amplitude, frequency, and phase of the flow oscillator need to be determined as accurately as possible. A schematic of the oscillator is given in fig.7.1. The angle θ' of the oscillator at point D can be expressed as function of the angle of the drive at point A , θ . Point C is the rotation of $\mathbf{e}_z \omega_{DC} \times \mathbf{r}_{DC}$ and must be the same point as the rotation of AB , $\mathbf{e}_z \omega_{AB} \times \mathbf{r}_{AB}$, plus the relative rotation of B to C , or $\mathbf{e}_z \omega_{BC} \times \mathbf{r}_{BC}$

$$\mathbf{e}_z \omega_{dc} \times \mathbf{r}_{dc} = \mathbf{e}_z \omega_{ab} \times \mathbf{r}_{ab} + \mathbf{e}_z \omega_{bc} \times \mathbf{r}_{bc} \quad (\text{G.1})$$

equating

$$\begin{bmatrix} \omega_d \\ \omega_{bc} \end{bmatrix} = \begin{bmatrix} y_d - y_c & y_c - y_b \\ x_c - x_d & x_b - x_c \end{bmatrix}^{-1} \begin{bmatrix} y_b - y_a \\ x_a - x_b \end{bmatrix} \omega_{ab} \quad (\text{G.2})$$

from which ω_{BC} and ω_{DC} can be determined at a given $\omega_{AB} = \theta$. The exact location of C can be determined by simple geometry, as $r_{CE}^2 = r_{BC}^2 - r_{BE}^2 = r_{CD}^2 - r_{DE}^2$ and $r_{BE} = r_{DB} - r_{DE}$, it follows that $r_{DE}^2 = \frac{1}{2} r_{DB}^2 (-r_{BC}^2 + r_{CD}^2 + r_{BD}^2)$ from which the angle θ' can be determined. The above can be evaluated to give an indication of the deviation from a depending on the arm lengths of the crank shaft mechanism. Figure 7.2 presents the result of a simulation of the motion of the oscillator angular position using the dimensions of the present setup ($r_{AB} = 20 \text{ mm}$, $r_{AB} = 590 \text{ mm}$, $r_{AB} = 200 \text{ mm}$). The amplitude can be changed by changing the length r_{AB} . Most experiments were made with a single setting resulting in an amplitude of about 2.9° .

From the analysis it is clear that the motion is very close to an exact sine, but has its center root slightly ahead of half a period. If the full sine period runs from its roots r_1 to r_3 with central root r_2 , an approximation can be taken with a θ dependent phase

$$\theta'(\theta) \cong \zeta_{\theta'} \sin \left(\theta + \frac{1}{2} \left(\frac{1}{2} - \frac{r_2 - r_1}{r_3 - r_1} \right) (1 - \cos \theta) \right) \quad (\text{G.3})$$

depending on a predetermined amplitude $\zeta_{\theta'}$.

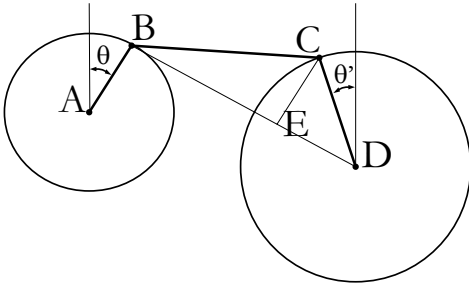


Figure 7.1 Schematic of the flow oscillator crankshaft mechanism. The drive angle θ covers 360° , the range of θ' is limited to a few degrees.

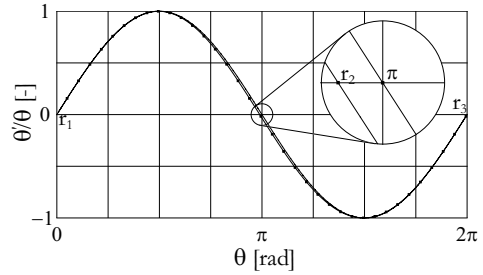


Figure 7.2 The oscillator angle is plotted over a period and compared with an exact sine. The oscillator has its central root, r_2 , ahead of a sine due to its non-symmetrical crank shaft mechanism.

The deflection angle of the flaps is measured by means of a pot meter, but was hampered by significant noise. A low pass FFT greatly increases the signal to noise ratio (taking twice the dominant frequency in the spectrum as a cut-off frequency) but cannot yield accurate phase and frequency information. An algorithm finding zero crossings and local maxima and minima of the low-passed signal was used to match the above equation as a predictor of the signal. The low-pass signal invariably shows Gibb's effects near the edges (inherent of the FFT process) so information near the edges of the domain was avoided. An error estimate is not available as the procedure is non-statistical in nature, but the results can be plotted and were often found the match the measurements perfectly. Low oscillation frequencies—with less than 2 periods per measurement—gave unreliable results requiring a longer measurement time.

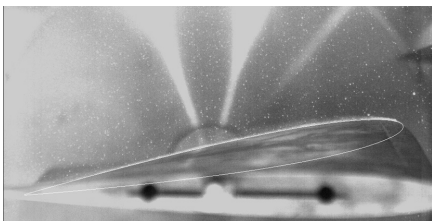
Appendix H

Pre-processing sequence

- 1 A standard Gaussian 9×9 kernel is defined

$$K_G \equiv K_G(9, 0.5) \quad (\text{H.1})$$

- 2 An image without the optical filter is used to find location of the hydrofoil to within 0.5 mm and to determine its angle of attack within 0.25° . The outline of the hydrofoil is placed on the reflection of the light sheet. An original unprocessed PIV image with cavitation is shown at right.

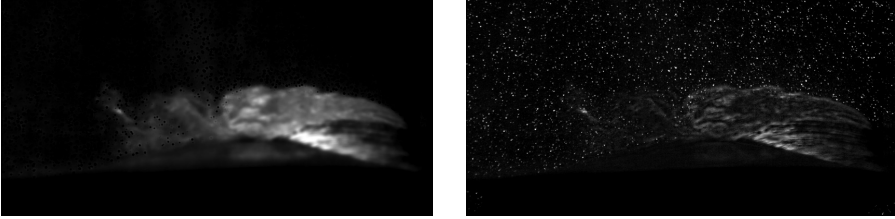


- 3 Next, a minimum filter is applied to the image in order to remove particle images within a 12×12 window. This result is smoothed with the Gaussian kernel (left)

$$\bar{I} = S(I, K_{12}, 1) K_G \quad (\text{H.2})$$

Subtracting this average from the original picture results in an image with mainly gradients. As this function can be locally negative, the minimum value of the gradient image is added (right)

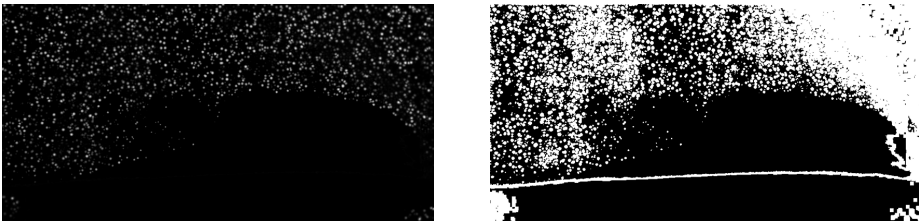
$$\tilde{I} = I - \bar{I} + \min(I - \bar{I}) \quad (\text{H.3})$$



- 4 The real part of the mSTD filter is applied to identify all particles in a low background level (left). Taking all non-zero points results in the first image filter (right).

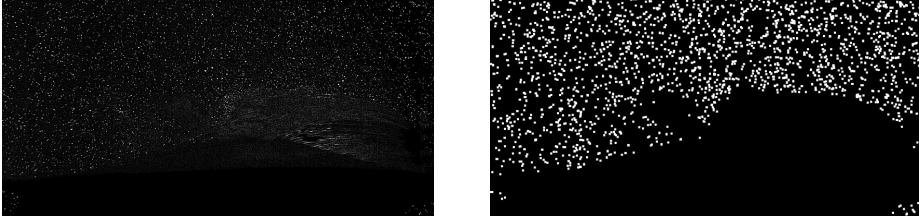
$$I_1 = \Re(\tilde{I} K_M(K_G)) \quad (\text{H.4})$$

Note that this step captures virtually all particles.



- 5 The Laplacian kernel is applied to locate all local maxima (left). In order to isolate pixels only, a threshold is implemented (Half the dynamic range of the picture). In order to reduce the risk of peak locking by retaining information around the particles, the pixels found are replaced by 5×5 blocks (right)

$$\mathbf{I}_2 = \left(\tilde{\mathbf{I}} K_{L8} > 512 \right) K_5 \quad (\text{H.5})$$

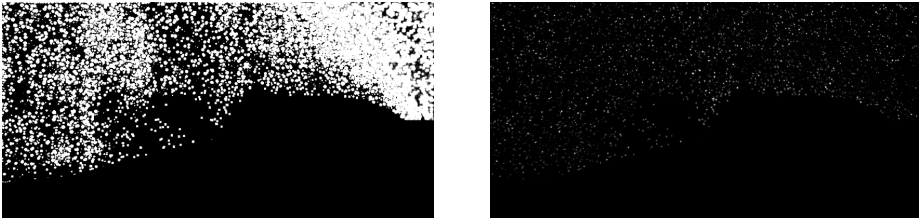


- 6 A mask containing the known hydrofoil location is defined, in order to exclude regions where water and vapor are known to be not present. This mask will exclude cavity reflections on the hydrofoil surface found by the above steps.

$$\mathbf{I}_3 \equiv \text{predefinedmask} \quad (\text{H.6})$$

The final filter combines the filters \mathbf{I}_1 and \mathbf{I}_2 and subtracts the predefined mask \mathbf{I}_3 (left). The final filter is multiplied with the average image $\tilde{\mathbf{I}}$ to be used for PIV interrogation (right)

$$\mathbf{R} = \tilde{\mathbf{I}} \cdot [(\mathbf{I}_1 > 0 \vee \mathbf{I}_2 > 0) \wedge (\mathbf{I}_3 > 0)] \quad (\text{H.7})$$



Note that the window sized of the kernels and threshold values for \mathbf{I}_1 and \mathbf{I}_2 depend on particle size and background. These values require some training toward an effective solution. The modified standard deviation performs well with images with a low-to-medium particle density and a very low background value. The Laplacian filter picks up local hotspots regardless on background intensity, so concentrated reflections of the cavity interface are sometimes picked up resulting in an isolated vector, which can be easily removed using the post-processing tools of the PIV software.

Appendix I

Cavity outline sequence

- 1 Starting from App. H, step 2. The real part of the mSTD filter is applied to identify all particles in a low background level resulting in the first image filter.

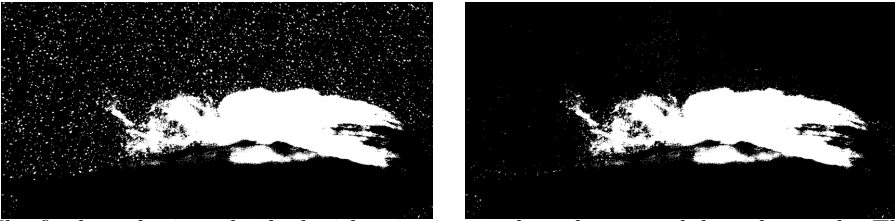
$$\mathbf{I}_1 = \Re(\mathbf{I}K_M(K_G)) \quad (\text{I.1})$$

- 2 An average intensity is taken whereby all values above $\pm 10\%$ intensity are retained. The exact value of the highpass filter was set at 30 counts. Note that the picture is now reduced to a 1 bit image (left)

$$\mathbf{I}_2 = \mathbf{I}(\mathbf{I} > \pm 10\%) \quad (\text{I.2})$$

All regions in \mathbf{I}_2 where the results of the PIV preprocessing filters \mathbf{I}_1 is nonzero, are set to zero (right)

$$\mathbf{I}_2(\mathbf{I}_1 > 0) = 0 \quad (\text{I.3})$$



- 3 The final results is multiplied with a 3×3 unity kernel to consolidate the result. The image is now 4-bit, with a gradual transition from the cavity edge.

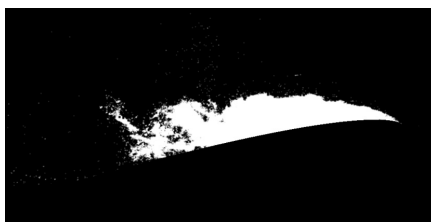
$$\mathbf{I}_3 = \mathbf{I}_2 K_3 \quad (\text{I.4})$$

- 4 A mask containing the known hydrofoil location is defined, in order to exclude regions where water and vapor are known to be not present. This mask will exclude particle reflections on the hydrofoil surface found by the above steps.

$$\mathbf{I}_4 \equiv \text{predefinedmask} \quad (\text{I.5})$$

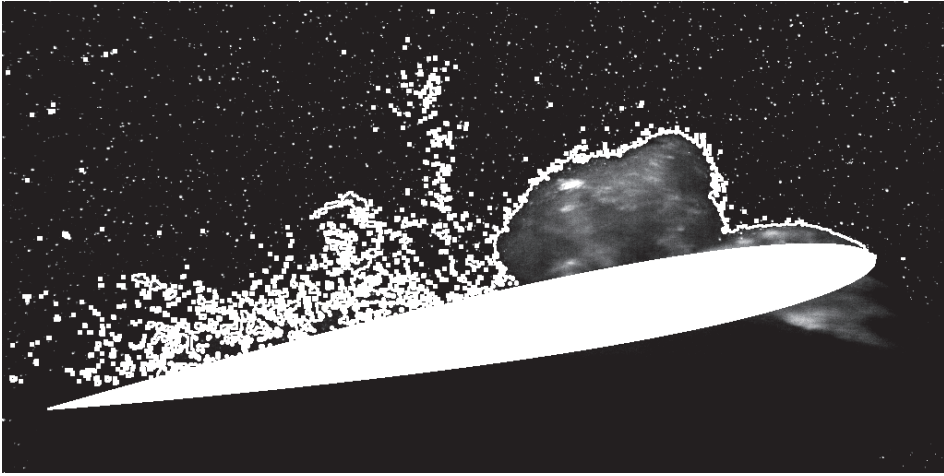
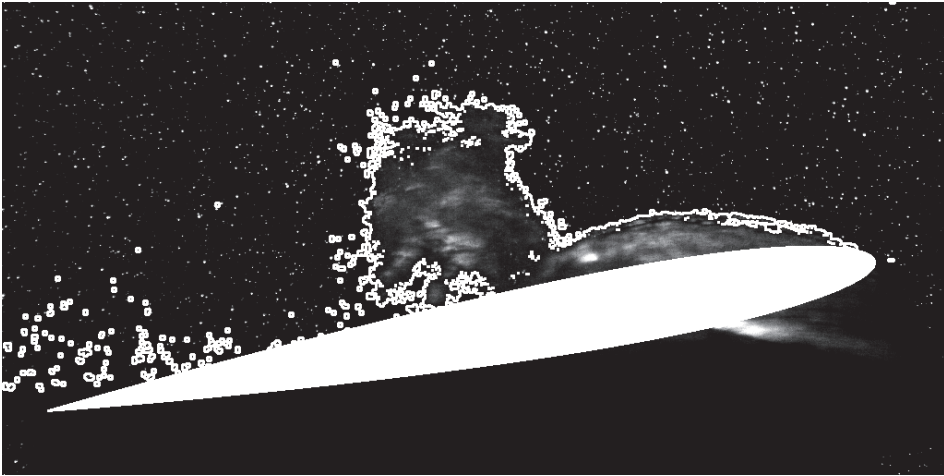
- 5 The resulting image, containing the cavity, is the resulting image \mathbf{I}_3 minus the known mask location, \mathbf{I}_4 :

$$\mathbf{R} = \mathbf{I}_4 \cdot [(\mathbf{I}_3 > 0) \wedge (\mathbf{I}_4 > 0)] \quad (\text{I.6})$$



The routine identified the cavity outline as well as one would determine it by eye, except in the closure region. Although the shed vortices and bubbles were found with a sensitive filter, noise and tunnel reflections were also located. A limited amount of noise was accepted at this point. Both techniques use the same functions and can be combined to reduce calculation time.

S

9.1.1 $t = 0.0 \text{ ms}$ 9.1.2 $t = 3.3 \text{ ms}$

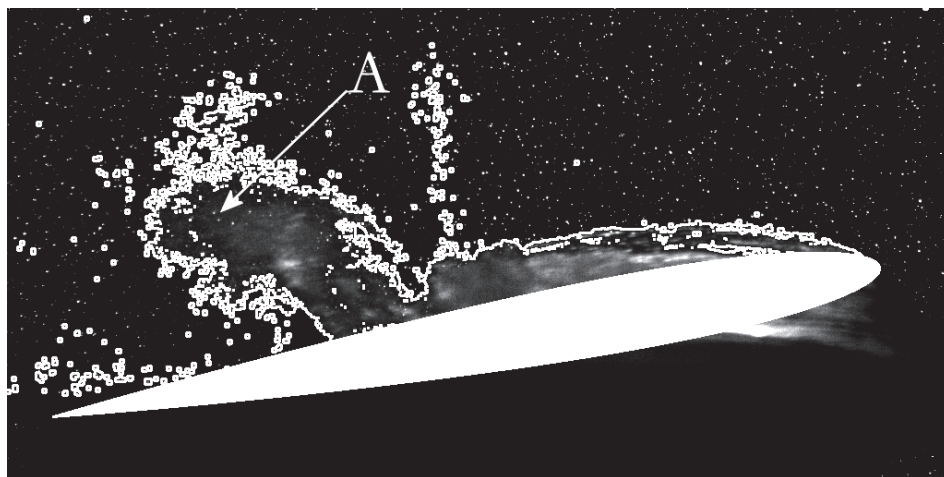
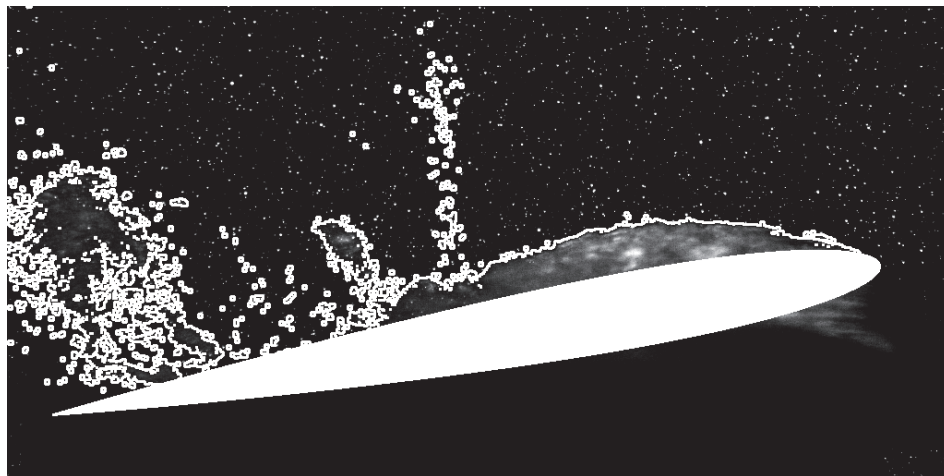
9.1.3 $t = 6.6 \text{ ms}$ 9.1.4 $t = 10.0 \text{ ms}$

Figure 9.1 An example of the cavity detection interface result as used fig. 5.27 and fig. 5.28. Raw PIV images showing the detected vapor regimes in white on the Twist-11N at $\alpha = -1^\circ$, $V_0 = 6.9 \text{ m/s} \pm 3.9\%$, $\sigma = 1.26 \pm 6.5\%$, $f_{FO} = 31.64 \text{ Hz}$. The hydrofoil location—with its leading edge at right—is indicated. The detection algorithm of the cavity clearly captures the attached cavity and the shed vapor structure. In fig. 9.1.3 the shed structure is captured but already shows particles in the captured region (A). The boundary of the vapor structure is not well-defined and the interface is now an encompassing vapor region. The vertical line of smaller captured regions is a reflection in the rear tunnel wall. These incidental smaller regions and reflections—most of them a pixel small but clearly outlined for presentation purposes—are averaged out in the three-dimensional reconstruction as can be seen in fig. 5.27 and fig. 5.28.

Appendix J

Kelvin-Helmholtz instability

The cavity is modeled as a two-dimensional dividing streamline around $z = 0$. The regions above and below the streamline are designated I and II , having a thickness h_I and h_{II} . A velocity difference V is present at the dividing streamline. Potential flow is assumed. A perturbation potential $\Phi = F(z) e^{i(kx - \omega t)}$ is added due to a linearized dividing streamline perturbation $\eta = C e^{i(kx - \omega t)}$. Substitution in Laplace's equation results in

$$\frac{d^2 F}{dz^2} - k^2 F = 0 \quad (\text{J.1})$$

with a solution in each region in the form of

$$F_i = c_{i,1} e^{kz} + c_{i,2} e^{-kz} \quad (\text{J.2})$$

The boundary conditions on the horizontal extremities of the domain are

$$\frac{\partial F}{\partial z} \Big|_{z=h_I} = \frac{\partial F}{\partial z} \Big|_{z=-h_{II}} = 0 \quad (\text{J.3})$$

so $c_{i,2} = -c_{i,1} e^{2kh_i}$ and the potential is

$$\Phi_i = c_i (e^{kz} - e^{k(2h_i - z)}) \frac{\eta}{C} \quad (\text{J.4})$$

The potential must match on the perturbed interface or

$$\frac{\partial \Phi}{\partial z} \Big|_{z=\eta} = \frac{\partial \eta}{\partial t} + u \frac{\partial \eta}{\partial x} = -i(\omega + uk) C e^{i(kz - \omega t)} \quad (\text{J.5})$$

with the local horizontal velocity $u = \tilde{u} \pm \frac{1}{2}V \approx \frac{1}{2}V$ as $V \gg \tilde{u}$. Matching the potential gives

$$c_1 = -i \frac{\frac{1}{2}Vk + \omega C}{1 + e^{2kh_I} k} \quad c_2 = -i \frac{\frac{1}{2}Vk - \omega C}{1 + e^{-2kh_{II}} k} \quad (\text{J.6})$$

The dynamic boundary condition requires a continuous pressure. Applying Bernoulli

$$\rho_i \frac{\partial \Phi_i}{\partial t} \pm \frac{1}{2} \frac{\partial \Phi_i}{\partial x} V + p_i + \rho g \eta + \gamma_i \frac{\partial^2 \eta}{\partial x^2} = C_i \quad (\text{J.7})$$

with γ the surface tension, acting on only one fluid. Note that for the undisturbed streamline Bernoulli reads

$$\frac{1}{2} \rho_i \left(\pm - \frac{1}{2} V \right)^2 + p_0 = C_i \quad (\text{J.8})$$

which can be subtracted from eq. J.7. Subtracting eq.J.7 for both fluids in region I and II , substituting eq. J.6 and writing $\gamma_i \frac{\partial^2 \eta}{\partial x^2} = -\gamma_i k^2 \eta$ yields:

$$\begin{aligned} & \frac{\omega^2}{k^2} (\rho_I \tanh kh_I + \rho_{II} \tanh kh_{II}) + \frac{\omega V}{k} (\rho_I \tanh kh_I - \rho_{II} \tanh kh_{II}) \\ & + (\rho_I \tanh kh_I + \rho_{II} \tanh kh_{II}) \frac{1}{4} V^2 + \frac{(\rho_I - \rho_{II}) g}{k} + (\gamma_I - \gamma_{II}) k = 0 \end{aligned} \quad (\text{J.9})$$

This parabolic expression in terms of ω results in stable surface perturbation when ω is real, or the discriminant of the above should not be negative or (after rewriting)

$$\begin{aligned} & \rho_I \rho_{II} V^2 \tanh kh_I \tanh kh_{II} \\ & + (\rho_I \tanh kh_I + \rho_{II} \tanh kh_{II}) \left((\rho_I - \rho_{II}) \frac{g}{k} + (\gamma_I - \gamma_{II}) \right) > 0 \end{aligned} \quad (\text{J.10})$$

As the experiments were performed with the cavity on the bottom of the hydrofoil, region I is vapor and region II is fluid, or

$$\begin{aligned} \rho_I &= \rho_v & \rho_{II} &= \rho_l \\ \gamma_I &= 0 & \gamma_{II} &= \gamma \\ h_I &= t & h_{II} &= -\infty \end{aligned} \quad (\text{J.11})$$

so

$$-\rho_v \rho_l V^2 \tanh kt + (\rho_v \tanh kt - \rho_l) \left((\rho_l - \rho_v) \frac{g}{k} - \gamma k \right) > 0 \quad (\text{J.12})$$

As $\rho_l \gg \rho_v$ (To illustrate, at 293° K, $\rho_l = 998.1 \text{ kg/m}^3$ and $\rho_v = 0.017 \text{ kg/m}^3$)

$$\begin{aligned} \rho_l + \rho_v \tanh kt &\approx \rho_l \\ \rho_l - \rho_v &\approx \rho_l \end{aligned} \quad (\text{J.13})$$

so the velocity between the layers can be expressed as

$$V < \sqrt{\frac{\gamma k^2 - \rho_l g}{\rho_v k \tanh kt}} \quad (\text{J.14})$$

For a real velocity, this means that

$$k > \sqrt{\frac{\rho_l g}{\gamma}} \quad (\text{J.15})$$

giving a maximum wave length of the disturbance of

$$\lambda_{max} < 2\pi \sqrt{\frac{\gamma}{\rho_l g}} \quad (\text{J.16})$$

With a surface tension of $\gamma = 7.29 \cdot 10^{-2} \text{ J/m}^2$, this wave length is $\lambda_{max} \approx 1.71 \cdot 10^{-2} \text{ m}$. Note that the velocity difference with this wave length between media reduces to zero for the cavity in either the top or bottom layer.

Appendix K

Additional experimental results

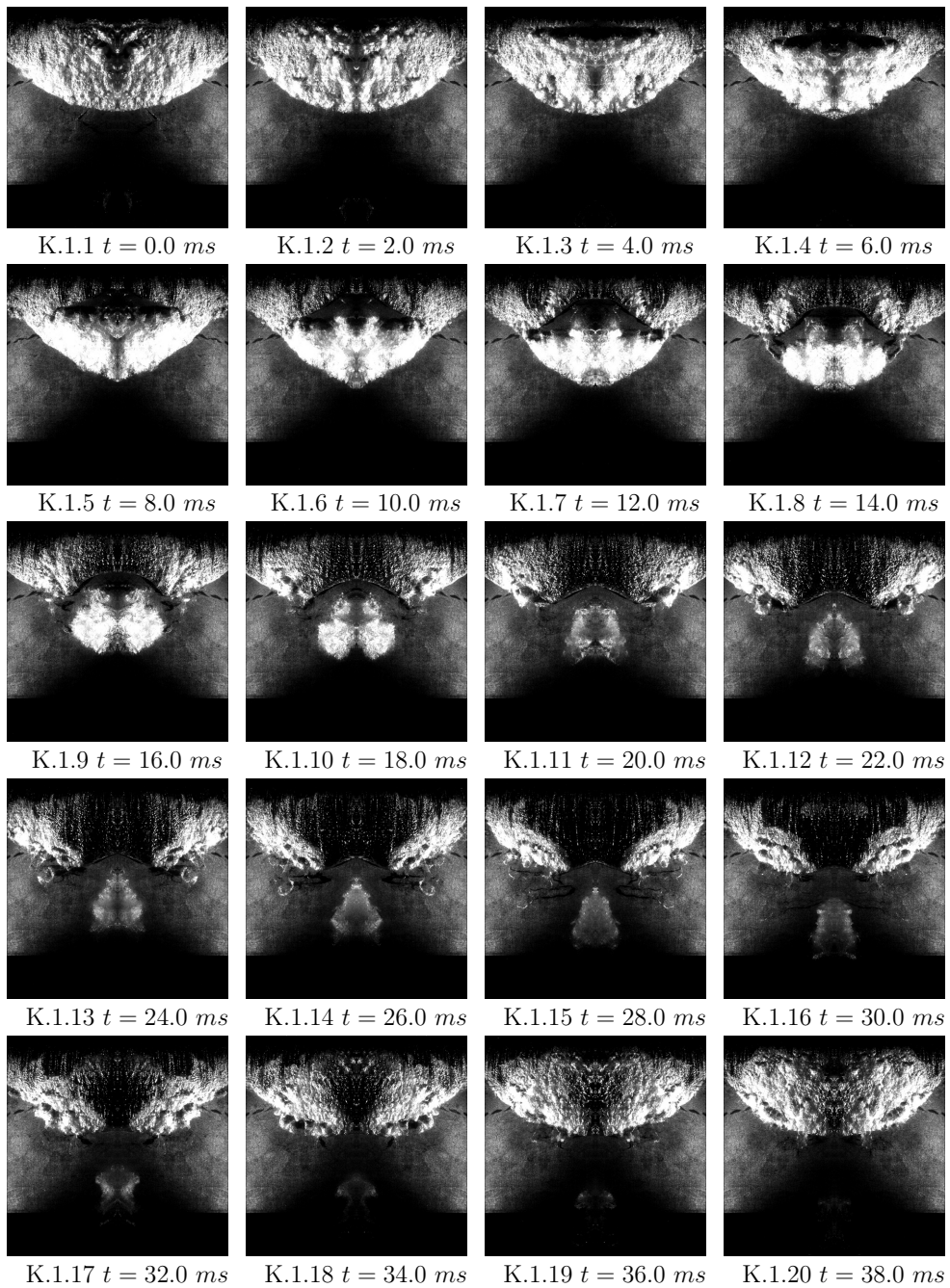


Figure 1 The Twist-11N hydrofoil at $\alpha = -1^\circ$, $V_0 = 6.58 \text{ m/s} \pm 4.1\%$, $\sigma = 1.13 \pm 6.9\%$. The 20 images show a full oscillation period. The left side of the image *is mirrored* as the illumination was insufficient at the right side. Note the similarity with the shedding for the Twist-8N hydrofoil in fig. 5.11 op page 120

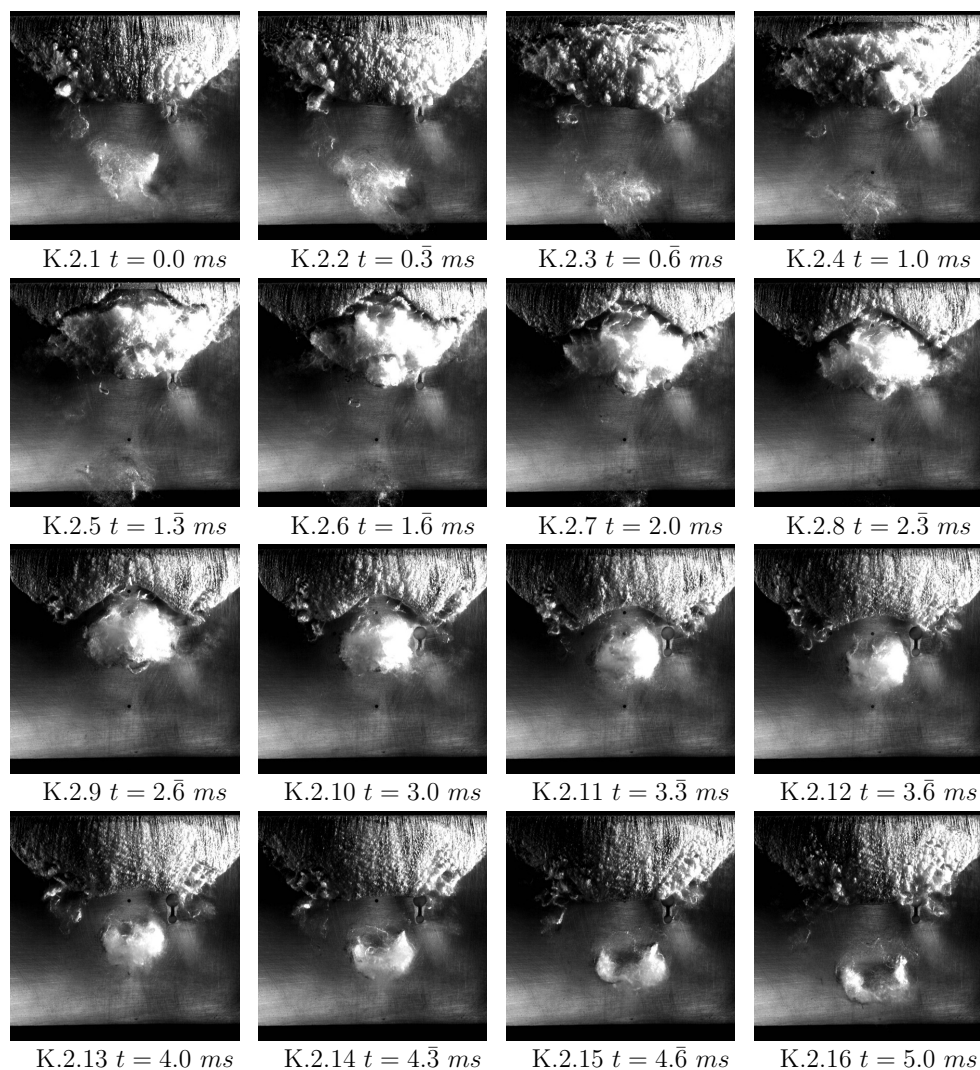


Figure 2 The Twist-11EPFL hydrofoil at $\alpha = -2^\circ$, $V_0 = 14.00 \text{ m/s}$, $\sigma = 1.11$, recorded and presented at $3,000 \text{ Hz}$. The shedding frequency is $f = 132 \pm \text{Hz}$, determined from local pressure measurements. The viewing area is not symmetrical as the viewing windows of the EPFL cavitation tunnel are placed eccentrically.

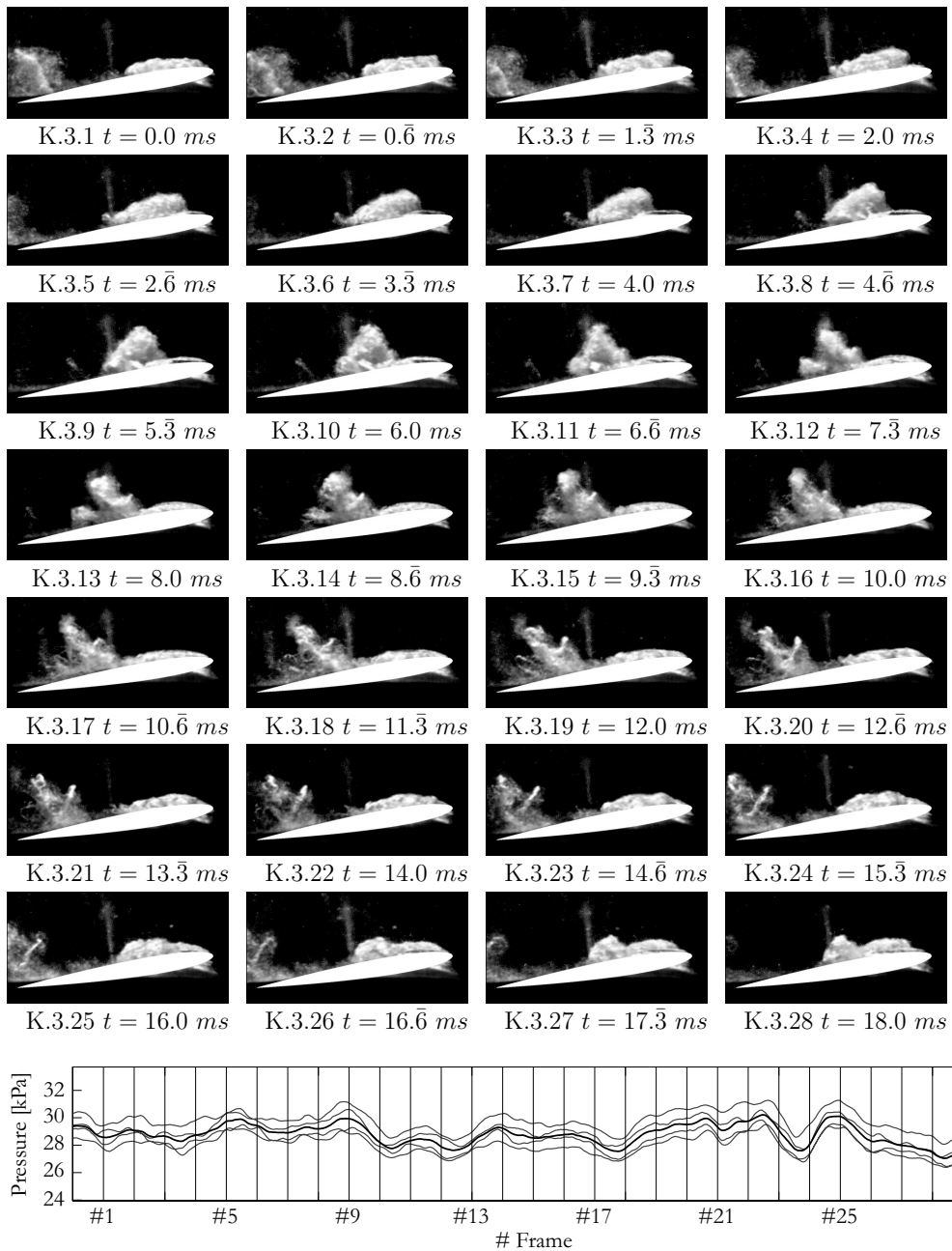


Figure 3 $\alpha = -2^\circ$, $V_0 = 6.75 \text{ m/s} \pm 3.95\%$, $\sigma = 1.10 \pm 6.74\%$. Shedding cycle from the PIV imaging presented at 1500 Hz (PIV particles removed by means of image analysis). The foil length is drawn to scale and positioned in the mid plane. The outlet plane pressure—measured on each tunnel wall—does not show a clearly identifiable trend with the shedding.

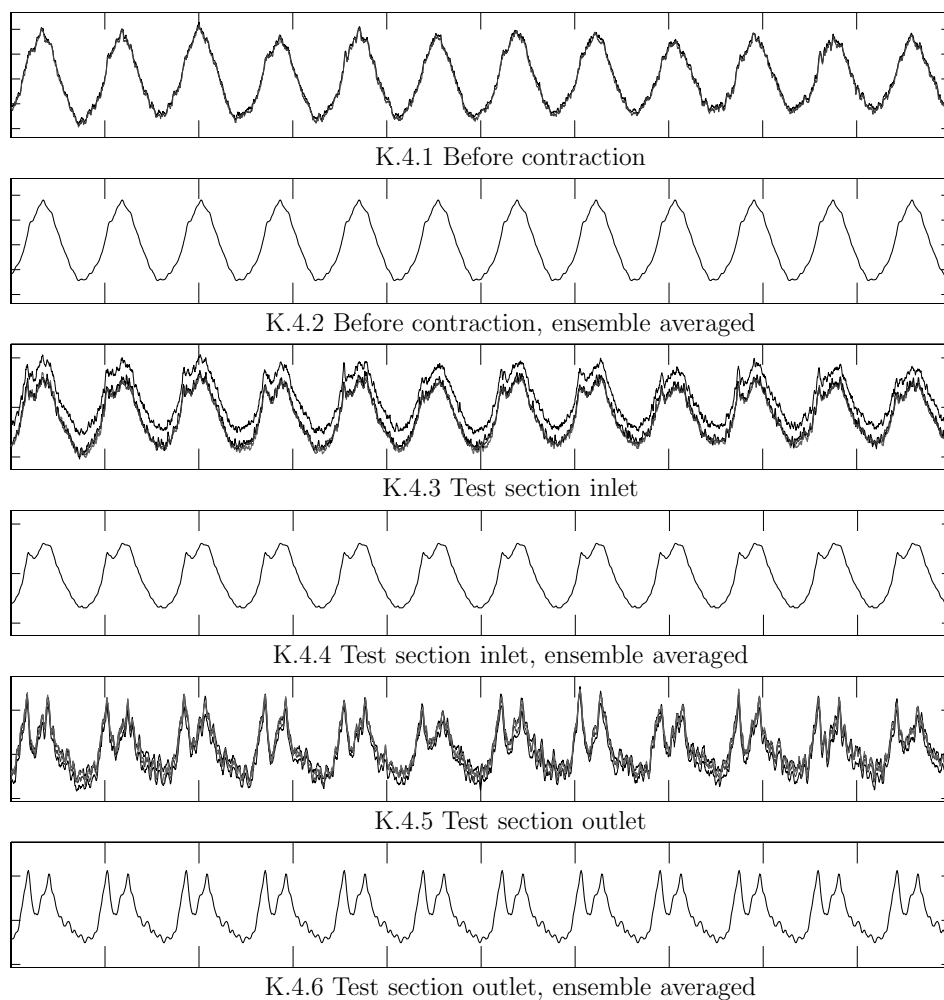


Figure K4 All pressure signals from the tunnel walls (scale removed) for one second during flow oscillation at 12 Hz before the contraction, at the test section entrance, and test section outlet plane, as in fig. 1, p. 59. All sensors are calibrated with the pressure at the tunnel central line. One sensor at the test-section inlet plane measures an offset due misalignment and did not participate in the determination of V_0 , p_0 , and σ . Note that the pressure measurements show similar values within a plane with only minor variations so that the pressure can be considered homogeneous in the planes at the inlet and outlet. The ensemble-averaged signal—for the presented case—shows good agreement indicating good repeatability from one oscillation to the next.

Bibliography

- ABBOTT, I. H. & VON DOENHOFF, A. E. 1959 *Theory of wing sections*. Dover Publications Inc, NY.
- ADRIAN, R. 1991 Particle-imaging techniques for experimental fluids mechanics. *Annu. Rev. Fluid Mech.* **23**, 261–304.
- ADRIAN, R.J., CHRISTENSEN, K.T. & LIU, Z.-C. 2000 Analysis and interpretation of instantaneous turbulent velocity fields. *Exp. in Fluids* **29**, 275–290.
- ARAKERI, V.H. 1975 Viscous effects on the position of cavitation separation from smooth bodies. *J. Fluid Mech.* **68(4)**, 779–799.
- ARNDT, R.E.A., ELLIS, C. & PAUL, S. 1995 Preliminary investigation of the use of air injection to mitigate cavitation erosion. *J. Fluids Eng.* **117**, 498–592.
- BACHERT, R. & STOFFEL, B. 2003 Messung instationärer, dreidimensionaler Effekte kavitierender Strömungen an einem Einzelprofil mit Hilfe der PIV / LIF Messtechnik. In *GALA-Fachtagung "Lasermethoden in der Strömungsmesstechnik"*, Braunschweig,.
- BALLICO, M 2000 Limitations of the Welch-Satterthwaite approximation for measurement uncertainty calculations. *Metrologia* **37**, 61–64.
- BELAHADJI, B., FRANC, J. P. & MICHEL, J. M. 1995 Cavitation in the rotational structures of a turbulent wake. *J. Fluid Mech.* **287**, 383–403.
- BERNAL, L.P. & ROSKO, A. 1986 Streamwise vortex structure in plane mixing layers. *J. Fluid Mech.* **170**, 449–525.
- BRENNEN, C.E. 1995 *Cavitation and bubble dynamics*. Oxford Engineering Science Series 44.
- BREWER, W. & KINNAS, S. 1997 Experiment and viscous flow analysis on a partially cavitating hydrofoil. *J. Ship Res.* **41(3)**, 161–171.
- BRILLOUIN, M. 1911 Les surfaces de glissement de Helmholtz et la resistance de fluides. *Annales de Chimie et de Physique* **23**, 145–230.

- CALLENAERE, M., FRANC, J.P. & MICHEL, J.M. 2001 The cavitation instability induced by the development of a re-entrant jet. *J. Fluid Mech.* **444**, 223–265.
- CARON, J.F, FARHAT, M. & AVELLAN, F. 2000 Physical investigation of the cavitation phenomenon. In *6th International Symposium on Fluid Control, Measurement and Visualization (Flucome 2000)*, Sherbrooke, Canada.
- CARON, J.-F. AND FARHAT, M. & AVELLAN, F. 2000 On the leading-edge cavity development of an oscillating hydrofoil. In *ASME Fluids Eng. Summer Div. Meeting, Boston, USA*.
- CASTRUP, H. 2000 Estimating category B degrees of freedom. In *Measurement and Science Conference, Anaheim*.
- CASTRUP, H. 2001 Distributions for uncertainty analysis. In *International Dimensional Workshop, Knoxville, TN*.
- CECCIO, S.L. & BRENNEN, C.E. 1991 Observations of the dynamics and acoustics of travelling bubble cavitation. *J. Fluid Mech.* **233**, 633–660.
- CHRISTENSEN, K.T. 2004 The influence of peak-locking errors on turbulence statistics computed from PIV ensembles. *Exp. in Fluids* **36**, 484–497.
- COUTIER-DELGOSHA, O., DEVILLERS, J.-F., LERICHE, M. & PICHON, T. 2005 Effect of wall roughness on the dynamics of unsteady cavitation. *J. Fluids Eng.* **127**, 726–733.
- CRIMI, P 1970 Experimental study of the effects of sweep on hydrofoil loading and cavitation. *J. Aeronautics* **4(1)**, 3–9.
- DANG, J. 2000 Numerical simulation of unsteady partial cavity flows. PhD thesis, Technical University of Delft, the Netherlands.
- DANG, J. & KUIPER, G. 1999 Re-entrant jet modeling of partial cavity flow on three-dimensional hydrofoils. *J. Fluids Eng.* **121(4)**, 781–787.
- DEEN, N.G., WESTERWEEL, J. & DELNOIJ, E. 2002 Two-phase PIV in bubbly flows: status and trends. *Chem. Eng. Technol* **25**, 97–101.
- DEEN, N.G., WESTERWEEL, J. & HJERTAGER, B.H. 2001 Upper limit of the gas fraction in PIV measurements in dispersed gas-liquid flows. In *5th International Conf. on Gas-Liquid and Gas-Liquid-Solid Reactor Eng., Melbourne, Australia*.
- DELNOIJ, E., WESTERWEEL, J., DEEN, N.G., KUIPERS, J.A.M. & VAN SWAALJ, W.P.M. 1999 Ensemble correlation PIV applied to bubble plumes rising in a bubble column. *Chem. Eng. Sc.* **54**, 5159–5171.
- EPPLER, R. & SHEN, Y.T. 1979 Wing sections for hydrofoils, Part 1: Symmetrical profiles. *J. Ship Res.* **23(3)**, 209–217.

- EPPLER, R. & SHEN, Y.T. 1981 Wing sections for hydrofoils, Part 2: Nonsymmetrical profiles. *J. Ship Res.* **25(3)**, 191–200.
- FARHAT, M. & AVELLAN, F. 2001 On the detachment of a leading edge cavitation. In *4th International Symposium on Cavitation, Pasadena, Ca, USA*.
- FARHAT, M., AVELLAN, F. & SEIDEL, U. 2002a Pressure fluctuation measurements in hydroturbine models. In *9th International Symposium on Transport Phenomena and Dynamics of Rotating Machinery*.
- FARHAT, M., GUENNOUN, F & AVELLAN, F. 2002b The leading edge cavitation dynamics. In *ASME Fluids Engineering Summer Division Meeting*.
- FOETH, E. J., VAN DOORNE, C. W. H., VAN TERWISGA, T.J.C. & WIENECKE, B. 2006 Time-resolved PIV and flow visualization of 3D sheet cavitation. *Exp. in Fluids* **40**, 503–513.
- FRANC, J.P. & MICHEL, J.M. 1985 Attached cavitation and the boundary numerical treatment. *J. Fluid Mech.* **154**, 63–60.
- FRANC, J.P. & MICHEL, J.M. 1988 Unsteady attached cavitation on an oscillating hydrofoil. *J. Fluid Mech.* **193**, 171–189.
- GOFF, J.A. 1957 Saturation pressure of water on the new Kelvin temperature scale. In *Transactions of the American society of heating and ventilating engineers, pp 347-354*.
- GREKULA, M & BARK, G. 2001 Experimental study of cavitation in a Kaplan model turbine. In *4th International Symposium on Cavitation, Pasadena, Ca, USA*.
- GUI, L., WERELEY, S.T. & KIM, Y.H. 2003 Advances and applications of the digital mast technique if particle image velocimetry experiments. *Meas. Sc. Technol.* **14**, 1820–1828.
- HALLANDER, J. & BARK, G. 1998 Some statistical properties of cloud cavitation on a foil in unsteady flow. In *ASME Fluid Eng. Div. Summer Meeting, Washington DC, USA*.
- HART, D.P., BRENNEN, C.E. & ACOSTA, W.L. 1990 Observations of cavitation on a three dimensional hydrofoil. In *25th Cavitation and Multiphase Flow Forum*.
- VAN DER HEUL, D., VUIK, C. & WESSELING, P. 2000 Efficient computation of flow with cavitation by compressible pressure correction. In *ECCOMAS, Barcelona*.
- HOEIJMAKERS, H.W.M., JANSSENS, M.E. & KWAN, W. 1998 Numerical simulation of sheet cavitation. In *3rd International Symposium on Cavitation, Grenoble, France*.
- VAN DER HOUT, A.J. 2007 The interaction of sheet and vortex cavitation. Master's thesis, Technical University of Delft.

- HUNT, J.C.R., WRAY, A. & MOIN, P. 1988 Eddies, stream, and convergence zones in turbulent flows. *Tech. Rep.*. Center for Turbulence Research Report CTR-S88.
- IYER, C.O. & CECCIO, S.L. 2002 The influence of developed cavitation on the flow of a turbulent shear layer. *Phys. Fluids* **14**(10), 3414–3431.
- JACOBS, E.N. & PINKERTON, R.N. 1931 Pressure distribution over a symmetrical airfoil section with trailing edge flap. *Tech. Rep.*. NACA.
- JEONG, J. & HUSSAIN, F. 1995 On the identification of a vortex. *J. Fluid Mech.* **285**, 69–94.
- JESSUP, S., BERBERCIJ, W. & REMMERS, K. 1994 Cavitation performance analysis of 49 naval surface ship propellers with standard and new blade sections. In *20th Symposium on Naval Hydrodynamics*.
- JIMENEZ, J. 1983 A spanwise structure in the plane mixing layer. *J. Fluid Mech.* **132**, 319–336.
- JOHNSON, V.E. & HSIEH, T. 1966 The influence of the trajectories of gas nuclei on cavitation inception. In *6th Symposium on Naval Hydrodynamics, Washington D.C.*
- KATO, H., YAMAGUCHI, H., MAEDA, M., KAWANAMI, Y. & NAKASUMI, S. 1999 Laser holographic observation of cavitation cloud on a foil section. *J. Visualization* **2**(1), 37–55.
- KATZ, J. 1984 Cavitation phenomena within regions of flow separation. *J. Fluid mech.* **140**, 397–436.
- KAWANAMI, Y., KATO, H., YAMAGUCHI, H., TAGAYA, Y. & TANIMURA, M. 1997 Mechanism and control of cloud cavitation. *J. Fluids Eng.* **119**(4), 778–795.
- KHALITOV, D.A. & LONGMIRE, E.K. 2002 Simultaneous two-phase PIV by two-parameter phase discrimination. *Exp. Fluids* **32**, 252–268.
- KIGER, K.T. & PAN, C. 2000 PIV technique for the simultaneous measurement of dilute two-phase flows. *J. Fluids Eng.* **112**, 811–818.
- KNAPP, R.T. 1955 investigation on the mechanics of cavitation and erosion damage. *Trans. ASME* pp. 1045–1054.
- KOOP, A.H. 2007 The structure of unsteady three-dimensional sheet cavitation, STW progress report. *Tech. Rep.*. University of Twente.
- KOOP, A.H., HOEIJMAKERS, H.W.M., SCHNERR, G.H. & FOETH, E.J. 2006 Design of a twisted cavitating hydrofoil using a barotropic flow method. In *6th International Symposium on Cavitation*.

- KOSIWCZUK, W., CESSOU, A., TRINITÈ, M. & LECORDIER, B. 2005 Simultaneous velocity field measurements in two-phase flows for turbulent mixing of sprays by means of two-phase PIV. *Exp. Fluids* **39**, 895–908.
- KRAG, B. & WEGNER, W. 1985 Generation of two-dimensional gust fields in subsonic wind tunnels. *Tech. Rep.*. Institut für Flugmechanik, Deutsches Forschungs- und Versuchsanstalt für Luft- und Raumfahrt e.V.
- KUBOTA, A., KATO, H. & YAMAGUCHI, H. 1992 A new modeling of cavitation flows: a numerical study of unsteady cavitation on a hydrofoil section. *J. Fluid Mech.* **240**, 59–96.
- KUBOTA, A., KATO, H., YAMAGUCHI, H. & MAEDA, M. 1989 Unsteady structure measurement of cloud cavitation on a foil section using conditional sampling technique. *J. Fluids Eng.* **111**, 204–210.
- KUIPER, G. 1981 Cavitation inception on ship propeller models. PhD thesis, Technical University of Delft.
- KUIPER, G. 1982 Some experiments with specific types of cavitation on ship propellers. *J. Fluids Eng.* **1**, 105–114.
- KUIPER, G. 2001 New developments around sheet and tip vortex cavitation on ships' propellers. In *4th International Symposium on Cavitation, Pasadena, Ca, USA*.
- KUNZ, R.F., BOGER, D.A., STINEBRING, D.R., CHYZEWSKI, T.S. & GIBELING, H.J. 1999 Multi-phase CFD analysis of natural and ventilated cavitation about submerged bodies. In *ASME/JSME Joint Fluids Engineering Conference*.
- LABERTEAUX, K.R. & CECCIO, S.L. 2001 Partial cavity flows Part 2. Cavities forming on test objects with spanwise variation. *J. Fluid Mech.* **431**, 43–63.
- DE LANGE, D.F. 1996 Observations and modeling of cloud cavitation behind a sheet cavity. PhD thesis, University of Twente, the Netherlands.
- DE LANGE, D.F. & DE BRUIN, G.J. 1998 Sheet cavitation and cloud cavitation, re-entrant jet and three-dimensionality. *Appl. Scientific Res.* pp. 91–114.
- DE LANGE, D.F., DE BRUIN, G.J. & VAN WIJNGAARDEN, L. 1993 Observations of cloud cavitation on a stationary 2D profile. In *IUTAM-symposium (Bubble Dynamics and Interface Phenomena)*, Birmingham, UK.
- LASHERAS, J. C., CHO, J. S. & MAXWORTHY, T. 1986 On the origin and evolution of streamwise vortical structures in a plane, free shear layer. *J. Fluid Mech.* **172**, 231–258.
- LASHERAS, J. C. & CHOI, H. 1988 Three-dimensional instability of a plane free shear layer: an experimental study of the formation and evolution of streamwise vortices. *J. Fluid Mech.* **189**, 53–86.

- LE, Q., FRANC, J.P. & MICHEL, J.M. 1993*a* Partial cavities: Global behavior and mean pressure distribution. *J. Fluids Eng.* **115**, 243–248.
- LE, Q., FRANC, J.P. & MICHEL, J.M. 1993*b* Partial cavities: Pressure pulse distribution around cavity closure. *J. Fluids Eng.* **115**, 249–254.
- LECOFFRE, Y. & BONNIN, J. 1979 Cavitation tests and nucleation control. In *ASME Symposium on Cavitation Inception*.
- LINDAU, O. & LAUTERBORN, W. 1999 Laser-produced cavitation - Studied with 100 million frames per second. In *15th International Symposium on Nonlinear Acoustics*.
- LINDKEN, R. & MERZKIRCH, W. 2002 A novel PIV technique for measurements in multiphase flows and its application to two-phase bubbly flows. *Exp. Fluids* **33**, 814–825.
- LINDKEN, R., WESTERWEEL, J. & WIENEKE, B. 2005 Development of a self-calibrating stereo μ -PIV system and its application to the three-dimensional flow in a T-shaped mixer. In *6th Int. Symp. on PIV, Pasadena, California, USA*.
- LIU, Z., SATO, K. & BRENNEN, C.E. 1993 Cavitation nuclei population dynamics in a water tunnel. In *ASME Cavitation and Multiphase Flow*.
- MCKENNEY, E.A. & BRENNEN, C.E.A. 1994 On the dynamics of acoustics of cloud cavitation on an oscillating hydrofoil. *Fluid Machinery and Devices* **190**, 195–202.
- MEI, R. 1996 Flow fidelity of flow tracer particles. *Exp. in Fluids* **22**, 1–13.
- MEIBURG, E. & LASHERAS, J.C. 1988 Experimental and numerical investigation of the three-dimensional transition in plane wakes. *J. Fluid Mech.* **190**, 1–37.
- METTIN, R., KREFTING, D., APPEL, J., KOCH, P. & LAUTERBORN, W. 2001 Stereoscopic high-speed recording of bubble structures. In *3rd Conference on Ultrasound in Processing*.
- VAN DER MEULEN, J.H.J. & YE, Y.P. 1982 Cavitation inception scaling by roughness and nuclei generation. In *14th Symposium on Naval Hydrodynamics*.
- MICHEL, J.P. 1978 Demi-cavité formée entre une paroi solide et un jet plan de liquide quasi parallèles: Approche théorique. *Tech. Rep.*. DRME 77/352 N4 Report.
- O' HERN, T.J. 1990 An experimental investigation of turbulent shear flow cavitation. *J. Fluid Mech.* **215**, 365–391.
- OKAMOTO, K. 2001 PIV Challenge. www.pivchallenge.org, case A.
- PASQUERO, C., PROVENZALE, A. & WEISS, J.B. 2002 Vortex statistics from Eulerian and Lagrangian time series. *Phys. Rev. Lett.* **89** (28).

- PATTERSON, J.B. & E.C., MORRIES. 1994 Measurement of absolute water density, 1°C to 40°C. *Metrologia* **31**, 277–288.
- PEREIRA, F. 1997 Prédiction de l'érosion de cavitation : Approche énergétique. PhD thesis, École Polytechnique Fédérale de Lausanne.
- PEREIRA, F., FARHAT, N. & AVELLAN, F. 1993 Dynamic calibration of transient sensors by spark generated cavity. In *IUTAM symposium on Bubble Dynamics and Interface Phenomena, Birmingham, UK*.
- RAFFEL, M., WILLERT, E. & KOMPENHANS, J. 1998 *Particle Image Velocimetry*. Springer.
- REISMAN, G.E., MCKENNEY, E.A. & BRENNEN, C.E. 1994 Cloud cavitation on an oscillating hydrofoil. In *20th Symposium on Naval Hydrodynamics, Santa Barbara, California*.
- REISMAN, G.E., WANG, Y.C. & BRENNEN, C.E. 1998 Observations of shock waves in cloud cavitation. *J. Fluid Mech.* **355**, 255–283.
- ROOD, E.P. 1991 Review - Mechanisms of cavitation inception. *J. Fluids Eng.* **113**, 163–175.
- SATO, K. & SHIMOJO, S. 2003 Detailed observations on a starting mechanism for shedding of cavitation cloud. In *5th International Symposium on Cavitation*.
- SCHMIDT, S.J., SEZAL, I.H. & SCHNERR, G.H. C 2006 Compressible simulation of high-speed hydrodynamics with phase change. In *European Conference on Computational Fluid Dynamics*.
- SCHNERR, G.H., SCHMIDT, S.J., SEZAL, I.H. & THALHAMER, M. 2006 Shock and wave dynamics of compressible liquid flows with special emphasis on unsteady load on hydrofoils and on cavitation in injection nozzles. In *Sixth International Symposium on Cavitation, Wageningen, The Netherlands*.
- SENOÇAK, I. & SHYY, W. 2002 Evaluation of cavitation models for Navier-Stokes equations. In *ASME FEDSM2002-31001*.
- SHEN, Y.T. 1985 Wing sections for hydrofoils, Part 3: Experimental verifications. *J. of Ship Res.* **29(1)**, 39–50.
- SHEN, Y.T. & GOWING, S. 1986 Pressure measurements on an oscillating foil in fully wetted and cavitating conditions. In *1st International symposium on cavitation*.
- SHRIDHAR, G. & KATZ, J. 2000 Flow structure and modeling issues in the closure region of attached cavitation. *Phys. Fluids* **12(4)**, 895–911.

- SHRIDHAR, G., KATZ, J. & KNIO, O. 1999 The flow structure in the near field of jets and its effect on cavitation inception. *J. Fluid Mech.* **398**, 1–44.
- STUTZ, B. 2003 Influence of roughness on the two-phase flow structure of sheet cavitation. *J. Fluids Eng.* **125**, 652–659.
- STUTZ, B. & REBOUD, J.L. 1997 Experiments on unsteady cavitation. *Exp. in Fluids* **22**, 191–198.
- TAKAHASHI, S., WASHIO, S., UEMURA, K. & OKAZAKI, O. 2003 Experimental study of cavitation starting at and flow characteristics close to the point of separation. In *5th International Symposium on Cavitation*.
- TASSIN LEGER, A.L., BERNAL, L.P. & CECCIO, S.L. 1998 Examination of the flow near the leading edge of attached cavitation, Part 2: Incipient breakdown of two-dimensional and axisymmetric cavities. *J. Fluid Mech.* **376**, 91–113.
- TASSIN LEGER, A.L., LI, C.Y., CECCIO, S.L. & BERNAL, L.P. 1995 Velocity field measurements of cavitating flows. *Exp. in Fluids* **20**, 125–130.
- VAN TERWISGA, T.J.C., KUIPER, G. & VAN RIJSBERGEN, M.X. 1999 On experimental techniques for the determination of tip vortex cavitation on ship propellers. *Tech. Rep.. MARIN*.
- THEODORSEN, T. & GARRICK, I.E. 1933 General potential theory of arbitrary wing sections. *Tech. Rep.. NACA ACR No. L4F16*, Report 452.
- ULLUM, U., SCHMIDT, J. J., LARSEN, P. S. & MCCLUSKEY, D. R. 1998 Statistical analysis and accuracy of PIV data. *J. Visualization* **1(2)**, 205–216.
- VAZ, G. 2005 Modelling of sheet cavitation on hydrofoils and marine propellers using boundary element methods. PhD thesis, Instituto Superior Técnico, Lisbon, Portugal.
- VILLAT, H. 1914 Sur la validité des solutions de certain problem d'hydrodynamique. *J. de Mathematiques* **6(10)**, 231–290.
- WALLIS, G.B. 1969 *One-dimensional two-phase flow*. McGraw-Hill Book Co.
- WATANABE, M. & PROSPERETTI, A. 1994 The effect of gas diffusion on the nuclei population downstream of a cavitation zone. *Cavitation and Gas-Liquid Flow in Fluid Machinery and Devices* **190**, 211–220.
- WESTERWEEL, J. 1993 Digital particle image velocimetry; Theory and application. PhD thesis, Technical University of Delft.
- WESTERWEEL, J. 1997 Fundamentals of digital particle image velocimetry. *Measuring Sci. and Technol.* **8**, 1379–1392.

- VAN WIJNGAARDEN, E., BOSSCHERS, J. & KUIPER, G. 2005 Aspects of the cavitation propeller tip vortex. In *ASME Fluids Engineering Division Summer Meeting and Exhibition*.
- WIKSTRÖM, N. & BARK, G. 2003 Large Eddy Simulation for cavitating submerged objects. In *Eighth International Conference on Numerical Ship Hydrodynamics*.
- WOSNIK, M., QIN, Q. & ARNDT, R.E.A. 2006 Identification of large scale structures in the wake of cavitating hydrofoils using LES and time-resolved PIV. In *International Symposium on Cavitation*.
- WU, T. Y. 1972 Cavity and wake flows. *Annu. Rev. Fluid Mech.* **4**, 243–284.
- YU, P.-W. & CECCIO, S. L. 1996 Diffusion induced bubble populations downstream of a partial cavity. In *ASME Symposium on Cavitation and Gas-Liquid Flows in Fluid Machinery*.

Acknowledgements

First of all, I would like to thank Frits Sterk, Hans van der Hek, and Peter Poot of the support staff of the section Ship Hydromechanics at the University of Delft who, Gratia Leges, assisted in keeping the tunnel operational. I assume you too have enjoyed walking the short one-hundred-and-fifty-meter stroll to-and-fro the cavitation tunnel to repair a small incident or to avoid a minor disaster, just as I have enjoyed the countless hours with a soldering iron, or behind the milling machine and the lathe.

I would like to thank Do Ligtelijn of Wärtsilä Propulsion Netherlands for his presence and contribution during our informal project meetings where the latest results were presented.

Of these results, half of them were from Arjen Koop, the numerical counterpart from Twente University of the work group. I enjoyed your presentations during which you explained the basis of your work with great precision and sincerity.

Cas van Doorne helped me during the first year of the project with the trial PIV setup and during that time significant progress was achieved. It was also great to work with someone who was also of the opinion that July and August are best spent in hermetically-sealed laboratories without ventilation or air conditioning (except for the equipment). Arne van der Hout assisted me during my final year, first for his master thesis work and later as a project member, working on the idiosyncratic local pressure and force measurements. I would like to thank both of you for your help.

The PIV equipment was periodically rolled out of the Laboratory of Aero & Hydrodynamics at the faculty of Mechanical Engineering of the University of Delft to the cavitation tunnel. I would like to thank Jerry Westerweel for his cooperation and use of the instrumentarium and Wilco Tax for aiding in rolling and helping to set up the equipment.

Je voudrais remercier Dr. Mohamed Farhat pour avoir facilité ma visite au Laboratoire Machine Hydrauliques à l'École Polytechnique Fédérale de Lausanne entre le pinot noir du canton de Vaud et ses mesures des pressions. Par ailleurs, je souhaiterais exprimer ma gratitude à Philippe Ausoni pour m'avoir apporté son aide au utilisation du tunnel de cavitation à grande vitesse.

I am thankful for Gert Kuiper's role as my unofficial supervisor and the discussions we have had on the finer issues of the measurements and interpretation of the results. I would like to thank Harry Hoeijmakers for his efforts as my indirect supervisor and his thorough proof-reading on this thesis. I would like to thank my direct supervisor, Tom van Terwisga, for his enthusiastic efforts in keeping the project on track and for the many philosophical discussions we have had on metaphysical subjects such as structure, deadlines, and planning.

This project has been financed by the Royal Netherlands Navy and the Dutch Technology Foundation STW. I would like to thank both institutions for their contributions. Finally, I would like to thank all the industrial members of the user committee for their participation and especially Leo Korstanje and Corine Meulemans of STW for chairing our formal meetings and their genuine interest in the project.

Evert-Jan Foeth

6 Maart 2008
Wageningen

Curriculum Vitae

Evert-Jan Foeth was born on October 10th 1975 in Ede, the Netherlands. In 1994, he graduated from high school (VWO), 't Hooghe Landt College in Amersfoort. He studied Naval Architecture and Maritime Engineering at the Technical University of Delft from 1994 to 2000. His thesis work was supervised by professor Gert Kuiper, based on laboratory work on cavitation performed at the University of Michigan, Mechanical Engineering and Applied Mechanics, supervised by professor Steven L. Ceccio. After his graduation, he stayed for nearly three years at Wärtsilä Propulsion Netherlands at the ship propulsion hydrodynamics department. In 2003 he worked with professor Gert Kuiper on the subject of cavitation erosion at the Maritime Research Institute Netherlands (MARIN). The resulting paper was awarded the Lewis F. Moody award by the American Society of Mechanical Engineers (ASME) for the most outstanding original paper dealing with the practice of fluids engineering. Later that year he started to work on a PhD on the structure of three-dimensional sheet cavitation performed at the cavitation tunnel in Delft under the supervision of professor Tom van Terwisga, including a brief stay at the Laboratoire Machine Hydraulique at the École Polytechnique Fédérale de Lausanne with Dr. Mohamed Farhat. After having finished his PhD research in 2007, he returned to MARIN to work at the ship propulsion department.

